Experimental Analysis of the Impacts of Aerosolized Liquids on Flare Emissions

by

Olanrewaju W. Bello

A thesis submitted in partial fulfillment of the requirements
for the degree of Doctor of Philosophy

Department of Mechanical Engineering
University of Alberta

Abstract

This study characterized flare-like flame emissions and improved methods of reducing flare emissions during well completion operations in the upstream oil and gas industries. Flowback fluids are water-based solutions that return to the earth's surface with extracted oil and gas during and after the completion of hydraulic fracturing. Droplets of the flowback fluids are likely to become entrained in the flare gas and burn in an exposed flame. Sodium and chloride ions, which are prevalent in flowback fluids, can influence the particle emissions from flaring. In trying to mitigate flare emissions, steam-assisted flares, which are often used in the downstream oil and gas industries as a strategy to produce "smokeless" combustion, were compared with liquid water. Three fuels were used to investigate this comparison: pure propane, pure methane, and a mixture of 90% methane and 10% propane, the latter approximating the typical volumetric higher heating value of Alberta flare gas. Both steam and liquid water were injected into the flare through the fuel stream. The result of the investigation suggests that liquid water-assisted flares in the oil and gas industries would likely produce lower emissions with a lower operating cost than steam-assisted flares. This finding initiated the second study, in which liquid water injected through the fuel stream was compared with liquid water injected through the air stream into the flare. Liquid water with impurities (NaCl) was also investigated because NaCl is a surrogate species for the impurities contained in the water used at offshore and downstream oil and gas facilities. Liquid water injection through the air stream (external injection) directed very close to the base of the flame ensured water was present early in the combustion process and reduced NO_x emissions to a greater extent compared to when the water was injected through the fuel stream. External liquid water injection into turbulent non-premixed flames can effectively reduce black carbon without a need for costly boiler operation to produce steam. NaCl impurities in the injected liquid water cause an

increase in soot emissions. The increase in soot emissions due to NaCl addition initiated the third study.

The third study investigates the effect of sodium chloride on the charge state of soot nanoparticles evolved in a laminar diffusion flame by measuring the soot particle size distribution (PSD), average charge per particle, and charge fraction at various locations within the flame. A charged monodispersed coagulation model was employed to ascertain whether coagulation was the primary cause of the differences observed in particle emissions when NaCl is introduced into flames. The effect of sodium chloride on a methane flame was investigated by comparing the experimentally measured data for methane-only and methane-NaCl flames. The addition of NaCl particles to the laminar diffusion flame did not have a significant effect on the particles in nucleation region of the flame. The majority of the incipient soot particles in both flames are uncharged, and their sizes are nearly the same, with diameters of approximately 5 nm or less. However, the size of soot particles differs by approximately 10% to 25% between methane-only and methane-NaCl flames in the coagulation-dominated region (i.e., between HAB 47 mm and 55 mm) of the flame. The net charge on soot particles within the coagulation region of the methane-only flames is negative while it changes to positive with NaCl addition. The fraction of charged particles and ion concentration decreases with NaCl addition within the coagulation region and more uncharged particles are witnessed. Interestingly, the coagulation model results for charged and uncharged particles in coagulation processes were identical. The study reveals that the smaller particle size in methane-NaCl flames is primarily a result of oxidation rather than a reduction in particle charge. NaCl promotes oxidation in specific flame regions, leading to differences in soot evolution between methane-only and methane-NaCl flames.

Preface

This study involved the improvement of a lab-scale flare setup with and without water- and steam-assist. The burner setup described in Chapter 3 for the liquid water-assisted flare design was done by me. I ran the experiments and did a thorough data analysis for Chapters 2, 3, and 4 myself, except Chapter 2 for which Milad Zamani helped me in running the steam-assisted flare experiments and collecting the data and Chapter 3 for which Ehsan Abbasi-Atibeh helped me in running the particle image velocimetry (PIV) experiment. One of the research projects conducted, although not incorporated into this thesis, was a collaborative research initiative led by Dr. Jason Olfert at the University of Alberta.

Chapters 2 of this thesis has been published as

- W. O. Bello, M. Zamani, E. Abbasi-Atibeh, W. L. Kostiuk and S. J. Olfert, "Comparison of emissions from steam- and water-assisted lab-scale flames.," Fuel, vol. 302, p. 121107, 2021. https://doi.org/10.1016/j.fuel.2021.121107.

In this journal article, I undertook the responsibility for conducting experiments, collecting and analyzing data, and writing the manuscript. M. Zamani provided assistance with the experiments and data collection. J.S. Olfert and L.W. Kostiuk served as supervisory authors, contributing to concept formation and manuscript editing.

Chapters 3 of this thesis has been published as

- W. O. Bello, E. Abbasi-Atibeh, W. L. Kostiuk and S. J. Olfert, " Effects of external injection of deionized water and water with impurities on Water-assisted flares.," Fuel, vol. 340, p. 127602, 2023. https://doi.org/10.1016/j.fuel.2023.127602.

In this journal article, I undertook the responsibility for conducting experiments, collecting and analyzing data, and writing the manuscript. E. Abbasi-Atibeh provided assistance with the PIV experiment, data collection and manuscript editing. J.S. Olfert and L.W. Kostiuk served as supervisory authors, contributing to concept formation and manuscript editing.

Chapters 4 of this thesis has not yet been published as

- W. O. Bello, M. Kazemimanesh, W. L. Kostiuk and S. J. Olfert, " The Effect of Sodium Chloride on the Charge State of Soot Particles in a Laminar Diffusion Flame," Yet unpublished, University of Alberta, 2023.

In this yet unpublished article, I undertook the responsibility for conducting experiments, collecting and analyzing data, and writing the manuscript. M. Kazemimanesh, J.S. Olfert and L.W. Kostiuk served as supervisory authors, contributing to concept formation and manuscript editing.

Published article not included in this thesis as

- T. Sipkens, U. Trivanovic, A. Naseri, W. O. Bello, A. Baldelli, M. Kazemimanesh, A. K. Bertram, L. W. Kostiuk, C. J. Corbin, S. J. Olfert and N. S. Rogak, "Using two-dimensional size distributions to better understand the mixing state of soot and salt particles produced in gas flares.," Journal of Aerosol Science, vol. 158, p. 105826, 2021. https://doi.org/10.1016/j.jaerosci.2021.105826.

In this journal article, I was responsible for conducting experiments, collecting and analyzing data for particle size distribution.

Acknowledgments

I would like to extend my sincere thanks to my supervisors, Professor Jason Scott Olfert and Professor Larry William Kostiuk, for sharing their wealth of experience and knowledge and for their consistent advice and support during my studies at the University of Alberta. Thank you for being a smart mentor, an enthusiastic leader, and a kind friend.

Professor Bob Koch is greatly appreciated for serving on my PhD supervisory committee. I also thank Professor Andrew Martin and Professor Lexuan Zhong for serving as the arm's length on my candidacy examination committee. It was an honour to have Professor Ge Li serve as the chair of my candidacy examination. All their insights into my work were priceless.

I would like to thank Dr. Ehsan Abbasi-Atibeh for providing support in the area of particle image velocimetry (PIV) analysis for my second project and Dr. Mohsen Kazemimanesh for his support on the Santoro burner's experiment. I am also grateful to all my colleagues in the University of Alberta thermofluid research laboratory, specifically Kerry Cheng and Milad Zamani.

Lastly, I owe my gratitude to my wife for her unwavering sources of encouragement and support. I also want to express my gratitude to her because her love and support have made this thesis possible. I would like to gratefully acknowledge the financial support of the Natural Sciences and Research Council (NSERC) of Canada through the FlareNet grant. I would also like to acknowledge the incredible support of the Nigerian government (Petroleum Technology Development Fund Overseas Scholarship).

Table of Contents

List of Tables

List of Figures

Nomenclature

List of Symbols

F_z	upward rate of momentum of the fuel-assist mixture (mN)
z	axial direction of the flame or height above the exit of the burner (m)
$\dot{m}_f$	fuel mass flow rate (kg/s)
$\dot{m}_a$	assist mass flow rate (kg/s)
$\bar{v}_f$	average fuel exit velocity (m/s)
$\bar{v}_a$	average assist exit velocity (m/s)
$\bar{v}$	average exit velocity for gases or vapors (m/s)
ρ	fluid density (kg/m^3)
A	cross-sectional area (m^2)
$\dot{B}$	initial upward rate of the buoyancy force (mN/s)
ρ_{air}	ambient air density (kg/m^3)
ρ_f	fuel density (kg/m^3)
ρ_a	assisting fluid density (kg/m^3)
$\rho_{product}$	combustion exhaust product density (kg/m^3)
$\dot{V}_f$	fuel volume flow rate (m^3/s)

$\dot{V}_{\mathrm{a}}$	assisting fluid volume flow rate (m^3/s)
$\dot{V}_{\mathrm{product}}$	combustion products volume flow rate (m^3/s)
g	gravitational constant (9.81 m/s^2)
$EI_{\mathrm{NO}x}$	NO_x Emission indices (g/kg of fuel)
EI_{BC}	Black carbon Emission indices (g/kg of fuel)
MFR	Mass Flow Ratio
k_{g}	gas thermal conductivity
h_{fg}	latent heat of evaporation
P_{∞}	partial pressure of the gas
T_{d}	droplet temperature
T_{∞}	temperature of the gas
D_{v}	diffusion coefficient of water vapour
ρ_{p}	density of the water droplet
R	universal gas constant
θ	Atomizer's angle (degree)
z_1, z_2, z_3	Atomizer's axial directions (mm)
r	Atomizer radial direction (mm)
F_q	charge fraction

$\bar{q}$	average charge per particle
N_{total}	total particle number concentration (cm^{-3})
$N_{\text{uncharged}}$	number concentration of uncharged particles (cm^{-3})
I	electrometer current (Ampere)
e	electron charge (1.6×10^{-19} C)
Q	electrometer sample volumetric flow rate (m^3/s)
G	Fuchs correction factor
$W_{p,q}$	repulsive or attractive electrostatic force
$\beta_{p,q}$	coagulation coefficient between charged particles (m^3/s)
β^*	coagulation coefficient of uncharged particles (m^3/s)
i, j	Particle sizes (m)
p, q	number of charges per particles
N	Number concentration (m^{-3})
N_{+1}	Number concentration of +1 charge particles (m^{-3})
N_{-1}	Number concentration of -1 charge particles (m^{-3})
N_0	Number concentration of neutrally charge particles (m^{-3})
$B(i,p)$	mobility of particles of size i and charge p (s/kg)
d_p	Particle median diameter (nm)

C_c	Cunningham slip correction factor
μ	viscosity of the gas (Pa.s)
ε_0	permittivity of free space (8.855×10^{-12} F/m)
k_b	Boltzmann's constant (1.3806×10^{-23} J/K)
T	absolute flame temperature (K)
d_p, d_q	diameter of the charged particles (nm)
λ_p	particle mean free path (nm)
$\alpha_{p,q}$	Fuchs stability function
a	Constant flame gas acceleration due to buoyancy (25 m/s^2)
U_z	axial flame gas velocity (m/s)
t	Flame residence time (second)

List of Acronyms

PSD	Particle Size Distribution
PIV	Particle Image Velocimetry
IEA	International Energy Agency
BC	Black carbon
NO_x	Oxides of nitrogen
$PM_{2.5}$	Particulate matter of 2.5 μm diameter
US	United states
PAH	Polycyclic Aromatic Hydrocarbon
HACA	H-abstraction-C_2H_2 addition
HHV_V	Volumetric Higher Heating Value
SLPM	Standard Litre Per Minute
PAX	Photoacoustic extinctiometer
SMPS	Scanning Mobility Particle Sizer
DMA	Differential Mobility Analyzer
UCPC	Ultrafine Condensation Particle Counter
AFT	Adiabatic Flame Temperature
NASA	National Aeronautics and Space Administration

CEA	Chemical Equilibrium with Applications
CMD	Count Median Diameter
GSD	Geometric Standard Deviation
SLR	Single-lens reflex
ASTM	American Society for Testing and Materials
HAB	Height above burner
UHC	Unburned hydrocarbons
Nd:YLF	Neodymium-doped Yttrium Lithium Fluoride
FFT	Fast Fourier Transform
GMM	Gaussian Mixture Models

Chapter 1

Introduction

This chapter provides an overview of flaring in the oil and gas sector and its effects, as well as information on downstream oil and gas facilities, upstream oil and gas sites, soot formation, and the hydrodynamic, thermodynamic, and chemical effect of water on soot. It also outlines the problem statement and the set of thesis objects.

1.1 Flaring

Fossil fuels, including coal, oil, and natural gas, account for almost 80% of the world's energy supply [1]. Global energy consumption is forecast to rise gradually over the coming years, with emerging economies driving the majority of this growth. Estimates show that global oil demand will rise by 0.8% per year until 2030, leading to the demand of approximately 103 million barrels per day [2]. This reveals that more oil and natural gas extraction will continue, and more extraction will eventually lead to more flaring of unwanted gases. Flaring is the open flame combustion of unwanted or waste hydrocarbon or associated gases from refineries, oil wells, and chemical industries [3]. Two methods by which oil and gas production sites dispose waste and unwanted gases are venting and flaring [4]. Flaring is generally preferred because of its lower potential for global warming. For example, the global warming potential of CH_4 is 28-36 times higher than carbon dioxide (CO_2), which is a byproduct of CH_4 combustion, thus making the flaring of unwanted flammable gases at oil and gas production sites preferable to venting [5]. According to

the World Bank's latest report [6], approximately 150×10^9 m^3 of natural gas is flared annually worldwide at oil and gas production sites, which increased by 3% between 2018 and 2019 [6]. More than 90% of global natural gas flaring occurs at upstream/offshore oil and gas production sites [5]. An analysis done in 2015 revealed a total of 13,605 flaring sites, with 12,227 of these being upstream, 861 downstream, and 517 industrial [5]. Moreover, according to the IEA methane tracker for 2020 [7], about 115 x 10^9 m^3 of methane was emitted through venting and leakage. Upstream oil and gas facilities refer to all that relate to the exploration and production of crude oil and natural gas. It also refers to the procedures required in drilling and bringing oil and natural gas deposits to the surface, often known as production, and this mostly occurs in the middle of nowhere. Downstream oil and gas facilities encompass everything involved in transforming crude oil and natural gas into different kinds of ready to use products. Among the most apparent products are Liquid petroleum gas, Naphtha, bitumen for road construction, aviation fuels, Lubricating oils, kerosene, and diesel [8].

While efficient flaring reduces CH_4 emissions [9], it is also known to release emissions such as, unburnt hydrocarbons, carbon monoxide (CO), oxides of nitrogen (NO_x), and soot, which is composed predominantly of black carbon (BC) [7]. Globally, it has been approximated that 38% of BC is released from fossil fuel combustion [10]. BC can affect rainfall patterns and cause earth surface material with high surface albedo like snow or ice to melt thereby reducing their surface albedo, because it acts as a radiative forcing agent. In the 20^{th} century, it is assumed to be one of the causes of artic warming and contributes to global mean surface warming [10, 11]. The BC total global emission is estimated in the industrial era to be 14,000 Gg/year with radiative forcing value of 1.1 Wm^{-2} and 90% uncertainty bounds of 0.17 to 2.1 Wm^{-2} [11]. In addition, Janssen et al. [12], have argued that particles from combustion sources are more closely connected to poor human

health than particles from other sources. They also classified BC as a particulate matter with aerodynamic diameters of less than 2.5 μm ($PM_{2.5}$). The health effect of BC cannot be overemphasized because it has been linked to cardiovascular and pulmonary diseases [13]. Landrigan et al. [13], related $PM_{2.5}$ pollution to be the cause of myocardial infarction, hypertension, congestive heart failure, arrhythmias, cardiovascular mortality, chronic obstructive pulmonary disease, and lung cancer. They further stated that $PM_{2.5}$ might be connected to the rise in the occurrence of premature birth and low birth weight.

NO_x being another exhaust substance which is an environmentally hazardous substance released during flaring operation. NO_x mainly includes nitric oxide (NO) and nitrogen dioxide (NO_2). NO is the main form of oxides of nitrogen that are majorly found in flaring emissions [14]. Therefore, if NO released from flaring react with oxygen, it produces ozone within the lower atmosphere ($NO + HC + O_2 + \text{sunlight} \rightarrow NO_2 + O_3$), which is undesirable [14, 15]. Moreover, ozone is a substance that protects the upper atmosphere of the earth by shielding the earth and preventing direct high intensity of ultraviolent rays. In contrast, the same ozone is dangerous to human health when closer to humans or if found in the lower part of the atmosphere. It causes respiratory problems in humans. In addition, [14] also said NO_2 has the ability to delay chemical pneumonitis and pulmonary edema, which makes the substance highly toxic and hazardous in nature. It has a suffocating odour. The quest to reduce all these effects brings us to the question of how to suppress the formation of soot and NO_x in flaring.

1.2 Flaring at downstream oil and gas facilities (Assisted flares)

Hydrocarbon gas flaring at downstream oil and gas facilities is done mostly to dispose of unwanted gases during petrochemical processing or during an emergency. Flared gas consists of a mixture

of different gases, typically methane, ethane, propane, *n*-butane, isobutane, *n*-pentane, isopentane, 2,2-dimethylpropane, *n*-hexane, ethylene, propylene, 1-butene, carbon monoxide, carbon dioxide, hydrogen sulfide, hydrogen, oxygen, nitrogen, and water in varying proportions [16]. In recent years, growing concerns over environmental preservation have prompted most oil-producing and developed countries to impose stricter regulations on emissions [5, 17, 18, 19]. For example, in 2018, the Government of Canada finalized regulations for reducing 40-45% of methane (CH_4) emissions (released through venting and fugitive emission) by 2025 [7, 9, 20]. Also, many US State regulations require "smokeless" combustion (defined as a plume opacity of less than 20%) for the majority of the time a flare is operated in pressure-relieving applications at refineries and petrochemical facilities [21]. In light of such regulations, the oil and gas and petrochemical industries have made efforts to reduce soot emissions, which are one of the main factors now considered in flare design for refineries and petrochemical facilities [3, 15]. Typically, soot emissions are reduced by using "assisted" flares, which force steam, air, or liquid water into the combustion zone of the flare [15, 21, 22, 23, 24]. For steam-assisted flares, steam is entrained into the flare through either a series of steam injectors, a single pipe nozzle positioned at the center of the flare, or a manifold positioned around the edge of the flare tip. Air-assisted flares use either high-pressure air or a low-pressure forced-air system. The high-pressure air system uses the same injection method as described for steam-assisted flares, while the low-pressure forced-air system makes use of a blower to inject the air coaxially with the flare gas at the flare exit [21]. Water-assisted flares use multiple nozzles fitted to the flare head unit to inject an atomized spray of water into the combustion zone of the flare [25, 26, 27]. This particular use of assisting fluid is rare, being reserved mostly for horizontal flare applications and situations where there is a need to eliminate excess wastewater or brine [21]. Although assisted flares typically reduce emissions,

studies have shown that over-steaming [22] or over-watering [26] the flare can reduce flare combustion efficiency or extinguish the flare, resulting in high unburnt hydrocarbon or aldehydes emissions and poor hydrocarbon destruction efficiencies [21, 22, 23, 25, 26, 28]. The assisting fluids also control noise and flame luminosity or radiation [15, 29].

1.3 Flaring at upstream oil and gas sites (Unassisted flares)

Figure 1.1 shows a sketch of a typical upstream oil well site. The oil well is created by drilling the well and pumping/injecting a highly pressurized (upwards of 69,000 kPa [30]) fracturing fluid consisting of slick-water and sand deep into the well to create fractures which make the rock where oil and gas are trapped more permeable [31, 32, 33, 34]. Fractures in the rock allow oil and gas to flow to the well, where a jack pump extracts the oil. During the first four weeks of well completion, approximately 30% of the fracking fluid injected into the well returns to the Earth's surface with the extracted oil and gas as *flowback water*. Thereafter, *produced water*, which comprises of naturally occurring water in the formation, remaining hydraulic fluid, and chemical transformation products, also steadily rises with the oil and gas resources [31, 35, 36, 37, 38]. Notable chemical constituents of flowback and produced water include chloride, sodium, calcium, bicarbonate, sulfate, potassium, and magnesium [39, 40]. The difference between the flowback water and produced water is the change in the concentration of their chemical constituents and their corresponding total dissolved solids. The oil, gas and flowback or produced water that return to the earth's surface are directed to the separator [41, 42, 43] where the oil and gas are extracted. During the separation process, the flowback and produced water may aerosolize and enter the flare stream and potentially increase flare emissions [44].

To prevent the entrainment of wastewater into the flared gases after separation, a knockout drum (also called a flare drum, knockout pot or compression suction drum), is used to remove liquid droplets from the gas stream by slowing down the gases [45]. It is believed that only droplets less than 300 μm leave the knock out drum [45, 46]. The liquid entrainment into the flare may occur during the early stages of the well completion process (when the formation water is produced at its highest rate) or during the well-cleaning process, which may cause the separator on an upstream site to release surfactants carried by the crude oil or the flowback water's additives. These surfactants may in turn promote emulsification of the oil-water and thus the production of foam, which might further reduce the separator's efficiency and cause produced water droplets to exit the separator [46, 47, 48, 49]. The resulting aerosolized flowback liquid has the potential to mix with gases directed to the flare and thus possibly to affect its combustion efficiency and emissions [34, 50]. Recent research on flares in the Bakken region of North Dakota indicates that flowback fluid droplets were transported into the flares because sodium, one of the most dominant ions in flowback fluids, was found to be prevalent in the emission measurements [47]. Despite the widespread usage of hydrofracturing and the sizeable quantity of flaring that occurs globally, little is known about the impact of sodium chloride from flowback operations on the rate at which soot particles coagulate in flares.

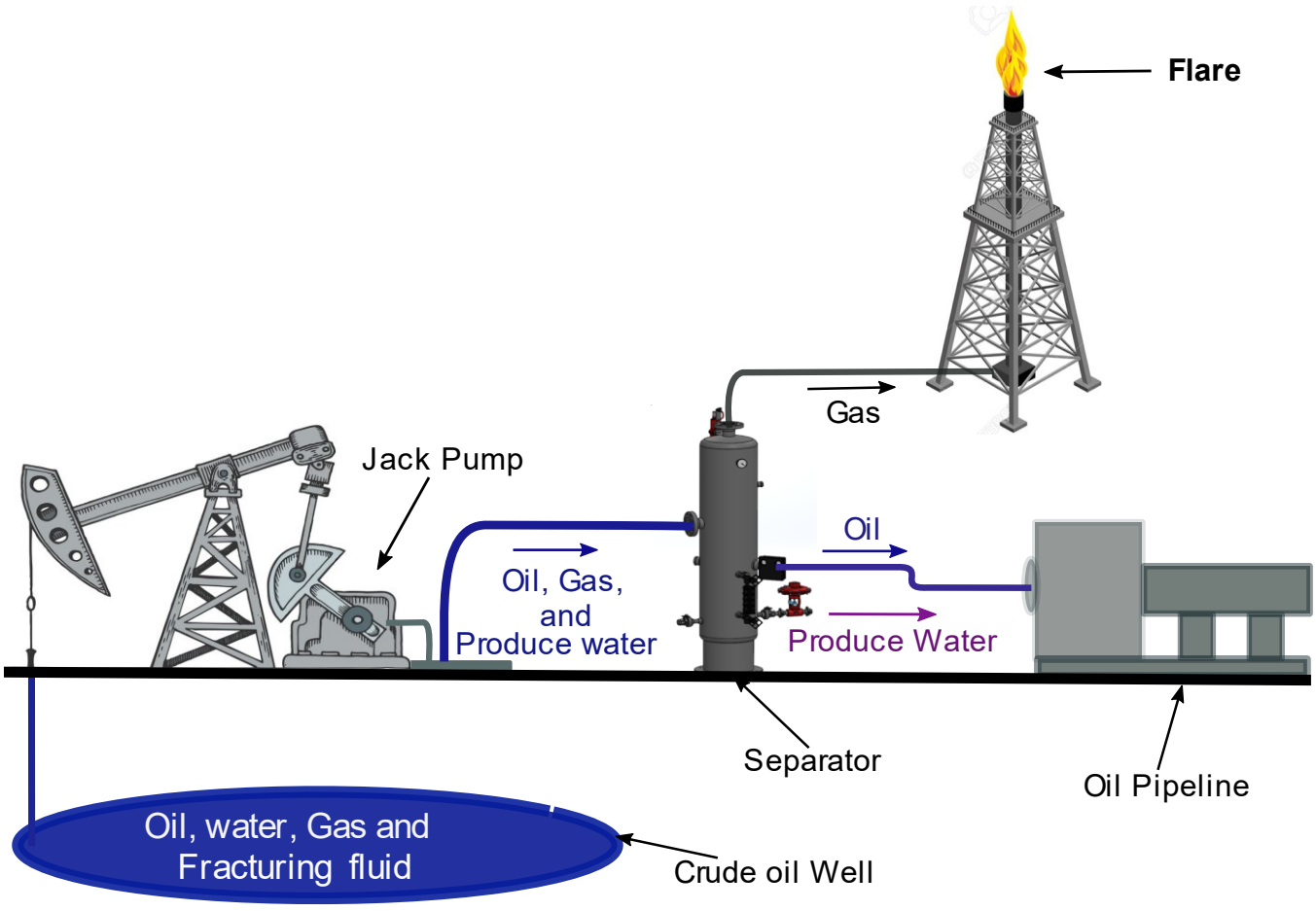

Figure 1.1: Oil well site. (Adapted from [197])

1.4 Soot formation

Soot is an end product of combustion consisting of chain-like aggregates of sphere-like units in the form of amorphous carbon [51]. As fuels are burnt, they produce soot particles in the high-temperature, fuel-rich regions of the flame. Soot particles from flames have been seen in a wide range of conditions, from laminar premixed [52-58] and diffusion flames [59-65] to turbulent

flames [66, 67, 68] and have been found to share common structures. According to the type of flame and the locations inside a particular flame, soot particles' nanostructure, coagulation and aggregation characteristics evolve. To understand how soot is formed, it is necessary to consider seven significant steps: fuel pyrolysis, PAH (Polycyclic Aromatic Hydrocarbon) formation, large PAH formation, soot inception, soot surface growth, soot aggregation, and oxidation. Figure 1.2 shows the pictorial view of the evolution of soot in flames.

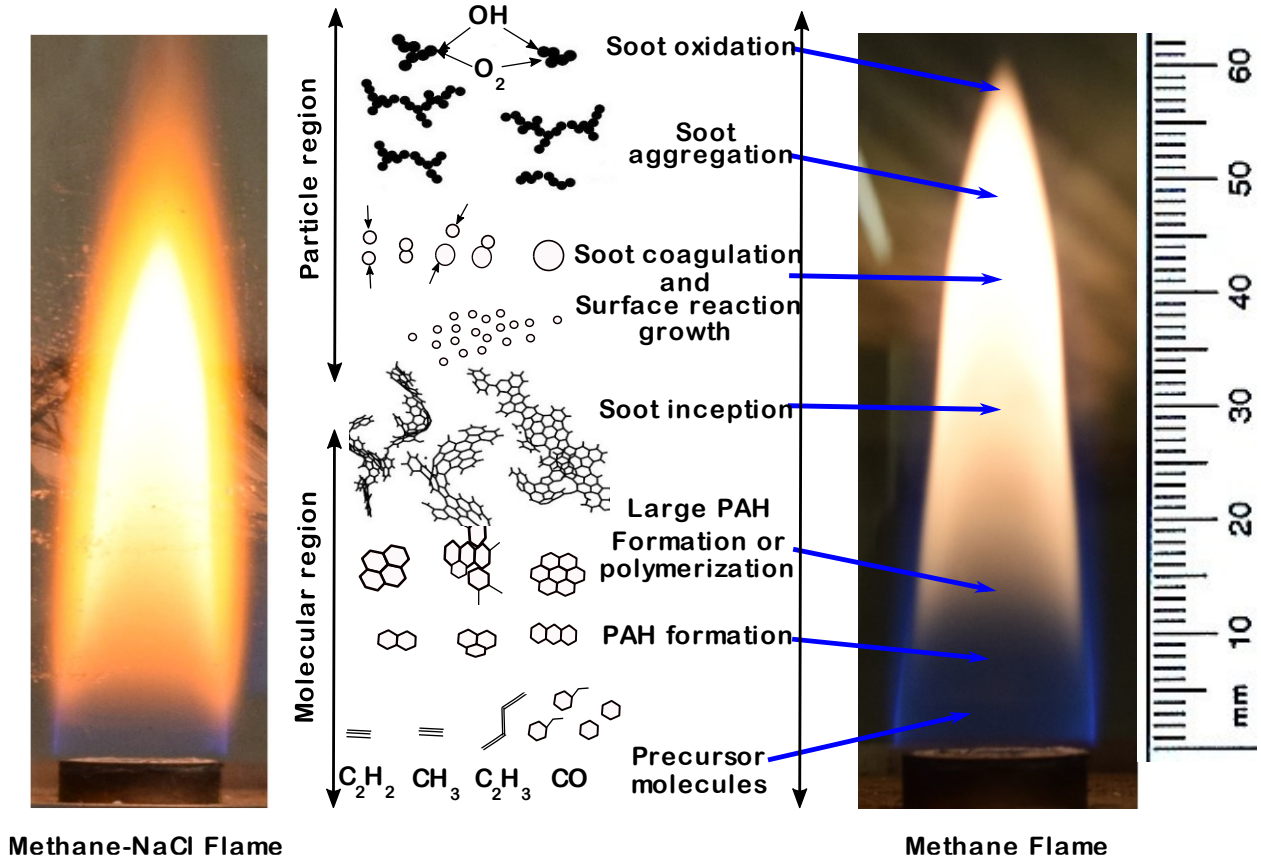

Figure 1.2: The evolution of soot in flames. (Adapted from [69])

The fuel pyrolysis zone of the flame is where the fuel undergoes thermal degradation at high temperature in the absence of oxygen to create precursor molecules (the first primary

hydrocarbons) [70]. Acetylene, methyl, and vinyl are presumed to be incipient species in soot formation. Frenklach [71] suggested that acetylene reacts with propargyl to form the first aromatic ring. Polycyclic aromatic hydrocarbons (PAHs) are considered the main precursor to soot [72]. As explained by Frenklach and Wang [73], PAHs grow through H-abstraction-C_2H_2 addition (HACA). The abstraction of hydrogen from aromatic molecules will form aromatic radicals, and these aromatic radicals will continue to react with acetylene molecules to create more aromatic rings, which are added to the existing ones to form large PAHs. The transition of the molecular precursors (PAHs) in the gas phase to particulate matter in the condensed phase is called soot inception or nucleation [74]. In premixed and diffusion flames, researchers like Öktem et al. [75], Megaridis and Dobbins [62], Wang [76], Chang et al. [77], Puri et al. [78], Santoro et al. [79], and De Falco et al. [80] have studied the development and properties of incipient soot particles. The incipient soot particles are almost spherical, 1–5 nm in diameter, and are also known as precursor nanoparticles. These nucleated materials are termed primary soot particles and start to undergo a surface growth process. In surface growth, acetylene is one of the dominant mass growth species [76]. The HACA-based soot growth mechanism at the surface of the particle increases the soot particle mass as well as the condensation of PAHs on the surfaces. Coagulation describes the collisional process between two particles due to their Brownian motion [81]. In spite of the fact that coagulation does not change the total mass of soot particles, it alters the particle size distribution and soot morphology and reduces the number concentration of soot. Coagulation usually occurs between a pair of large and small particles immediately after nucleation. Particle aggregation can occur either when soot primary particles collide and stick together to form fractal aggregates (chain-like structures) or when two soot aggregates aggregate together [71]. It is also important to note that soot inception, surface growth, coagulation, and aggregation may occur at

the same location in the flame. One other major process is soot oxidation, whereby the soot particle surface reacts with O_2 and OH radicals. The oxidation of soot with O_2 occurs in lean fuel conditions, while in rich fuel conditions OH is dominant [82]. This process reduces the number density and size of the soot particles. All the above-described soot formation processes occur in non-premixed and premixed flames.

1.5 Effect of alkali metals on soot formation and emissions

Several studies on soot formation and emissions have investigated the number of particles generated within and exiting the flame, and these investigations have revealed that introducing salt into the flames leads to an increase in the mass concentration of soot. [50, 83-88]. Salt has been seen to affect the oxidation and the coagulation of soot particles in flames. The introduction of NaCl into a flame yields noteworthy effects on radical concentrations, specifically those of H, O, O_2, and OH [89]. Earlier researchers have also indicated that the process of soot oxidation in flames is primarily associated with the interaction of hydroxyl radicals (OH) on the surface, and O_2 plays a secondary role [90-94]. A two-reaction mechanism ($Na + OH + M \leftrightarrow NaOH + M$ and $NaOH + H \leftrightarrow Na + H_2O$ [95, 96] or $K + OH + M \leftrightarrow KOH + M$ and $KOH + H \leftrightarrow K + H_2O$ [97, 98]) has been employed to elucidate the fast removal of OH and H radicals within the flame environment [99]. Chlorine has also been confirmed to be an indirect contributor to the reduction of OH radical concentration. The concentration of OH at different heights above the burner for a methane premixed flame has also been studied, and it has been confirmed that the concentration of OH reduces with the addition of alkali salt [100]. Also, Kazemimanesh et al. [83] discovered that NaCl inhibited soot oxidation by scavenging OH radicals at the flame's open tip. Previous research has shown that the introduction of alkali metals into a flame leads to a reduction in the size of soot

particles, mostly as a result of decreased coagulation. Consequently, these diminished soot particles exhibit enhanced susceptibility to oxidation [101].

Particle coagulation is an important soot growth process, which results in the soot particles growing in size while the soot concentration decreases. Haynes et al. [85] proposed that when alkali metals are added to the flame, the incipient soot particles are charged earlier, making them resistant to further coagulation and thereby resulting in an increased soot number concentration with smaller soot sizes. Kousaka et al. [102] further identifies that the combustion of salts as a process produces highly charged aerosols which affects the coagulation of charged particles. It was further reported that the coagulation of bipolar charged NaCl particles produced by a bipolar corona discharge led to an increase in the agglomeration size when compared with the ones without bipolar charging [103]. It has also been confirmed that coagulation process is hindered by electrostatic repulsion when unipolar-charged soot particles are present, but it is enhanced when there are bipolar-charged soot particles. This enhancement is due to electrical forces such as the image force, ion-induced Van der Waal's force and Coulomb attraction force [104]. In addition, the particle size distribution, the number density, and the morphology of soot are all shaped to some extent by coagulation. Primary particle diameter, temperature, and residence time are few of the characteristics that also affect soot coagulation [105]. The coagulation rate of aerosol particles in relation to their charge state has been studied experimentally and theoretically by several researchers [104, 106-113].

Moallemi et al. [84] used a co-annular burner to investigate the effect of NaCl on soot formation in a laminar methane diffusion flame and discovered that the addition of NaCl reduces coagulation of soot primary particles (increases their number concentration), which in turn causes a reduction in the mobility diameter of the agglomerates. However, there are two unique ideas for how alkali

salts influence the coagulation of soot in flames, both of which assume that the salts can become ionized due to their low ionization potential. The first idea, proposed by Bulewicz et al. [114], suggests that alkali metals reduce the number of soot particles by neutralizing soot precursors and suppressing their nucleation. The second idea proposes that alkali metals only interact with soot particles after the nucleation of soot particles and increase their charge, leading to smaller soot particles due to increased electrostatic repulsion [85]. However, Mitchell and Miller [101] suggest that most soot particles are neutralized by alkali salts, which then reduce coagulation rates and resulted to smaller soot particles, making them more susceptible to oxidative destruction. These conflicting views suggest that it is important to measure the soot formation process in flames with and without NaCl addition to understand the mechanisms that affect particle size and number concentration.

Adding NaCl into the flame can reduce NO_x emissions, as the existence of sodium in the combustion zone lowers the concentrations of active radicals, such as OH, H, and O, leading to less NO_x formation [89]. Roth [115] also showed that the scavenging of OH radicals in the flame by sodium hinders the oxidation of carbon species resulting in high BC emissions. Adding NaCl into the flame was confirmed by Morgan and Rosocha [116] to delay the formation of larger polycyclic aromatic hydrocarbons (PAHs).

1.6 Physical and chemical effect of water on flare emissions

Flame emissions are known to be influenced by both the thermal and chemical effects of assisting fluids injection [117-127]. Thermal and chemical effects of water addition on flame extinction and emissions have been studied for laminar [120, 121, 124, 127, 128, 129] and turbulent flames [130,

131, 132]. Vicariotto and Dunn-Rankin [120] compared the effects of various diluents, including water, argon, nitrogen, and carbon dioxide, added to the fuel side of the laminar non-premixed flame, on the peak temperatures and the extinction limits of flames. They showed that non-premixed flames diluted with water have similar peak temperatures and extinction limits compared to other diluents at the same heat capacity, highlighting that the thermal effect of water addition is more significant than the chemical effect in laminar flames that are not close to extinction. However, in laminar non-premixed flames close to extinction, the chemical effects become noticeable, as illustrated by Padilla et al. [121]. This work explored water-assisted laminar non-premixed flames near extinction in counterflow configuration. Water and non-reacting species with similar thermodynamic and transport properties were tested, and a computational technique was used to explore the chemical impact of the added water in a similar configuration. In turbulent flames with water addition, the extinction might still occur in a spatially inhomogeneous way throughout the flame; therefore, chemical effects also play an important role [130, 131, 132].

Diluting the fuel with steam reduces the flame temperature and NO_x emissions [24, 28, 133]. However, adding liquid water causes a more significant decrease in NO_x emissions because its lower temperature and high enthalpy of evaporation results in a lower flame temperature [134-140]. Previous studies revealed that the effectiveness of water entrainment into the flame in lowering NO_x emission could be attributed mainly to thermal effects, dilution, and the reduction of N_2 concentration in the vicinity of flames [29, 125, 127, 141-144]. Fuss et al. [145] further investigated the effect of liquid water and steam addition on CH_4-air flames. They revealed that liquid water and steam reduce the flame burning velocity, a primary property of a flammable mixture, by reducing the adiabatic flame temperature and reaction rates. The lower flame burning velocity enables better dilution of the combustible mixture with the assisting fluid leading to a

lower NO_x emission mainly due to the lower concentration of N_2 [146, 147, 148]. Apart from temperature effects, the chemical effect of water on the reaction kinetics changes the radical pool, thereby directly affecting the formation of NO_x [23, 149]. Liu and Kim [150] discovered that water increased the radical pool of the flame, leading to higher reaction rates and heat release. Therefore, a drop in flame temperature might not be the only mechanism to reduce NO_x, as adding water will increase both oxygen (O) and hydroxyl (OH) radicals. According to the Zeldovich mechanism, a higher O concentration increases NO_x, while according to the Fenimore mechanism, a higher OH concentration reduces NO_x [151]. An experimental study by Li et al. [152] also showed that adding water to the flame reduced NO_x emission significantly by removing CH radicals. However, it was found that the thermal effect of water addition in flames in reducing NO_x emission is more significant than its chemical effect [118]. More recent research has also revealed that water injection into the flame might decrease the emission of hydrocarbons and NO_x by improving fuel-air mixing [134, 135, 136].

1.7 Problem statement

There are two cases where liquid water enters the flare streams, namely, in water-assisted flares and in the atomization of the flowback fluid at upstream oil and gas sites. Flaring liquid droplets at upstream and downstream oil and gas facilities can affect flare emissions. The flared liquid droplets at downstream oil and gas facilities (*i.e.* feedwater for water-assisted flares) have low concentrations of impurities, whereas at upstream sites, the flared liquid droplets have a high concentration of impurities [39, 47, 50, 153]. The study of these flared liquid droplets on emissions is essential to predicting the degree of their effect on climate, ecosystems, and humans [13].

To properly understand the effect of flared liquid droplets on flare emissions and hence how better to reduce emissions, this study first explores the effect of pure water alone on emissions. It is a well-known fact that steam-assisted flares are often used by the downstream oil and gas industry in an effort to produce "smokeless" combustion or to reduce soot formation. The addition of unheated liquid water to flames is known to suppress soot formation but is rarely used in industrial flares. To the best of the author's knowledge, no study has been done to compare the effects of steam-assisted flaring with the those created by adding deionized water (pure water) to the flare. Since utilizing unheated liquid water saves the energy required to convert water to steam, it would be useful to investigate the relative extent to which unheated water and steam individually affect soot formation and NO_x emissions during flaring.

The second investigation of this work explore how different configurations of water injection (i.e., coaxially injected water versus radially injected water or internally injected water versus externally injected water) and impurities affect emissions in order to determine if radially or coaxially injected liquid water suppresses emissions more than steam.

Finally, the aerosolization of liquid droplets into the flares at upstream and downstream sites almost certainly results in the burning of salts with the flared gases. Kazemimanesh *et al.* [34] and Moallemi *et al.* [84] discovered that the entrainment of NaCl into the flame reduces coagulation of soot primary particles which in turn reduces the mobility diameter of soot and increases their number concentration. It was suspected that the reduction in coagulation rate experienced by Kazemimanesh *et al.,* [34] and Moallemi *et al.* [84] might be due to the electric charge on the particles. Hence, this work seeks to understand some fundamental characteristics of soot formation when impurities are present in the flared liquid droplets. In particular, this research examines the coagulation rate and the charge state of soot particles with and without the addition of NaCl.

1.8 Thesis Objectives

The primary objective of this thesis is to understand emissions from unassisted and assisted flares at upstream and downstream oil and gas sites, where feedwater and produced water droplets could potentially be entrained in the flares. Given that sodium cations and chloride anions exhibit significantly higher concentrations than other ions in both feedwater and produced water, sodium chloride was used as the impurity added to flames studied in this work. In addition to assessing and describing the ultimate condition of emissions resulting from the entrainment of feedwater and produce water, which was carried out on a laboratory scale using a turbulent non-premixed diffusion flame under controlled conditions, it is essential to further understand the evolution of soot particles.

In order to achieve above main objective, the following sub-objectives were set for this study:

- To compare the effects of steam- and liquid water-assist on turbulent non-premixed diffusion flame emissions. The reason for making this the first step is to better understand the effect of pure liquid water on flare emissions. To fully understand this interaction, a baseline case was set in order to establish the effect of pure liquid water on flare emissions and then compare the results with those of steam-assisted flares. An intermediate lab-scale flame was used for this investigation.
- To compare nozzle placement for water assisted flares and determine the effect of water impurities on flare emissions.
- To study the soot formation process when NaCl is introduced into a flame.

Chapter 2

Comparison of emissions from steam- and water-assisted lab-scale flames[1]

2.1 Overview

This experimental work was conducted on a large, turbulent, non-premixed lab-scale flare at the University of Alberta. Its goal was to determine and compare the effects on NO_x and soot emissions of adding unheated liquid water droplets and steam to a non-premixed turbulent flame fueled by methane, propane, and a mixture of methane and propane.

Studies have grouped the effects of steam- or water-assist on the production of NO_x and soot emissions in flames into the three mechanisms: hydrodynamic [23, 137], chemical [23, 125, 133, 137], and thermodynamic [23, 25, 133, 154, 155]. In terms of hydrodynamics, assisting fluid reduces soot emissions by increasing the turbulence intensity of the flow and promoting the mixing of the flare gas with oxygen [156]. In the chemical mechanism, radicals play an important role in flame chemistry, and the manipulation of their concentrations by introducing an assisting fluid alters soot formation. Principal radicals in hydrocarbon flames are hydrogen atoms (H), hydroxyl radicals (OH), oxygen atoms (O), and methyl radicals (CH_3) [157]. Evidence suggests that an increase in water addition causes an increase in hydroxyl radicals [137, 158], and also decreases the concentration of nitrogen radicals [125], the former suppresses soot production while the latter

[1] This chapter is based on the underlisted published journal article:
W. O. Bello, M. Zamani, E. Abbasi-Atibeh, W. L. Kostiuk and S. J. Olfert, "Comparison of emissions from steam- and water-assisted lab-scale flames.," *Fuel,* vol. 302, p. 121107, 2021. https://doi.org/10.1016/j.fuel.2021.121107.

inhibits the formation of NO_x [137, 159, 160]. However, two ways have been used to explain the changes to flame chemistry when water is added [3, 21, 23, 157]. First, the excess radicals cause reactions that create CO, CO_2, and H_2 when water vapor reacts with carbon molecules [3, 21, 23]. Second, the polymerization and the formation of long-chained oxygenated compounds that burn at a reduced rate are impeded when water molecules are introduced [3, 23]. In the case of the thermodynamic mechanism, the addition of water vapor in the flare causes the peak temperature to decrease, which in turn reduces the reaction rates, lessens polymerization and thermal cracking [23, 137] and NO_x formation.

Although many studies have been conducted on soot reduction due to water or steam addition in other combustion systems (internal combustion engines [137, 160, 161], gas turbine engines [125, 126], and furnaces [162]), few studies have been conducted on assisted flares. Singh et al. parametrically studied the effect of steam- and air-assist on ethylene flares to investigate the importance of flare operation parameters and identified that better mixing of fuel with steam and air led to more complete combustion and drastically reduced the formation of soot [156]. McDaniel [22] conducted an experimental study using a sampling probe suspended over a flare to continuously monitor emissions from steam- and air-assisted flares. He studied nitrogen-diluted propylene fuels and concluded that steam- and air-assisted flares had high combustion efficiencies (> 98 %) when good industrial operating practices were used. Ahsan et al. [28] introduced steam and air co-flows to natural gas flames and discovered that the emission indices for NO_x and BC significantly decreased compared to the unassisted flares. They also noted that a relatively wide range of flow rates of steam- or air-assist produced high combustion efficiency and low pollutant emissions. Examining different assisting fluids, namely, air, steam, and inert mixtures with the same molecular mass as air or steam, Zamani et al. [133] concluded that any changes that lead to

a higher characteristic flame temperature, namely, more oxygen in the assisting fluid, less steam or other diluents with lower specific heat capacities, and less radiation heat losses, increased the NO_x production. Thus, the thermal mechanism explained their NO_x emission indices results. In addition, they stated that steam addition affects soot formation through temperature and chemical effects. In propane flames, while steam addition lowered the characteristic product temperature due to dilution, it also reduced the radiation, but the rise in NO_x emissions was used to infer a net increase in temperature. Meantime, the addition of H and OH radicals reduced BC formation through the reaction of OH radicals with carbon particles and CO (water–gas shift reaction) [23], resulting in a significant decrease in BC emissions. Furthermore, Bussman and Knott [163] and Leary et al. [25] found that water injection into the flare reduced noise and radiation levels.

The authors are unaware of any studies in the literature which investigated using liquid water to suppress NO_x and soot emission in flares. The motivation of this study is, therefore, to address this gap. As a result, the goal of this experimental work is to determine and compare the effect of liquid water droplets and steam addition in a non-premixed turbulent flame with fuels of methane, propane, and a mixture of methane and propane on NO_x and soot emissions. Since evaporated liquid water and steam would have the same chemical effect on the flame, the importance of thermodynamic and hydrodynamic mechanisms will be at the focus of interpreting the data collected. Also, there is a large difference in the enthalpies of the flames because of the state of each assisting fluid. A comparison between the two assisting fluids (steam or liquid water) is important, as water-assisted flares may potentially have lower operating costs and greenhouse gas emissions because energy would not be required to convert water to steam.

2.2 Experimental setup

2.2.1 Fuels

Two fuels and a mixture of the two were used in this study:

a. methane of 99% purity (Praxair, ME 2.0-K) with a volumetric higher heating value (HHV_V) of 36.2 MJ/m^3.
b. propane of 99.5% purity (Praxair, PR 2.5IS-FX) with an HHV_V of 90.2 MJ/m^3, and
c. 90% pure methane and 10% pure propane with an HHV_V of 41.6 MJ/m^3, which is typical of Alberta flare gas [164, 165].

Two mass flow controllers (Alicat MCR, 50 standard L/min) were used to measure the flow rate of the fuel streams. The total flow rate of the fuel for all cases was 20 SLPM.

2.2.2 Water-assisted flare

Figure 2.1 shows a schematic diagram of the water-assisted flare. The stainless-steel burner used for this study had an exit diameter of 5.08 cm and had the same design as the burner used by Jefferson [50]. At the center of the burner, a vibrating mesh nebulizer was fitted inside a 2.54 cm diameter tube. The exit of the nebulizer was offset 2.54 cm below the tip of the burner to prevent the flame from damaging the micro-perforated vibrating membrane of the nebulizer. Two nebulizers were used in this study to span the range of liquid flow rates. The first nebulizer (Tekceleo H-360-M12), atomized water with a droplet diameter of 12 ± 3 μm with a flow rate ranging from 2 g/min to 6 g/min. The second nebulizer (Tekceleo H-360-M40) had a droplet diameter of 40 ± 3 μm at a flow rate ranging from 7 g/min to 25 g/min. As shown in Appendix A, the droplets evaporate soon after injection (on the order of tens to hundreds of milliseconds), and

well before the flame front, thus it is not expected that droplet diameter would have a significant effect on the results. It should be noted that the flow rate of water from the 40-μm nebulizer was visually unsteady with respect to time (*i.e.*, pulsating) when used at low flow rates (7 to 10 g/min), while the flow was steady at higher flow rates. The 12-μm nebulizer was visually steady at all flow rates. The water flow rate was controlled by changing the frequency of the vibration mesh generator, and the flow rate was measured with an electronic balance (A&D, model HF-6000G, with an uncertainty of ±0.1 g) and a stopwatch. A water-dispensing bottle was placed on the balance and connected to the nebulizer with an inline filter (McMaster-Carr, model 4795K2). Excess water in the atomizer was pumped back into the water-dispensing bottle through the drain/return line. The liquid water flow rate uncertainty was calculated at each flow rate and was less than 0.4% of the reading.

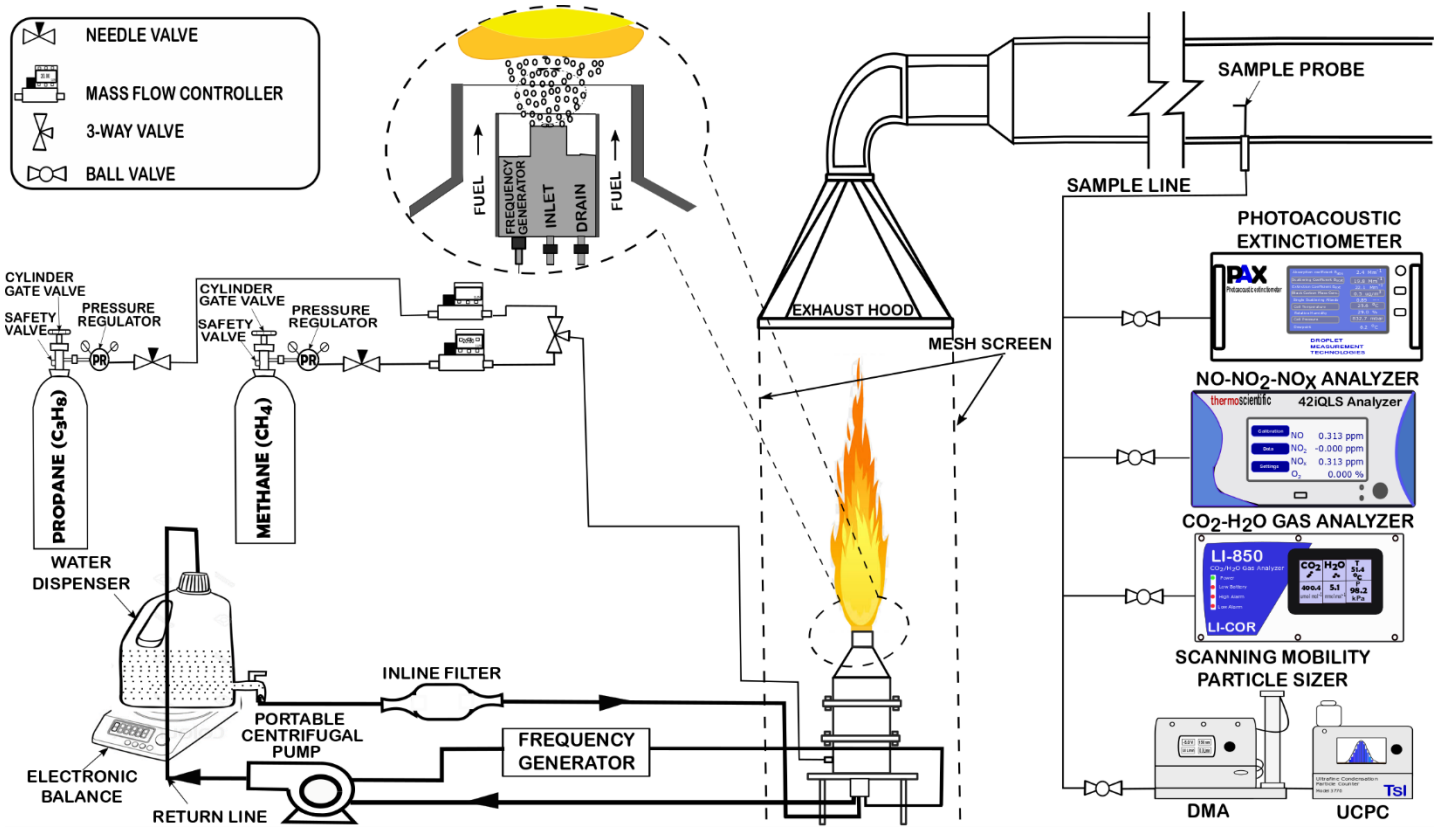

Figure 2.1: Schematic of the lab-scale test facility for water-assisted flare.

The velocity field of the atomized water droplets from the 40 µm nebulizer was measured using Particle Image Velocimetry (PIV) within the plane of a laser sheet (setup not shown here). The PIV was done to quantify the characteristics of the atomized water, i.e., the velocity of water droplets being introduced to the flame. The velocity of the atomized water is used to calculate the momentum and buoyancy of the injected water. For these tests, the nebulizer was removed from the burner and run without the flame at flow rates of 7, 10, 15, 20, and 25 g/min. The 40 µm water droplets were illuminated using a thin sheet of a pulsed YAG laser at 532 nm wavelength. The

Mie scattered light from the water droplets was captured using a Photron FASTCAM NOVA S9 camera at a frequency of 10 Hz at a resolution of 1024×1024 pixels, with a pixel-to-mm ratio of 19.15 with each image pair captured at dt = 400 μs. In order to calculate the two-component velocity vector field within the imaged plane, as well as to estimate the momentum flux of water droplets in water-assisted flares, 600 image pairs taken over 60 seconds were post-processed using DaVis software (version 10.1). The interrogation window size was 32 × 32 pixels with a window overlapping of 75 % resulting in a spatial resolution of 1.67 mm.

The instantaneous and mean upward velocity profiles (v) of water droplets are illustrated in Fig. 2.2 for water flow rates ranging from 7 g/min to 25 g/min. In Fig. 2.2, the instantaneous velocity of water droplets was calculated as the average of the upward component of velocity vectors measured within a 3 mm thick spatial window centered at 25.4 mm above the nebulizer exit plane within the plane of the laser sheet. This window corresponds to the burner exit location in the water-assisted flare experiments. The radial boundaries of this spatial window were between -0.16 ≤ (r/d) ≤ 0.16, where the origin of the 2D coordinate system was located on the centerline of the burner, and d is the diameter of the inner tube (*i.e.,* 2.54 cm). As illustrated in Fig. 2.2, the mean velocity of water droplets from the 40 μm nebulizer was in the range of 1.44 m/s ≤ $\bar{v}$ ≤ 2.65 m/s. As expected, the velocity of the droplets does not strongly depend on the water flow rate as the vibration mesh nebulizer produces more droplets per unit time at higher water flow rates rather than higher velocity droplets. PIV analysis also determined that the shape of the injected water spray was cone-like with a cone angle of approximately 22 degrees.

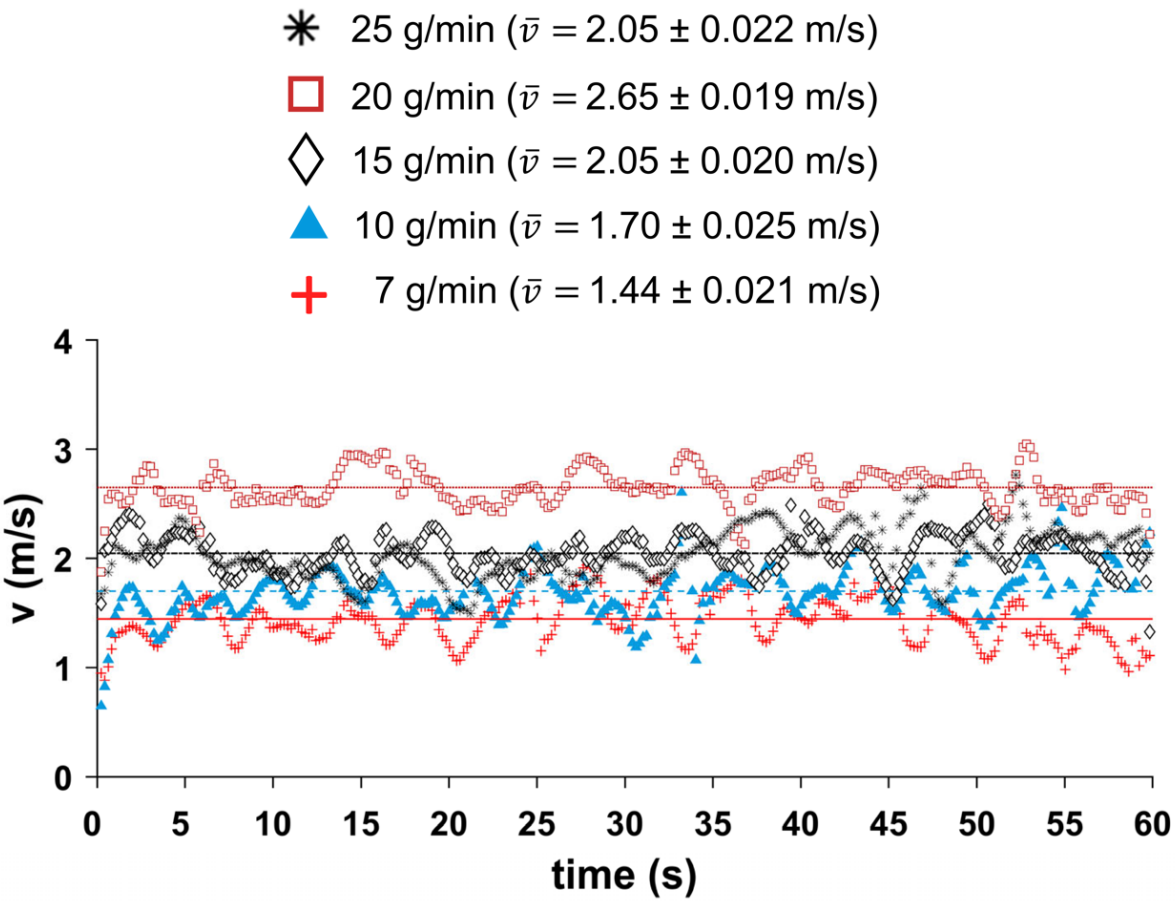

Figure 2.2: The instantaneous and mean upward velocity profiles (v) of water droplets exiting the 40 µm nebulizer for water flow rates ranging from 7 g/min to 25 g/min. The lines show the mean velocity ($\bar{v}$) over 60 seconds and uncertainties represent a 95% confidence interval in the mean.

2.2.3 Steam-assisted flare

An overview of the steam-assisted flare experimental setup is shown in Figure 2.3. The burner was geometrically similar to that of the water-assisted burner, with the exception that steam flowed through a 2.54 cm diameter tube. The downward offset of the steam tube exit was also the same

as the atomizer (2.54 cm). Steam was supplied by a laboratory electric steam generator (Sussman, MBA18), and its total flow rate was measured by a calibrated cone flowmeter (Cameron NUFLO cone differential pressure flowmeter Series 3000). In order to supply the low flow rates of steam needed for these experiments, the steam line was divided into two lines by a tee. One line had a plug valve and a precision valve to control the low flow rates of steam to the burner through a 6 m heated line (Dekoron Unitherm, Series 200) with a temperature set point of 150 °C. The other line carried the excess steam through an identical heated hose with a temperature set point of 115 °C and was directed to a heat exchanger to condense the steam, where that water flow rate was measured with an electronic balance and a stopwatch. The steam flow rate to the burner was determined to be the difference between the total flow rate out of the electric steam generator (measured by the cone flowmeter) and the measured flow rates of the excess steam line (measured by the electronic balance). The flow rate of steam used in this study varied from 3.5 to 32 g/min. Due to the limited range of the precision valve, for the flow rates below 20 g/min, the total flow rate was set at 100 g/min, and for the flow rates between 20 to 35 g/min, the total flow rate was set at 200 g/min. The steam supply system was able to bypass the precision valve to calibrate the total flow rate out of the electric steam generator. The steam flow rate uncertainty was calculated at each flow rate and was found to be less than 10% of the reading.

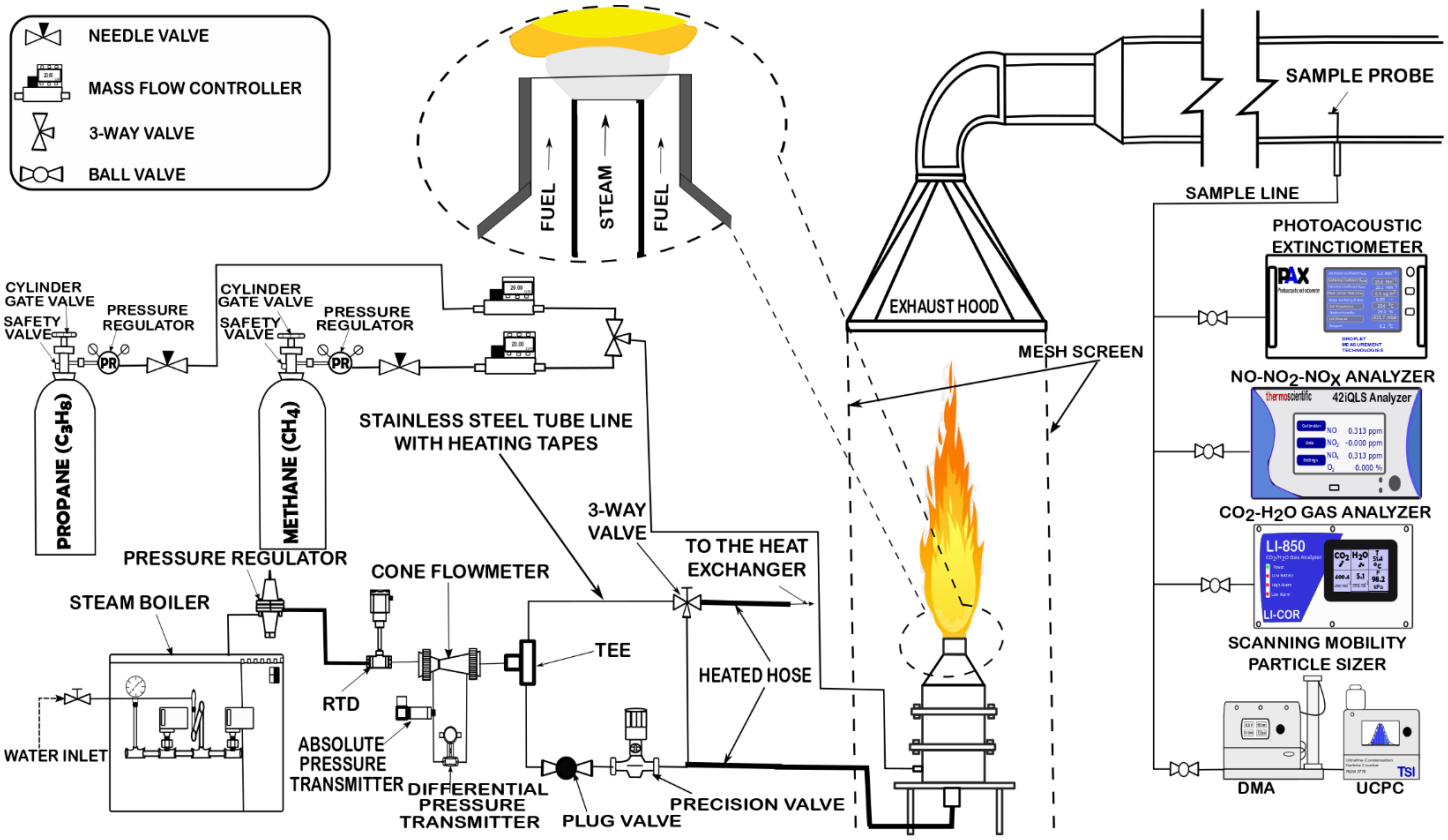

Figure 2.3: Schematic of the lab-scale test facility for steam-assisted flare.

2.2.4 Sampling system and Instruments

The exhaust gases were collected by an exhaust hood with square sides at the height of 157 cm above the tip of the burner. The perimeter of the exhaust hood to the floor of the lab was enclosed by vinyl-coated polyester mesh (McMaster Carr, part number: 7871T66) to reduce flame instability from the air currents in the lab and to allow entrainment of combustion air. The exhaust products were diluted with the room air as they entered into the exhaust hood, and the dilution

ratio of the exhaust products ranged from ~16 for the propane test condition to ~42 for the methane test condition. The dilution ratio was calculated using the carbon-balance method adopted from [166].

A stainless-steel sampling probe was connected to the exhaust duct 6 meters downstream of the exhaust hood to collect well-mixed exhaust samples. A copper tube 2 meters long connected the sample probe to a stainless-steel manifold, and then drawn to the various instruments by each of their internal vacuum pumps. The instruments were used to measure both gaseous and particulate exhaust products. A photoacoustic extinctiometer (Droplet Measurement Technologies, PAX) was used to measure the absorption of the exhaust using a wavelength of 870 nm. The mass of black carbon was found by assuming that the absorption was due to black carbon alone and that the black carbon mass absorption cross-section has a value of 4.74 m^2/g as recommended by the manufacturer [167].

A NO_x analyzer (Thermo-scientific, 42iQLS) was used to measure the exhaust product NO_x concentration using a chemiluminescence technique. A non-dispersive infrared gas analyzer (LI-COR Biosciences, LI-850) uses absorbance to measure the CO_2 concentration. The CO_2 was measured to calculate the dilution ratio of the exhaust products.

In addition, a scanning mobility particle sizer (SMPS), which is the combination of a differential mobility analyzer (DMA; TSI Model 3080) and an ultrafine condensation particle counter (UCPC; TSI Model 3776), was used to measure the size distribution of the particles in the exhaust. The DMA is a device that uses an electrostatic classifier to separate particles based on their electrical mobility, and the UCPC uses an optical detector to count particles that have undergone particle growth through the condensation of butanol vapor.

Emission indices were calculated via carbon balance using the method described by Ahsan et al. [28]. During testing, all fuel flows were set to the same flow rate (20 standard L/min), and the system was allowed to warm up for 30 minutes to reach steady operation. Then, the diluted combustion products were sampled, and CO_2, NO_x, black carbon concentration, and particle size distribution were measured. The assist fluid (either liquid water or steam) was introduced into the flame at the lowest flow rate, the system was allowed to stabilize, and the same measurements were taken. This process was repeated while incrementally increasing the assisting flow until the maximum flow was reached.

2.3 Results and Discussion

In interpreting the results of the data collected, reference will be made to different parameters used to characterize the flow as it emerges from the burner exit. These parameters were manipulated experimentally, and the flame response was observed in terms of the emission indices for NO_x, black carbon concentrations, and particle size distribution. The most primitive of these parameters is the ratio of the mass flow rate of assist fluid to the fixed mass flow rate of the fuel stream. The experimental results will show that the same mass flow rate of liquid water and steam does not result in the same outcomes; therefore, it is necessary to consider other parameters to characterize the flow.

2.3.1 Characterizing parameters of the flows

The other parameters needed to characterize the flow were:

1) the rate of the vertical momentum of the combined fuel and assist mixture flowing out the burner, which is expressed as a force (in Newtons) into the quiescent room air,
2) the rate that the body force (in N/s) associated with gravity (referred to here as a buoyancy force, even though this is not the common term used for water droplets) of the combined fuel and assist flows in their reactant state, and the flow of the products of combustion, into the room air,
3) the adiabatic flame temperature calculated from a stoichiometric mixture of the fuel, assist, and room air that is fully oxidized (Note: these flame temperatures are used in estimating the rate of the buoyancy force of the products formed within the room air)

The rate of momentum of the flow emerging from the burner was seen as a parameter of interest as its magnitude is important in driving the initial mixing of fuel and air that is needed to support the combustion processes. The upward rate of momentum of the fuel-assist mixture (F_z) was approximated as the sum of the products of mass flow rates and characteristic velocities of flows in the z-direction at the burner exit,

$$F_z = \dot{m}_\mathrm{f}\,\bar{v}_\mathrm{f} + \dot{m}_\mathrm{a}\,\bar{v}_\mathrm{a} \tag{2.1}$$

where $\dot{m}_\mathrm{f}$, $\dot{m}_\mathrm{a}$, $\bar{v}_\mathrm{f}$, and $\bar{v}_\mathrm{a}$ are the fuel mass flow rate, assist mass flow rate, average fuel exit velocity, and average assist exit velocity all in the z-direction, respectively. In the case of gases and vapors, the average exit velocity is defined as,

$$\bar{v} = \frac{\dot{m}}{\rho A} \tag{2.2}$$

where ρ is the fluid density, and A is the cross-sectional area of the steam tube or annulus between the burner and steam tube. For this calculation, the temperature and pressure of the fuel at the burner exit were at laboratory conditions (25 ºC and 93.8 kPa). The steam temperature at the burner exit was measured to be 105 ºC, and it was assumed to be at ambient pressure (93.8 kPa). For the atomizer, the cross-sectional area of the atomizer holes (and the number of holes) is unknown. However, based on the PIV measurements shown in Figure 2.2 above, the mean velocity of the entrained liquid water droplet was 1.98 ± 0.6 m/s (the precision uncertainty was calculated using 95% confidence interval). So, an approximate value of 2 m/s was used to calculate the rate of momentum of the injected liquid water for this work.

Figure 2.4 presents the rate of upward momentum of the fuel-assist mixture exiting the burner for the three fuels and both of the assists. The figure shows that propane has a higher initial momentum than the other fuels because it has a higher density. Also, the water assist has a higher initial momentum than steam because it has a higher exit velocity. The key observation being that there can be an order of magnitude difference between the no assist case to the maximum assist case.

While Figure 2.4 shows the rate of momentum at the exit of the burner, it does not remain constant as the fluid progresses downstream because there are external gravitational body forces (buoyancy forces) on the fluids even before the reaction occurs. This external force can either be additive or subtractive of the upward momentum depending on the density of the different fuel and assist components relative to the density of the surrounding air. As a result, the different fuels and assist fluids can either enhance or reduce mixing as the flow progresses downstream. Based on a control-

surface analysis, the initial upward rate of the buoyancy force ($\dot{B}$) of the fuel and assist fluid mixture (reactants) as it leaves the burner is:

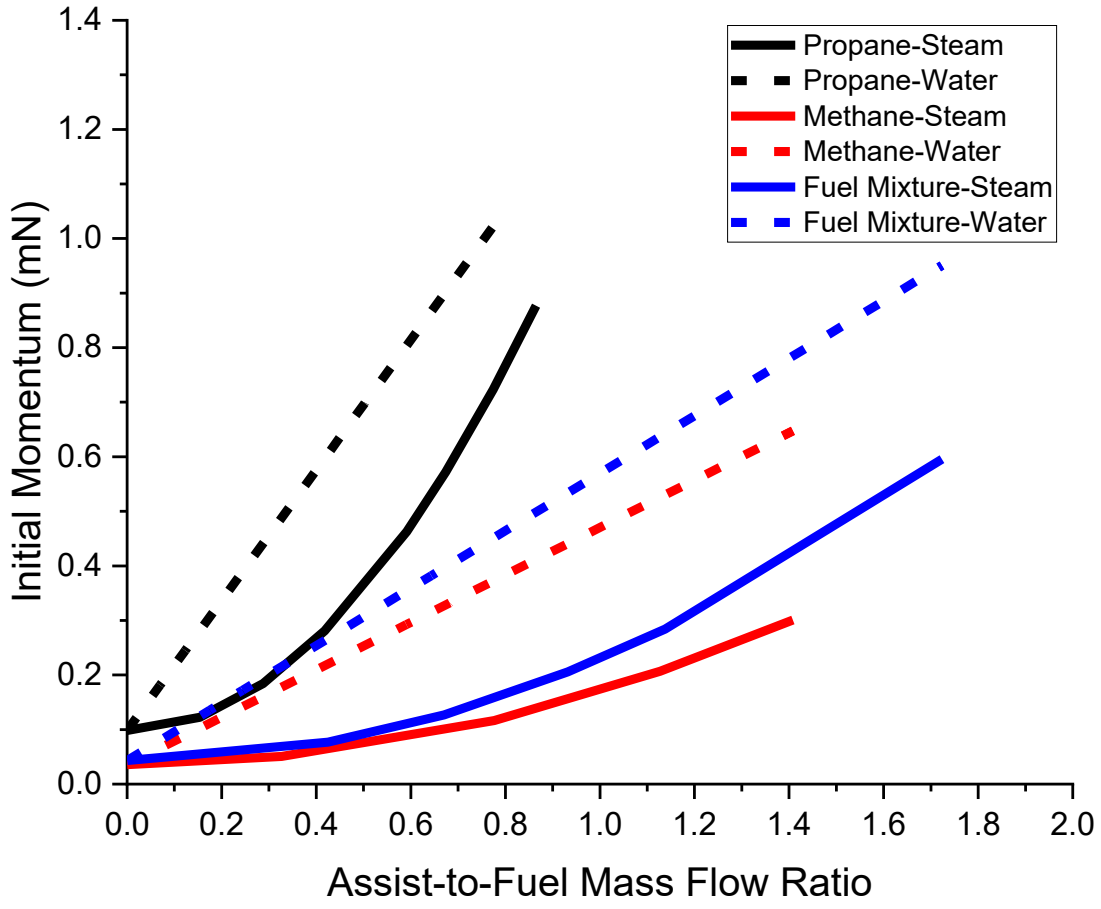

Figure 2.4: The rate of upward momentum of the fuel-assist mixture with respect to their corresponding assist-to-fuel mass flow ratio.

$$\dot{B}_{\text{reactants}} = \left[(\rho_{\text{air}} - \rho_{\text{f}})\ \dot{V}_{\text{f}}\, g\right] + \left[(\rho_{\text{air}} - \rho_{\text{a}})\ \dot{V}_{\text{a}}\, g\right]. \tag{2.3}$$

Assuming an adiabatic stoichiometric reaction, the rate of the buoyancy force for the combustion products crossing a control surface above the flame is:

$$\dot{B}_{\text{products}} = \left[\left(\rho_{\text{air}} - \rho_{\text{product}}\right)\ \dot{V}_{\text{product}}\, g\right] \tag{2.4}$$

where ρ_{air}, ρ_{f}, ρ_{a}, ρ_{product}, $\dot{V}_{\text{f}}$, $\dot{V}_{\text{a}}$, $\dot{V}_{\text{product}}$, and g are the ambient air density, fuel density, assisting fluid density, combustion exhaust product density, fuel volume flow rate, assisting fluid volume flow rate, combustion products volume flow rate and the gravitational constant ($9.81\ \text{m/s}^2$), respectively. The rate of the buoyancy force is shown in Figures 2.5a and 2.5b as a function of assist-to-fuel mass flow ratio for the different fuel and assist fluids and combustion exhaust product.

The initial upward buoyancy force of the methane and its mixture with 10 % propane are positive because they are less dense than ambient air, but the initial upward buoyancy force of propane is negative because it is denser than ambient air. Since the steam is less dense than air, its initial upward buoyancy force is positive and increases with increasing assist mass flow. However, liquid water is much denser than air, so its initial upward buoyancy force is negative and increasingly negative with increasing assist mass flow. Figure 2.5a shows all the potential combinations of fuels and assist streams, and how they can either be additive or subtractive from the initial rate of momentum exiting the burner (Figure 2.4). Comparing the range of magnitudes of these rates of buoyancy forces relative to those of the rates of momentum results on a time scale (*i.e.*, $\tau_{\text{reactants}} = F_z/\dot{B}_{\text{reactants}}$) that has the potential to profoundly affect the reactant flow before combustion is complete (defining the characteristic combustion time as the ratio of flame length to the exit fuel velocity).

Figure 2.5b shows that the rate of the buoyancy force of the products created by combustion is always positive, and one to two orders of magnitude greater than buoyancy associated with the reactants. It is also important to note that the rate of buoyancy created for the propane flames are more than twice that of the other fuels. There appears to be very little impact of adding either steam or water, in the amounts used in these experiments, on this upward force of a particular fuel. The average change in the characteristic rate of product buoyancy from no assist to maximum assist is 0.82 and 0.50 mN/s for the water and steam assist cases, respectively, which is notably smaller than the buoyancy changes seen on the reactants side. Therefore, the overall hydrodynamics are controlled by the buoyancy of the products.

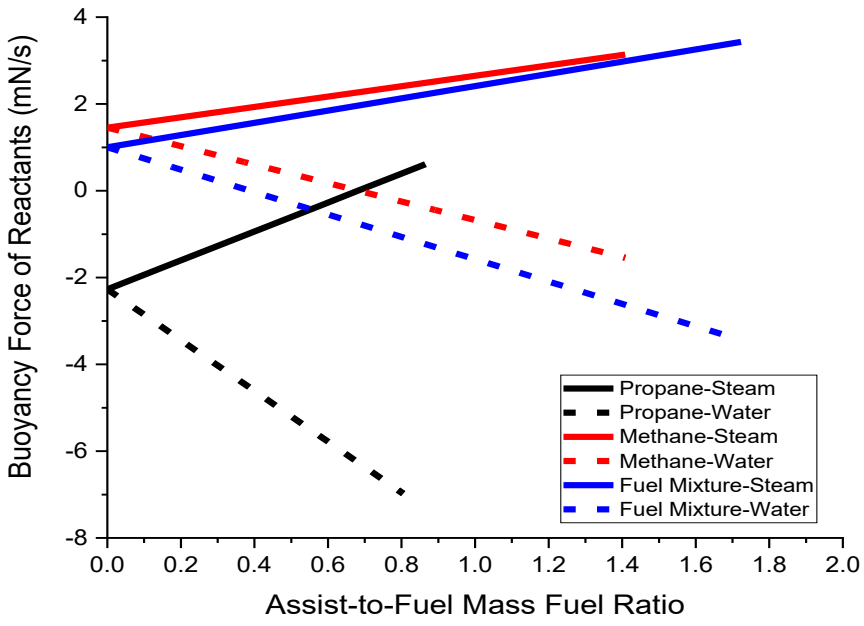

(a.)

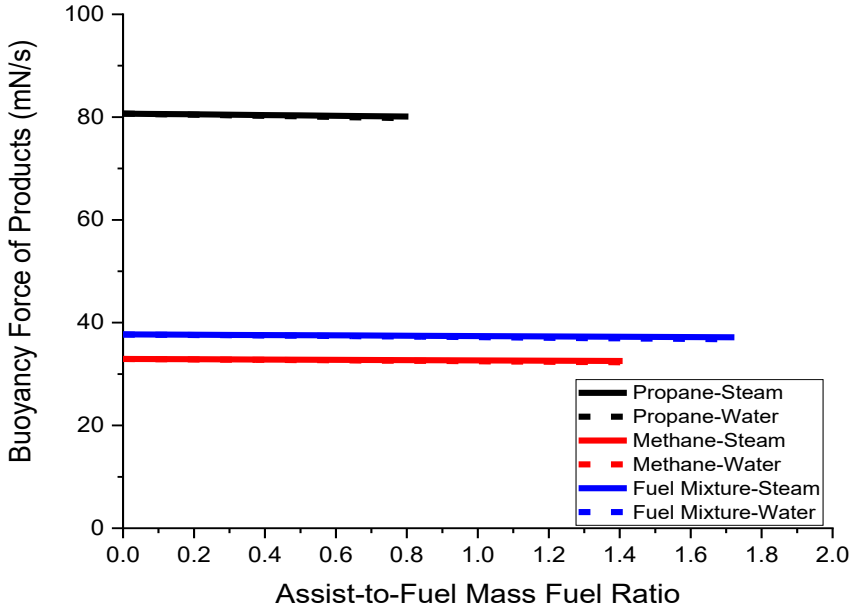

(b.)

Figure 2.5: Upward rate of the gravitational body force as a function of assist-to-fuel mass flow ratio for (a) reactants and (b) products.

The characteristic adiabatic flame temperature (AFT) was computed using the NASA CEA (Chemical Equilibrium with Applications) program. For this calculation the temperature selected was 25 °C, and the pressure was 93.8 kPa. Figure 2.6 shows the adiabatic flame temperature of the fuel-assist mixture when burned with a stoichiometric amount of air, and the composition of the products is only N_2, CO_2, H_2O. As shown in the figure, at 1.6 assist-to-fuel mass flow ratio for the fuel mixture case, liquid water can be seen to reduce the flame temperature by approximately 150 K more than steam. Since liquid water reduces the flame temperature more than steam, the expectation is that this will correspond with liquid water reducing more emissions compared to steam as flame temperature has a significant effect on emissions [156] as discussed in the sections below. It should be emphasized that these estimated flame temperatures do not include radiation heat losses. The highest radiation is for the highly luminous yellow propane flame, but all flames have reduced radiation once water is added. As a result, the actual peak flame temperature is lower than the AFT with no assist and does not drop as dramatically when assist is added (especially for the propane flame since the lower radiation compensates for the dilution with inert components).

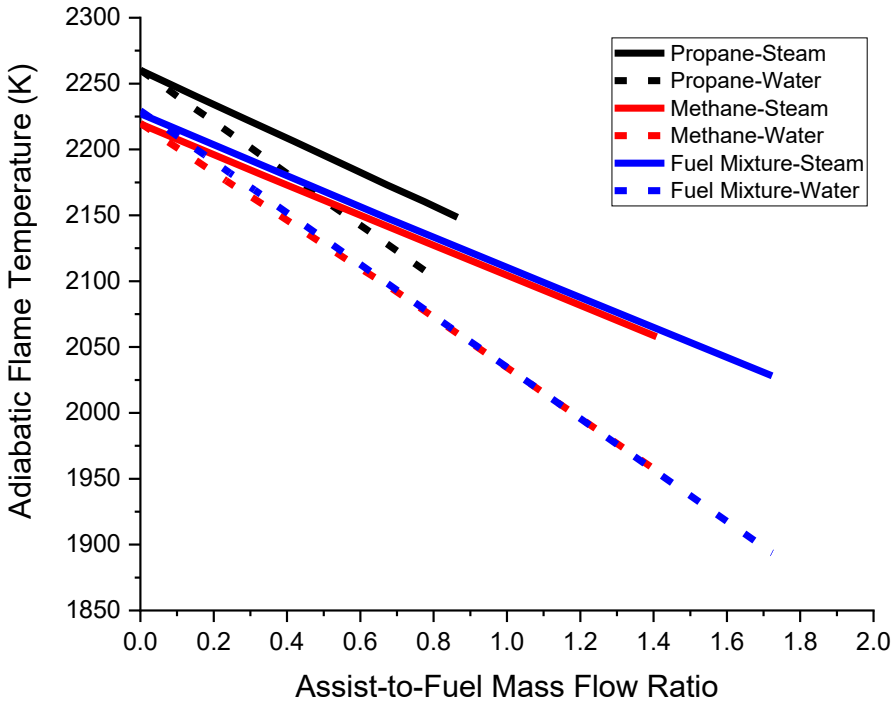

Figure 2.6: Adiabatic flame temperature with the corresponding assist-to-fuel mass flow ratio.

2.3.2 NO_x emission indices

Figure 2.7 shows the NO_x emission indices for the three fuels as a function of the ratio of the assist (water or steam) mass flow rate to the fuel mass flow rate. The three graphs show a decreasing trend of NO_x emission indices as the steam and water flow rate was increased. Generally, the rate of decrease in NO_x was linear except for the data associated with the 40-µm droplet nebulizer operating in an unsteady pulsating mode, as described earlier. It was observed that liquid water suppressed more NO_x emissions compared to steam at the same flow rate. At an assist-to-fuel *MFR* of 0.8, with methane fuel (Figure 2.7a), methane-propane fuel mixture (Figure 2.7b), and propane

fuel (Figure 2.7c), liquid water reduces EI_{NOx} by ~3.0 times, ~2.5 times and, ~40% more than steam, respectively. Other studies have shown that steam-assist reduces NO_x emission [28, 156, 168]. As well, Ahsan et al. [169] flared methane fuel in a lab-scale burner (flow rate of 20 standard L/min with a 1-inch diameter burner with an internal tube of ¼-inch for the coflow of steam) and found the EI_{NOx} reduced by ~30% at an MFR of 0.8, which is identical to the result presented in this work for the methane case.

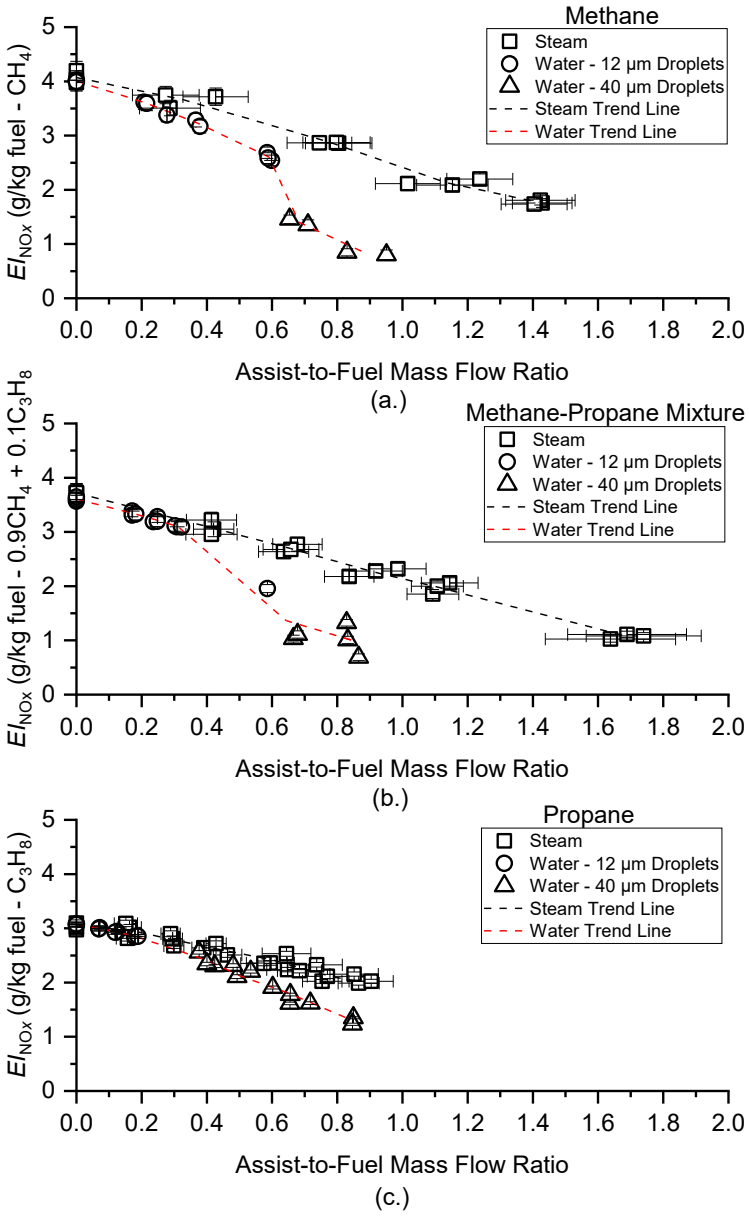

Figure 2.7: NO_x emission indices of flames with steam and liquid water addition: (a) methane fuel, (b) fuel mixture (90% methane + 10% propane) (c) propane fuel.

To test whether NO_x emissions are linked to their thermal formation mechanism, Figure 2.8 shows the NO_x emission indices as a function of the adiabatic flame temperature. The results show that NO_x emissions reduce approximately linear with a decrease in the adiabatic flame temperature, except for the methane fuel and fuel mixture (Figure 2.8a and b) cases associated with the pulsating low flow rate of the 40-µm droplet nebulizer between 7 g/min and 10 g/min. The entire flow range of the 12-µm droplet nebulizer and the higher flow rate range (between 11 g/min and 25 g/min) of the non-pulsating 40-µm droplet nebulizer (used for the propane flame) was linear and independent of the phase of the water. When steam was injected into the flame, the EI_{NOx} was reduced by ~50% between the adiabatic flame temperatures of 2100 K and 2270 K for all three fuel cases. As discussed in Section 2.3.1, the hydrodynamics of the flames with the two assist fluids are very similar (*cf.* Figure 2.5b), while the adiabatic flame temperature of the water-assist is much smaller than the steam-assist (*cf.* Figure 2.6). Thus, these results support the idea that thermal effects (adiabatic flame temperature), rather than hydrodynamic effects, are the prime determinant of NO_x emissions [154, 170].

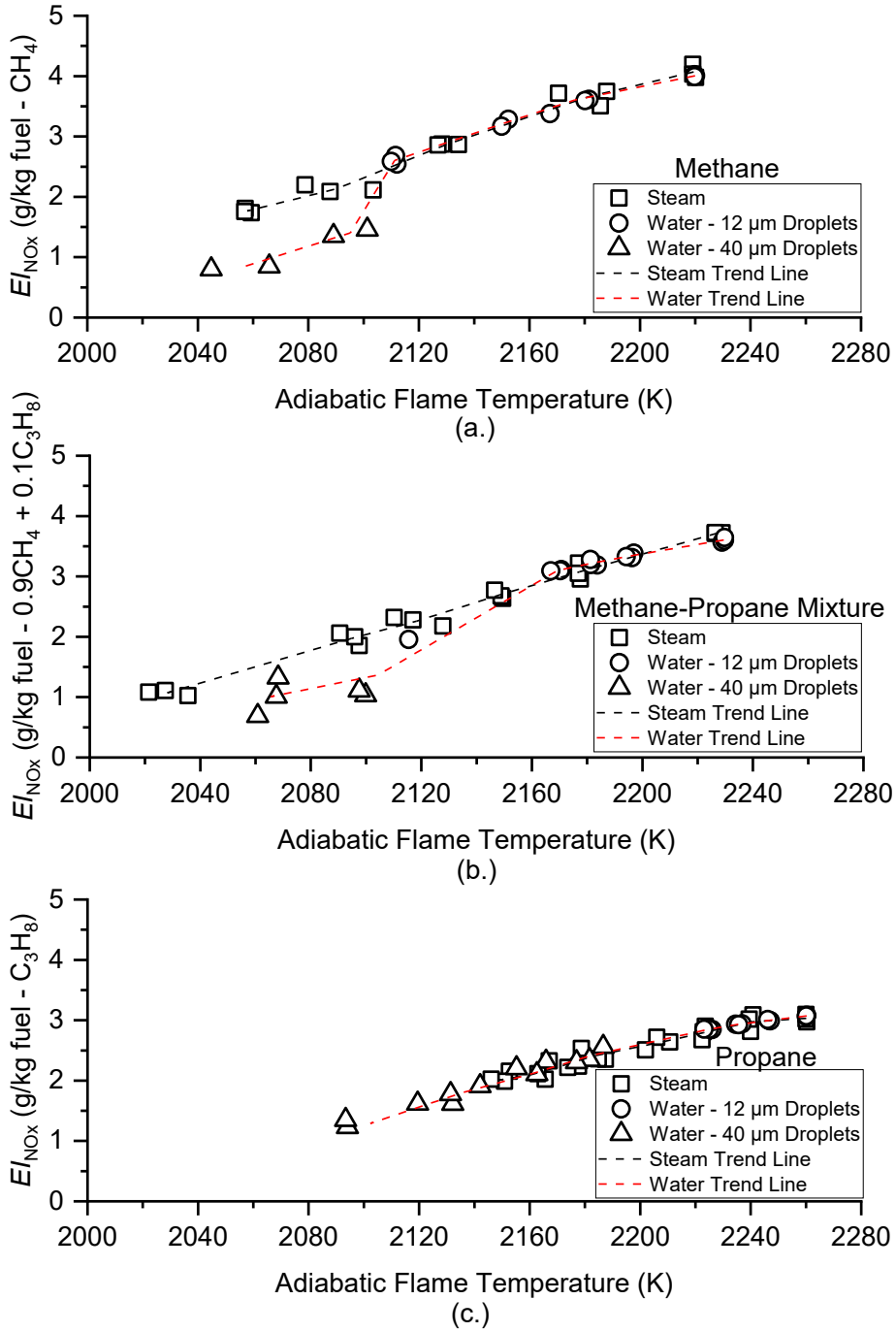

Figure 2.8: Adiabatic flame temperature with the corresponding NO_x emission indices for steam and liquid water addition: (a) methane fuel (b) fuel mixture (90% methane + 10% propane) (c) propane fuel.

2.3.3 Particle emissions

2.3.3.1 Black carbon emission indices

Figure 2.9 shows that BC emission indices decreased with an increase in the assist-to-fuel MFR. The figure shows that liquid water reduces soot emissions more than steam at the same assist-to-fuel-mass ratio. For all three fuels at 0.8 assist-to-fuel MFR, liquid water assist reduces black carbon emissions (EI_{BC}) by approximately an order of magnitude more than steam assist. Studies have revealed that flame temperature [72, 154, 155], assist momentum [23, 169], and the chemical [23, 125] mechanisms are the ways BC formation can be mitigated when steam or water is added to the flame. The presented results show that the temperature plays a significant role in the BC production because with an increase in assist-to-fuel mass flow ratio, a corresponding decrease in BC emission indices was experienced, and this also corresponds to a decrease in flame temperature. This means that the different temperature fields between liquid water and steam injection had a significant effect on the BC emissions. Liquid water cools the flame greater than the steam, and consequently drops the EI_{BC} more than steam. The chemical effect on the flame was not seen as the reason for the difference because these assists have the same chemical composition. Similarly, the global hydrodynamics (dominated by the buoyancy of the products) were expected to be similar, thereby leaving temperature as the impacting parameter.

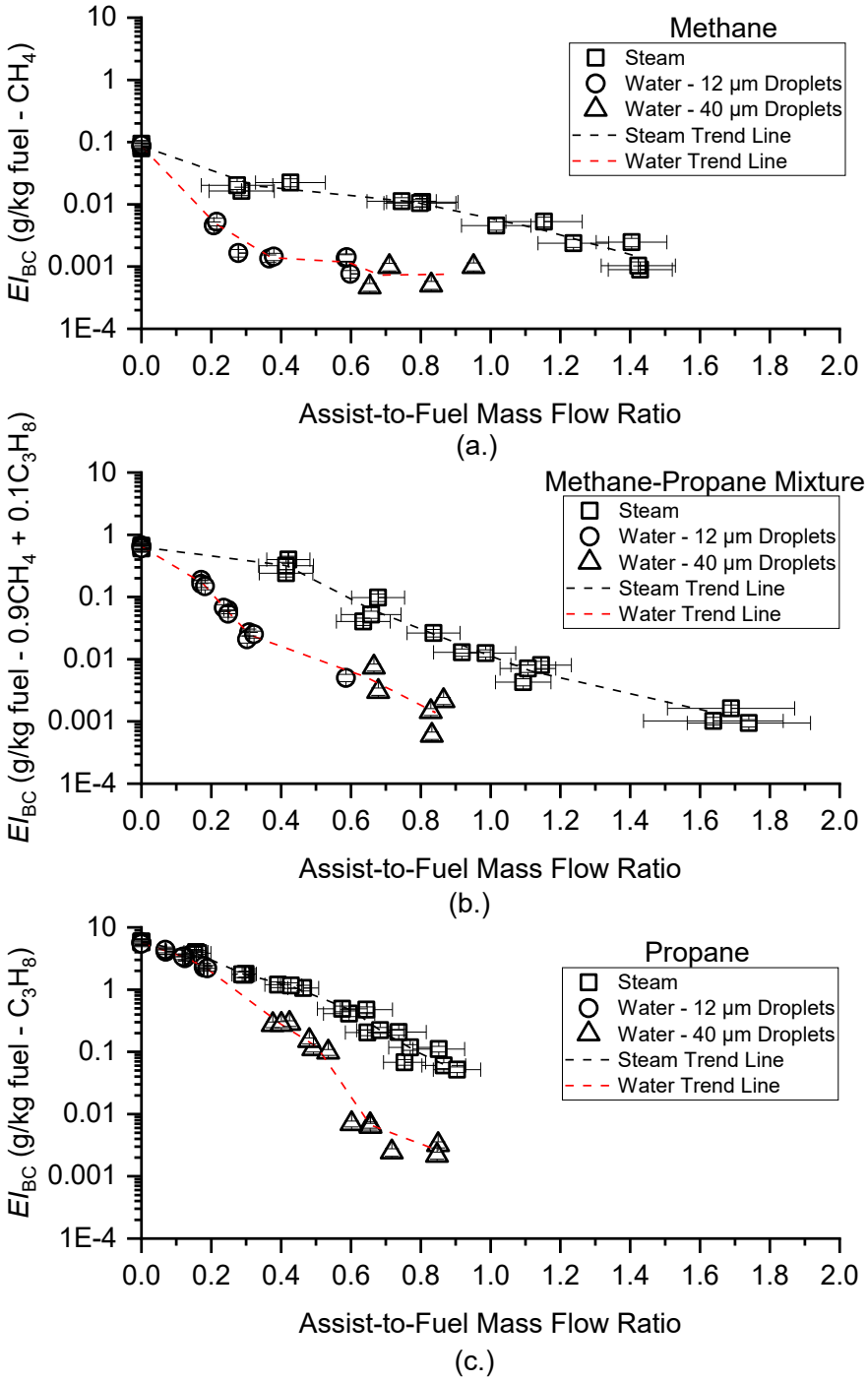

Figure 2.9: Black carbon emission indices of flames with steam and liquid water addition with propagated errors. (a.) Methane fuel (b.) Fuel mixture (90% methane + 10% propane) (c.) Propane fuel.

2.3.3.2 Particle size distribution of steam- and water-assisted flares

Figure 2.10 shows the particle size distributions of pure methane, the fuel mixture, and pure propane for both liquid water and steam addition experiments. For the methane fuel case (Figure 2.11a and b), an increase in assisting fluid flow rate caused a corresponding decrease in particle number concentration, and liquid water decreased particle concentration more than steam. For the fuel mixture case, at a very similar assist-to-fuel MFR (0.83 for water (Figure 2.11c) and 0.85 for steam (Figure 2.11d)), water reduces particle number concentration by ~1 order of magnitude more than steam. Also, for propane fuel, at 0.85 assist-to-fuel MFR, liquid water reduces the particle number concentration by 2 orders of magnitude more than steam. Figure 2.11 shows the particle-count median diameter (CMD) of the same distributions as a function of assist-to-fuel MFR. The figure shows that the CMD decreases with an increase in the assist-to-fuel MFR. Also, as shown in Appendix A, the geometric standard deviation (GSD) of all size distributions is relatively similar with an approximate value of 1.9.

The trends in particle concentration and median particle size are similar to those shown in other works. Trivanovic et al. [165] tested thirteen different fuel of volumetric higher heating value ranging from 35.8 MJ/m^3 to 75.17 MJ/m^3 with a constant fuel flow rate of 156 standard L/min. They used a similar burner geometry as used in this work and confirmed that liquid water reduces particle number concentration and the median soot diameter. They also showed that the rise in the number concentration and CMD (but with a similar GSD) corresponds to an increase in HHV_V, which is also seen in this study. Sipkens et al. [88] using the same burner and atomization system

with propane fuel, also observed that the addition of liquid water resulted in soot size distributions with lower CMDs and number concentrations but similar GSDs.

The size distribution of particles emitted *from* the flame is a function of soot formation processes occurring *within* the flame. The soot formation process involves the nucleation of condensed-phase materials, surface growth, coagulation into fractal structures, and oxidation [76]. A reduction in particle nucleation and surface growth, or an increase in oxidation, will result in lower mass concentrations, smaller median particle sizes and lower number concentrations as observed here. The width of the distribution is mostly driven by coagulation within the flame and in the post-flame region, and as such, most soot size distributions tend to reach similar distribution widths (*i.e.* 'self-preserving size distribution' [105]), and the distributions tend to be log-normal with similar GSDs [171] as was also observed here. The fact that the CMD decreases with water addition but the distributions have a similar GSD, results in cases where the concentration of small particles is higher than cases with no water addition (see Figure 2.10f, for example) even though the total number concentration decreases.

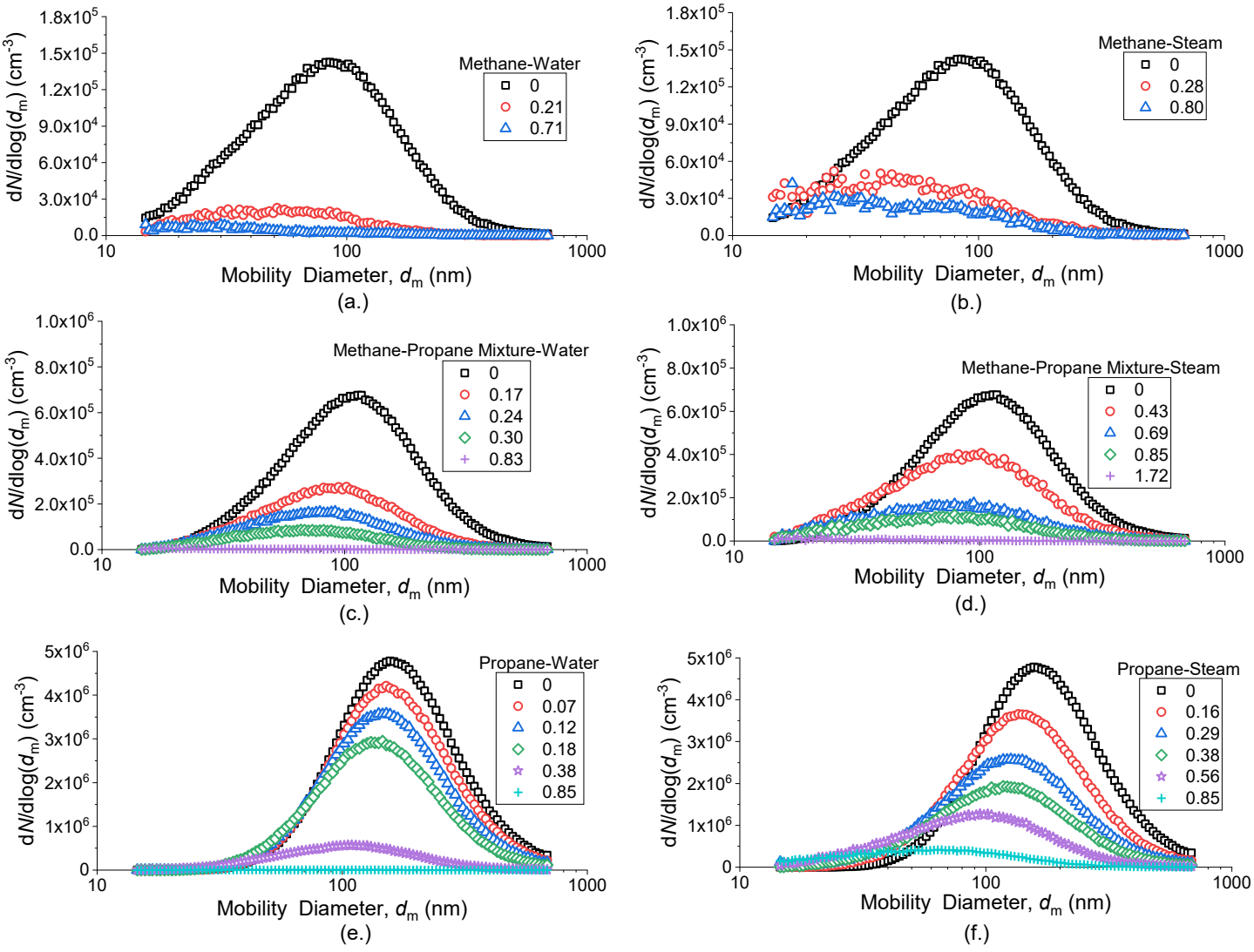

Figure 2.10: Particle size distribution. (a.) Methane-water flame. (b.) Methane-steam flame. (c.) Fuel mixture – water flame (90% methane + 10% propane). (d.) Fuel mixture – steam flame (90% methane + 10% propane). (e.) Propane-water flame. (f.) Propane-steam flame.

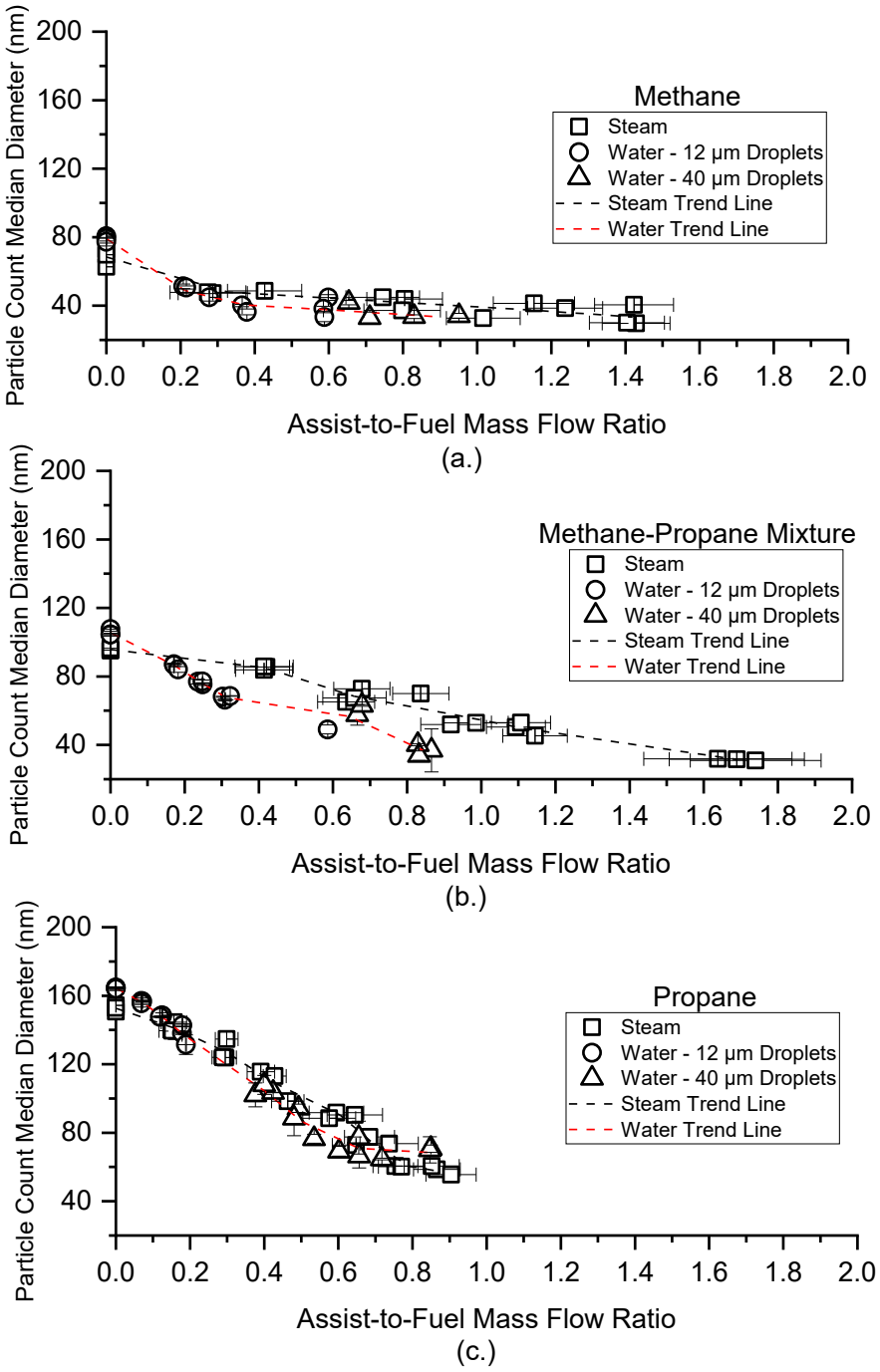

Figure 2.11: Particle count median diameter of flames with steam and liquid water addition with propagated errors. (a.) Methane fuel (b.) Fuel mixture (90% methane + 10% propane) (c.) Propane flame.

2.4 Conclusion

This paper investigated several fundamental emission parameters related to water- and steam-assisted flaring and included emission indices for black carbon (BC), particle-number, and NO_x, as well as particle-count mean diameter and particle-size distribution. These quantities were computed for three different hydrocarbon fuels, and the effect of adding liquid water or steam to the fuel side of these non-premixed turbulent jet flames. The importance of thermodynamic and hydrodynamic mechanisms was interpreted based on the collected data, as chemical mechanisms were not expected to play a role since both assists used in this study are chemically identical (H_2O).

It was concluded that with an equal mass ratio of steam and liquid water to fuel, water suppressed soot and NO_x more effectively than steam. The NO_x, soot, and particle-number emissions indices for the three fuel cases (propane, methane, and 10 % propane and 90 % methane) decrease as the assist-to-mass flow ratio increases, irrespective of the assist type.

The flared gases (propane, methane, and 10 % propane and 90 % methane) had a significant effect on the quantity and trends of BC and NO_x emissions, as well as particle size distribution for either assist and were readily relatable to the adiabatic flame temperature. Liquid water-assist flare had a slightly smaller particle-count median diameter compare to the steam-assist flare. In general, the thermodynamic mechanism (*i.e.*, the adiabatic flame temperature) appears to play the major role in controlling emissions, while in this study the hydrodynamic mechanisms associated with the upward momentum and buoyancy at the burner exit, or the buoyancy of the hot products were not seen as being as important.

The emissions of assisted flares in the oil and gas industry will depend on many factors, including fuel composition, flare geometry, crosswinds, assist momentum, and others. This study showed

that the thermodynamic mechanism has an important effect on emissions. Hence, water-assisted flares in the oil and gas industries would likely produce lower emissions than steam-assisted flares if other factors remained the same. This could have a cost-benefit to industry as water-assisted flares have a lower operating cost compared to steam-assisted flares (*i.e.*, less water is required to get an equivalent reduction in emissions, and it costs less to treat water than it does to produce an equivalent amount of steam). In this study, the hydrodynamics of the flames was quite similar for a given fuel, irrespective of the assist fluid, and the initial momentum of the assist fluids was quite low. It is well known that higher assist momentum increases the mixing of the reactants and reduces emissions [133]. Thus, future work could focus on examining the role of the initial momentum of water injection on flare emissions (*i.e.*, high momentum water injection compared to low momentum water injection).

Chapter 3

Effects of External Injection of Deionized Water and Water with Impurities on Water-assisted Flares[2]

3.1 Overview

A recent study by Bello et al. [24] investigated the chemical, thermodynamic, and hydrodynamic effects on emissions in water- and steam-assisted flares. The efficacy of using internally-injected atomized water (water injected on the fuel side of the flame front) to suppress NO_x and black carbon (BC) emissions was demonstrated in turbulent non-premixed flames. It was also shown that liquid water-assisted flares suppressed NO_x and BC emissions more effectively than air- and steam-assisted flares [24, 28].

This study aims to investigate the gap in the literature related to the quantification of emission parameters and flow visualization of liquid water injection into turbulent non-premixed flames. The focus is to quantify emissions of non-premixed flames with water added externally, i.e., to the *air side of the non-premixed flame*. This work builds on our previous work [24, 28, 133], where the water was added from the fuel side and mitigates the design and safety challenges presented by internally-injected flares. Therefore, common water sources, such as the boiler feedwater used

[2] This chapter is based on the underlisted published journal article:
W. O. Bello, E. Abbasi-Atibeh, W. L. Kostiuk and S. J. Olfert, " Effects of external injection of deionized water and water with impurities on Water-assisted flares.," *Fuel,* vol. 340, p. 127602, 2023. https://doi.org/10.1016/j.fuel.2023.127602.

at downstream oil and gas facilities and the seawater used at offshore oil and gas platforms [15, 25], can be injected externally to reduce flare emissions without a need for costly boiler operation. Research has been done to measure noise and radiation from flares with externally injected seawater [25], but no work has been done on the emission characterization of turbulent non-premixed flames with externally injected liquid water. This work also investigates the effects of external injection of water with impurities, such as NaCl, the most significant impurity in common water sources, on flare emissions. For this purpose, a range of NaCl concentrations was injected into the flame. Two-dimensional, two-component particle image velocimetry was employed to quantify the 2D projection of the velocity vector field of the atomized liquid water within the laser plane.

3.2 Experimental method

Experiments were conducted using a setup that consisted of a two-inch turbulent non-premixed jet flame burner, atomizers, emission measuring instruments, and a PIV system. An earlier version of this setup is described in detail elsewhere [24]. Compared to the previous version of the experimental setup, two major modifications were made in the present study. First, the burner was modified to allow the external injection of atomized liquid water using four atomizers instead of internal injection using only one atomizer. Second, PIV was used, which allowed time-resolved velocity field measurements of the atomized liquid water droplets for momentum and buoyancy analysis. A single-lens reflex (SLR) camera was also used to capture the flame and the laser-illuminated liquid water spray simultaneously to visually explore the flame and water spray interactions close to the flame.

3.2.1 Burner setup with four atomizers

Figure 3.1 shows a 2D projection view of the burner assembly. The burner exit has an inner diameter of 50.8 mm and an outer diameter of 57.1 mm, which corresponds to the ASTM standard (internal to external diameter ratio of 0.89) for a schedule 40 pipe used typically for flares. This burner configuration has been used extensively by various researchers, including Bello et al. [24], Roth [115], Sipkens et al. [88], Jefferson [50], and Kazemimanesh et al. [172]. The fuel used was propane (C_3H_8) with a purity of 99.5% (Praxair, PR 2.5IS-FX). A mass flow controller (Alicat, MCR 50 SLPM) was used to maintain a constant fuel flow rate of 20 standard L/min (SLPM) (at a reference temperature and pressure of 25°C and 101.325 kPa).

In the new configuration of the burner, water is injected radially into the turbulent non-premixed flame by four atomizers distributed evenly around the flame at an angle, θ, which is defined as the angle between the atomizer centerline and the vertical line in the laboratory coordinate system, as shown in Fig. 3.1. The four atomizers (P&S-360-M12, Tekceleo) injected water with a droplet diameter of 12 ± 3 μm, with the flow rate of each atomizer ranging from 2.1 ± 0.2 g/min to 8.1 ± 0.1 g/min, leading to the highest assist-to-fuel mass flow ratio (MFR) of 0.91. While the water-to-fuel MFR values in flames under study were not close to MFR values causing extinction as measured by Padilla et al. [20], it should be noted that in turbulent flames with an external injection of liquid water, the extinction might still occur in a spatially inhomogeneous way throughout the flame; therefore, chemical effects also play an important role. The mass flow rate of injected water was measured using an electronic balance and a timer (OHAUS Scout, model H-5854, with an uncertainty of ± 0.1 g). The atomizers were positioned radially and produced cone-like sprays expanding with a cone angle of ~22 degrees. The atomizer angles studied were θ = 20°, θ = 40°,

and $\theta = 60°$. A direction normal to the atomizer plane for $\theta = 20°$, $\theta = 40°$, and $\theta = 60°$ are denoted as z_1-, z_2-, and z_3-direction, respectively. A range of θ was chosen to allow all the injected water to be consumed by the flame. For reference, the injection angles can also be expressed as a range of heights above the burner (HAB) at which the injected water would intercept the centerline of the burner. The ranges of dimensionless HAB, normalized by the inner diameter of the burner (50.8 mm), covered for $\theta = 20°$, $\theta = 40°$, and $\theta = 60°$ injection angles are approximately 3 to 12, 1.5 to 3.5, and 0.5 to 1.5, respectively. The horizontal distance from the exit center of the atomizer to the center of the burner varied from 95 mm to 135 mm (i.e., 95, 105, 115, 125, and 135 mm).

The emission measurements were performed with all four atomizers running at average total water flow rates ranging from approximately 8 to 33 g/min. However, during PIV, only the two atomizers within the laser sheet were running at the same individual atomizer flow rate as in emission measurements, i.e., half the total flow rate, to eliminate the interference of the spray field from the other two atomizers located within the vertical plane to the laser sheet with the spray field within the laser plane.

An overview of the experimental conditions is presented in Table 3.1. The first row in Table 3.1 represents the adiabatic flame temperature of a stoichiometric C_3H_8 and air mixture at 1 atm with a reactant temperature of 298.15 K, which is used as the reference temperature. Each experiment was repeated three times to ensure repeatability, and average values are reported in the data analysis.

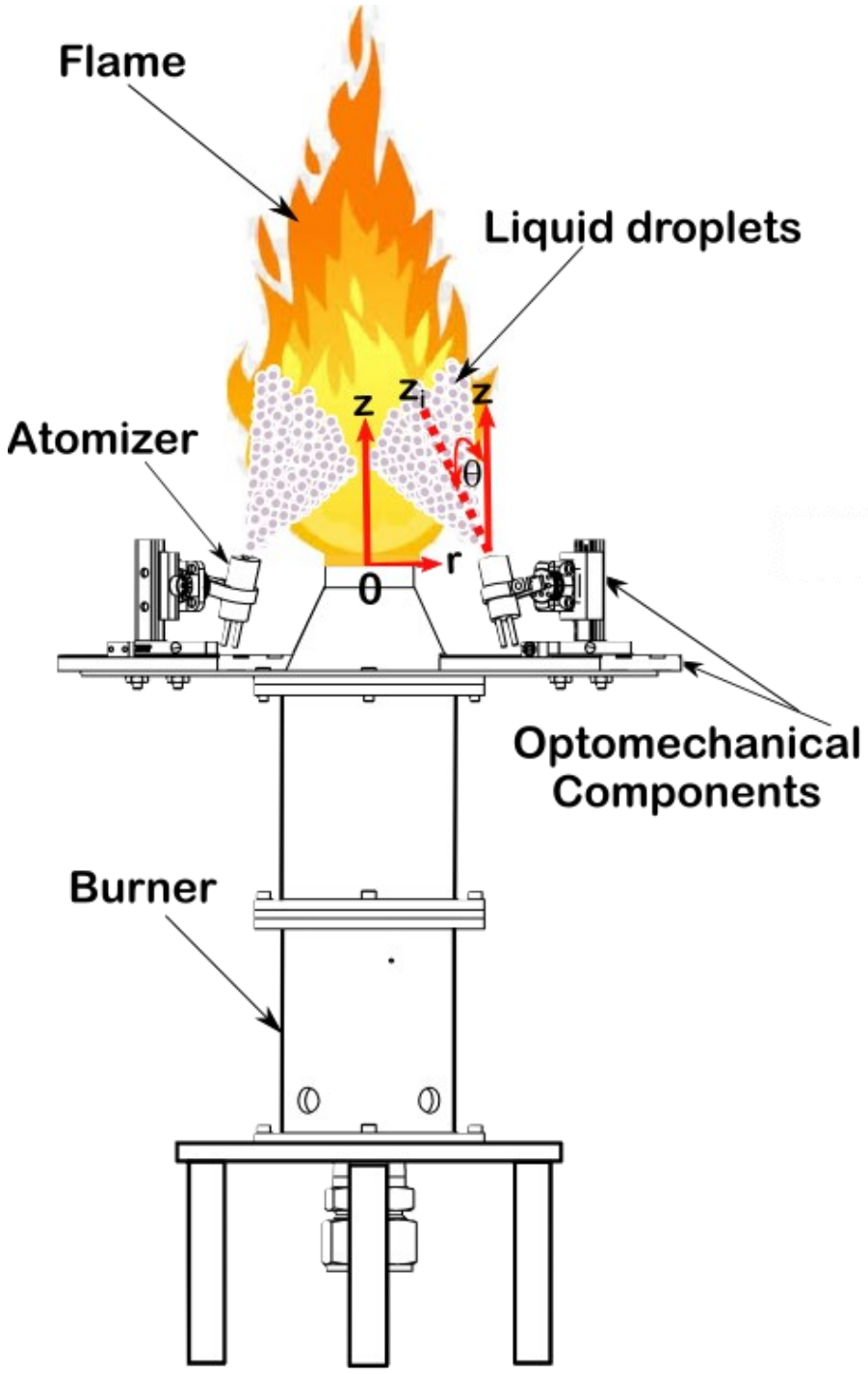

Figure 3.1: A 2D projection view of the burner with radially positioned atomizers. Note that only 2 out of 4 atomizers in the projection plane are shown for clarity.

Table 3.1: Experimental conditions for emission measurements at a constant propane flow rate of 20 SLPM.

θ [1]	Radial location of atomizer exit center from the center of the burner [2] mm	Total liquid flow rate (H_2O + NaCl) g/min	NaCl % mass ratio	Adiabatic flame temperature K
NA	NA	0.00	0.000	2265
60°	95	8.09	0.000	2219
60°	95	12.12	0.000	2196
60°	95	17.63	0.000	2165
60°	95	23.79	0.000	2130
60°	95	32.09	0.000	2082
40°	95	9.12	0.000	2213
40°	95	13.85	0.000	2186
40°	95	20.49	0.000	2149
40°	95	26.19	0.000	2116
40°	95	31.52	0.000	2087
20°	95	9.69	0.000	2210
20°	95	14.50	0.000	2182
20°	95	21.40	0.000	2142
20°	95	27.95	0.000	2106
20°	95	33.11	0.000	2078
60°	105	30.06	0.000	2094
60°	115	30.77	0.000	2089
60°	125	32.87	0.000	2079
60°	135	32.68	0.000	2079
60°	95	31.49	0.005	2086
60°	95	32.08	0.050	2083
60°	95	32.94	0.350	2078
60°	95	29.41	3.500	2101

[1] θ is the angular displacement of atomizers with 0° in the z-direction

[2] Burner radius is 25.4 mm

3.2.2 Emission measurements

Figure 3.2 shows the fuel, water injection, and emission measurement systems of the flame test facility. The emission measurement instruments used in this work are a photoacoustic extinctiometer (Droplet Measurement Technologies, PAX) for BC mass concentration measurements, a NO_x analyzer (Thermo Scientific, 42iQLS) for NO_x concentration measurements. The concentrations of CO and unburned hydrocarbons (UHC) were measured in our previous works by Ahsan et al. [28] and Milad et al. [133] at similar MFR values using gas chromatography. These species were not detected in these tests (i.e., they were below the detection limit of our gas chromatograph), and carbon conversion efficiency [28, 133] remained near 100%. A scanning mobility particle sizer (SMPS), comprising of a differential mobility analyzer (TSI model 3080) and ultrafine condensation particle counter (TSI model 3776), was used to measure the particle size distribution of the soot. The result section of this work contains the size distributions of the particle emissions measured by the SMPS for all operating conditions; however, the discussion of the particle emissions will focus on the BC mass concentration measurements made by the PAX. The details of the emission measurement equipment, measurement techniques, and experimental setup can be found in the previous work [24].

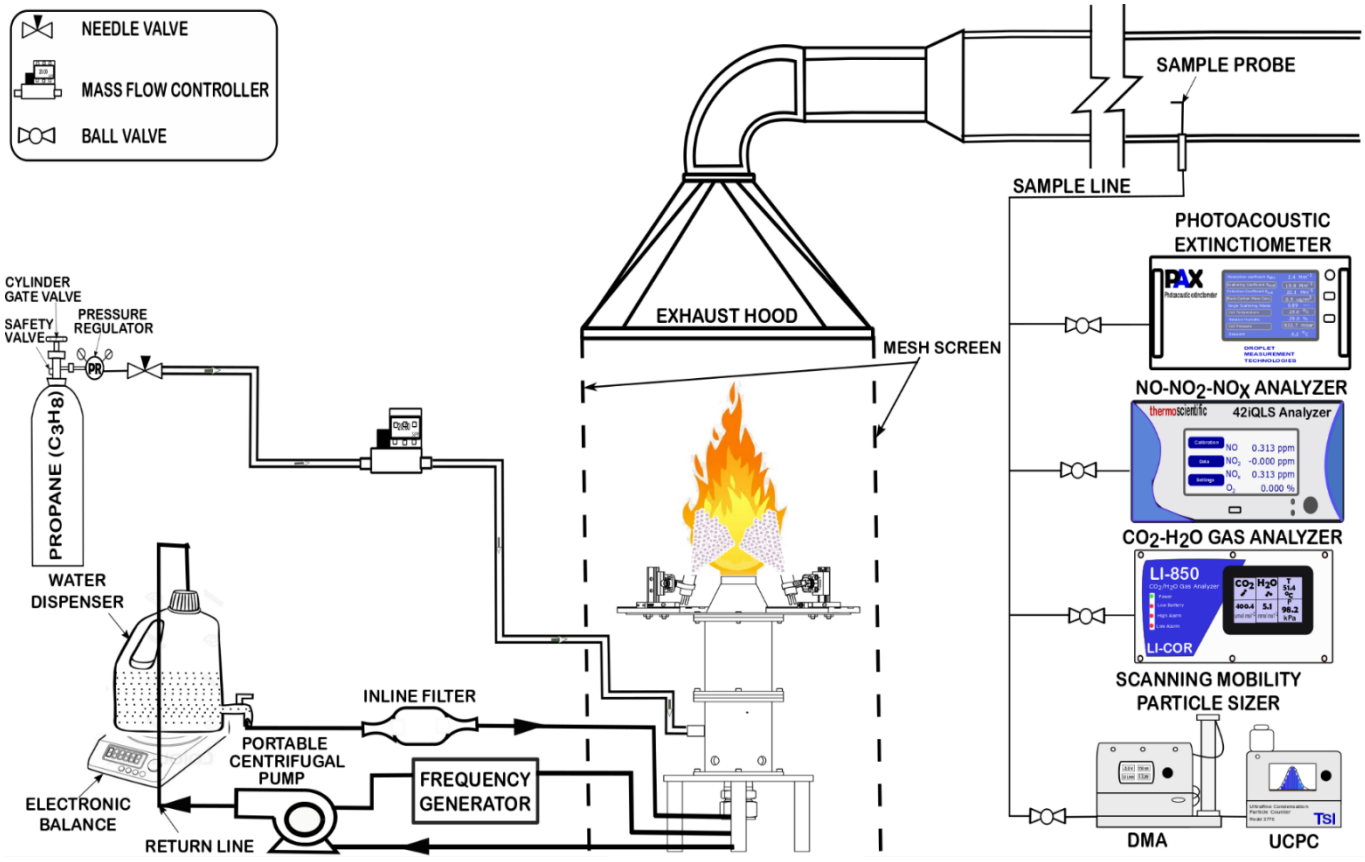

Figure 3.2: Schematic of the test facility for water-assisted flares and emission measurements.

3.2.3 Particle image velocimetry setup

A two-dimensional, two-component particle image velocimetry (PIV) was used in this study to quantify the 2D projection of the velocity vector field of the atomized water droplets within the plane of the laser sheet. Figure 3.3 illustrates the PIV system, which consists of a visible dual cavity neodymium-doped yttrium lithium fluoride (Nd:YLF) laser at 527 nm wavelength (Litron

LD30-527), Photron FASTCAM NOVA S9 camera with a narrow bandpass filter (527/20 nm) mounted on the camera lens, and programmable timing unit. The spray of atomized water droplets from the two atomizers facing each other was illuminated by a thin sheet (~ 1.5 mm thick) of laser light crossing the plume of water droplets. This diagnostic is non-intrusive and does not affect the streamlines of spray droplets. The light scattered from the water droplets was captured using the high-speed camera at a resolution of 1024 × 1024 pixels. A programmable timing unit was used to synchronize the laser and the camera.

Time-resolved PIV image pairs were then post-processed using DaVis 10 software to calculate the velocity field of atomized water droplets. In post-processing, a larger interrogation window of 64 × 64 pixels is refined using a grid-refinement cross-correlation technique to a 16 × 16 pixel grid in 5 passes with a window over-lap of 75% for the smallest interrogation window. The pixel-to-mm calibration ratio was 10.735 mm^{-1} calculated using calibration images corresponding to a measurement area of approximately 95 × 95 mm^2. Due to the window overlapping of 75%, velocity vectors were calculated at the grid spacing of 373 μm. However, independent velocity vectors were achieved at the size of the smallest interrogation window resulting in a spatial resolution of 1.49 mm. A Fast Fourier Transform (FFT) algorithm was used to calculate the droplet velocity through cross-correlation. Based on the time delay, the FFT algorithm was used to compute the displacements of the detected droplets and, therefore, the velocity components.

A major challenge in using the atomized water droplets as tracer particles in PIV was that the spatial density of droplets (number of droplets per unit volume) could not be controlled independently from the water flow rate of the atomizers; hence, it could not be optimized for PIV, i.e., 8-10 droplets in each interrogation window [173]. The significant overlap of water droplets resulted in saturated spots within the PIV images causing correlation errors in PIV processing in

these regions. In each PIV test, 4000 time-resolved PIV images were captured at an imaging speed of 4 kfps to freeze the motion of the water droplets. These series of images were used to generate time-resolved PIV images at a reduced imaging frequency by skipping between images. Finally, 400 image pairs were post-processed at the reduced frequency of 2 kfps in each experiment to minimize correlation errors and ensure statistical accuracy.

The PIV images were post-processed to generate the velocity vector field of the water spray from an atomizer, as well as the averaged water droplet velocities at various heights above the atomizer exit in the z_2-direction (i.e., analysis only performed at $\theta = 40°$). The PIV test window of approximately 95 × 95 mm^2 was manually divided into cells of 169 squares of 7 × 7 mm and 26 rectangles of 4 × 7 mm and 1 square of 4 × 4 mm, giving 196 cells. The velocity vectors used to generate velocity distributions for each subsection using 400 image pairs were 144,400 for each velocity component. To eliminate spurious velocity vectors caused by correlation errors in PIV processing due to the high density of water droplets, the velocity vector fields were post-processed by fitting multimodal Gaussian distributions to the data using the Gaussian Mixture Models (GMM) filtering algorithm in MATLAB. This work uses three or four-mode Gaussian distributions to fit the PIV velocity vector fields. Velocity vector distributions with a mean magnitude of 0 to 0.1 m/s were removed from the data since these were an artifact of saturation in the images (i.e., particles appear to be motionless because the PIV algorithm mistakenly correlates the wrong droplet pair in the images). The mean value of the filtered velocity vector distribution was then used to report the mean velocity for liquid water droplets in each cell. Examples of the multimodal Gaussian distributions for the velocity vector fields over three cells are shown in Appendix B for the angled water injection with a flow rate of 2.1 g/min.

The SLR images were taken in manual mode in similar lighting (i.e., dark) with no post-processing and no filtering. The settings are identical for all images and are as follows: shutter speed (exposure time) of 1/3200 s, camera aperture of F6.3, and ISO of 6400. Therefore, the color change between images can be recognized.

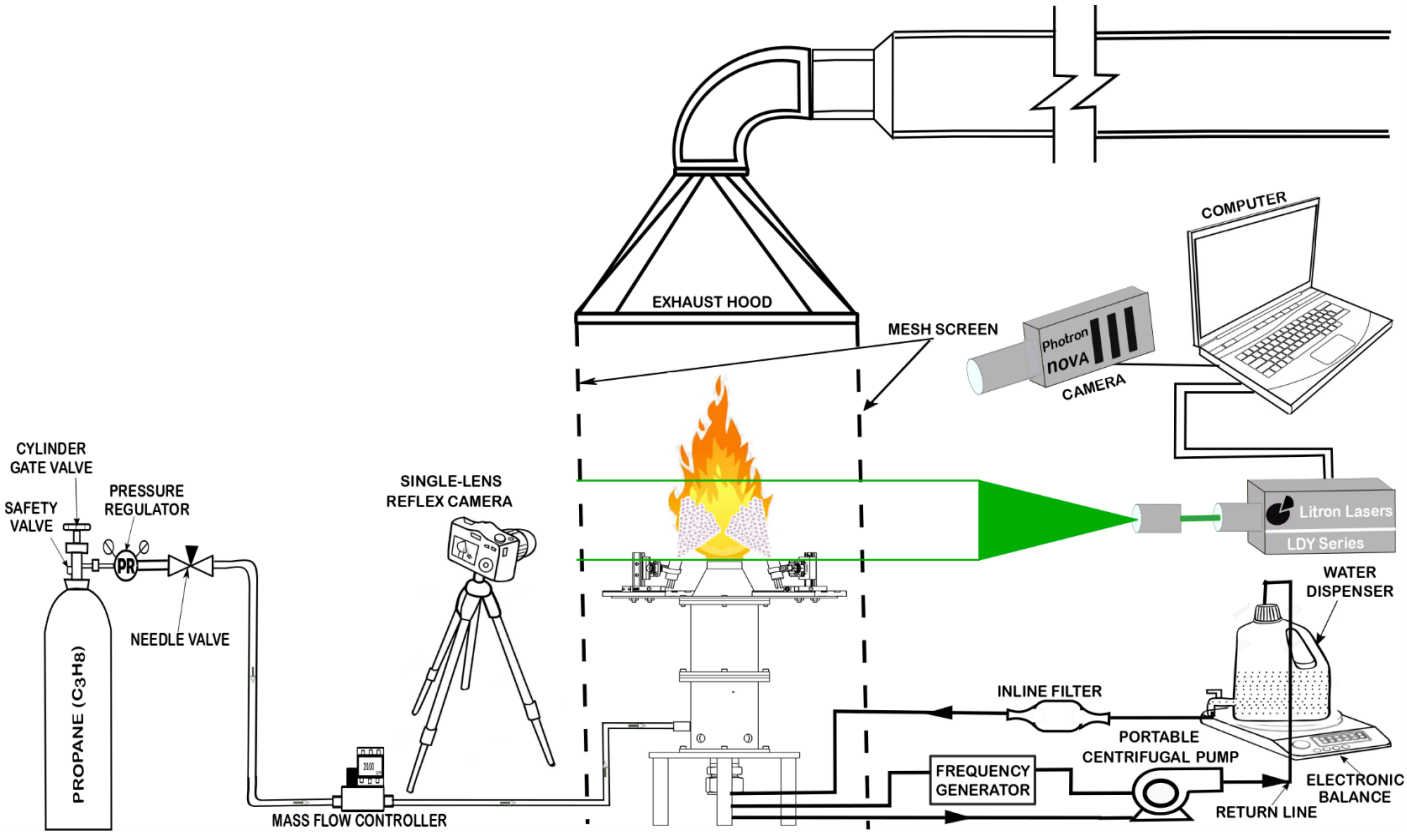

Figure 3.3: Schematic of the test facility for water-assisted flares and PIV.

3.3 Results and discussion

Figure 3.4 shows SLR images when pure liquid water and NaCl solutions are injected into the flame. The colors and luminosity of flames are influenced by the concentrations of the generated soot and the NaCl introduced into the flame. The flames' yellow colors are mostly due to incandescence from soot particles at the wavelength range of 340 – 600 nm [174]. In contrast, the orange color is attributed to the excited Na^+ radicals at around 589 nm at flame temperature [116]. Figure 3.4a shows that the luminosity of the flame at the base is reduced as θ increases and the water is injected closer to the base of the flame. In Fig. 3.4b, it can be seen that as the atomizers moved closer to the burner, i.e., as the distance between the center of the atomizers and the burner decreased from 135 mm to 95 mm, the flame luminosity and width at the base decreased. The flames in Fig. 3.4c show a change in color from yellow to gold to orange as the NaCl concentration increases.

a.

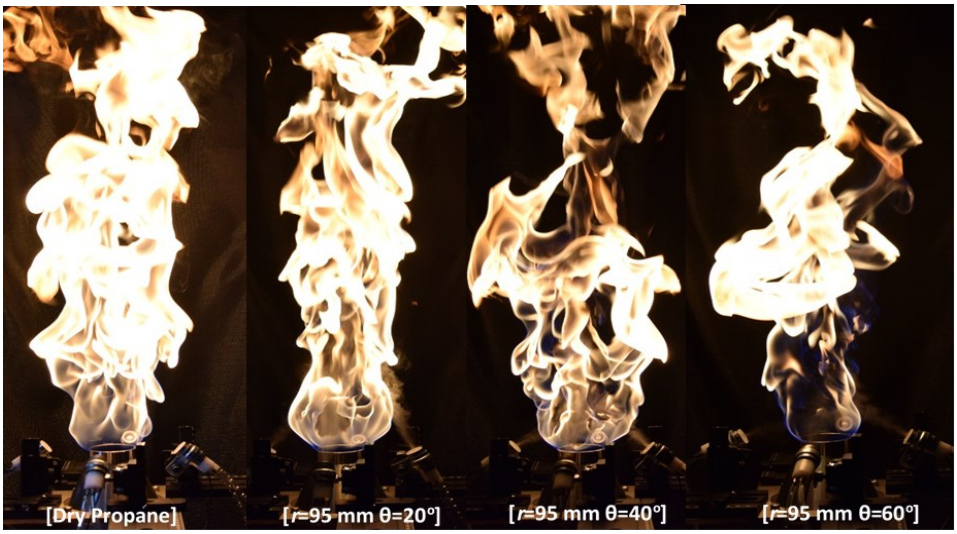
[Dry Propane]
[r=95 mm θ=20°]
[r=95 mm θ=40°]
[r=95 mm θ=60°]

b.

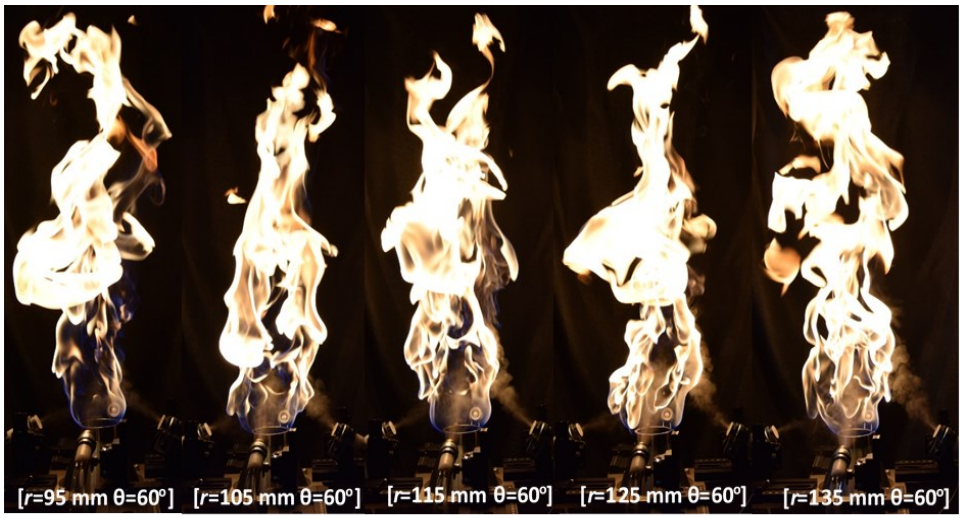
[r=95 mm θ=60°]
[r=105 mm θ=60°]
[r=115 mm θ=60°]
[r=125 mm θ=60°]
[r=135 mm θ=60°]

c.

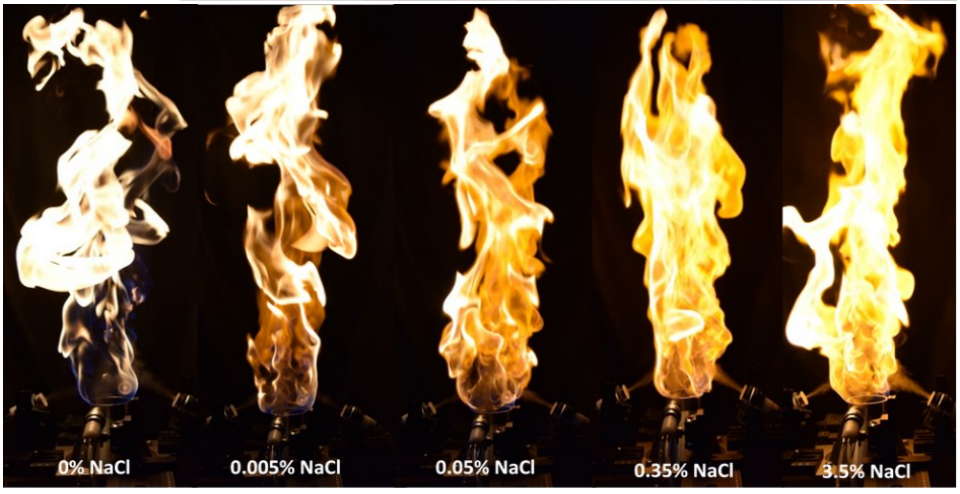
0% NaCl
0.005% NaCl
0.05% NaCl
0.35% NaCl
3.5% NaCl

Figure 3.4: Flame images: (a) angular and (b) and horizontal displacement of the atomizers, (c) injection of NaCl solutions at various concentrations.

3.3.1 PIV analysis of the liquid water spray velocity field

The PIV was carried out on a turbulent flow carrying water droplets injected into the flame, as shown in Figure 3.5. Figures 3.5a and 3.5c illustrate sample SLR images of the flame and water spray, as well as the PIV test window. By examining the SLR images (on the order of 100 images), it was observed that almost all water droplets traveled well into the flame before evaporation, although the number density of the droplets decreased after penetrating the flame. The fact that water droplets pass through the flame front suggests that the flame was locally quenched, and the droplets affect the local flame temperature, reaction kinetics, and emissions. Furthermore, as the droplets pass through the high-temperature zone and follow the upward flow of the bulk gas, the evaporating water droplets participate in chemical reactions. Therefore, the chemical effects of water on soot and NO_x suppression occur at higher locations in the flame compared to internal injection. For more images on water spray and flame interactions, please see Appendix B.

Figures 3.5b and 3.5d show the velocity vector field for one angled atomizer at $\theta = 40°$ in z- and r-coordinates with a dashed line representing the z_2-direction (the angle of the atomizers). Figure 3.6 also illustrates the mean water droplet velocity magnitude along the centerline of the atomizer spray at $\theta = 40°$ in the z_2-direction calculated using 2D linear interpolation over the velocity data. PIV analysis to calculate the velocity field illustrated in these figures was only performed for the lowest (2.1 ± 0.2 g/min) and the highest flow rates (8.1 ± 0.1 g/min) when the atomizers were located at $r = 95$ mm and $\theta = 40°$. The PIV analysis was done with a single atomizer to increase

the spatial resolution of the PIV analysis, assuming that the velocity field at the exit of all four atomizers was similar. The red box indicates the analysis window in each figure. Figures 3.5b and 3.5d show that the water droplets exited the atomizer at an angle $\theta = 40°$ and continued their path at the same angle until they passed through the reaction zone, where they were deflected upward and lost their radial momentum (by drag) by a flow with increasing buoyancy (due to increased temperature) and decreasing droplet mass (due to evaporation). Eventually, the droplets were converted to vapor as they followed the upward flow of fuel and exhaust gas mixture. As illustrated in Fig. 3.5b, the upward deflection of the droplets with the lower momentum (i.e., the lower water flow rate) started about 55 mm away from the center of the burner (r = 55 mm), while the droplet spray with a higher momentum (i.e., the higher water flow rate) started deflecting upward at r = 40 mm (Fig. 3.5d). The upward deflection became more significant at about r = 25 mm for both flow rates, and eventually, the droplets were fully following the bulk gas flow upward with almost no radial momentum (top left corner of the red boxes in Figs. 3.5b and 3.5d). Furthermore, as illustrated in Fig. 3.6, the water droplets at the higher and the lower flow rates exited the atomizer at around 1.4 m/s and 0.8 m/s, respectively, which was orders of magnitude larger than the droplet settling velocity. However, at both flow rates, the droplet velocities appear to be converging towards 1 m/s, i.e., the upward velocity of the bulk gas at z_2 larger than 100 mm, which showed that these water jet momentum fluxes caused an indistinguishable difference in the gas flows on the fuel side of the flame, minimizing the air entrained into the flame. Hence, the experiments focus on the extent that the water interacts with the flame earlier or later in the process.

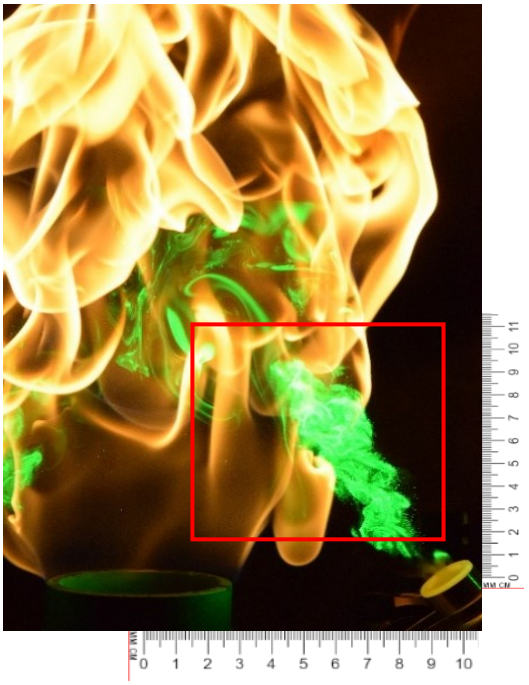

(a)

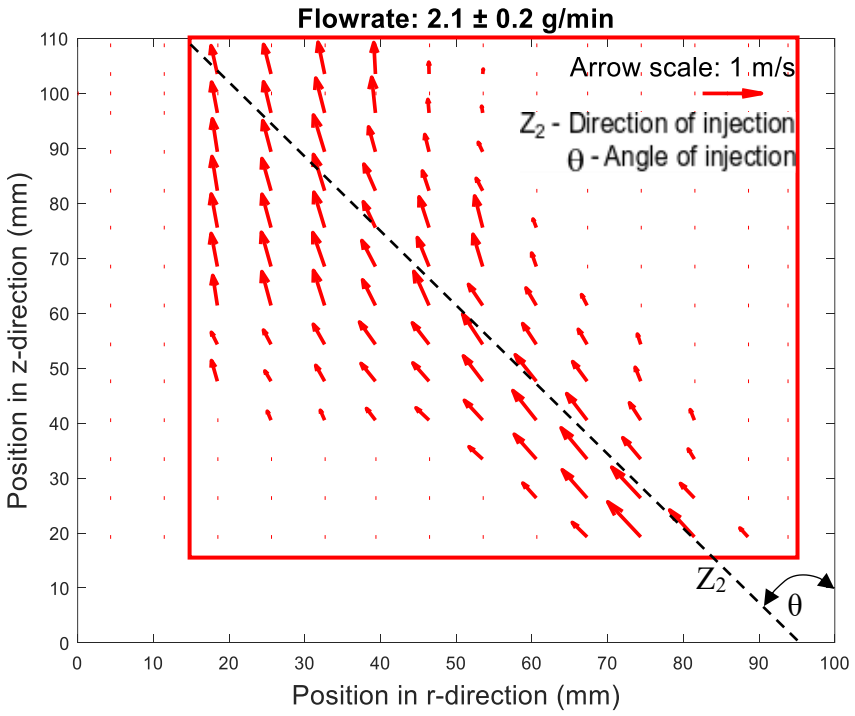
Flowrate: 2.1 ± 0.2 g/min
Arrow scale: 1 m/s
Z_2 - Direction of injection
θ - Angle of injection
Z_2
θ
Position in z-direction (mm)
Position in r-direction (mm)

(b)

(c)

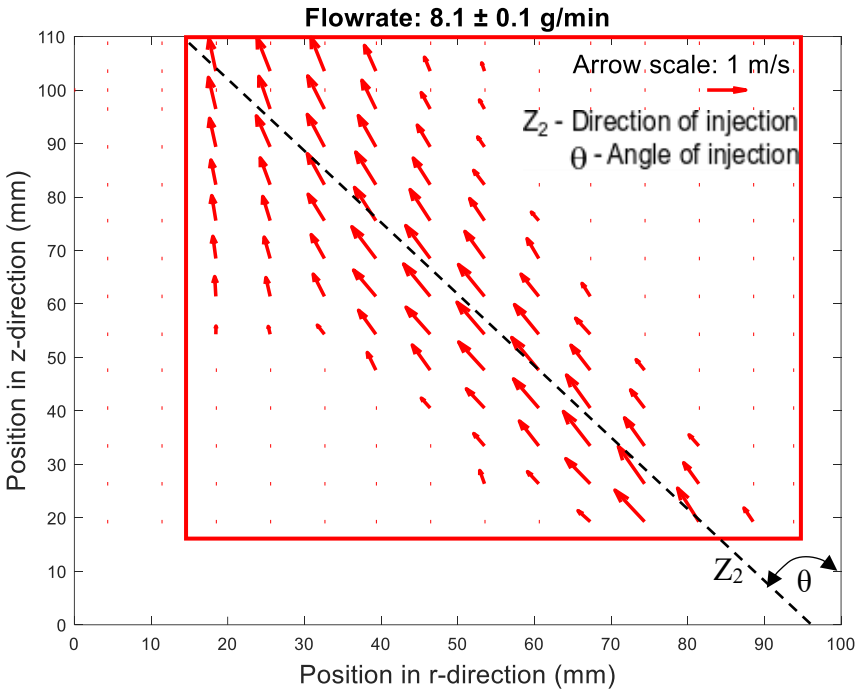
Flowrate: 8.1 ± 0.1 g/min
Arrow scale: 1 m/s
Z_2 - Direction of injection
θ - Angle of injection
Z_2
θ
Position in z-direction (mm)
Position in r-direction (mm)

(d)

Figure 3.5: Single atomizer SLR images and PIV velocity vector fields at atomizer angle, $\theta = 40°$ (z_2 - indicated as a dashed line), and displacement of 95 mm from the center of the burner: (a) and (b) sample SLR image and PIV results for a water flow rate of 2.1 g/min, respectively, (c) and (d) sample SLR image and PIV results for a water flow rate of 8.1 g/min, respectively.

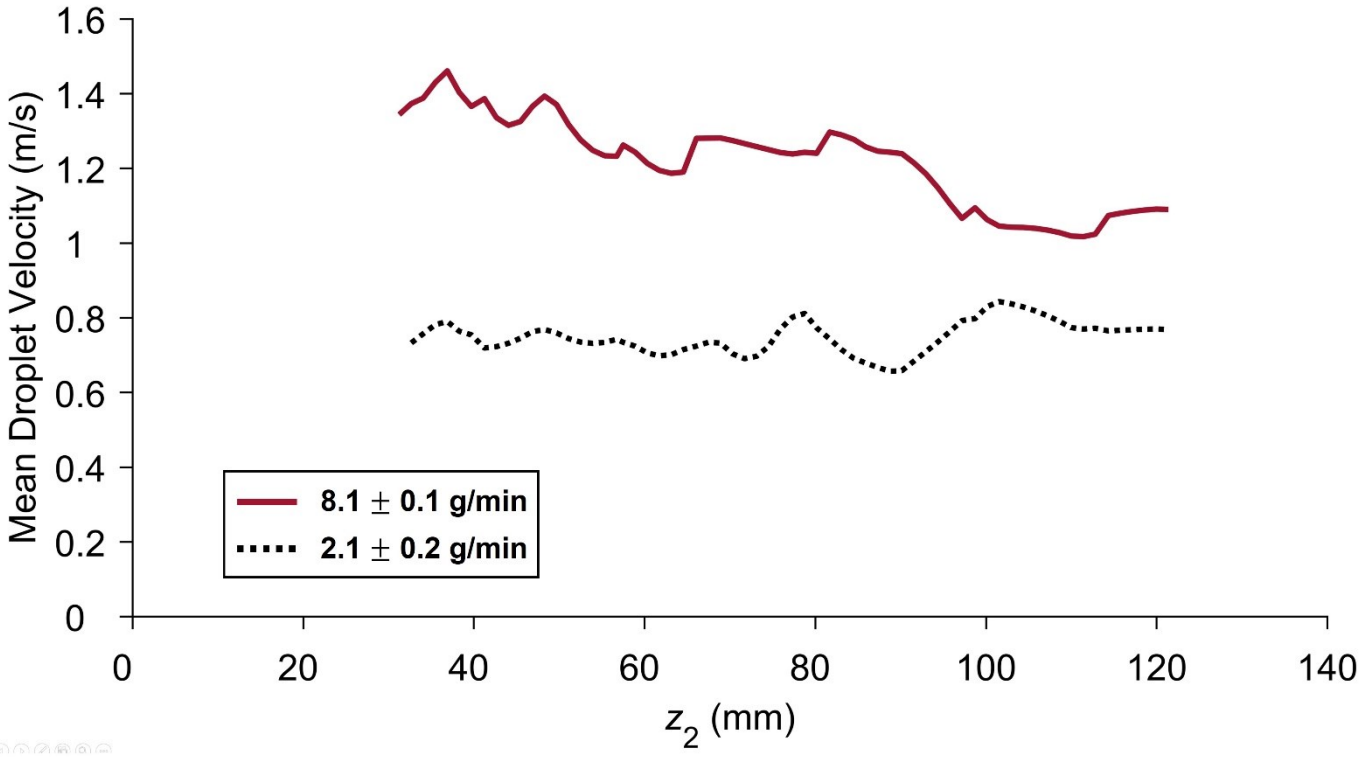

Figure 3.6: Mean water droplet velocity magnitude (i.e., speed) as observed along the centerline of the atomizer spray ($\theta = 40°$) at the lowest (2.1 g/min) and the highest (8.1 g/min) flow rates in z_2-direction.

3.3.2 Effect of atomizers' angular displacement on emissions

This study explores how the location of water injected into the flame affects NO_x and BC emissions. Figure 3.7 shows the BC emission indices (EI_{BC}) plotted against the corresponding assist-to-fuel mass flow ratio ('assist' refers to the fluid, i.e., water, steam, or NaCl solution, added to the flame) for the external injection of liquid water with atomizers positioned at 95 mm away from the center of the burner at angles of 20°, 40°, and 60°. Figure 3.7 also presents the internal injection of steam and liquid water from Bello et al. [24] using the same burner for comparison. At the MFR range of 0 to 0.25, the external injection of liquid water showed similar EI_{BC} results compared to the internal injection of liquid water and steam. However, at MFR values above 0.25, the internal injection of liquid water is more effective in suppressing BC, followed by internal steam addition, which showed almost the same EI_{BC} as in the external injection of liquid water at $\theta = 60°$. It is also illustrated that by decreasing θ, the external water injection into the flame became less effective in suppressing BC at higher MFRs. While external water injection at $\theta = 20°$ and $\theta = 40°$ produced the same EI_{BC} as the internal injection of steam at MFRs in the range of 0 to 0.4, at MFR values higher than 0.85, internal injection of steam suppressed EI_{BC} more significantly by approximately one order of magnitude.

Figure 3.7 illustrates two contributing effects in suppressing BC from the flames under study. First is the temperature effect, where adding assisting fluid, i.e., liquid water or steam, into the flame reduces the flame temperature, thereby decreasing the rate of fuel pyrolysis and BC formation. It is discernible that the addition of liquid water would reduce the flame temperature more than steam, as water has lower enthalpy compared to steam by both the sensible enthalpy and the enthalpy of evaporation. Second is the spatial-temporal scale of flame interactions with the

assisting flow of water or steam (i.e., the location of introducing the assisting flow into the flame is defined as *spatial,* and how early on the assisting flow is added into the flame is defined as *temporal* effects). In internal injection, the mixing of the assisting water or steam with fuel occurs before or near the burner exit, and the thermal and chemical effects are involved at the very early stages of combustion, i.e., a part of the fuel is already premixed with the assisting fluid before combustion. In external injection, on the other hand, the liquid water spray is added to the flame well above the burner exit, where the chemical reactions involved in BC generation have already started, and therefore, the effects of water injection do not participate in those early stages. As illustrated in Fig. 3.7, in external water injection, by decreasing the angle of the atomizers, i.e., tilting the atomizers towards the upright position, the water entrainment into the flame is higher above the burner exit plane, and therefore, more BC is produced. Based on these results, it can be concluded that external liquid water injection into turbulent non-premixed flames and potentially industrial flares can effectively reduce BC or soot, but the reduction in BC emissions is more significant if the water is injected as close as possible to the base of the flame where soot formation is just beginning. One main advantage of external liquid water injection is that it can be implemented into the existing systems without a need for significant structural modifications to the flare stack.

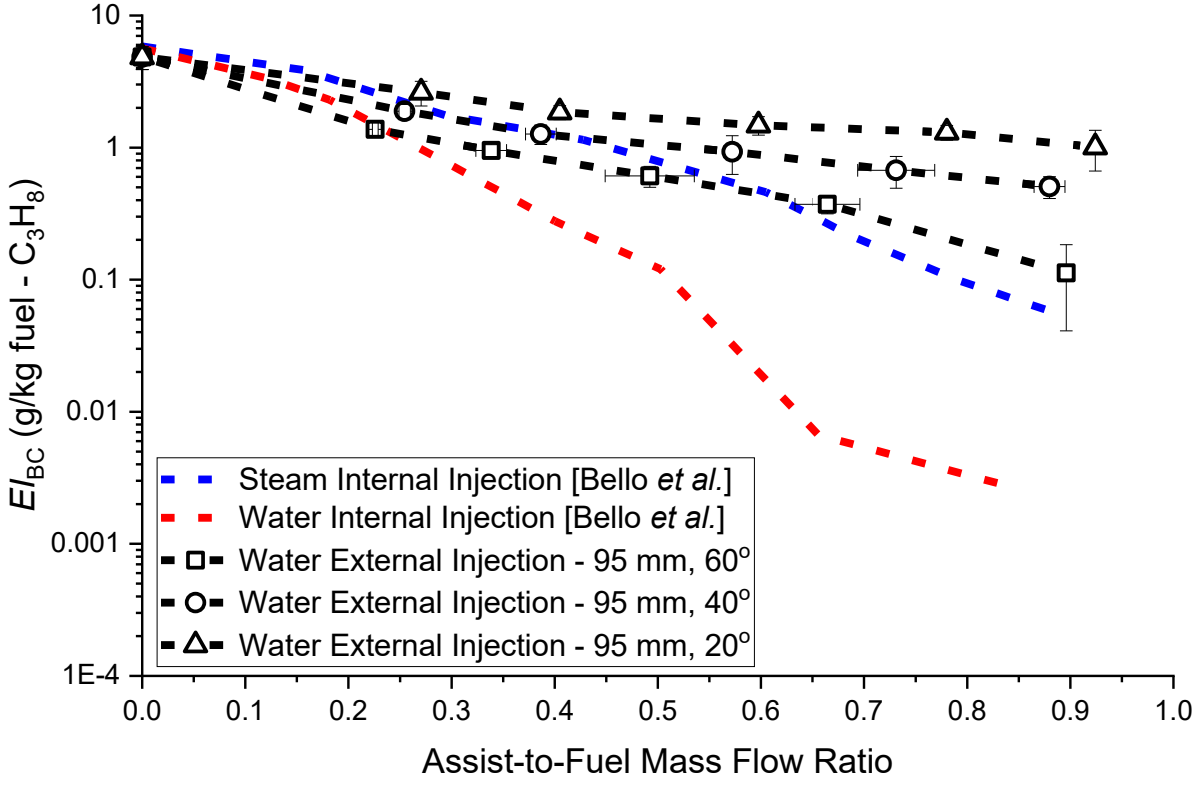

Figure 3.7: BC emission indices (EI_{BC}) of propane flame with steam and liquid water addition.

Figure 3.8 shows the NO_x emission indices (EI_{NO_x}), plotted against the corresponding assist-to-fuel mass flow ratio for the external injection of liquid water with atomizers positioned at 95 mm away from the center of the burner at angles of 20°, 40°, and 60°. The figure also presents EI_{NO_x} plotted against the corresponding MFR values for internal water and steam injection from the work of Bello et al. [24]. It should be noted that EI_{NO_x} for the propane flame without assisting fluid for this present study differs from the previous work of Bello et al. [24] by approximately 6%, which creates a small offset between the data sets. Figure 3.8 shows that EI_{NO_x} for the angles of 20° and 40° are similar to each other and steam injection, while in the case of external injection of water at

θ = 60°and within the MFR range of 0.2 to 0.65, EI_{NO_x} was approximately 80% and 25% lower compared to the internal injection of steam and liquid water, respectively. Since all cases with liquid water injection (internal or external) have the same global adiabatic flame temperature (see Table 3.1) at the same MFR, the differences in EI_{NO_x} are due to local effects of the water on the combustion process. These results demonstrate that adding liquid water directly into the base of the flame (i.e., the liquid water injection at θ = 60°) reduces NO_x even more than the internal injection of liquid water. The addition of liquid water directly into the flame front, compared to internal injection, which is more evenly distributed in the fuel, causes the spatially inhomogeneous low-temperature flame zone, i.e., the locally quenched flame zone, to coincide with the NO_x production zone of the flame downstream of the burner base leading to a reduction in EI_{NO_x}. However, by further decreasing the atomizer angles to 40° and 20° (i.e., delaying the water entrainment even further), EI_{NO_x} increased almost two times at high MFR values, which was more than both the water injection at θ = 60° and internal water injection and had almost the same EI_{NO_x} as the internal steam injection. These results highlight the spatial-temporal effects of water addition into flames on NO_x emissions and suggest that both time and space play important roles when adding assisting fluid to non-premixed flames to reduce NO_x emissions.

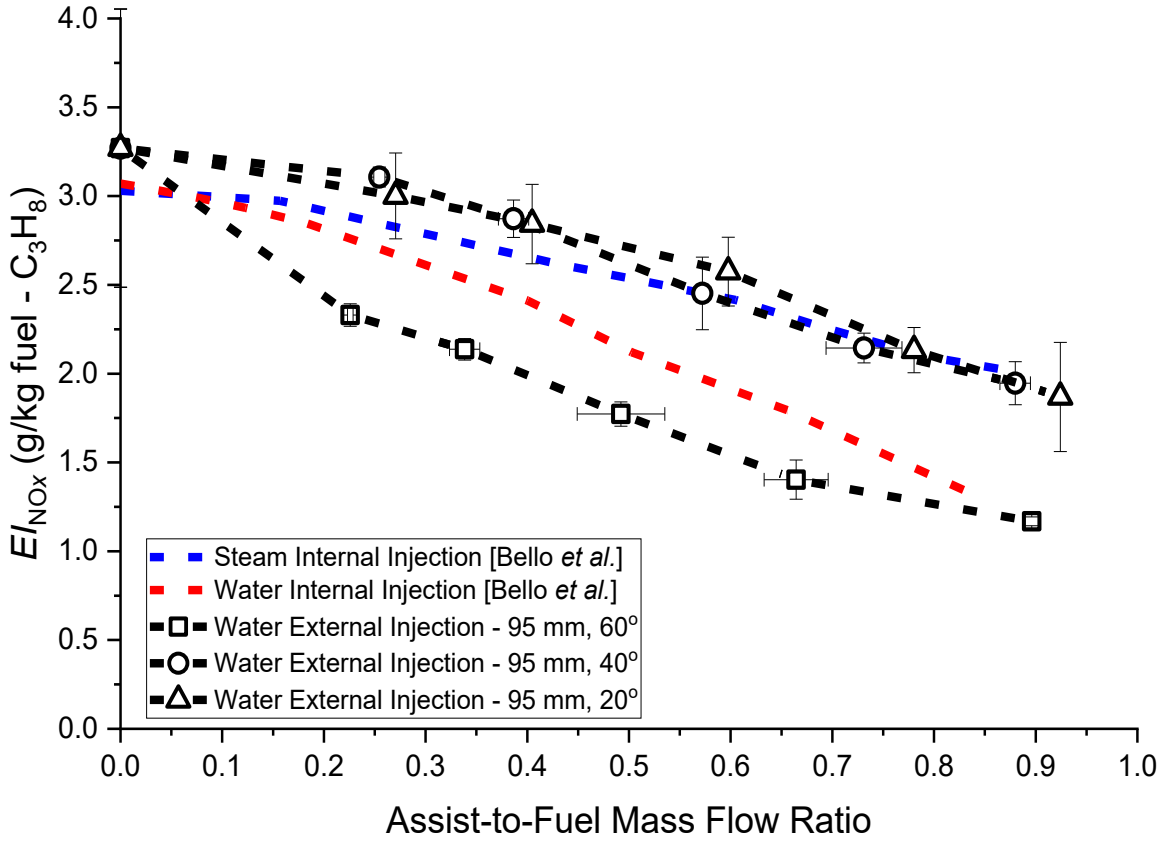

Figure 3.8: NO_x emission indices (EI_{NO_x}) of the propane flame with their corresponding assist-to-fuel mass flow ratio.

3.3.3 Effect of atomizers' horizontal displacement on emissions

Figure 3.9 presents EI_{BC} and EI_{NO_x} plotted against the horizontal displacement of the atomizer's exit from the center of the burner. As the atomizers' horizontal displacement varies between r = 135 mm and r = 95 mm, the extent of the atomizer exit centerline at θ = 60° crosses the outer burner diameter (i.e., r = 28.6 mm) between z = 61.5 mm and z = 38.4 mm, respectively, thereby

introducing the water lower in the flame. The results show that EI_{BC} decreased by almost an order of magnitude as the atomizers moved closer to the center of the burner, which can be attributed to the chemical and thermodynamic effects of water addition being injected closer to the base of the flame at the early stages of combustion. It can be assumed that the closer the atomizers are to the center of the burner, the earlier in the combustion process water reacts with the polycyclic aromatic hydrocarbons (PAHs) created immediately after fuel pyrolysis. This early interaction might hinder the formation of soot precursors. Also, the rate at which fuel undergoes thermal cracking reduces because of the water injection, and this thermal effect decreases the formation of soot. In addition, the increase in OH radicals due to water injection [122, 123, 124] leads to the oxidation of soot precursors reducing soot emissions, as shown by Lee et al. [127] that the mole fraction of soot precursors (i.e., acetylene) reduced in water-assisted non-premixed flames. Figure 3.9 also shows no significant change in EI_{NO_x} for the various distances of the atomizers, mainly due to a limited change in the horizontal distance of the atomizers. The slight differences in EI_{NO_x} noticed might be due to the uncertainty in the total water flow rate of the four atomizers in various experiments.

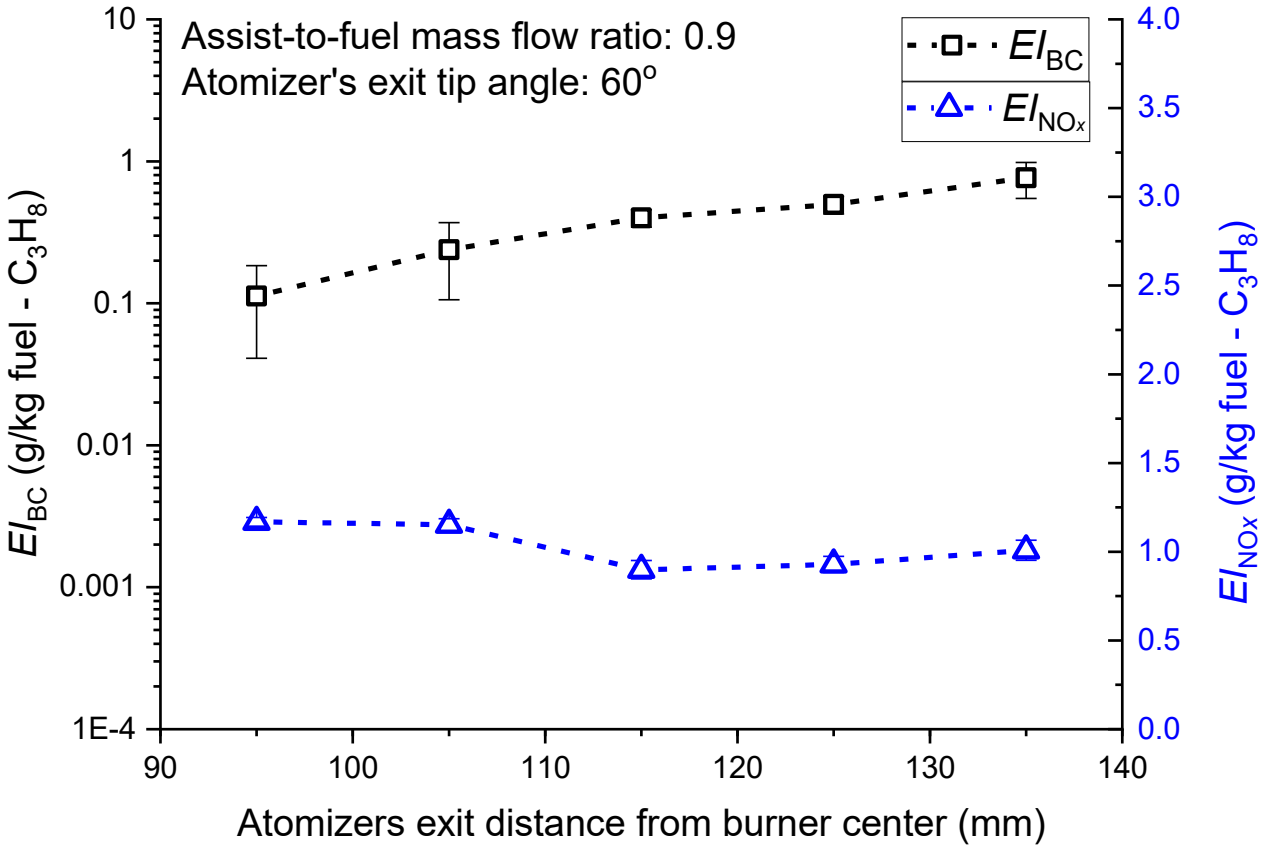

Figure 3.9: EI_{BC} and EI_{NO_x} plotted against the ratio of the atomizers' exit distance from the center of the burner to the burner exit radius at MFR= 0.9 and θ = 60°.

3.3.4 Effect of NaCl solution on emissions

Figure 3.10 shows EI_{BC} and EI_{NO_x} plotted against NaCl concentration at a constant MFR = 0.9, θ = 60°, and the atomizers center exit positioned at r = 95 mm. It should be noted that NaCl solutions with various concentrations contained the same flow rate of water. It can be seen that the injection of deionized water had approximately the same EI_{BC} and EI_{NO_x} as in the cases of NaCl addition to

the flame with concentrations of 0.005% and 0.05%. This shows that small concentrations of NaCl did not have a significant effect on BC and NO_x emissions. However, higher concentrations of NaCl, i.e., 0.35% and 3.5% injected at the same water flow rate and angle as in the case of deionized water, decreased EI_{NO_x} by about 20% and 40%, respectively, compared to the deionized water while EI_{BC} was increased by approximately 2 and 7 times, respectively.

Note that the reduction in EI_{NO_x} is not due to a reduction in the adiabatic flame temperature: the total liquid flow rate (H_2O + NaCl) is almost constant in these experiments, and the addition of NaCl causes a small increase in the theoretical adiabatic flame temperature (19 K for the 3.5% NaCl solution, see Table 3.1). The significant change in NO_x and BC emissions at almost constant adiabatic flame temperature highlights the chemical effects of adding NaCl to the flames on NO_x suppression and soot increase. According to Lissianski et al. [89], when NaCl is added to the flame, it reduces the concentrations of radicals, such as H, O, and OH. Specifically, Na is known to play a direct role in removing OH and H radicals through the reactions Na + OH + M $\leftrightarrow$ NaOH + M and NaOH + H $\leftrightarrow$ Na + H_2O, where M is an energy-removing collision partner [175]. Also, chlorine plays an indirect role in reducing OH radical concentrations. Hydroperoxyl (HO_2) radicals can produce more OH when reacted with hydrogen through: H + HO_2 $\rightarrow$ OH + OH. But the HO_2 radical can be scavenged by Cl through the reaction: HO_2 + Cl $\rightarrow$ HCl + O_2, preventing the formation of OH [175]. Furthermore, since O radicals are produced by the reaction: H + O_2 $\leftrightarrow$ OH + O, a reduction in the H radical concentration due to Na will also result in a reduction in O radicals, as also stated by Lissianski et al. [89]. The reductions in these three radicals profoundly affect NO_x and soot emissions, as observed in Figure 3.10. According to the Zeldovich mechanism and the reaction: O + N_2 $\leftrightarrow$ NO + N, a reduction in O radicals results in reduced NO_x emissions

[151]. However, the reduction in the OH radical reduces the oxidation of soot ($C_{(s)}$ + OH → CO + ½H_2 [176]).

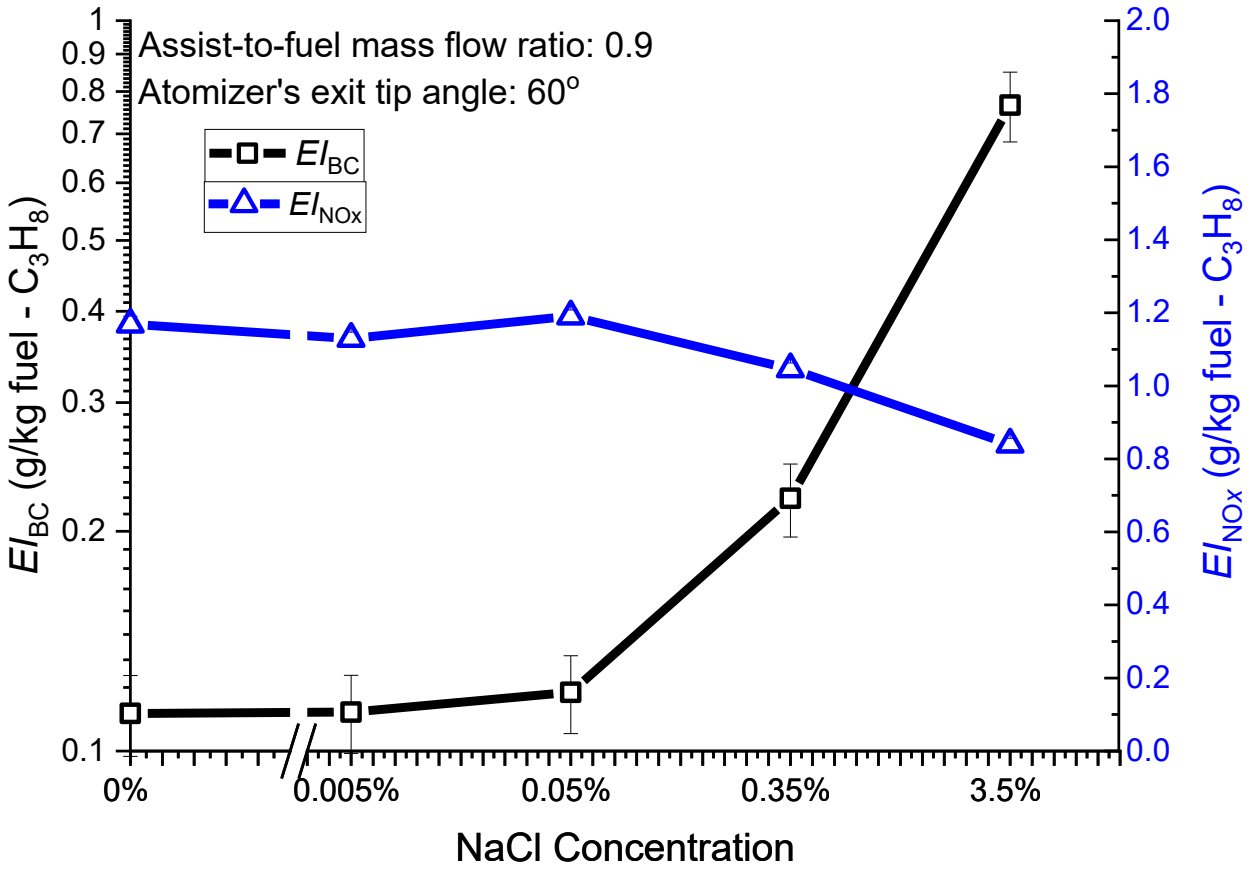

Figure 3.10: EI_{BC} and EI_{NO_x} as a function of NaCl concentration at a constant MFR = 0.9 and θ = 60°.

3.3.5 Particle size distributions (PSDs)

Figure 3.11a shows the particle size distribution of the turbulent non-premixed propane flame with internal liquid water injection at the different assist-to-fuel mass flow ratios (*MFRs*) presented

in Bello et al. [24]. Figure 3.11b, 3.11c, and 3.11d show the particle size distribution for external liquid water injection at different atomizer's angles (i.e., $\theta = 20°$, $\theta = 40°$, and $\theta = 60°$) and at the same horizontal displacement from the center of the burner (i.e., r = 95 mm). Figures 3.11a to 3.11d reveal that increasing water injection reduces the soot particle number concentration. Also, the internal injection of liquid water reduces the particle number concentration more significantly compared to external water injection at the same assist-to-fuel mass flow ratio. Comparing the different angles of external water injection, it is observed that injecting water closer to the base of the burner is more effective in suppressing the number concentration of particles (and by proxy, the mass concentration as explained above). Figure 3.11e shows the particle size distribution at the same flow rate but different horizontal displacement of the atomizer from the center of the burner (i.e., r = 95, r = 105, r = 115, r = 125 and r = 135 mm). As the atomizers moved closer to the center of the burner (i.e., introducing the water lower in the flame), the soot particles were more effectively suppressed.

Figure 3.11f shows the particle size distribution at various concentrations of NaCl solution at the same liquid flow rate, atomizer's angle, and horizontal displacement from the center of the burner. It is illustrated that adding pure deionized liquid water (i.e., 0% NaCl concentration) decreased the soot particle number concentration compared to the dry propane flame. However, the addition of higher concentrations of NaCl increased the particle number concentration. Note that the total liquid flow rate (i.e., H_2O + NaCl) is almost constant while changing NaCl concentration in all experiments. As illustrated in Fig. 3.11f, by introducing water into the propane flame, the soot was suppressed, and therefore, the number of particles decreased compared to the dry propane flame. However, NaCl addition resulted in a significant increase in particle concentration, as illustrated

in Fig. 3.11f, mainly due to the emission of NaCl particles formed by the nucleation of evaporated NaCl as observed in several other studies [34, 88, 172].

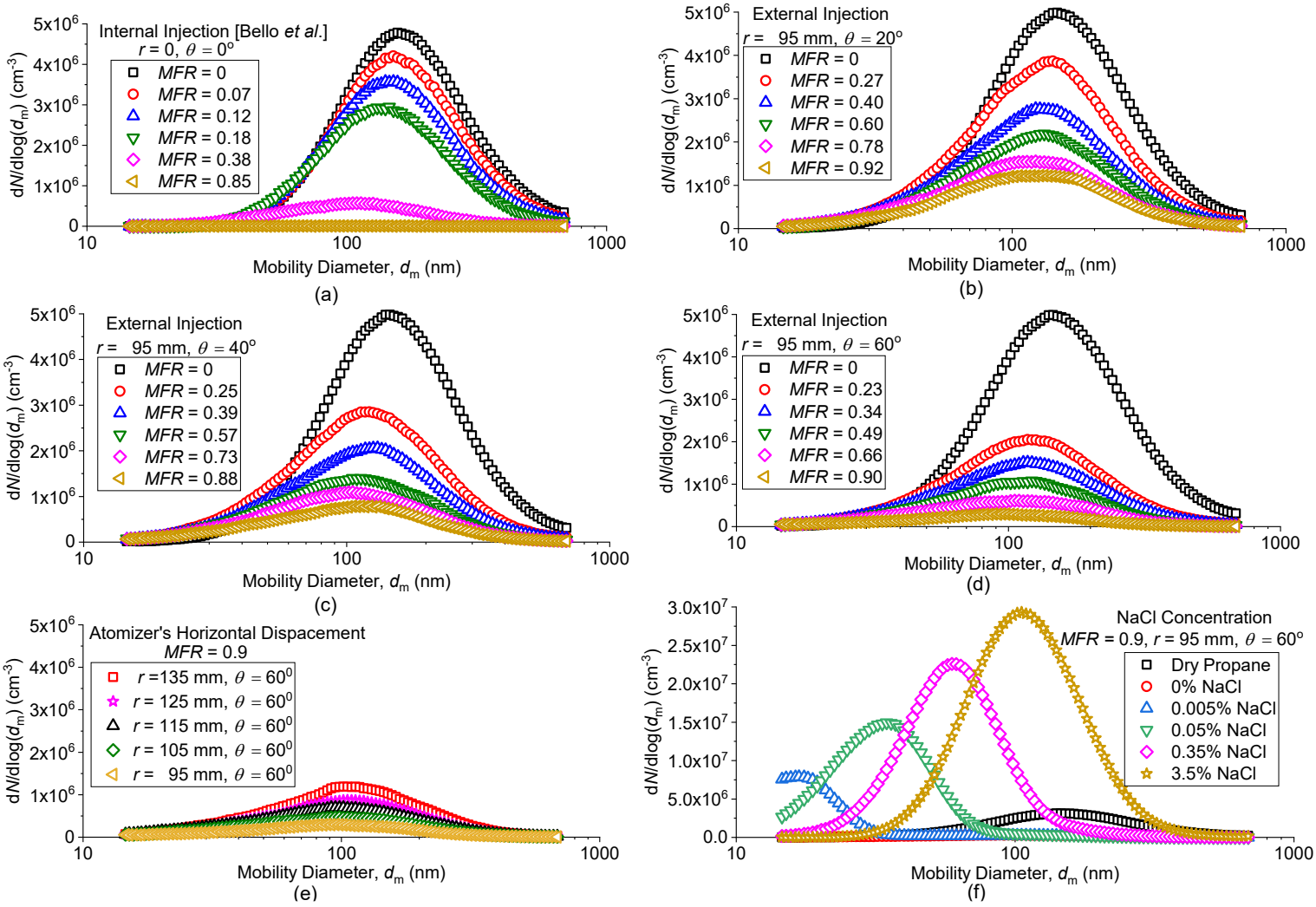

Figure 3.11: Particle size distribution: (a) Internal injection of water (Bello et al. [24]), (b-f) external water injection at $\theta = 20°$ and $r = 95$ mm, $\theta = 40°$ and $r = 95$ mm, and $\theta = 60°$ and $r = 95$ mm, different horizontal displacement from the center of the burner and $\theta = 60°$, and various NaCl concentrations and $\theta = 60°$, respectively.

Figure 3.12 illustrates the count median diameter of the particles shown in Figs. 3.11a to 3.11d with their corresponding *MFR* for internal water injection, internal steam injection, and external water injection at r = 95 mm and $\theta = 20°$, $\theta = 40°$, and $\theta = 60°$. Figure 3.12 illustrates that the particle count median diameter (CMD) was reduced with increasing *MFR*. In this study, the CMD for the propane flame without assisting fluid differs from the previous work of Bello et al. [24] by approximately 6%, which creates a small offset between the data sets. It can be assumed that without the offset, for *MFR* ranging from 0 to 0.4, the internal injection of liquid water and steam and the external injection of liquid water have approximately the same reduction in CMD. But, between *MFR* ranging from 0.4 to 0.6, internal injection of liquid water resulted in smaller particle sizes than others. The reduction of CMD could be linked to the increased soot oxidizing effect of OH, which was due to the injection of water into the flame.

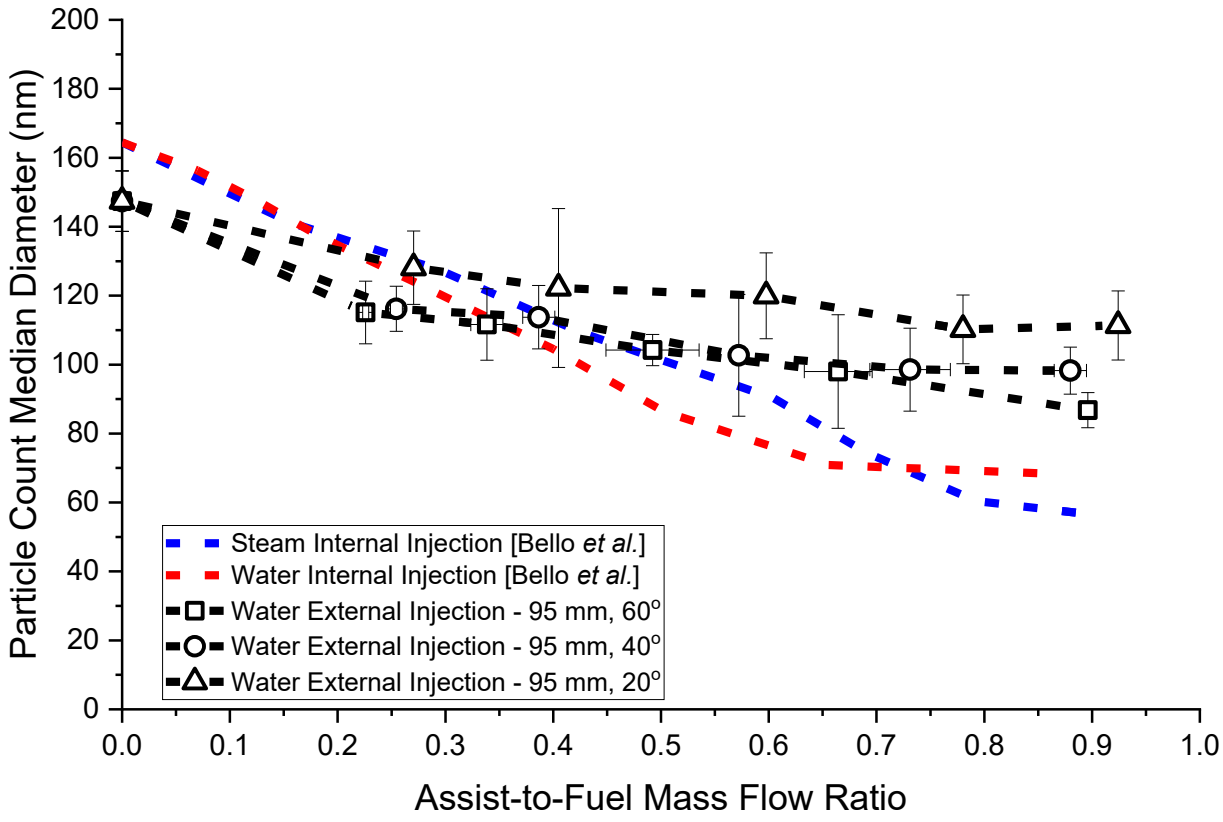

Figure 3.12: CMD with the corresponding *MFR* values.

Figure 3.13 shows the CMD against atomizers' horizontal displacement from the center of the burner. The figure reveals that the particle size increased almost linearly as the atomizer was moved farther away from the center of the burner.

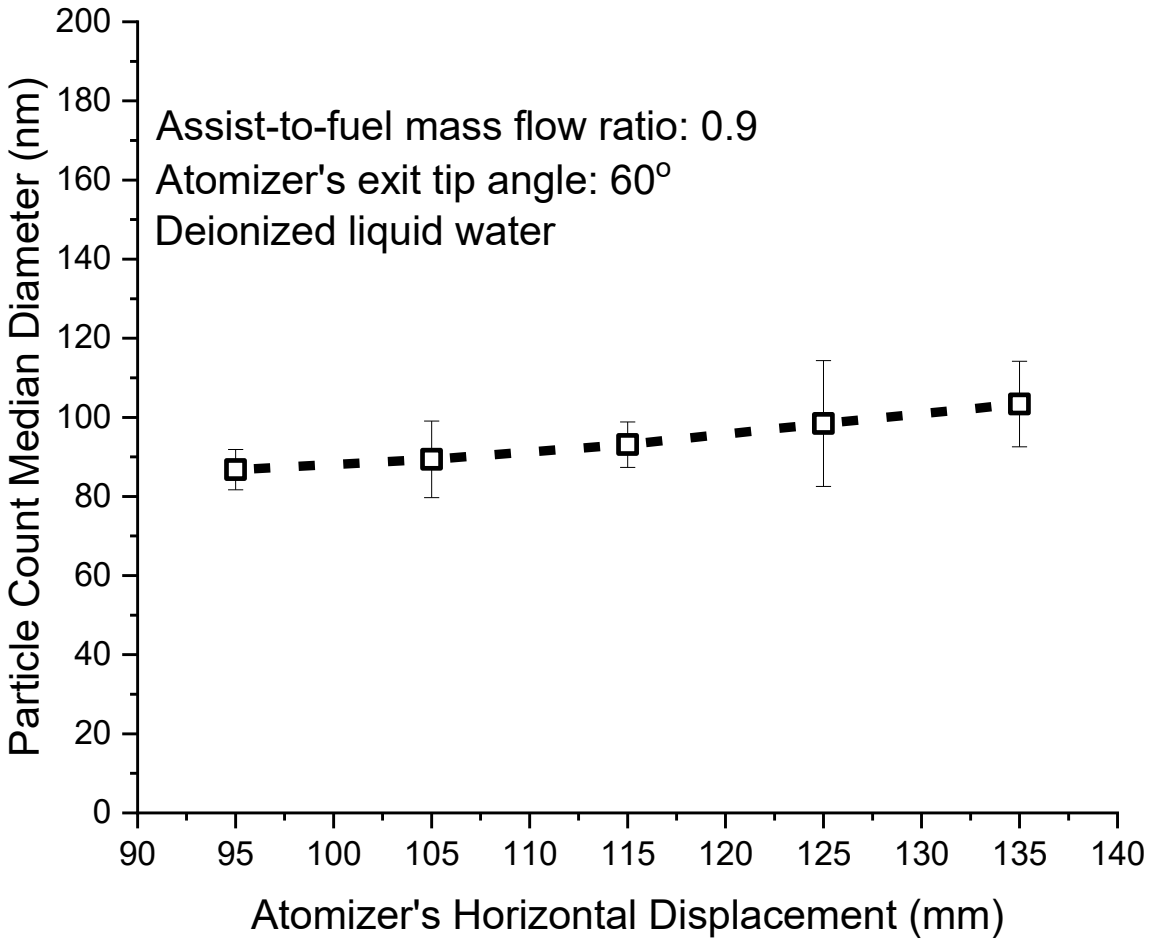

Figure 3.13: CMD with the corresponding atomizer's horizontal displacement.

Figure 3.14 shows the CMD as a function of NaCl concentration at the same liquid flow rate, atomizer angle, and horizontal displacement (*MFR* = 0.9, $\theta = 20°$, and r = 95 mm). As seen in Fig. 3.14, CMD was larger in the case of deionized water compared to the smallest concentration of NaCl, showing that adding low NaCl concentration reduced particle sizes compared to adding only deionized water at the same flow rate. According to Sipkens et al. [88] and Kazemimanesh et al. [172], NaCl appears as distinct particles from soot aggregates, and an increase in NaCl

concentration will result in an increased number concentration of isolated NaCl particles. Sipkens et al. [88] also showed that introducing a small NaCl concentration (note that the lowest NaCl concentration in this work is smaller than the lowest NaCl concentration in Sikpens et al. [88]) created a bimodal particle size distribution. The first mode is the salt with a small CMD but higher concentration, while the second mode is the soot with a lower concentration but a larger CMD. This work presents a single CMD for the bimodal distribution because the second mode is not visible. Therefore, the count median diameter is around the mode of the higher concentration NaCl particles. It is also illustrated in Fig. 3.14 that CMD increased as the NaCl concentration increased.

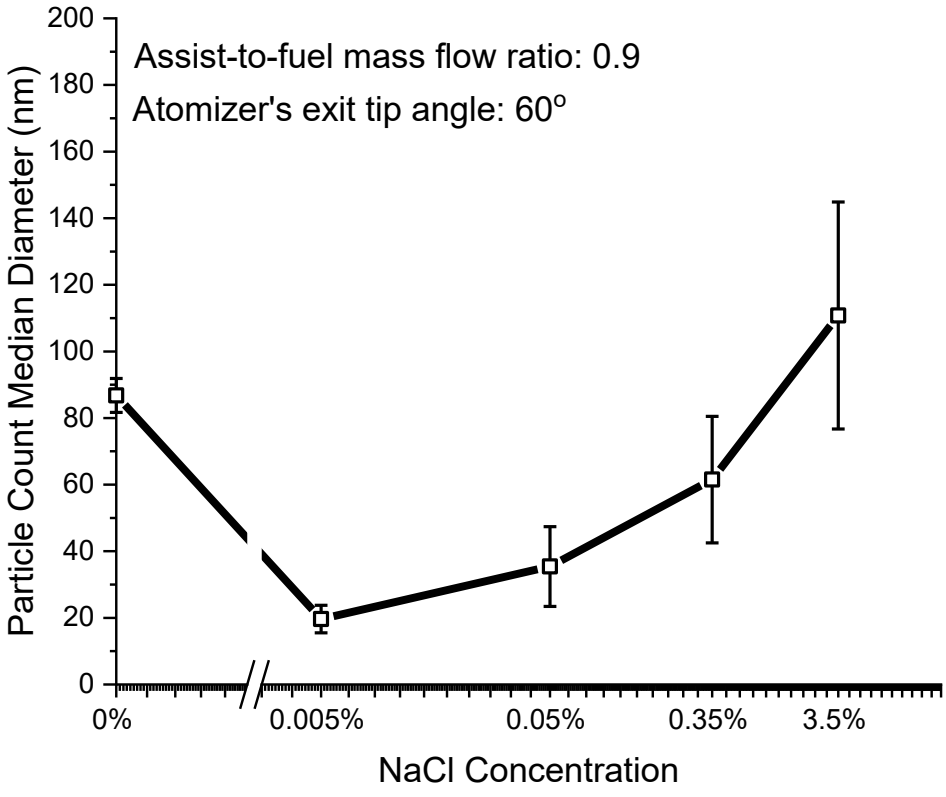

Figure 3.14: CMD with their corresponding NaCl concentration.

3.4 Conclusion

The SLR images of the flame and water spray, in conjunction with PIV analysis, showed that almost all water droplets traveled well into the flame before evaporation by locally quenching the flame leading to spatial-temporal effects on local flame temperature, reaction kinetics, and emissions. Furthermore, the water jet momentum fluxes caused an indistinguishable difference in the gas flows on the fuel side of the flame, minimizing the amount of air entrained into the flame by the injectors.

The BC emission measurements revealed the importance of the spatial-temporal scale of flame interactions with the assisting flow of water in suppressing BC emissions. It was shown that the earlier the water was involved in the combustion process (higher angle), the more effective the water addition would be in suppressing BC emissions. Although externally injected water (i.e., water on the air side of the non-premixed flame) is less effective at suppressing BC emissions than internally injected water (i.e., water on the fuel side of the non-premixed flame), it was found that external injection can be as effective as steam injection if the water is injected close to the base of the flame. Therefore, it can be concluded that external water injection into turbulent non-premixed flames can effectively reduce BC without a need for costly boiler operation to produce steam. One main advantage of external water injection is that it can be implemented into the existing systems without a need for significant structural modifications to the flare stack.

The NO_x emission measurements showed that water addition into flames effectively reduces NO_x through thermal, i.e., Zeldovich mechanism, and chemical effects, i.e., producing more active radicals such as OH and H. It was also illustrated that the thermal effects of water addition are more significant in reducing NO_x emissions, as the addition of liquid water at the later stages of

combustion causes the lower-temperature flame zone, i.e., the locally quenched flame zone, to coincide with the NO_x production zone of the flame leading to an effective reduction of NO_x. Therefore, it was concluded that the external water injection close to the base of the flame is the most effective in reducing NO_x emissions. It should be noted the spatial-temporal scale needs to be investigated based on operational parameters and the geometry of flames to satisfy both the thermal and chemical effects of water addition in favor of NO_x reduction.

The results of NaCl solution addition to flames at the same liquid flow rate and spatial-temporal scales as in the case of deionized liquid water showed that small concentrations of NaCl did not affect BC and NO_x emissions. However, higher concentrations of NaCl, i.e., 3.5%, decreased NO_x and increased BC emissions by 40% and 700%, respectively, compared to the deionized liquid water. This significant change in emissions at almost constant adiabatic flame temperature highlights the chemical effects of adding NaCl to the flames on NO_x suppression and soot increase, as NaCl removes active combustion radicals, such as H, O, and OH, retarding the Zeldovich and soot oxidation mechanisms. Therefore, adding high concentrations of NaCl solution as assisting fluid into flames has opposite effects on NO_x and BC emissions, i.e., reducing the former and increasing the latter. However, applying typical boiler feedwater used for steam-assisted flares at downstream oil and gas facilities as assisting fluid is feasible in suppressing both NO_x and BC emissions, as the NaCl concentration is generally lower than 500 ppm, and therefore, its capability to suppress emissions is similar to pure water.

Chapter 4

The Effect of Sodium Chloride on the Charge State of Soot Particles in a Laminar Diffusion Flame[3]

4.1 Overview

This study investigates the effect of sodium chloride on charge state of soot nanoparticles evolved in a laminar diffusion flame by measuring the soot particle size distribution (PSD), average charge per particle and charge fraction at various locations within the flame. The well-studied Santoro burner with methane as the fuel (at 0.35 L/min) and co-flow (at 70 L/min) was used, which produced a stable laminar diffusion flame with flame height of 61 mm. Samples of soot nanoparticles were extracted via a tiny orifice in a tubular 3-mm probe at various heights above the burner (HAB) and were immediately diluted by a factor of a few thousands. Following sampling, a scanning mobility particle sizer (SMPS), with lower measurement limit of 1 nm, was used to determine the size distribution of particles. The combination of a differential mobility analyzer (used as an electrostatic precipitator), a condensation particle counter and an electrometer were used to determine the fraction of charged particles and the average charge per particle. And, to further gain an in-depth understanding of the coagulation rate of soot particles, this study used an existing charged monodispersed coagulation model to understand the rate at which soot particles total concentration and median particle diameter are changing with time. Also, there has

[3] This chapter is based on the underlisted unpublished manuscript:
W. O. Bello, Mohsen Kazemimanesh, W. L. Kostiuk and S. J. Olfert, " The Effect of Sodium Chloride on the Charge State of Soot Particles in a Laminar Diffusion Flame," *Yet unpublished,* University of Alberta, 2023.

been a lot of work put into studying how neutral aerosols coagulate, but much less is known about how charged particles and how quickly they coagulate in flames with and without salt. However, aerosol particles are often intentionally or unintentionally charged, necessitating an investigation of their coagulation behaviour.

4.2 Experimental setup

Two different experimental setups were used in this work. Figure 4.1 Arrangement A is the schematic for the first experimental setup used to determine the particle size distribution (PSD) at different heights above the burner (HAB) in the flame, while Fig. 4.1 Arrangement B shows the second experimental setup which was used to measure the charge state of particles in the flame. The experimental equipment in this investigation included a co-flow burner, a sampling and dilution system, a device for producing NaCl particles, and instruments for measuring the size distribution and charge of the particles as shown in Figure 4.1. The arrangement for the experimental setup is similar to that of Moallemi et al. [84] and Kazemimanesh et al. [83] but with additional measurement equipment.

A co-annular Santoro burner [79] was used in the produce a steady laminar diffusion flame at atmospheric pressure. A quartz tube shield with a diameter of 115 mm was erected around the burner, and a ceramic honeycomb was placed on top of the shield to prevent ambient air entrainment and reduce the impact of room air currents. Two longitudinal thin slits in the shield permitted vertical translation of a sample probe, while the burner was positioned on two motor-driven translation stages that could move with an accuracy of 0.03 mm in the vertical direction. Methane was selected as the fuel because it is main component of natural gas and it has a lower

propensity to soot (to avoid clogging the probe to quickly). Two mass flow controllers were used (Omega, Model FMA-774A and Cole-Parmer, Model 32907-71, respectively) to control the fuel and air flow rates at 0.35 and 70.0 SLPM (standard liters per minute at 25 °C and 1 atm), respectively. The resulting flame had a visual height of 61 mm.

4.2.1 NaCl entrainment setup

Sodium chloride solution droplets were produced by nebulizing a 25% aqueous solution of sodium chloride using an Aerogen Solo Nebulizer. The sodium chloride solution was nebulized and passed through a diffusion dryer (TSI Inc., Model 3062), producing crystalline particles with a median diameter of about 130 nm, and the mass concentration of the sodium chloride particles at the fuel tube outlet before combustion was previously calculated to be approximately 45 ng/cm^3 [84]. The NaCl particles changed the colour of the flame when they were added, and they also produced a strong yellow-orange colour at the outer cone of the flame. Moallemi et al. [84], performed a prior investigation on a similar flame using the same quantity of NaCl and discovered that the addition of NaCl had the lowest and the highest temperature difference of 13 K and 40 K when compared with flame without NaCl addition. This temperature difference reveals that there is no significant difference between the temperature of flame with and without NaCl addition.

4.2.2 Particle sampling and dilution setup

The sampling system used in this study is similar to that used in previous studies [83, 84, 177]. The sample probe was a horizontal stainless-steel tube of 3.175 mm outer diameter and 125 μm wall thickness with a pinhole of 0.3 mm in diameter, facing downward on the centerline of the

flame. Nitrogen was directed through the upstream side of the probe and downstream of the probe was connected to a vacuum pump, while the flow rates were adjusted to extract the sample through the pinhole. Particles extracted from the pinhole for measurement were rapidly quenched and diluted to minimize chemical reactions and particle coagulation during transit to ensure the integrity of the sample collected. A mass flow controller (Omega, Model FMA-5540) was used to adjust the flow rate of the diluent nitrogen upstream of the pinhole to 19.7 SLPM. The flow rate of the vacuum pump (GAST, Model DAA-P501) was approximately 23 SLPM to keep the sampling system under negative pressure. The pressure was monitored at the pinhole position using a digital manometer (Dwyer, Model 475-1-FM) to control the gauge pressure within the range of 149.5 to 373.7 Pa to confirm flow was going into the sample probe. From the main sampling and dilution line, a subsample is extracted using an eductor pump (AIR-VAC, Model AVR093H) and routed to a non-dispersive infrared CO_2 gas analyzer (LICOR, Model 840-A) and to other particle measuring devices described below. The dilution ratio was then obtained from the concentration of CO_2 in the undiluted sample was divided by the concentration of CO_2 in the diluted sample. The concentration of the undiluted CO_2 at various HABs in the flame measured by Moallemi et al. [84] and Kasemimanesh et al. [83] and was used in this study. As with previous studies [83, 84, 177], the dilution ratio was set to be sufficiently high that the particle size distribution was independent of the dilution ratio (i.e., coagulation in the sample probe was sufficiently low that further dilution did not skew the size distribution). Based on the particle size distribution at each HAB and the stability of the flame, the dilution ratio utilized in this investigation was between 9000 and 11000, and dilution ratios higher than these made the flame unstable or caused it to blow off.

.

4.2.3 Particle size distribution measurement instruments

Figure 4.1 Arrangement A shows the schematic for the particle size distribution instruments. A scanning mobility particle sizer (SMPS; TSI Inc., Model 3938E57) was used to measure the size distribution of particles using the manufacturer's software (TSI Inc., Aerosol Instrument Management version 11.0.1). The SMPS comprises of a bipolar diffusion charge neutralizer (TSI Inc., Model 3088), a differential mobility analyzer (DMA; TSI Inc., Model 3086), a nano-enhancer (TSI Inc., Model 3757), and a condensation particle counter (CPC; TSI Inc., Model 3750). The aerosol and sheath air flow rates for SMPS were set at 1.0 L/min and 10 L/min, respectively, which offered a 1–50 nm particle size measurement range. The scan time for each sample in this study was 50 s and five SMPS measurements were taken at each HAB. A constant dilution was maintained during each measurement. After accounting for dilution, the average of the five SMPS data was used to create the particle size distribution plots.

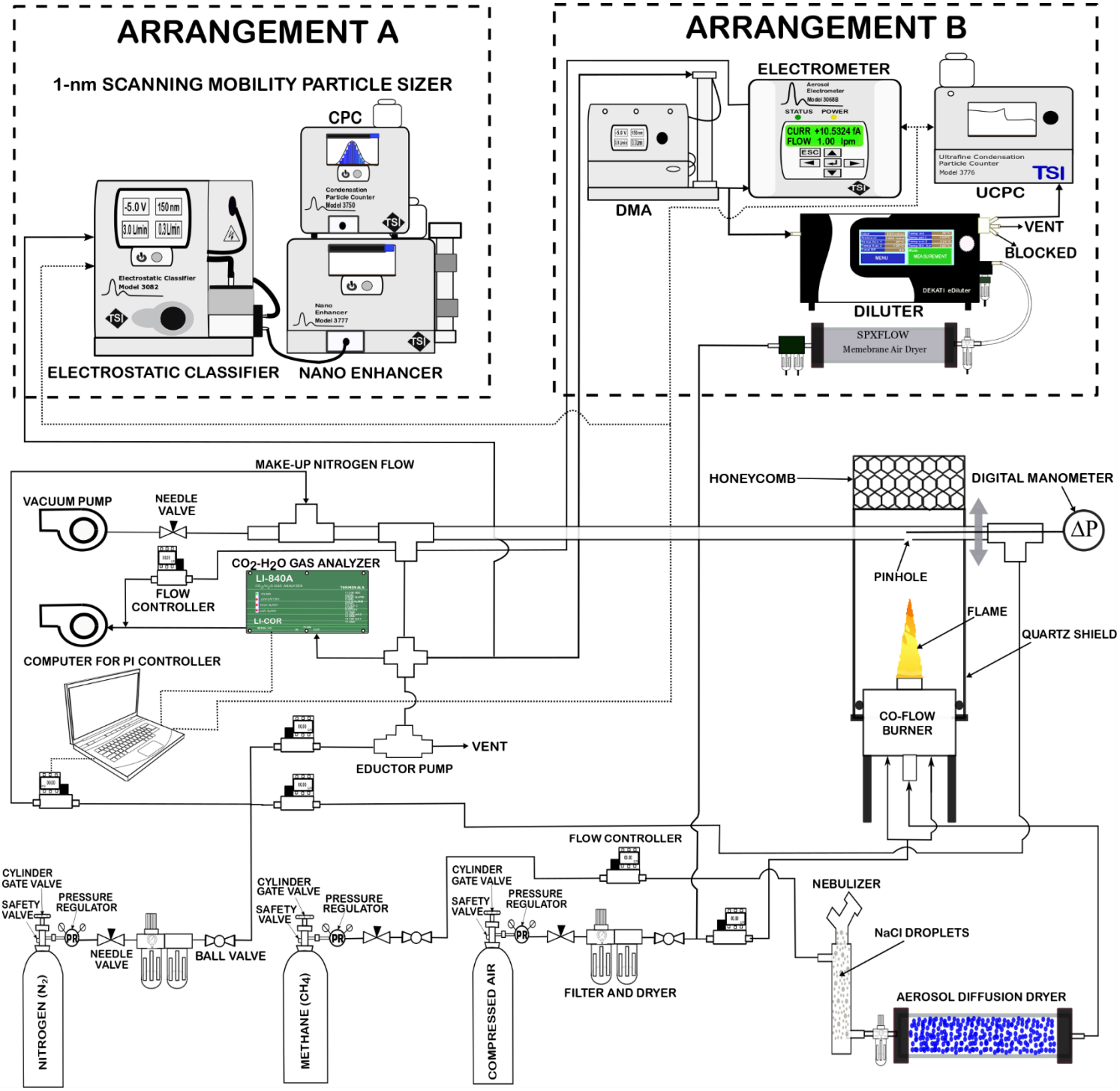

Figure 4.1: Experimental setup schematic for particle size distribution and charged particle measurement including co-flow burner, NaCl entrainment setup, particle sampling and dilution setup and measuring devices.

4.2.4 Particle charge state measurement

To determine the average charge per particle and the fraction of charged particles, the following instruments in Fig. 4.1 Arrangement B were used: a DMA (TSI Inc., Model 3081) was used as an electrostatic precipitator, a CPC (TSI Inc., Model 3776), an aerosol electrometer (TSI Inc., Model 3068B), and a particle diluter (Dekati eDiluter Pro) operating with particle-free dry compressed air. The polydisperse particles extracted from the flame were directed to the DMA while its sheath flow was turned off such that the aerosol flow is the only flow in the electric field. The aerosol was split into two flows at the exit of the DMA: one flow went to the electrometer, while the other flow went to the CPC through a particle diluter with a dilution factor of 25. The additional diluter was used to prevent CPC from saturating due to the high particle concentrations. Within 60 seconds of sampling, the DMA voltage was turned off for 30 seconds to measure the total concentration of all particles (positively- and negatively-charged particles as well as uncharged particles) and the average charge on each particle, then the DMA voltage is turned on and set to the highest voltage (10 kV) for the remaining 30 seconds to measure the total concentration of uncharged particles and to confirm they indeed carry zero charges. The number fraction of charged particles (F_q) and the average charge per particle ($\bar{q}$) were calculated as.

$$F_q = \frac{(N_{\text{total}} - N_{\text{uncharged}})}{N_{\text{total}}} \tag{4.1}$$

$$\bar{q} = \frac{I}{N_{\text{total}}\, e\, Q} \tag{4.2}$$

where N_{total} is the CPC concentration when the DMA voltage is turned off, $N_{\text{uncharged}}$ is the CPC concentration when the DMA voltage is turned on to the highest voltage, I is the

electrometer current, e is the electron charge (1.602×10^{-19} C), and Q is the electrometer volumetric flow rate.

4.3 Monodispersed coagulation model

A coagulation model accounting for particle electric charge was used to compare experimental results to determine the significance of particle charge in the coagulation of the particles in the flame with NaCl. The model was based on the work of Adachi et al. [110] and Vemury et al. [178] and is summarized here. For simplicity (and lower computation time) the model assumes monodisperse spherical particles. The rate of change in the number concentration of particles with charge p is,

$$\frac{\mathrm{d}N_p}{\mathrm{d}t} = \frac{1}{2}\sum_{q=-\infty}^{q=\infty} \beta_{q,p-q}\, N_{p-q}\, N_q \; - \sum_{q=-\infty}^{q=\infty} \beta_{q,p}\, N_p\, N_q - B\frac{e^2}{\varepsilon_0}\, p\, N_p \sum_{q=-\infty}^{q=\infty} q\, N_q \tag{4.3}$$

where N_p on the left side of equation (4.3) gives the number concentration of particles carrying p elementary charges. $\beta_{q,p-q}$ represents the coagulation coefficient between two particles, and one carrying a charge of p while the other carries $p–q$ charge. The first term on the right-hand side of the equation describes the generation of new particles with p charge through the collision between particles bearing q and $p–q$ charges. The second term is the reduction in the number of particles with p charge as a result of their coagulation with other particles. The third term on the right-hand side describes the loss of particles from the volume due to electrostatic dispersion. If the positive and negative charges in a given volume of gas are not perfectly balanced, then the mutual electrostatic repulsion between the particles causes them to be transported out of the volume. In

Equation (4.3), e is the elementary charge, ε_0 is the permittivity of free space, and $B = C_c/3\pi\mu d_p$ is the mobility of a particle of size d_p [179] where C_c is the Cunningham slip correction factor and μ is the viscosity of the gas. Equation (4.3) assumes that no charges (ions) are created, which means that once the initial condition is defined, the total charge stays the same. As described later, the ion concentration is estimated from the particle charge measurements and Fuchs's charging theory. It is important to note that ions can also induce electrostatic dispersion in the coagulation model. However, as will be demonstrated later, the ion concentration is significantly lower than that of charged particles, rendering its effect negligible.

The Brownian coagulation coefficient of uncharged monodisperse particles (β^*) transitioning from the free-molecular to the continuum regime was calculated using Zebel's expression [180] with Fuchs correction factor (G) [181],

$$\beta^* = \frac{8k_bTC_c}{3\mu}\, G \tag{4.4}$$

where,

$$G = \frac{1}{\dfrac{d_p}{d_p + \sqrt{2}\,\delta'} + \dfrac{\pi\lambda_p}{\sqrt{2}\,d_p}} \tag{4.5}$$

and,

$$\delta' = \frac{1}{3d_p\lambda_p}\left[(d_p + \lambda_p)^3 - (d_p^2 + \lambda_p^2)^{3/2}\right] - d_p \tag{4.6}$$

where k_b is Boltzmann's constant, T is the absolute temperature, d_p is particle median diameter, and λ_p is particle mean free path. According to Moallemi et al. [84], the centerline flame temperature from the exit of the fuel tube to the peak height of the flame was between 450–1950 K, these temperature measurements were used in the coagulation model calculations of this study.

The coagulation coefficient between charged particles ($\beta_{p,q}$) is

$$\beta_{p,q} = \beta^* W_{p,q} \tag{4.7}$$

where $W_{p,q}$ for the repulsive electrostatic force is

$$W_{p,q} = \frac{\alpha_{p,q}}{e^{\alpha_{p,q}} - 1}\,, \tag{4.8}$$

and for the attractive electrostatic force is

$$W_{p,q} = \frac{|\alpha_{p,q}|}{1 - e^{|\alpha_{p,q}|}}. \tag{4.9}$$

Here, $\alpha_{p,q}$ is the Fuchs stability function [178, 181], defined as the ratio of electrostatic energy to thermal energy of colliding particles,

$$\alpha_{p,q} = \frac{2pqe^2}{4\pi\varepsilon_0 k_b T(d_p + d_q)}. \tag{4.10}$$

In Appendix C, the coagulation model in this study was validated by reproducing the Fuchs stability functions in the work of Adachi et al. [110] and the monodisperse coagulation result in Vemury et al. work [178].

The model requires the initial condition of the particle number concentration for each charge state. Since the particle size of the soot is relatively small (< 50 nm) it is assumed that the particle can only have charge states of −1, +1, and 0 charges. The number concentration of each charge state is determined by the measurements at each HAB by,

$$N_{-1} = \frac{1}{2} N_{\text{total}}\left(F_q - \bar{q}\right) \tag{4.11}$$

$$N_{+1} = \frac{1}{2} N_{\text{total}}\left(F_q + \bar{q}\right) \tag{4.12}$$

$$N_0 = N_{\text{total}}\left(1 - F_q\right) \tag{4.13}$$

where N_{-1}, N_{+1} and N_0 are the number concentration of particles with −1, +1, and 0 charges, respectively, and N_{total} is the total particle number concentration.

To calculate the ion concentration between HABs, we employed the numerical implementation of Fuchs's bipolar charging model, as written by Woo et al. [182]. The approach used to determine the positive and negative ion concentrations involved adjusting the concentrations of positive and negative ions while keeping their ion mobilities constant in order to attain the measured charge fraction and average charge per particle.

Since the measurements were made at different HABs, a relationship is needed to compute the time between HAB measurements. In the proposed model of Roper [183] and Santoro et al. [184], the reacting flow acceleration due to buoyancy, a, is assumed to be constant (25 m/s^2) and the axial velocity (U_z) and residence time (t), are given as

$$U_z = \sqrt{2az} \tag{4.14}$$

$$t = \sqrt{2z/a} \tag{4.15}$$

where z is the height above burner.

4.4 Results and discussion

4.4.1 Particle size distribution

The particle size distribution (PSD) of the soot particles for methane and methane-NaCl flames from HABs of 30 to 60 mm is shown in Fig. 4.2a and b (each data point represents the average of five measurements). The figure illustrates the evolution of the soot particles from inception to oxidation with increasing height above the exit of the burner. It is observed that the particle size distribution for HAB of 30 to 40 mm for both cases are unimodal. It also shows that at these HABs, the particles with a median diameter less than 7 nm are more abundant and related to incipient soot particles (first mode) which also undergo surface growth [84, 177]. A bimodal distribution appears at HAB of 45 mm and becomes more distinct at 46 mm, where the first mode is the nucleation mode with median diameters near 4 nm, and the second mode is the agglomeration mode with median diameters near 25 nm. The median diameter for the first mode reduces as the height above the burner increases. Additionally, the second mode exhibits an increase in median diameter and a decrease in concentration as the height above the burner increases. The existence of the first mode in almost all the HABs suggests continuous nucleation throughout the measurement range (HAB 30 to 60 mm). The trends in the particle size distributions observed here are in general agreement with previous studies on laminar methane flames, which also identified modes related to soot inception, surface growth, coagulation, and oxidation [83, 84, 177].

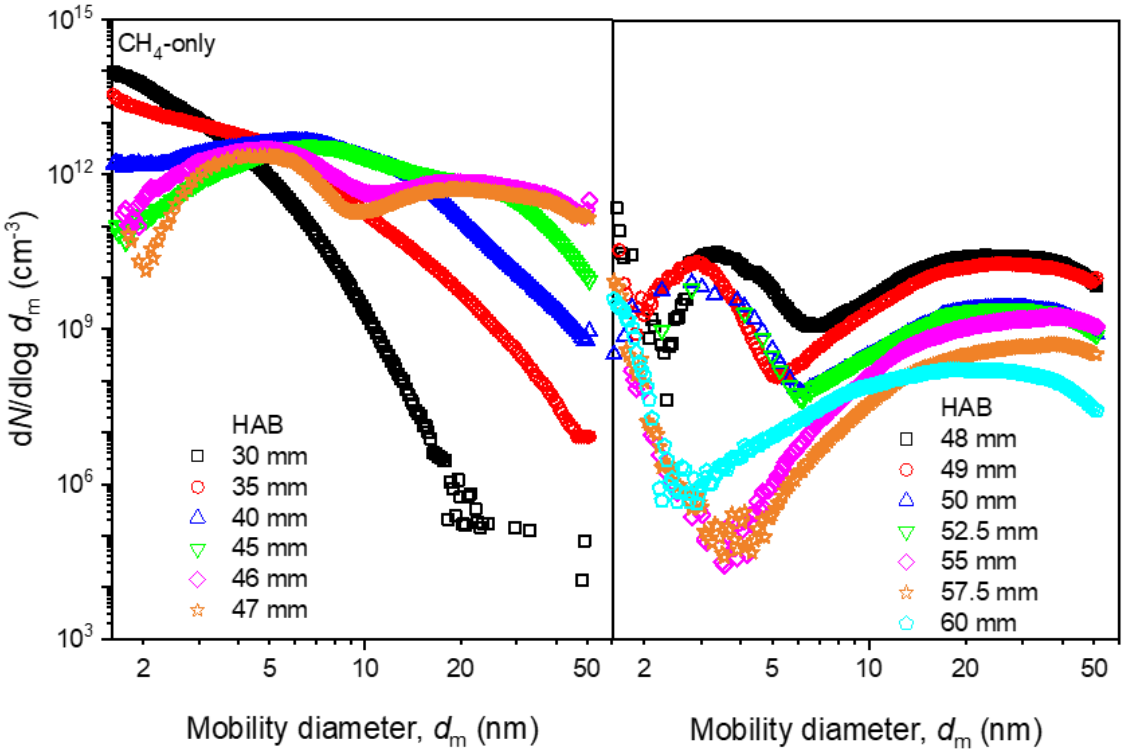
CH4-only
HAB
30 mm
35 mm
40 mm
45 mm
46 mm
47 mm
48 mm
49 mm
50 mm
52.5 mm
55 mm
57.5 mm
60 mm
dN/dlog dm (cm-3)
Mobility diameter, dm (nm)

(a)

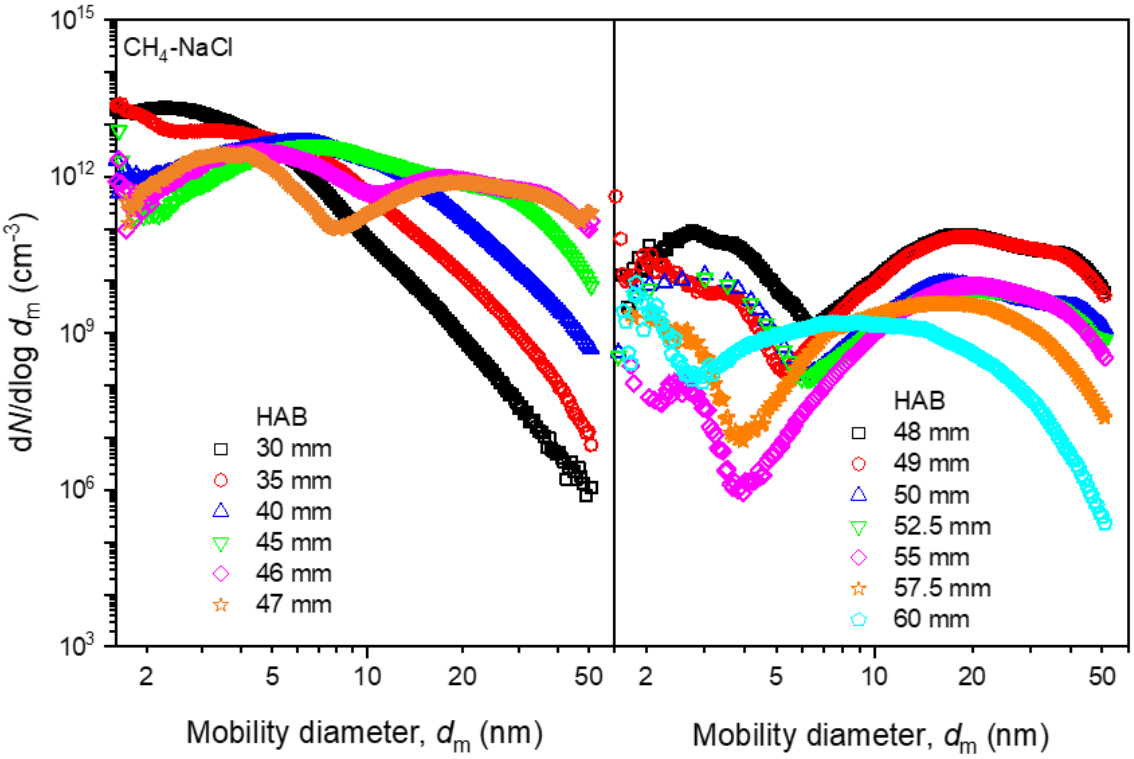
CH4-NaCl
HAB
30 mm
35 mm
40 mm
45 mm
46 mm
47 mm
48 mm
49 mm
50 mm
52.5 mm
55 mm
57.5 mm
60 mm
dN/dlog dm (cm-3)
Mobility diameter, dm (nm)

(b)

Figure 4.2: Particle size distribution with their corresponding HAB ranging from 30 to 60 mm for (a) methane-only flame (b) methane-NaCl flame.

4.4.2 Total concentration, count median diameter, average charge per particle and fraction of charged particles

Figure 4.3 summarizes the total number concentration, count median diameter (only considering particles within the SMPS measurement range), average charge per particle, and the fraction of charged particles from HAB = 30 mm to 60 mm for methane-only and methane-NaCl flames. The average charge per particle and charge fraction presented represents the average of six to fourteen measurement repeats, and the associated error bars indicate the uncertainty in the mean, with a 95% confidence interval.

Between HAB 30 mm and HAB 40 mm, for both flames, there is no significant difference in total concentration between the two cases (Fig. 4.3a), although the total concentration decreases by a factor of 5. Furthermore, within this same HAB range, the count median diameter of the methane-only and methane-NaCl flame are nearly the same, with a diameter of approximately 5 nm or less (Fig. 4.3b). This observation suggests that the presence of NaCl does not have a noticeable impact within this region of the flame where nucleation is the dominant particle formation mechanism. The average charge per particle and charge fraction are both close to zero within this HAB range, indicating that the majority of particles, specifically nascent soot, are uncharged (Fig. 4.3c and 4.3d). This finding aligns with the assertion made by Homann [185], who suggested that a greater number of soot particles are initially uncharged in hydrocarbon flames. Moreover, the results are consistent with prior measurements conducted by Maricq et al. [186] and comparisons of measured

particle size distributions with TEM findings by Öktem et al. [75] which indicated that a median particle diameter of less than 5 nm corresponds to incipient soot particles. Maricq et al. [186] further established that these incipient soot particles are uncharged.

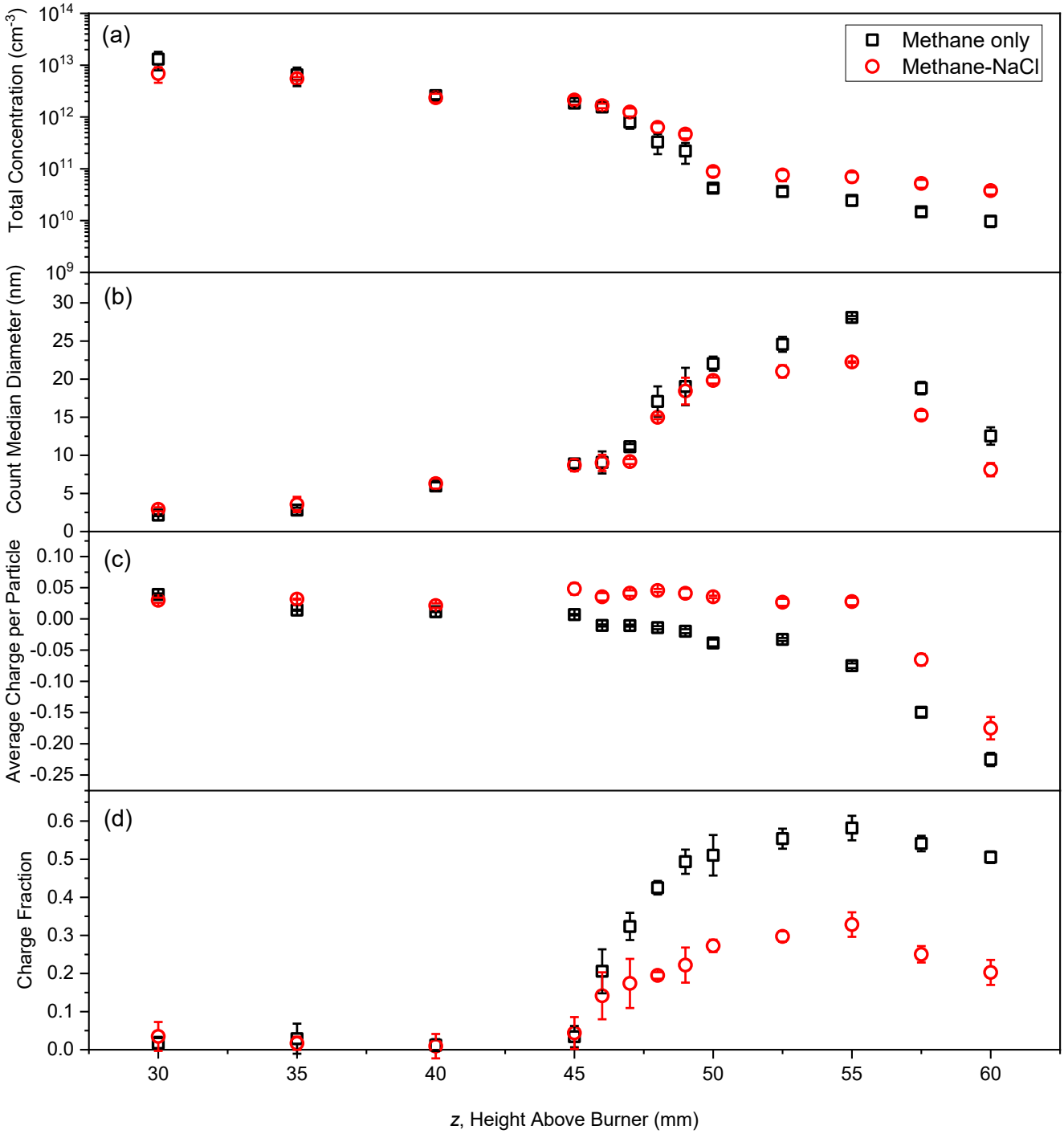

Figure 4.3: Total concentration, count median diameter, average charge per particle and charge fraction, for methane-only and methane-NaCl flames with their corresponding HABs ranging from 30 to 60 mm.

Between HAB 45 mm and 55 mm, there is a significant decrease in total number concentration attributable to coagulation, accompanied by a corresponding increase in count median diameter due to the combined effects of coagulation and surface growth. The influence of NaCl on both the total number concentration and count median diameter becomes increasingly noticeable, starting at HAB 46 mm, where soot coagulation is presumably more dominant. The introduction of NaCl into the methane flame results in a higher particle number concentration and a lower count median diameter within the HAB range of 46 mm to 55 mm. This suggests that NaCl mitigates the coagulation of soot particles, leading to the generation of smaller soot sizes and higher concentrations compared to methane-only cases. Notably, for the methane-only case at HAB 45 mm, the average charge per particle is zero. In contrast, for the methane-NaCl case, the average charge per particle is approximately +0.05, likely due to the higher concentration of positive ions, as will be discussed below.

Furthermore, the average charge per particle for HABs ranging from 46 mm to 55 mm in methane-only cases is negative; however, with the addition of NaCl, the average charge per particle is slightly positive. Interestingly, a sudden change in charge fraction becomes evident at HAB 46 mm, which is the region where coagulation begins to have a more pronounced impact. Between HAB 46 mm and 55 mm, for the methane-only case, approximately 20% to 58% of the particles

are either negatively or positively charged, while for the methane-NaCl case, this range is about 14% to 33%. This indicates that more uncharged particles are present when NaCl is added.

In the HAB range of 57.5 mm to 60 mm, both the total number concentration and median diameter decrease, likely due to soot oxidation near the flame front. In this region, the total concentration of soot particles is lower for the methane-only case compared to the methane-NaCl case, reflecting larger particle sizes in the methane-only flame. This finding suggests that despite some coagulation potentially occurring in this region, the predominant process is the oxidation of soot particles. The particles in the methane-only case at HABs of 57.5 mm to 60 mm are highly negatively charged, with an average charge per particle ranging from approximately -0.15 to -0.225; even with NaCl addition, the average charge per particle remains negative in this HAB range. Moreover, within this region, the addition of NaCl leads to a reduction in the fraction of charged particles, with the charge fraction being approximately two times lower compared to the methane-only flame.

The findings of this study are consistent with one of the two opposing hypotheses about the effect of alkali metals in flames, the first hypothesis [114] says that the introduction of alkali metals into flames neutralizes soot precursors and thereby inhibits soot nucleation, reducing the number of soot particles produced. It is clear that the result obtained in this study does not support this hypothesis because NaCl addition did not prevent soot nucleation. In the soot nucleation region of our flame, the particle number concentrations, and the median particle sizes for both methane-only and methane-NaCl cases are similar. Also, with the addition of NaCl, soot number concentration was not reduced but rather increased with a reduction in soot particle size. However, all the results in this study are in agreement with the findings of Kazemimanesh et al. [83] and Moallemi et al. [84]. These authors supported their findings with the second hypothesis [85], which stated that the addition of alkali metals to premixed diffusion flames does not have a significant effect on the

number concentration of particles in the soot nucleation region of the flame but has a great impact subsequent to that region. In the post-nucleation region of the flame, a smaller particle size and a higher particle number concentration were observed when compared to the case where no alkali metal was added to the flame indicating a decrease in the coagulation rate of soot particles. Similar results were found by Boncyzk [86] for alkali chloride additives while studying the impact of a series of alkali chlorides on soot formation in a propane diffusion flame. The result also support the findings of Wang et al. [187] who investigated the effect of potassium chloride (KCl) addition on soot formation during ethylene pyrolysis in a flow reactor and discovered that particle size distributions evaluated with a scanning mobility particle sizer revealed that the addition of KCl did not impact soot nucleation but did restrict soot size growth via coagulation. They noted that KCl neutralized the charged particles (lowered the fraction of multi-charged particles), which may have resulted in slower coagulation rates and smaller particles. Based on all these findings, it is important to note that researchers have yet to confirm the charge state of soot and with alkali-metals in flames.

4.4.3 Concentration of ions in flames

The Hoppel and Frick bipolar diffusion charging model [188], as presented in an open-source format by Woo et al. [182] was utilized to determine the total ion concentration, and both positively and negatively charged ions in the flame. The primary objective was to explore the impact of NaCl on charging; specifically within the height above the burner (HAB) range of 45 to 55 mm where the particles become charged. Key parameters affecting particle charging include positive and negative ion concentration, particle concentration, flame temperature, ion mobility, particle

diameter, and ion mass. The experimentally measured particle concentration, particle diameter, average charge per particle, and charge fraction in this work, and the measured temperature as recorded by Moallemi et al. [84], were incorporated into the bipolar charging model. Within this model, adjustments to ion concentration (both positive and negative) or ion mobilities can be made to achieve the experimental values for average charge per particle and charge fraction. The physical properties employed in simulating the bipolar diffusion charging model can be found in Appendix C.

We considered two scenarios to attain the experimentally-measured charge fraction and an average charge per particle with the model: i) changing ion electrical mobility values while attempting to keep the ratio between positive and negative ion concentrations constant or ii) adjusting the relative population of negative and positive ions while keeping the ion electrical mobilities constant. As shown in Appendix C, attempting to manipulate the ion electrical mobilities to attain the measured average charge per particle resulted in unrealistic mobility values (electrical mobilities would have to be orders of magnitude higher or lower than typical values). On the other hand, the latter method yielded physically plausible values for the total ion concentration to achieve the measured average charge per particle and charge fraction while using typical ion electrical mobilities.

Figures 4.4 depicts the total ion concentration, positive ion concentration, and negative ion concentration for both the methane-only and methane-NaCl flames, corresponding to HABs ranging from 45 mm to 55 mm. The figure reveals that the total ion concentration for methane-only and methane-NaCl flames are approximately 3 orders of magnitude lower than the soot particle concentration. The figure unveils that the total ion concentration at HABs 45 mm and 46 mm is approximately the same for both flames. This suggests that NaCl's influence on ion generation within this HAB range is minimal. However, for HABs ranging from 47 mm to 55 mm,

the total ion concentration in the methane-only flame is much higher than the ion concentration in the methane-NaCl flame, except at HAB 50 mm, where both flames exhibit similar ion concentrations.

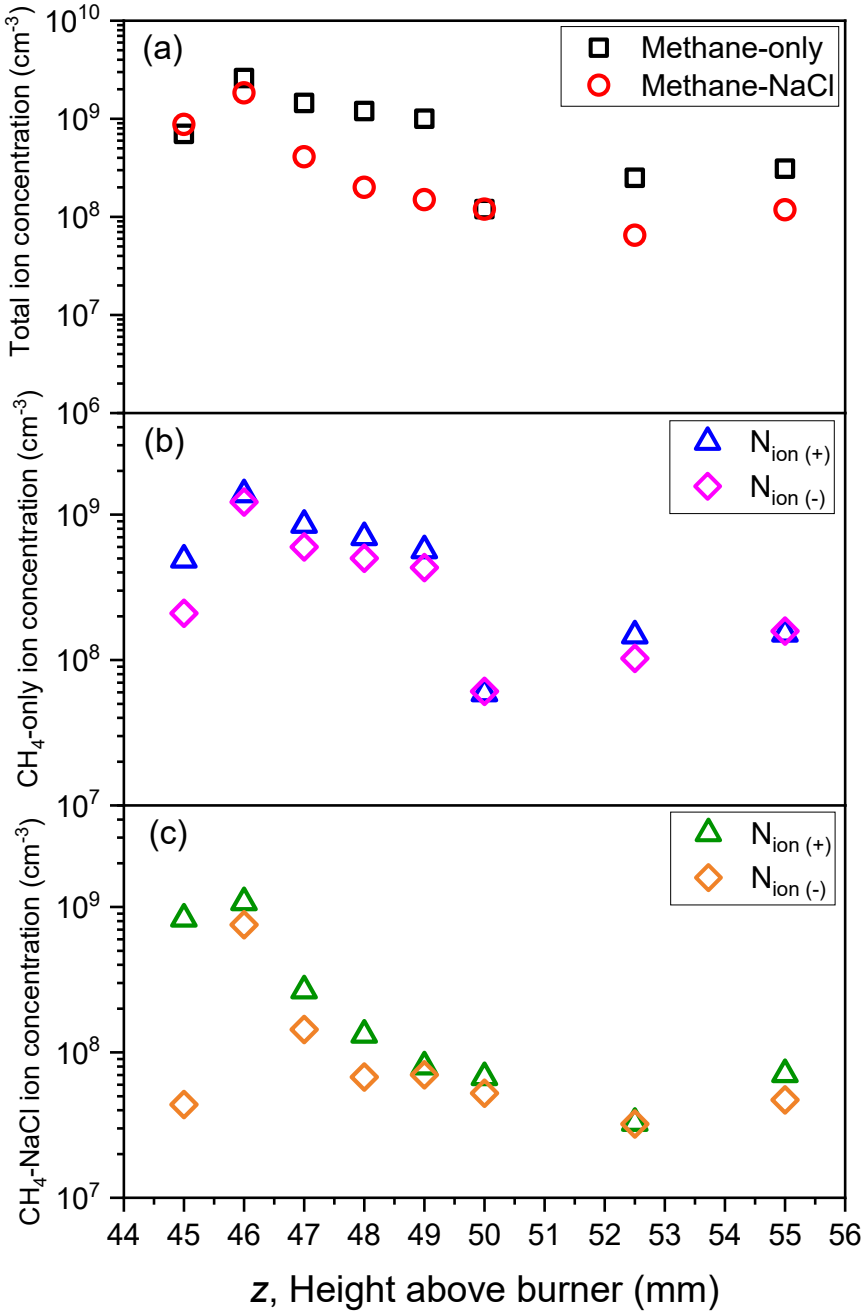

Figure 4.4: Ion concentration for methane-only and methane-NaCl flames with their corresponding

HABs ranging from 45 to 55 mm.

This can be further elucidated by considering that in a high-temperature flame numerous species undergo ionization and interact with each other. When NaCl is introduced into the flame, it can be inferred that the NaCl dissociates into sodium and chloride ions with equal concentrations. These ionized Na^+ and Cl^- ions rapidly react with other ions, forming new ion clusters. Hayhurst and Jones [189] show that ion recombination is a major process that take place in flames. Also, researchers have shown that the presence of alkali metal can enhance the concentration of hydrocarbon ions through a charge transfer process from alkali metal ions to hydrocarbon species [190, 191]. Conversely, this ion concentration decreases due to an increased ion recombination rate, resulting in an overall reduction in ion concentration [190]. Goodings and co-workers [192, 193] have also confirmed that the introduction of halogen elements (such as chloride in the form of HCl) into flames scavenge free electrons in a simple reaction of $HCl + e^- \leftrightarrow Cl^- + H$. All these could explain the observed reduction in ion concentration upon the addition of NaCl. The studies above have individually examined the influence of sodium or chloride on in-flame ion concentration. However, to the author's knowledge, this is the only study which shows that adding NaCl reduces the in-flame ion concentration.

4.4.4 Comparison of the coagulation model with experimental results

The monodisperse coagulation model simulation was conducted in a piecewise manner, starting at HAB 45 mm. This model exclusively considers coagulation and utilizes the following experimental data for initial conditions: total particle concentration, median diameter, average charge per particle, and charge fraction. At the end of each step, new values for particle

concentration, median diameter, average charge per particle, and charge fraction are determined. However, it's worth noting that the model's predictions for the average charge per particle and charge fraction did not align with the experimentally measured values (presented in Appendix C) because the coagulation model did not include particle charging due to the ions present. Linear interpolation of the average charge per particle and charge fraction was used to constrain the model at each step in the coagulation model. This ensures that particle charging is included in the coagulation model without the computational cost of running the charging model at each time step. It's important to also note that higher charge states (i.e., within the range of –2 to +2) were taken into account in the coagulation model. After each iteration, the interpolated average charge per particle and charge fraction were utilized to redistribute the sum of the number concentration of all charges obtained in the initial iteration to +1, –1, and 0 charged particles at each time step as the initial values for each subsequent iteration.

Figure 4.5 illustrates a comparison between the model predictions and the experimental measurements regarding the changes in particle number concentration and median diameter from HAB 45 mm to 57.5 mm, which mostly constitutes the region where coagulation is expected to dominate. The figure also presents the model's predictions for charged particles and the median diameter of the second mode of the particle size distribution (PSD) for HAB 45 to 60 mm. The figure shows that the model greatly underpredicts the particle concentration for HABs 45 to 47 mm. The higher concentration noticed in the experimental result compared to the model result can be attributed to the continuous production of new particles (nucleation mode) for both methane-only and methane-NaCl flames as shown in Figure 4.2a and 4.2b.

The model under-predicts particle concentration for the methane-NaCl flame and over-predicts it for the methane-only flame within the HAB range of 47 mm to 48 mm. This observation can be

elucidated by analyzing the first (nucleation) and second (agglomeration) modes of the PSD for this range. In the case of the methane-only flame, the first mode experiences a significant decrease in number concentration and count median diameter (CMD) between HAB 47 mm and HAB 48 mm. Simultaneously, the second mode sees a decrease in number concentration and an increase in CMD. This analysis for the methane-only flame suggests that coagulation is substantial, while nucleation is less significant. Moreover, oxidation is assumed to be occurring because the median diameter of particles in the first mode is decreasing. For the methane-NaCl flame, the first mode also witnesses a substantial decrease in number concentration and CMD between HAB 47 mm and HAB 48 mm. Conversely, the second mode remains nearly constant in terms of number concentration and CMD. The model clearly shows that coagulation will be significant for the methane-NaCl flame, however, since the CMD of the second mode remains constant for the HAB range, oxidation must also be taking place. The decrease in CMD of the first mode for this HAB range is further proof that oxidation is also significant for this HAB range.

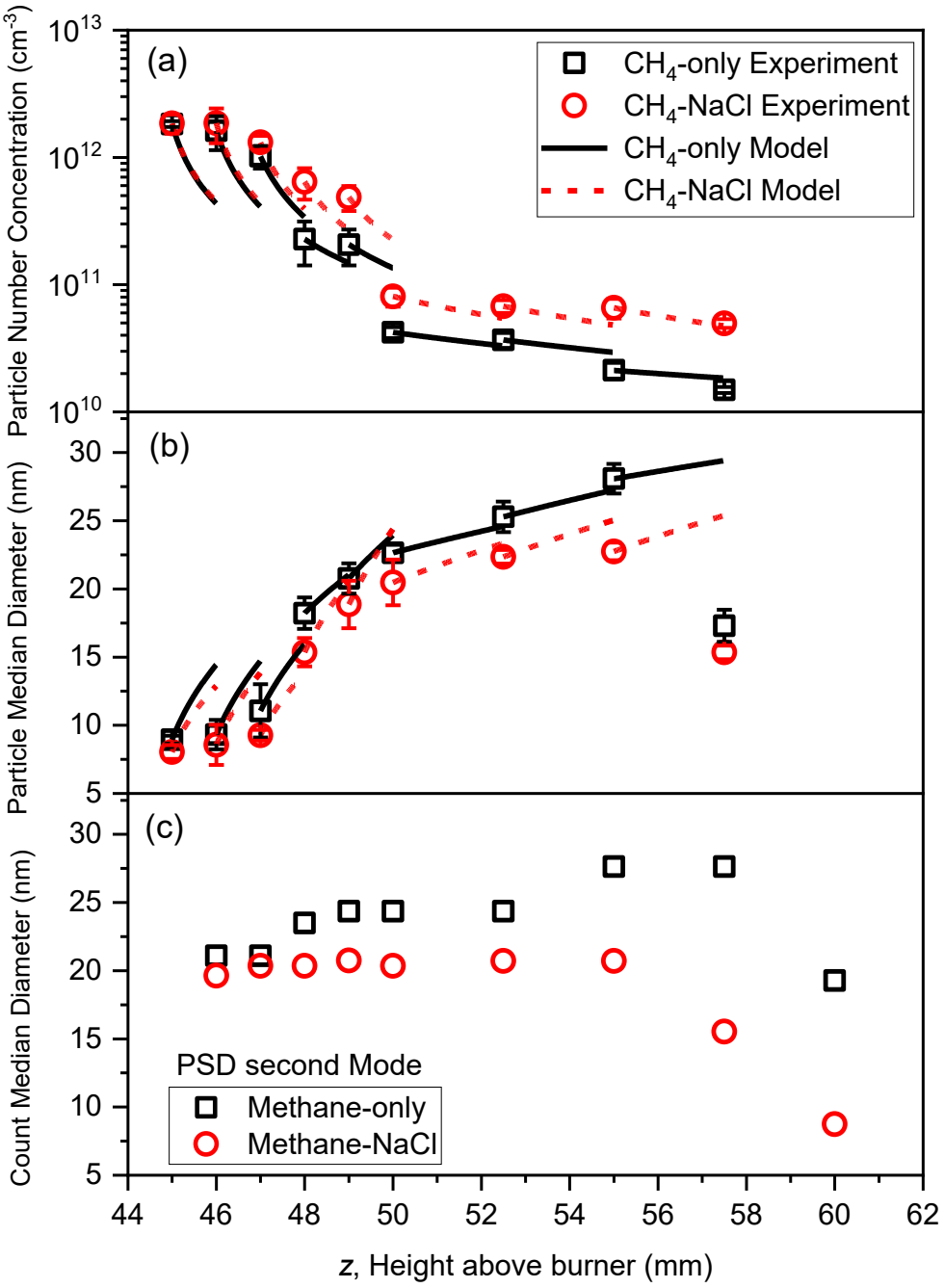

Figure 4.5: The change of particle number concentration, median diameter, and the second mode of the particle size distribution for methane-only and methane-NaCl flames with their corresponding HABs ranging from 45 to 60 mm.

The coagulation model underestimates the measured results for both flames within the HAB range of 48 mm and 49 mm. In both cases, there is a reduction in number concentration and CMD for the first mode within this range. However, for the methane-only flame, there is an increase in CMD and a decrease in number concentration for the second mode within this range. In contrast, for the methane-NaCl flame, the number concentration and CMD remain unchanged for the second mode.

Consequently, the observed differences in particle size and number concentration between HAB 47 mm and 49 mm are likely attributed to variations in oxidation processes. Additionally, the fraction of charged particles in this range for the methane-NaCl flame is approximately half that of the methane-only flame. This suggests that there might be difference in the coagulation rate of particles between the two flames, however, the model clearly indicates that the fraction of charged particles has an insignificant effect on the coagulation rate. As shown in Appendix C, even using a coagulation model with no particle charge, results in nearly the same coagulation rate.

There is a significant drop in particle number concentration in the transition from HAB 49 mm to 50 mm for both flames. The model tends to overestimate both the particle concentration and size for both flames, with the number concentration of particles in both flames decreasing by a factor of approximately 5. The substantial reduction in measured particle number concentration within this range for both flames may be attributed to a significant decrease in the number concentration of the second mode of the PSD. This decline in number concentration could potentially result from either particle oxidation, electrostatic dispersion-induced losses, or a combination of both processes occurring concurrently. However, the model indicates that losses due to electrostatic dispersion are minimal.

In the HAB range between 50 mm and 57.5 mm, the model reasonably predicts the number concentration within the measurement uncertainty. When we examine the median diameter of the

second modes for all HABs in this range (i.e., the coagulation mode of the PSD), we can draw the conclusion that particle oxidation becomes significant at HAB 57.5 mm for the methane-NaCl flame and HAB 60 mm for the methane-only flame. However, it's noteworthy that the model seems to overestimate the particle size for the methane-NaCl flame at HAB 55 mm but begins to over-predict the size at HAB 57.5 mm for the methane-only flame. Hence, in this region of the flame, particles in both flames oxidize.

Researchers have previously proposed that the smaller particle size observed in methane-NaCl flames (i.e., non-sooting flames) is a result of NaCl reducing the coagulation rate of particles through its effect on particle charge [194, 83, 84]. However, this study demonstrates that, despite differences in particle charge, the coagulation rate remains the same. Therefore, the disparity between methane-only and methane-NaCl flames is attributed to oxidation. Notably, NaCl enhances oxidation in the specific region of the flame (i.e., HAB 45 mm to 57.5 mm). It is important to note that Kazemimanesh et al. [83] have also provided clear evidence that NaCl has an opposite effect at higher HABs in sooting flames. Additionally, numerous authors [50, 87, 88] have also demonstrated that the addition of NaCl to flames leads to increased soot emissions.

4.5 Conclusion

This This work presented a detailed analysis of particle size distribution (PSD) and particle charging behavior in methane and methane-NaCl flames at different heights above the burner (HABs). The key findings and their implications can be summarized as follows:

This study investigated particle charging behavior and found that a significant percentage of particles in the nucleation region were uncharged, supporting previous research. The effect of NaCl addition in the coagulation-dominated region (HAB 45-55 mm) was attributed to NaCl enhancing particle oxidation, contrary to the common belief that it solely affects particle charging. Average charge per particle shifted from negative to positive with NaCl addition in the coagulation region, indicating a change in ion behavior. The fraction of charged particles decreased with NaCl addition, highlighting its role in neutralizing charged particles. The study provides insights into the complex interplay between ions and soot particles in flames, highlighting the role of NaCl in altering ion concentration and particle charging behavior. It was found that NaCl reduced in-flame ion concentration, which is attributed to ion recombination processes and charge transfer between alkali metals and hydrocarbon species. The coagulation model provided insights into particle behavior, but the noticed model's overestimations and underestimations of the measured results were attributed to oxidation, surface growth and nucleation not captured in the model. Interestingly, the model results were similar when considering both charged and uncharged particles in coagulation processes. This study reveals that the smaller particle size in methane-NaCl flames is primarily a result of oxidation rather than a reduction in particle charge. NaCl promotes oxidation in specific regions of the flame, leading to differences between methane-only and methane-NaCl flames.

Chapter 5

Conclusions and Future Work Recommendation

5.1 Summary and Conclusions

The entrainment of flowback water during well completion process at the upstream oil and gas facilities and the injection of water at the downstream oil and gas to suppress emissions has been found to contain some impurities which the surrogate species is NaCl. The combustion of NaCl with the flared gases has been found to increase soot emissions, decrease the size of soot, and also affect NO_x emission. These effects have made it important to carry out the investigations in Chapter 2, 3 and 4 of this work.

The second chapter of this work aimed to characterize various flare emission parameters, specifically focusing on the impact of assist fluids (liquid water and steam) on the combustion processes. Several key findings and implications emerged from the research: the study examined multiple parameters to characterize the flow, including momentum rates, buoyancy forces, and adiabatic flame temperatures. These parameters were essential in understanding the behavior of flare combustion process. The rate of upward momentum of the fuel-assist mixture was crucial for initiating fuel-air mixing necessary for combustion. Different fuels and assists had varying initial momenta, significantly impacting the combustion process. The buoyancy forces further influenced momentum as the flow progressed downstream and it played a critical role in combustion. The initial upward buoyancy force varied depending on the density of the fuel and assist components

relative to the surrounding air. The buoyancy forces on reactants could either enhance or reduce mixing as the flow progressed, affecting combustion efficiency. The adiabatic flame temperature (AFT), calculated for stoichiometric mixtures of fuel, assist, and air, demonstrated that liquid water reduced flame temperatures more than steam. This reduction in temperature had implications for emissions, particularly NO_x. NO_x emissions decreased as the ratio of assist-to-fuel mass flow rate increased, with liquid water being more effective at reducing NO_x compared to steam. These results were consistent with the decrease in adiabatic flame temperature, suggesting a strong thermal influence on NO_x formation. The black carbon (BC) emissions also decreased with an increase in the assist-to-fuel mass flow ratio. Liquid water proved more effective at reducing BC emissions compared to steam. Temperature was identified as a significant factor influencing BC production, as it correlated with changes in flame temperature. The addition of assist fluids influenced particle size distribution, with liquid water reducing particle number concentration more effectively than steam. The decrease in the count median diameter (CMD) indicated a reduction in particle nucleation and surface growth, likely related to temperature effects. In summary, this research demonstrated that assist fluids, particularly liquid water, could have a significant impact on combustion processes, including NO_x and BC emissions. The findings suggest that controlling temperature through the choice of assist fluid can be a valuable strategy for optimizing combustion efficiency and reducing emissions in practical applications. Additionally, the study emphasized the importance of considering multiple parameters in characterizing flows to gain a comprehensive understanding of combustion behavior.

The purpose of the second research, which is in Chapter 3 of this thesis is to fill a current knowledge gap by examining how liquid water injection into turbulent non-premixed flames affects emission parameter quantification and flow visualization. Emissions from non-premixed

flames in which water is introduced from outside (i.e., the air side of the flame) are the primary emphasis. The study in Chapter 3 is an expansion on our earlier efforts in Chapter 2, in which water was introduced to the fuel side of the flare, and it helps to address some of the design and safety concerns associated with internally-injected flares. To learn more about how water flow rate and position of water entrainment into the flare affect emissions, a variety of externally injected water configurations were tested at varying atomizer angles and radial displacements from the burner's centre. In order to simulate the presence of contaminants in the water used in offshore and downstream oil and gas facilities, a variety of sodium chloride (NaCl) concentrations were examined. The water droplet velocity field was utilized in the discussion of the flow visualization analysis to show how the water droplets' motion changed from being dominated by their momentum to being dominated by the buoyancy of the combustion products. This study used atmospheric turbulent non-premixed flames on a two-inch circular burner at a constant propane flow rate of 20 standard L/min, which is the same burner used in Chapter 2's study. It was discovered that the injection of external fluids, such as liquid water and NaCl solutions, influenced the flame's color and luminosity due to their impact on soot and excited species in the flame. This observation underscores the potential for controlling flame characteristics through external fluid injection. PIV analysis revealed that water droplets injected externally pass through the flame before evaporating, locally quenching the flame and affecting local temperature, reaction kinetics, and emissions. This suggests that the chemical effects of water on soot and NO_x suppression occur at higher locations in the flame compared to internal injection. The location and angle of atomizers for external water injection had a significant impact on emissions. Injecting water closer to the base of the flame was more effective in suppressing BC, as it affected the early stages of combustion. Additionally, the angle of injection influenced BC and NO_x emissions, emphasizing

the importance of both time and space when adding assisting fluid to reduce emissions. The addition of NaCl solutions to the flame exhibited a concentration-dependent effect on emissions. Low concentrations had minimal impact, but higher concentrations of NaCl reduced NO_x emissions while significantly increasing BC emissions. This outcome can be attributed to the chemical effects of Na and Cl radicals on the flame's chemistry, reducing OH, H, and O radicals, which in turn affect NO_x and soot emissions. External injection of fluids, especially liquid water, can be a viable strategy for reducing BC emissions in industrial flares without requiring significant structural modifications. This approach allows for fine-tuning of emission control based on atomizer placement and fluid composition. Hence, this research highlights the potential for external fluid injection to control emissions in non-premixed flames and provides insights into the spatiotemporal and chemical effects of fluid injection on flame behavior. These findings have implications for emission reduction strategies in various industrial and combustion processes, where the manipulation of external fluid injection parameters can be used to optimize emission control while considering the specific combustion conditions and objectives.

Since the addition of NaCl to flare in Chapter 3 of this work shows that black carbon (BC) which is the light-absorbing portion of emitted soot particles increases, then the Chapter 4 of this work seeks to understand the reason why NaCl causes more BC to be generated. Moallemi et al. [84] and Kashimemanesh et al. [34] try to find this reason but could not get to investigate the charge state and the coagulation rate of soot particle in flames. The influence of sodium chloride on the charge state and coagulation rate of soot nanoparticles developed in a laminar diffusion flame is investigated in the Chapter 4 of this work by measuring the PSD, average charge per particle, and charge fraction at different locations within the flame. With a 0.35 L/min methane fuel flow and a 70 L/min co-flow, the well-studied Santoro burner generated a 61 mm high, steady laminar

diffusion flame. At different heights above the burner (HAB), soot nanoparticle samples were collected via a small aperture in a tubular 3-mm probe and then quickly diluted by a factor of a few thousand. The sampled particles were first directed to a scanning mobility particle sizer (SMPS) with a lower measurement limit of 1 nm to obtain the particle size distribution of the soot particles. Finally, the fraction of charged particles and the average charge per particle were calculated using the measurements from a differential mobility analyzer (DMA) as an electrostatic precipitator, a condensation particle counter, and a Faraday cup electrometer. The experimental readings were verified by using a charged monodisperse coagulation model. This study investigated the particle size distribution and charging behavior of soot particles in methane and methane-NaCl flames at various heights above the burner (HABs). The PSD analysis revealed that the soot particles exhibited distinct modes related to soot inception, surface growth, coagulation, and oxidation. The presence of NaCl did not prevent soot nucleation and, in fact, led to smaller soot sizes and higher concentrations, particularly in the coagulation-dominated region. The charging behavior of soot particles showed that, in the nucleation-dominated region (HAB 30-40 mm), the majority of particles were uncharged. As coagulation became more pronounced (HAB 45-55 mm), the addition of NaCl led to a slightly positive charge on average, likely due to the higher concentration of positive ions. However, a significant fraction of particles remained uncharged when NaCl was added. The effect of NaCl addition in the coagulation-dominated region (HAB 45-55 mm) was attributed to NaCl enhancing particle oxidation, contrary to the common belief that it solely affects particle charging. The research offers a deeper understanding of the complex relationship between ions and soot particles within flames, emphasizing how NaCl can influence ion concentrations and the charging of particles. The study revealed that NaCl led to a decrease in ion concentration within the flame, a phenomenon attributed to ion recombination

processes and the transfer of charges between alkali metals and hydrocarbon species. A coagulation model was used to simulate particle behavior, and the noticed model's overestimations and underestimations of the measured results are attributed to oxidation, surface growth, and nucleation processes not considered in the model. The presence of charged particles had a minimal effect on the coagulation rate, highlighting the significance of uncharged particles in coagulation processes.

5.2 Recommendations for future work

Despite the tremendous progress in understanding the impacts of aerosolized liquids on flare emissions, there are still questions that need to be answered. Hence, recommendations for future studies are presented.

Fuel composition, flare geometry, crosswinds, assist velocity, and other variables influence the emissions from assisted flares in the oil and gas industry. Future work on the effects of liquid water addition on flare emissions should be carried out on a typical flare site, where all the variables that affect flare emissions will be considered.

To satisfy both the thermal and chemical effects of the external liquid water addition (i.e., water on the air side of the non-premixed flame) in favour of NO_x reduction, it is necessary to further investigate the spatial-temporal scale of the externally injected liquid water into flames based on operational parameters and the geometry of flames.

Produce or flowback water contains various elements, with chloride, sodium, calcium, bicarbonate, sulfate, potassium, and magnesium being the most prevalent in its composition. This

study, however, focused solely on the first two elements, namely sodium and chloride (NaCl). Previous research has shown that potassium (the third most prevalent element) can significantly affect the formation of soot particles. Even though the concentrations of other elements, such as calcium (Ca), bicarbonate (HCO_3), sulfate (SO_4), potassium (K), and magnesium (Mg), are notably lower than sodium and chloride in typical flowback/produced water, it remains valuable to investigate the impact of these elements alongside sodium chloride in non-sooting flames, specifically laminar diffusion flames. Experimental findings from prior studies suggest that potassium may exert a more substantial influence on soot particle formation in flames compared to sodium. Therefore, it would be interesting to compare the effects of each of these elements on soot particle formation.

The combustion of methane used in the laminar diffusion flame study represents the oil and gas industries flared gas in its most basic form. Possible future research might use a mixture of methane and propane like the one used in Chapter 2 of this study in order to make it more closely mimic a typical flared gas in Alberta. In contrast, ethylene was used as fuel in earlier studies on the evolution of soot in premixed flames. These fuels can also be used to study the evolution and charge state of soot in flames, and the results can be compared to existing results.

References

[1] British Petroleum, "bp Statistical Review of World Energy (71st edition)," Whitehouse Associates, London, 2022. bp.com/statisticalreview.

[2] International Energy Agency (IEA), "World Energy Outlook," IEA, France, 2022. www.iea.org/weo.

[3] K. B. Schnelle, R. F. Dunn and M. E. Ternes, Air Pollution Control Technology Handbook, Florida: Taylor and Francis Group, 2016.

[4] M. Johnson, L. Kostiuk and J. Spangelo, "A Characterization of solution gas flaring in Alberta," *Journal of the Air and Waste Management Association,* vol. 51, no. 8, pp. 1167-1177, 2001.

[5] D. C. Elvidge, D. M. Bazilian, M. Zhizhin, T. Ghosh, K. Baugh and F.-c. Hsu, "The potential role of natural gas flaring in meeting greenhouse gas mitigation targets.," *Energy Strategy Reviews,* vol. 20, pp. 156-162, 2018 (https://doi.org/10.1016/j.esr.2017.12.012).

[6] The World Bank (Global Gas Flaring Reduction Partnership), "Global Gas Flaring Tracker Report," The World Bank, Washington, DC, 2020.

[7] IEA (International Energy Agency), "IEA Methane Tracker 2020 (Reducing the environmental impact of oil and gas supply is a pivotal element of global energy transitions)," International Energy Agency, Washington, DC, March, 2020 (https://www.iea.org/reports/methane-tracker-2020).

[8] ABB Oil and Gas, Oil and gas production handbook: An introduction to oil and gas production, transport, refining and petrochemical industry., Oslo: ABB Oil and Gas, 2013. https://library.e.abb.com/public/34d5b70e18f7d6c8c1257be500438ac3/Oil%20and%20gas%20production%20handbook%20ed3x0_web.pdf.

[9] R. D. Tyner and R. M. Johnson, "A Techno-Economic Analysis of Methane Mitigation Potential from Reported Venting at Oil Production Sites in Alberta," *Environmental*

Science and Technology, vol. 52, no. 21, pp. 12877-12885, 2018. https://doi.org/10.1021/acs.est.8b01345.

[10] V. Ramanathan and G. Carmichael, "Global and Regional Climate Changes due to Black Carbon Submitted to as a Review Article November 16, 2007," *Nature-Geoscience,* vol. 1, pp. 221-247, 2007.

[11] T. C. Bond, S. J. Doherty, D. W. Fahey, P. M. Forster, T. Berntsen, B. J. DeAngelo, M. G. Flanner, S. Ghan, B. Kärcher, D. Koch, S. Kinne, Y. Kondo, P. K. Quinn, M. C. Sarofim, M. G. Schultz, M. Schulz, C. Venkataraman and H. Zhang, "Bounding the role of black carbon in the climate system: A Scientific Assessment," *Journal of Geophysical Research: Atmospheres,* vol. 118, no. 4 (doi:10.1002/jgrd.50171), pp. 5380-5552, 2013.

[12] N. A. Janssen, G. Hoek, M. Simic-Lawson, P. Fischer, L. v. Bree, H. t. Brink, M. Keuken, R. W. Atkinson, H. R. Anderson, B. Brunekreef and F. R. Cassee, "Black Carbon as an Additional Indicator of the Adverse Health Effects of Airborne Particles compared with PM10 and PM2.5," *Environmental Health Perspectives,* vol. 119, no. 12, pp. 1691-1699, 2011.

[13] P. J. Landrigan, R. Fuller, N. J. Acosta, O. Adeyi, R. Arnold, N. (. Basu, A. B. Baldé, R. Bertollini, S. Bose-O'Reilly, J. I. Boufford, P. N. Breysse and T. Chiles, "The Lancet Commission on Pollution and Health," *The Lancet,* vol. 391, no. http://dx.doi.org/10.1016/S0140-6736(17)32345-0, pp. 462-512, 2018.

[14] C. E. Baukal, "Everything you need to know about NOx," *Metal Finishing,* vol. 103, no. 11, p. 18–24, 2005.

[15] John Zink Hamworthy, Combustion Handbook (Design and Operations), Florida: Taylor and Francis Group, 2013.

[16] A. E. Emam, "Gas Flaring in Industry: An Overview," *Petroleum and Coal,* vol. 57, no. 5, pp. 532-555, 2015.

[17] The World Bank, "Regulation of Associated Gas Flaring and Venting (A Global Overview and Lessons from International Experience)," World Bank, Washington, DC, 2004.

[18] I. Aye and E. O. Wingate, "Nigeria's Flare Gas (Prevention of Waste & Pollution) Regulations 2018," *Environmental Law Review,* vol. 29, no. 2, pp. 119-127, 2019.

[19] U.S. Department of Energy, "Natural Gas Flaring and Venting: State and Federal regulatory overview, trends, and impacts," U.S. Department of Energy, New York, 2019. https://www.energy.gov/sites/prod/files/2019/08/f65/Natural%20Gas%20Flaring%20and%20Venting%20Report.pdf.

[20] IEA (International Energy Agency), "IEA Methane Tracker 2020 (Canada steps up its efforts to reduce methane emissions)," International Energy Agency, Washington, DC, March, 2020 (https://www.iea.org/commentaries/canada-steps-up-its-efforts-to-reduce-methane-emissions).

[21] American Petroleum Institute (API), "Pressure-Relieving and Depressuring Systems (ANSI/API Standard 521, Fifth Edition)," API Publishing Services, Washington, D.C. , 2008.

[22] M. McDaniel, "Flare Efficiency Study," U.S. Environmental Protection Agency Research (EPA-600/2-83-052), Austin, Texas, 1983.

[23] D. Castineira and T. F. Edgar, "CFD for Simulation of Steam-Assisted and Air-Assisted Flare Combustion Systems," *Energy and Fuels,* vol. 20, no. 3, pp. 1044-1056, 2006.

[24] W. O. Bello, M. Zamani, E. Abbasi-Atibeh, W. L. Kostiuk and S. J. Olfert, "Comparison of emissions from steam- and water-assisted lab-scale flames.," *Fuel,* vol. 302, p. 121107, 2021. https://doi.org/10.1016/j.fuel.2021.121107.

[25] K. Leary, D. Knott and R. Thompson, "Water-injected flare tip reduce radiated heat, noise," *Oil and Gas Journal,* vol. 100, no. 18, pp. 76-83, 2002.

[26] C. A. H. Williams, "Apparatus for Reducing Smoke Emission from Elevated Flare Stacks". London, England Patent 3,162,236, 22 December 1964.

[27] D. A. Chesters, "Flare". Walton-on-Thames, England Patent 4,634,370, 6 January 1987.

[28] A. Ahsan, H. Ahsan, J. S. Olfert and L. W. Kostiuk, "Quantifying the carbon conversion efficiency and emission indices of a lab-scale natural gas flare with internal coflow of air or steam," *Experimental Thermal and Fluid Science,* vol. 103, pp. 133-142, 2019.

[29] A. Mazas, B. Fiorina, D. Lacoste and T. Schuller, "Effects of Water Vapor Addition on the Laminar Burning Velocity of Oxygen-enriched Methane Flames.," *Combustion and Flames,* vol. 158, no. 12, pp. 2428-2440, 2011.

[30] A. T. Blewett, M. A. Weinrauch, L. P. Delompre and G. G. Goss, "The effect of hydraulic flowback and produced water on gill morphology, oxidative stress and antioxidant response in rainbow trout (Oncorhynchus mykiss)," *Scientific Reports,* vol. 7, p. 46482, 2017 (DOI: 10.1038/srep46582).

[31] R. Y. Glazer, T. F. Davidson, J. J. Lee and E. M. Webber, "An Inventory and Engineering Assessment of Flared Gas and Liquid Waste Streams from Hydraulic Fracturing," *Current Sustainable/Renewable Energy Reports,* vol. 4, pp. 219-231, 2017 (https://doi.org/10.1007/s40518-017-0089-x).

[32] C. Clark, A. Burnham, C. Harto and R. Horner, "Hydraulic Fracturing and Shale Gas Production: Technology, Impacts, and Regulations," Argonne National Laboratory (U.S. Department of Energy: ANL/EVS/R-12/5), Chicago, 2013.

[33] Y. Xu, O. Adefidipe and H. Dehghanpour, "Estimating fracture volume using flowback data from the Horn River Basin: A material balance approach," *Journal of Natural Gas Science and Engineering,* vol. 25, no. 4, pp. 253-270, 2015 (http://dx.doi.org/10.1016/j.jngse.2015.04.036).

[34] M. Kazemimanesh, C. Kuang, W. L. Kostiuk and S. J. Olfert, "Effect of sodium chloride on the evolution of size, mixing state, and light absorption of soot particles from a

smoking laminar diffusion flame.," *Combustion and Flame,* vol. 218, no. 4, pp. 168-178, 2020 (https://doi.org/10.1016/j.combustflame.2020.04.001).

[35] G. E. Elliott, P. Trinh, X. Ma, P. B. Leaderer, H. M. Ward and C. N. Deziel, "Unconventional oil and gas development and risk of childhood leukenia: Assessing the evidence," *Science of the Total Environment,* vol. 576, pp. 138-147, 2017 (http://creativecommons.org/licenses/by-nc-nd/4.0/).

[36] United States Environmental Protection Agency (EPA-600-R-16-236ES), "Hydraulic Fracturing for Oil and Gas: Impacts from the Hydraulic Fracturing Water Cycle on Drinking Water Resources in the United States.," Office of Research and Development, Washington, DC, 2016 (www.epa.gov/hfstudy).

[37] J. A. Kondash, E. Albright and A. Vengosh, "Quantity of flowback and produced waters from unconventional oil and gas exploration.," *Science of the Total Environmental,* vol. 574, pp. 314-321, 2017 (http://dx.doi.org/10.1016/j.scitotenv.2016.09.069).

[38] B. K. Gregory, D. R. Vidic and A. D. Dzombak, "Water Management Challenges Associated with the Production of Shale Gas by Hydraulic Fracturing.," *Elements,* vol. 7, no. 3, pp. 181-186, 2011 (DOI: 10.2113/gselements.7.3.181).

[39] A. Moallemi, "Experimental Investigation of the Effect of NaCl Additive on the Formation and Evolution of Particles in a Diffusion Flame.," Department of Mechanical Engineering, University of Alberta, Edmonton, Alberta, 2017.

[40] U.S. Geological Survey, "USGS investigations of water produced during hydrocarbon reservoir development," U.S. Department of the Interior, Washington, DC, November 2014 (http://dx.doi.org/10.3133/fs20143104).

[41] J. T. Gallegos, V. A. Brian, S. S. Haines and A. M. Engle, "Hydraulic fracturing water use variability in the United States and potentials environmental implications," *Water Resources Research,* vol. 51, pp. 5839-5845, 2015 (doi:10.1002/2015WR017278).

[42] A. Garcia-Aristizabal, P. Capuano, R. Raffaella and P. Gasparini, "Multi-hazard risk pathway scenarios associated with unconventional gas development: Identification and challenges for their assessment.," *Energy Procedia,* vol. 125, pp. 116-125, 2017.

[43] J. D. Arthur, B. Bohm and M. Layne, "Hydraulic Fracturing Considerations for Natural Gas Wells of the Marcellus Shale," in *The Ground Water Protection Council 2008 Annual Forum*, Cincinnati, Ohio, 2008.

[44] R. S. Wild and C. K. Jones, "Polynuclear aromatic hydrocarbons in the United Kingdom environment: A preliminary source inventory and budget," *Environmental Pollution,* vol. 88, no. 1, pp. 91-108, 1995 (https://doi.org/10.1016/0269-7491(95)91052-M).

[45] I. M. Stewart, Surface Production Operations: Design of Gas-Handling Systems and Facilities (3rd Edition, Volume 2), Waltham, USA: Gulf Professional Publishing (Elsevier), 2014.

[46] API (American Petroleum Institute), "Pressure-relieving and Depressuring Systems (API Standard 521, Sixth Edition)," API Publishing Services, Washington, 2014.

[47] Z. Milani and M. Johnson, "Remote Detection of Sodium Signatures as an Indicator of Liquid Carry-Over into Flare Flames in the Bakken Oil Production Region.," in *American Geophysical Union, Fall meeting 2019*, San Francisco, December, 2019 (https://ui.adsabs.harvard.edu/abs/2019AGUFM.A43M2917M/abstract).

[48] American Petroleum Institute (API Recommended Practice 521), "Guide for Pressure-Relieving and Depressuring Systems," API Publishing Services, Washington, D.C., 1997.

[49] M. Stewart and K. Arnold, "Emulsions and Oil Treating Equipment Selection Sizing and Troubleshooting," in *Crude Oil Treating Systems*, Houston, Texas, Gulf Professional Publishing, 2009, pp. 1-79.

[50] A. M. Jefferson, "Exploratory Experiments to Determine Effects of Injected Aerosolized Water, Hydrochloric Acid, and Sodium Chloride Solutions on Lab-Scale Flare

Emissions.," Department of Mechanical and Aerospace Engineering, Carleton University, Ottawa, Ontario, 2017 - https://doi.org/10.22215/etd/2017-11970.

[51] L.-H. Dorey, N. Bertier, L. Tessé and F. Dupoirieux, "Soot and radiation modeling in laminar ethylene flames with tabulated detailed chemistry," *Comptes Rendus Mecanique,* vol. 339, no. 12, pp. 756-769, 2011. DOI: 10.1016/j.crme.2011.09.004.

[52] A. Abid, J. Camacho, D. Sheen and H. Wang, "Quantitative measurement of soot particle size distribution in premixed flames – The burner-stabilized stagnation flame approach," *Combustion and Flame,* vol. 156, no. 10, p. 1862–1870, 2009. doi:10.1016/j.combustflame.2009.05.010.

[53] A. Abid, N. Heinz, E. Tolmachoff, D. Phares, C. Campbell and H. Wang, "On evolution of particle size distribution functions of incipient soot in premixed ethylene–oxygen–argon flames.," *Combustion and Flame,* vol. 154, no. 4, p. 775–788, 2008. doi:10.1016/j.combustflame.2008.06.009.

[54] J. Camacho, C. Liu, H. Wang, C. Gu, H. Lin, Z. Huang, Q. Tang, X. You, C. Saggese, Y. Li, H. Jung, L. Deng and I. Wlokas, "Mobility Size and Mass of Nascent Soot Particles in a Benchmark Premixed Ethylene Flame.," *Combustion and Flame,* vol. 162, no. 10, pp. 3810-3822, 2015. doi: 10.1016/j.combustflame.2015.07.018.

[55] M. Alfè, B. Apicella, A. Tregrossi, A. Ciajolo and J.-N. Rouzaud, "The effect of temperature on soot properties in premixed methane flames.," *Combustion and Flame,* vol. 157, no. 10, p. 1959–1965, 2010. doi:10.1016/j.combustflame.2010.02.007.

[56] K. Homann, "Carbon formation in premixed flames.," *Combustion and Flame,* vol. 11, no. 4, pp. 265-287, 1967. doi:10.1016/0010-2180(67)90017-X.

[57] C. Russo, M. Alfe, F. Stanzione, A. Tregrossi, A. Ciajolo and J.-N. Rouzaud, "Probing structures of soot formed in premixed flames of methane, ethylene and benzene.," *Proceedings of the Combustion Institute,* vol. 34, no. 1, p. 1885–1892, 2013. doi:10.1016/j.proci.2012.06.127.

[58] F. Xu, K.-C. Lin and G. Faeth, "Soot Formation in Laminar Premixed Methane/Oxygen Flames at Atmospheric Pressure.," *Combustion and Flame,* vol. 115, no. 1-2, p. 195–209, 1998. doi:10.1016/S0010-2180(98)00017-0.

[59] R. Dobbins and C. Megaridis, "Morphology of flame-generated soot as determined by thermophoretic sampling.," *Langmuir,* vol. 3, no. 2, p. 254–259, 1987. doi:10.1021/la00074a019.

[60] I. Kennedy, C. Yam, D. Rapp and R. Santoro, "Modeling and measurements of soot and species in a laminar diffusion flame.," *Combustion and Flame,* vol. 107, no. 4, p. 368–382, 1996. doi:10.1016/S0010-2180(96)00092-2.

[61] C. Kim, A. El-Leathy, G. Faeth and F. Xu, "Soot surface growth and oxidation in laminar diffusion flames at pressures of 0.1–1.0 atm.," *Combustion and Flame,* vol. 136, no. 1-2, p. 191–207, 2004. doi:10.1016/j.combustflame.2003.09.017.

[62] C. Megaridis and R. Dobbins, "Soot aerosol dynamics in a laminar ethylene diffusion flame.," *Symposium (International) on Combustion,* vol. 22, no. 1, p. 353–362, 1989. doi:10.1016/S0082-0784(89)80041-4.

[63] A. Veshkini, S. B. Dworkin and M. J. Thomson, "Understanding soot particle size evolution in laminar ethylene/air diffusion flames using novel soot coalescence models," *Combustion Theory and Modelling,* vol. 20, no. 4, pp. 707-734, 2016. http://dx.doi.org/10.1080/13647830.2016.1169319.

[64] M. Smooke, C. McEnally, L. Pfefferle, R. Hall and M. Colket, "Computational and experimental study of soot formation in a coflow, laminar diffusion flame.," *Combustion and Flame,* vol. 117, no. 1-2, p. 117–139, 1999. doi:10.1016/S0010-2180(98)00096-0.

[65] J. Cain, A. Laskin, M. Kholghy, M. Thomson and H. Wang, "Molecular characterization of organic content of soot along the centerline of a coflow diffusion flame.," *Physical Chemistry Chemical Physics,* vol. 16, no. 47, pp. 25862-25875, 2014. doi:10.1039/c4cp03330b.

[66] A. D'Anna, M. Commodo, S. Violi, C. Allouis and J. Kent, "Nano organic carbon and soot in turbulent non-premixed ethylene flames.," *Proceedings of the Combustion Institute,* vol. 31, no. 1, p. 621–629, 2007. doi:10.1016/j.proci.2006.07.062.

[67] Ü. Köylü and G. Faeth, "Structure of overfire soot in buoyant turbulent diffusion flames at long residence times.," *Combustion and Flame,* vol. 89, no. 2, p. 140–156, 1992. doi:10.1016/0010-2180(92)90024-J.

[68] B. Hu, B. Yang and Ü. Köylü, "Soot measurements at the axis of an ethylene/air non-premixed turbulent jet flame.," *Combustion and Flame,* vol. 134, no. 1-2, p. 93–106, 2003. doi:10.1016/S0010-2180(03)00085-3.

[69] S. Izvekov and A. Violi, "A coarse-grained molecular dynamics study of carbon nanoparticle aggregation," *Journal of Chemical Theory and Computation,* vol. 2, no. 3, pp. 504-512, 2006. DOI: 10.1021/ct060030d.

[70] A. D. Vallero, Environmental Biotechnology: A Biosystems Approach (2nd Edition), London, UK: Academic Press (Elsevier), 2015. https://doi.org/10.1016/C2012-0-06127-3.

[71] M. Frenklach, "Reaction mechanism of soot formation in flames," *Physical Chemistry Chemical Physics,* vol. 4, no. 11, pp. 2028-2037, 2002. DOI: 10.1039/b110045a.

[72] H. Bohm, M. Bonig, C. Feldermann, H. Jander, G. Rudolph and H. G. Wagner, "Pressure Dependence of Formation of Soot and PAH in Premixed Flames," in *H. Bockhorn (Ed.): Soot Formation in Combustion - Mechanisms and Models*, Berlin Heidelberg, Springer Series in Chemical Physics Vol. 59, 1994. https://doi.org/10.1007/978-3-642-85167-4, pp. 145-159.

[73] M. Frenklach and H. Wang, "Detailed Mechanism and Modeling of Soot Particle Formation.," in *Bockhorn H. (eds) Soot Formation in Combustion*, Berlin, Heidelberg, Springer Series in Chemical Physics, Vol. 59, 1994. https://doi.org/10.1007/978-3-642-85167-4, pp. 165-192.

[74] C. Irimiea, A. Faccinetto, X. Mercier, I.-K. Ortega, N. Nuns, E. Therssen, P. Desgroux and C. Focsa, "Unveiling trends in soot nucleation and growth: When secondary ion mass spectrometry meets statistical analysis.," *Carbon,* vol. 144, no. 12, pp. 815-830, 2019. https://doi.org/10.1016/j.carbon.2018.12.015.

[75] B. Öktem, M. Tolocka, M. Johnston, B. Zhao and H. Wang, "Chemical species associated with the early stage of soot growth in a laminar premixed ethylene–oxygen–argon flame.," *Combustion and Flame,* vol. 142, no. 4, p. 364–373, 2005. doi:10.1016/j.combustflame.2005.03.016.

[76] H. Wang, "Formation of nascent soot and other condensed-phase materials in flames," *Proceedings of the Combustion Insttitute,* vol. 33, no. 9, pp. 41-67, 2011. doi:10.1016/j.proci.2010.09.009.

[77] H.-C. Chang, R. Dobbins and R. Fletcher, "The evolution of soot precursor particles in a diffusion flame.," *Combustion and Flame,* vol. 115, no. 3, p. 285–298, 1998. doi:10.1016/S0010-2180(98)00010-8 .

[78] R. Puri, T. Richardson, R. Santoro and R. Dobbins, "Aerosol dynamic processes of soot aggregates in a laminar ethene diffusion flame.," *Combustion and Flame,* vol. 92, no. 3, p. 320–333, 1993. doi:10.1016/0010-2180(93)90043-3.

[79] R. Santoro, H. Semerjian and R. Dobbins, "Soot particle measurements in diffusion flames.," *Combustion and Flame,* vol. 51, no. C, p. 203–218, 1983. doi:10.1016/0010-2180(83)90099-8.

[80] G. De Falco, A. D'Anna, M. Commodo, P. Minutolo, C. Bonavolontà and G. Pepe, "Optical and electrical characterization of carbon nanoparticles produced in laminar premixed flames.," *Combustion and Flame,* vol. 161, no. 12, p. 3201–3210, 2014. doi:10.1016/j.combustflame.2014.05.021.

[81] P. R. Lindstedt, "Simplified Soot Nucleation and Surface Growth Steps for Non-Premixed Flames.," in *Bockhorn H. (eds) Soot Formation in Combustion.*, Berlin, Heidelberg,

Springer Series in Chemical Physics, vol 59, 1994. https://doi.org/10.1007/978-3-642-85167-4, pp. 417-441.

[82] R. M. Kholghy, "The Evolution of Soot Morphology in Laminar Co-Flow Diffusion Flames of the Surrogates for Jet A-1 and a Synthetic Kerosene.," Master's Thesis, University of Toronto, Toronto, 2012. https://tspace.library.utoronto.ca/bitstream/1807/33270/9/Kholghy_Mohammad%20Reza_201211_MASc_thesis.pdf.

[83] M. Kazemimanesh, C. Kuang, W. L. Kostiuk and S. J. Olfert, "Effect of sodium chloride on the evolution of size, mixing state, and light absorption of soot particles from a smoking laminar diffusion flame.," *Combustion and Flame,* vol. 218, no. 4, pp. 168-178, 2020. https://doi.org/10.1016/j.combustflame.2020.04.001.

[84] A. Moallemi, M. Kazemimanesh, W. L. Kostiuk and S. J. Olfert, "The effect of sodium chloride on the nanoparticles observed in a laminar methane diffusion flame.," *Combustion and Flame,* vol. 188, pp. 273-283, 2018. https://doi.org/10.1016/j.combustflame.2017.10.009.

[85] S. Haynes, H. Jander and G. H. Wagner, "The effect of metal additives on the formation of soot in premixed flames.," *Symposium (International) on Combustion,* vol. 17, no. 1, pp. 1365-1374, 1979. (https://doi.org/10.1016/s0082-0784(79)80128-9).

[86] P. Bonczyk, "In-situ optical measurement of additive effects on particulates in a sooting diffusion flame," *Combustion and Flame,* vol. 51, no. C, pp. 219-229, 1983. doi: 10.1016/0010-2180(83)90100-1.

[87] O. Bello, E. Abbasi-Atibeh, L. Kostiuk and J. Olfert, "Effects of external injection of deionized water and water with impurities on Water-assisted flares," *Fuel,* vol. 340, p. 127602, 2023. DOI: 10.1016/j.fuel.2023.127602 .

[88] A. T. Sipkens, U. Trivanovic, W. O. Bello, A. Naseri, A. Baldelli, M. Kazemimanesh, A. Bertram, C. J. Corbin, S. J. Olfert and N. S. Rogak, "Using two-dimensional size distributions to better understand the mixing state of soot and salt particles produced in gas

flares.," *Journal of Aerosol Science,* vol. 158, p. 105826, 2021. https://doi.org/10.1016/j.jaerosci.2021.105826.

[89] V. V. Lissianski, M. V. Zamansky and M. P. Maly, "Effect of Metal-Containing Additives on NOx Reduction in Combustion and Reburning," *Combustion and Flame,* vol. 125, pp. 1118-1127, 2001.

[90] R. Puri, R. J. Santoro and K. C. Smyth, "The oxidation of soot and carbon monoxide in hydrocarbon diffusion flames," *Combustion and Flame,* vol. 97, no. 2, p. 125–144, 1994. DOI: 10.1016/0010-2180(94)90001-9.

[91] A. Garo, G. Prado and J. Lahaye, "Chemical aspects of soot particles oxidation in a laminar methane-air diffusion flame," *Combustion and Flame,* vol. 79, no. 3-4, pp. 226-233, 1990. DOI: 10.1016/0010-2180(90)90134-D.

[92] C. Fenimore, "Oxidation of soot by hydroxyl radicals," *Journal of Physical Chemistry,* vol. 71, no. 3, pp. 593-597, 1967. DOI: 10.1021/j100862a021.

[93] H. Guo, P. M. Anderson and P. B. Sunderland, "Optimized rate expressions for soot oxidation by OH and O2," *Fuel,* vol. 172, pp. 248-252, 2016. DOI: 10.1016/j.fuel.2016.01.030.

[94] S.-Y. Lee, S. R. Turns and R. J. Santoro, "Measurements of soot, OH, and PAH concentrations in turbulent ethylene/air jet flames," *Combustion and Flame,* vol. 156, no. 12, pp. 2264-2275, 2009. DOI: 10.1016/j.combustflame.2009.09.005.

[95] D. E. Jensen and G. A. Jones, "Kinetics of flame inhibition by sodium," *Journal of the Chemical Society, Faraday Transactions 1: Physical Chemistry in Condensed Phases,* vol. 78, no. 9, pp. 2843-2850, 1982. DOI: 10.1039/F19827802843.

[96] A. J. Hynes, M. Steinberg and K. Schofield, "The chemical kinetics and thermodynamics of sodium species in oxygen-rich hydrogen flames," *The Journal of Chemical Physics,* vol. 80, no. 6, pp. 2585-2597, 1983. DOI: 10.1063/1.447052.

[97] E. T. Mchale, "Flame inhibition by potassium compounds," *Combustion and Flame,* vol. 24, pp. 277-279, 1975. https://doi.org/10.1016/0010-2180(75)90159-5.

[98] D. E. Jensen, G. A. Jones and A. C. H. Mace, "Flame inhibition by potassium," *Journal of chemical society faraday transactions 1 ,, ,* vol. 75, pp. 2377-2385, 1979.

[99] P. Badhuk and R. V. Ravikrishna, "Flame inhibition by aqueous solution of Alkali salts in methane and LPG laminar diffusion flames," *Fire Safety Journal,* vol. 130, p. 103586, 2022. https://doi.org/10.1016/j.firesaf.2022.103586.

[100] M. Slack, J. Cox, A. Grillo, R. Ryan and O. Smith, "Potassium kinetics in heavily seeded atmospheric pressure laminar methane flames," *Combustion and Flame,* vol. 77, no. 3-4, pp. 311-320, 1989. DOI: 10.1016/0010-2180(89)90137-5.

[101] J. Mitchell and D. Miller, "Studies of the Effects of Metallic and Gaseous Additives in the Control of Soot Formation in Diffusion Flames," *Combustion and Flame ,* vol. 75, no. 1, pp. 45-55, 1989. doi:10.1016/0010-2180(89)90086-2.

[102] Y. Kousaka, K. Okuyama, M. Adachi, K. Ebie, M. Adachi and K. Ebie, "Measurement of electric charge of aerosol particles generated by various methods," *Journal of Chemical Engineering of Japan,* vol. 14, no. 1, pp. 54-58, 1981. DOI: 10.1252/jcej.14.54.

[103] A. Gutsch and F. Löffler, "Electrically enhanced agglomeration of nanosized aerosols," *Journal of Aerosol Science,* vol. 25, pp. 307-308, 1994. DOI: 10.1016/0021-8502(94)90383-2.

[104] K. Ghosh, S. Tripathi, M. Joshi, Y. Mayya, A. Khan and B. Sapra, "Modeling studies in coagulation of charged particles and comparison with experiments.," *Journal of Aerosol Science,* vol. 105, pp. 35-47, 2017. http://dx.doi.org/10.1016/j.jaerosci.2016.11.019.

[105] S. K. Friedlander, Smoke, dust, and haze : fundamentals of aerosol dynamics (2nd Edition)., New York: Oxford University Press, 2000. https://app.knovel.com/hotlink/toc/id:kpSDHFADE1/smoke-dust-haze-fundamentals/smoke-dust-haze-fundamentals.

[106] B. Eliasson, W. Egli, J. Ferguson and H. Jodeit, "Coagulation of bipolarly charged aerosols in a stack coagulator," *Journal of Aerosol Science,* vol. 18, no. 6, pp. 869-872, 1987. doi:10.1016/0021-8502(87)90143-1.

[107] S. Dhanorkar and A. Kamra, "Effect of coagulation on the particle charge distribution and air conductivity.," *Journal of Geophysical Research,* vol. 106, no. 11, pp. 12,055-12,065, 2001. (DOI: 0148-0227/01/2000JD900709$09.00).

[108] P. M. Simones and K. S. Loyalka, "Measurements of Charged Aerosol Coagulation.," *Nuclear Technology,* vol. 189, no. 1, pp. 45-62, 2015. https://doi.org/10.13182/NT14-14.

[109] M. Simones, K. S. Loyalka, C. Dufffy, R. MacLoughlin, A. Tatham and P. Power, "Measurement of the size and charge distribution of sodium chloride particles generated by an Aeroneb Pro® pharmaceutical nebulizer.," *European Journal of Nanomedicine,* vol. 6, no. 1, pp. 29-36, 2014. (DOI: 10.1515/ejnm-2013-0018).

[110] M. Adachi, K. Okuyama and Y. Kousaka, "Electrostatic Coagulation of Bipolarly Charged Aerosol Particles.," *Journal of Chemical Engineering of Japan,* vol. 14, no. 6, pp. 467-473, 1981. DOI: 10.1252/jcej.14.467.

[111] B. Eliasson and W. Egli, "Bipolar Coagulation - Modeling and Application," *Journal of Aerosol Science,* vol. 22, no. 4, pp. 429-440, 1991. DOI: 10.1016/0021-8502(91)90003-Z .

[112] S. Verdoold and J. Marijnissen, "Modeling a bipolar-coagulation reactor using coupled population balances.," *Journal of Electrostatics,* vol. 69, no. 3, pp. 240-254, 2011. (doi:10.1016/j.elstat.2011.03.018).

[113] S. Park, K. Lee, M. Shimada and K. Okuyama, "Coagulation of bipolarly charged ultrafine aerosol particles.," *Journal of Aerosol Science,* vol. 36, no. 13, pp. 830-845, 2005. (doi:10.1016/j.jaerosci.2004.10.013).

[114] E. M. Bulewicz, D. G. Evans and P. J. Padley, "Effect of metallic additives on soot formation processes in flames," *Symposium (International) on Combustion,* vol. 15, no. 1, pp. 1461-1470, 1975. DOI: 10.1016/S0082-0784(75)80404-8.

[115] S. C. Roth, "Gas- and Particulate-phase Emissions from Lab-scale Flares Experiencing Liquid Carryover," Department of Mechanical and Aerospace Engineering, Carleton University, Ottawa, Ontario, 2022.

[116] W. L. Morgan and L. A. Rosocha, "The Physics and Plasma Chemistry of an RF Needle in a Saltwater Aerosol," *IEEE Transactions on Plasma Science,* vol. 40, no. 12, pp. 3174-3184, 2012.

[117] S. Li and F. Willians, "NOx formation in two-stage methane–air flames," *Combustion and Flame,* vol. 118, no. 3, pp. 399-414, 1999 - https://doi.org/10.1016/S0010-2180(99)00002-4.

[118] H. Guo, W. S. Neill and G. J. Smallwood, "A numerical study on the effect of water addition on NO formation in counterflow CH4/air premixed flames," *Journal of Engineering for Gas Turbines and Power,* vol. 130, pp. 054502-054505, 2008 - https://doi.org/10.1115/1.2432890.

[119] S. Lee, C. H. Shin, S. Choi and O. C. Kwon, "Characteristics of NOx emissions of counterflow nonpremixed water-laden methane/air flames.," *Energy,* vol. 164, no. 9, p. 523–535, 2018. https://doi.org/10.1016/j.energy.2018.09.017.

[120] M. Vicariotto and D. Dunn-Rankin, "Temperature profiles and extinction limits of a coflow water-vapor laden methane/air diffusion flame," *Experiments in Fluids,* vol. 59, p. 136, 2018. https://doi.org/10.1007/s00348-018-2589-x.

[121] R. E. Padilla, D. Escofet-Martin, T. Pham, W. J. Pitz and D. Dunn-Rankin, "Structure and behavior of water-laden CH4/air counterflow diffusion flames," *Combustion and Flame,* vol. 196, pp. 439-451, 2018. https://doi.org/10.1016/j.combustflame.2018.06.037.

[122] A. Atreya, T. Crompton and J. Suh, "A Study of the Chemical and Physical Mechanisms of Fire Suppression by Water," *Fire Safety Science ,* vol. 6, pp. 493-504, 2000. DOI:10.3801/IAFSS.FSS.6-493.

[123] J. Suh and A. Atreya, "The Effect of Water Vapor on Counterflow Diffusion Flames," in *International Conference on Fire Research and Engineering, National Institute of Standards and TEchnology (NIST)*, Orlando, Florida, 1995.

[124] R. Seiser and K. Seshadri, "The influence of water on extinction and ignition of hydrogen and methane flames," *Proceedings of the Combustion Institute,* vol. 30, pp. 407-414, 2005. doi:10.1016/j.proci.2004.08.220.

[125] D. Zhao, H. Yamashita, N. Kitagawa and N. F. T. Arai, "Behavior and Effect on NOx Formation of OH Radical in Methane-Air Diffusion Flame with Steam Addition," *Combustion and Flame,* vol. 130, no. 4, pp. 352-360, 2002.

[126] J. Park, S.-C. Kim, S.-I. Keel, D.-s. Noh, C.-B. Oh and D. Chung, "Effect of Steam addition on Flame Structure and NO formation in H2-O2-N2 Diffusion Flame," *International Journal of Energy Research,* vol. 28, no. 12, pp. 1075-1088, 2004.

[127] S. Lee, H. Ha, D. Dunn-Rankin and O. C. Kwon, "Effects of pressure on structure and extinction limits of counterflow nonpremixed water-laden methane/air flames," *Energy,* vol. 134, no. 1, pp. 545-553, 2017. http://dx.doi.org/10.1016/j.energy.2017.06.051.

[128] S. Lee, R. Padilla, D. Dunn-Rankin, T. Pham and O. C. Kwon, "Extinction limits and structure of counterflow nonpremixed H2O-laden CH4/air flames," *Energy,* vol. 93, pp. 442-450, 2015 - http://dx.doi.org/10.1016/j.energy.2015.09.047.

[129] V. Rao and M. Bardon, "The effect of water on gas phase soot formation in laminar diffusion flames," *Combustion and Flame,* vol. 55, no. 1, pp. 73-78, 1984 (doi: 10.1016/0010-2180(84)90150-0).

[130] V. R. LECOUSTRE, P. NARAYANAN, H. R. BAUM and A. TROUVE, "Local Extinction of Diffusion Flames in fires," *INTERNATIONAL ASSOCIATION FOR FIRE SAFETY SCIENCE,* vol. 10, pp. 583-595, 2011. DOI: 10.3801/IAFFS.FSS.10-583.

[131] I. Sakurai, J. Suzuki, Y. Kotani, H. Naito and A. Yoshida, "Extinguishment of propane/air co-flowing diffusion flames by fine water droplets," *Proceedings of the Combustion Institute ,* vol. 34, p. 2727–2734, 2013.

[132] J. Richarda, J. Garoa, J. Souila, J. Vantelon and V. Knorre, "Chemical and physical effects of water vapor addition on diffusion flames," *Fire Safety Journal,* vol. 38, p. 569–587, 2003. doi:10.1016/S0379-7112(03)00012-2.

[133] M. Zamani, E. Abbasi-Atibeh, S. Mobaseri, H. Ahsan, A. Ahsan, S. J. Olfert and W. L. Kostiuk, "An experimental study on the carbon conversion efficiency and emission indices of air and steam co-flow diffusion jet flames.," *Fuel,* pp. 1-11 (119534), 2020 (https://doi.org/10.1016/j.fuel.2020.119534).

[134] O. Armas, R. Ballesteros, F. Martos and J. Agudelo, "Characterization of light duty diesel engine pollutant emissions using water-emulsified fuel.," *Fuel,* vol. 84, no. 7-8, pp. 1011-1018, 2005 - doi: 10.1016/j.fuel.2004.11.015..

[135] C. Bolszo, A. Narvaez, V. McDonell, D. Dunn-Rankin and W. Sirignano, "Pressure-swirl atomization of water-in-oil emulsions.," *Atomization and Sprays,* vol. 20 , no. 12, p. 1077, 2010.

[136] D. Tarlet, J. Bellettre, M. Tazerout and C. Rahmouni, "A numerical comparison of spray combustion between raw and water-in-oil emulsified fuel.," *International Journal of Spray and Combustion Dynamics,* vol. 2, no. 1, pp. 1-20, 2010.

[137] F. L. Dryer, "Water Addition to Practical Combustion Systems – Concepts and Applications," *Symposium International Combustion,* vol. 16, pp. 279-295, 1976.

[138] B. McCaffrey, "Momentum Diffusion Flame Characteristics and the Effects of Water Spray," *Combustion Science and Technology,* vol. 63, pp. 315-335, 1989.

[139] M. A. Psota, W. L. Easley, T. H. Fort and A. M. Mellor, "Water injection effects on NOx emissions for engines utilizing diffusion flame combustion," *Journal of Engines,* vol. 106, no. 3, pp. 1835-1843, 1997.

[140] D. Singh, T. Nishiie, S. Tanvir and L. Qiao, "An experimental and kinetic study of syngas/air combustion at elevated temperatures and the effect of water addition," *Fuel,* vol. 94, no. 3, pp. 448-456, 2012. https://doi.org/10.1016/j.fuel.2011.11.058.

[141] T. Le Cong and P. Dagaut, "Experimental and Detailed Modeling Study of the Effect of Water Vapor on the Kinetics of Combustion of Hydrogen and Natural Gas, Impact on NOx.," *Energy and Fuels,* vol. 23, no. 2, pp. 725-734, 2009. doi: 10.1021/ef800832q.

[142] I. Fells and A. Rutherford, "Burning Velocity of Methane-air flames.," *Combustion and Flame,* vol. 13, no. 2, pp. 130-138, 1969.

[143] V. Babkin and A. V'Yun, "Effect of water vapor on the normal burning velocity of a methane-air mixture at high pressures.," *Combustion, Explosion, and Shock Waves,* vol. 7, no. 3, pp. 339-341, 1971.

[144] K. Zejlinger, "Influence of Water Injection on Nitric Oxide Formation in Petrol Engines," in *In Air PollutionControl in Transport Engines, Institute of Mechanical Engineers*, London, 1971.

[145] S. P. FUSS, E. F. CHEN, W. YANG, R. J. KEE, B. A. WILLIAMS and J. W. FLEMING, "INHIBITION OF PREMIXED METHANE/AIR FLAMES BY WATER MIST," *Proceedings of the Combustion Institute,* vol. 29, pp. 361-368, 2002.

[146] A. Hamins, D. Trees, K. Seshadri and H. Chelliah, "Extinction of nonpremixed flames with halogenated fire suppressants," *Combustion and Flame,* vol. 99, no. 2, pp. 221-230, 1994. https://doi.org/10.1016/0010-2180(94)90125-2.

[147] R. S. Sheinson, J. E. Penner-Hahn and D. Indritz, "The physical and chemical action of fire suppressants," *Fire Safety Journal,* vol. 15, no. 6, pp. 437-450, 1989. https://doi.org/10.1016/0379-7112(89)90015-5.

[148] K. Göckeler, O. Krüger and C. O. Paschereit, "Laminar burning velocities and emissions of hydrogen-methane-air-steam mixtures," in *Proceedings of ASME Turbo Expo 2014:*

Turbine Technical Conference and Exposition - GT2014-26811, Düsseldorf, Germany, 2014. https://doi-org.login.ezproxy.library.ualberta.ca/10.1115/1.4028460 .

[149] G. U. Blevins and J. R. Roby, "An experimental study of NOx reduction in laminar diffusion flames by addition of high levels of steam.," in *THE AMERICAN SOCIETY OF MECHANICAL ENGINEERS (ASME Paper)*, New York, 1995.

[150] Z. Liu and K. A. Kim, "A Review of the Research and Application of Water Mist Fire Suppression Systems – Fundamental Studies.," *Journal of Fire Protection Engineering,* vol. 10, no. 3, pp. 32-50, 2000.

[151] A. Bhargava, M. Colket, W. Sowa, K. Casleton and D. Maloney, "An Experimental and Modeling Study of Humid Air Premixed Flames," *Journal of Engineering for Gas Turbines and Power,* vol. 122, no. 3, pp. 405-411, 2000. https://doi-org.login.ezproxy.library.ualberta.ca/10.1115/1.1286921.

[152] S. Li, N. Ilincic and F. Williams, "Reduction of NOx Formation by Water Spray in Strained Two-Stage Flames," *Journal of Engineering for Gas Turbines and Power,* vol. 119, pp. 836-843, 1997.

[153] The Engineering ToolBox, "The Engineering ToolBox (Feed Water - Chemistry Limits)," American Boiler Manufacturers Association (ABMA recommended feed water chemistry limits for steam boiler), 2008. [Online]. Available: https://www.engineeringtoolbox.com/feedwater-chemistry-limits-d_1064.html. [Accessed 24 June 2021].

[154] P.-A. Glaude, R. Fournet, R. Bounaceur and M. Molière, "Adiabatic flame temperature from biofuels and fossil fuels and derived effect on NOx emission," *Fuel Processing Technology,* vol. 91, no. 3, pp. 229-235, 2010.

[155] A. Muller and S. Wittig, "Experimental Study on the Influence of Pressure on Soot Formation in a Shock Tube.," in *H. Bockhorn (Ed.) Soot Formation in Combustion - (Mechanisms and Models)*, Springer-Verlag Berlin Heidelberg, Springer Series in Chemical Physics Vol. 59, 1994, pp. 350-368.

[156] K. D. Singh, P. Gangadharan, T. Dabade, V. Shinde, D. Chen, H. H. Lou, C. P. Richmond and X. Li, "Parametric Study of Ethylene Flare Operation using Numerical Simulation," *Engineering Applications of Computational Fluid Mechanics,* vol. 8, no. 2, pp. 211-228, 2014.

[157] W. Wilson and R. Fristrom, "Radicals in Flame," APL Technical Digest, July-August, 1963.

[158] C. E. Roberts, D. Naegeli and C. Chadwell, "The Effect of Water on Soot Formation Chemistry," *Journal of Fuels and Lubricants (Section 4),* vol. 114, pp. 1656-1672, 2005. - https://www.jstor.org/stable/44721075.

[159] J. Serrano, F. Jimenez-Espadafor, A. Lora, L. Modesto-Lopez, A. Ganan-Calvo and J. Lopez-Serrano, "Experimental analysis of NOx reduction through water addition and comparison with exhaust gas recycling," *Energy,* vol. 168, pp. 737-752, 2019.

[160] I. Anufriev and E. Kopyev, "Diesel fuel combustion by spraying in a superheated steam jet," *Fuel Processiong Technology,* vol. 192, pp. 154-169, 2019.

[161] S. Kohketsu, K. Mori, K. Sakai and H. Nakagawa, "Reduction of Exhaust Emission with New Water Injection System in a Diesel Engine," in *The Engineering Society for Advancing Mobility Land Sea Air and Space*, Warrendale, Pennsylvania, 1996.

[162] A. I. Escuderoa, M. Aznara, L. I. Díeza, M. C. Mayoralb and J. M. Andrésb, "From O2/CO2 to O2/H2O combustion: The effect of large steam addition on anthracite ignition, burnout and NOx formation.," *Fuel Processing Technology,* vol. 206, p. 106432, 2020.

[163] W. R. Bussman and D. Knott, "Unique Concept for Noise and Radiation Reduction in High-Pressure Flaring," in *Offshore Technology Conference*, Houston-Texas, 2000.

[164] Alberta Energy and Utilities Board, "Alberta's Energy Researves 2005 and Supply/Demand Outlook 2006-2015," Alberta Energy and Utilities Board, Calgary, Alberta, 2006.

[165] U. Trivanovic, T. A. Sipkens, M. Kazemimanesh, A. Baldelli, A. M. Jefferson, B. M. Conrad, M. R. Johnson, J. C. Corbin, J. S. Olfert and S. N. Rogak, "Morphology and size of soot from gas flares as a function of fuel and water addition.," *Fuel,* vol. 279, no. 2, p. 118478, 2020 - https://doi.org/10.1016/j.fuel.2020.118478 .

[166] M. Kazemimanesh, "Effects of Non-hydrocarbon Liquids on Particulate Emissions of Flares," Department of Mechanical Engineering, University of Alberta, Alberta, 2014.

[167] Droplet Measurement Technologies, INC, "Photoacoustic Extinctiometer (PAX) Operator Manual (DOC-0301 Revision D-3)," Droplet Measurement Technologies, INC, Boulder, Colorado, USA, 2012.

[168] D. Pugh, P. Bowen, A. Valera-Medina, A. Giles, J. Runyon and R. Marsh, "Influence of steam addition and elevated ambient conditions on NOx reduction in a staged premixed swirling NH3/H2 flame," *Proceedings of the Combustion Institute,* vol. 37, no. 3, pp. 5401-5409, 2019.

[169] A. Ahsan, "Quantifying the Carbon Conversion Efficiency and Emission Indices of a Lab-Scale Steam-Assisted Flare," Department of Mechanical Engineering, University of Alberta, Edmonton, Alberta, 2019.

[170] M. N. Nabi, "Theoretical investigation of engine thermal efficiency, adiabatic flame temperature, NOx emission and combustion-related parameters for different oxygenated fuels.," *Applied Thermal Engineering,* vol. 30, no. 4, pp. 839-844, 2010.

[171] S. J. Harris and M. M. Maricq, "Signature size distributions for diesel and gasoline engine exhaust particulate matter.," *Journal of Aerosol Science,* vol. 32, pp. 749-764, 2001.

[172] M. Kazemimanesh, A. Baldelli, U. Trivanovic, O. Popovicheva, M. Timofeev, N. Shonija, Y. Obvintsev, C. Kuang, A. M. Jefferson, C. J. Corbin, G. G. Goss, D. S. Alessi, M. R. Johnson, S. N. Rogak and J. S. Olfert, "Particulate emissions from turbulent diffusion flames with entrained droplets: A laboratory simulation of gas flaring emissions," *Journal of Aerosol Science,* vol. 157, p. 105807, 2021. https://doi.org/j.jaerosci.2021.105807.

[173] M. Raffel, C. E. Willert, S. T. Wereley and J. Kompenhans, Particle Image Velocimetry (PIV): A Practical Guide, Berlin, Germany: Springer, 2018.

[174] T. T. Charalampopoulos and H. Chang, "In Situ Optical Properties of Soot Particles in the Wavelength Range from 340 nm to 600 nm," *Combustion Science and Technology,* vol. 59, no. 6, pp. 401-421, 1988. https://doi.org/10.1080/00102208808947108.

[175] F. J. Roesler, A. R. Yetter and L. F. Dryer, "Kinetic interactions of CO, NOx, and HCI emissions in postcombustion gases," *Combustion and Flame,* vol. 100, no. 3, pp. 495-504, 1995 -https://doi.org/10.1016/0010-2180(94)00228-K.

[176] D. H. Cotton, N. J. Friswell and D. R. Jenkins, "The Suppression of Soot Emissions from Flames by Metal Additives," *Combustion and Flame,* vol. 17, pp. 87-98, 1971. doi: 10.1016/S0010-2180(71)80142-6.

[177] M. Kazemimanesh, A. Moallemi, J. S. Olfert and L. W. Kostiuk, "Probe sampling to map and characterize nanoparticles along the axis of a laminar methane jet diffusion flame.," *Proceedings of the Combustion Institute,* vol. 36, p. 881–888, 2017. doi.org/10.1016/j.proci.2016.06.169.

[178] S. Vemury, C. Janzen and S. Pratsinis, "Coagulation of symmetric and asymmetric bipolar aerosols," *Journal of Aerosol Science,* vol. 28, no. 4, pp. 599-611, 1997. doi:10.1016/S0021-8502(96)00462-4.

[179] W. C. Hinds, "Electrical Mobility," in *Aerosol Technology (Properties, behavior, and measurement of airborne particles) - Second edition*, New York, John Wiley & Sons, Inc., 1999, pp. 320-322.

[180] G. Zebel, "Zur Theorie des Verhaltens elektrisch geladener Aerosole," *Kolloid-Zeitschrift,* vol. 157, no. 1, pp. 37-50, 1958. https://link.springer.com/content/pdf/10.1007/BF01734032.pdf.

[181] N. Fuchs, The Mechanics of Aerosols, New York: Pergamon Press, 1964.

[182] M. Woo, A. Boies, S. Hochgreb, M. Stettler, M. Schriefl, M. Knoll and R. Nishida, "Open-source modelling of aerosol dynamics and computational fluid dynamics: Bipolar and unipolar diffusion charging and photoelectric charging," *Computer Physics Communications,* vol. 278, p. 108399, 2022. DOI: 10.1016/j.cpc.2022.108399.

[183] F. G. Roper, "Soot Escape from Diffusion Flames: A Comparison of Recent Work in this Field.," *Combustion Science And Technology,* vol. 40, no. 5-6, pp. 323-329, 1984. doi:10.1080/00102208408923816.

[184] R. J. Santoro, T. T. Yeh, J. J. Horvath and H. G. Semerjian, "The Transport and Growth of Soot Particles in Laminar Diffusion Flames.," *Combustion Science and Technology ,* vol. 53, no. 2-3, pp. 89-115, 1987. doi:10.1080/00102208708947022.

[185] K. Homann, "Formation of large molecules, particulates and ions in premixed hydrocarbon flames; Progress and unresolved questions," *Symposium (International) on Combustion,* vol. 20, no. 1, pp. 857-870, 1985. DOI: 10.1016/S0082-0784(85)80575-0.

[186] M. M. Maricq, "A comparisonof soot size and charge distributions from ethane, ethylene, acetylene, and benzene/ethylene premixed flames.," *Combustion and Flame,* vol. 144, no. 7, pp. 730-743, 2006. doi:10.1016/j.combustflame.2005.09.007.

[187] M. Wang, J. Mei and X. You, "Effect of potassium chloride addition on soot formation during ethylene pyrolysis in a flow reactor ethylene pyrolysis in a flow reactor.," *Combustion and Flame ,* vol. 223, p. 118–126 , 2021. https://doi.org/10.1016/j.combustflame.2020.09.030.

[188] W. A. Hoppel and G. M. Frick, "The Nonequilibrium Character of the Aerosol Charge Distributions Produced by Neutralizes," *Aerosol Science and Technology,* vol. 12, no. 3, pp. 471-496, 1990. DOI: 10.1080/02786829008959363.

[189] A. N. Hayhurst and H. R. N. Jones, "Ions and soot in flames," *Journal of the chemical society, Faraday Transactions 2: Molecular and Chemical Physics,* vol. 83, pp. 1-27, 1987. https://doi.org/10.1039/F29878300001.

[190] A. B. Fialkov, "Investigations on ions in flames," *Progress in Energy and Combustion Science ,* vol. 23, no. 5–6, pp. 399-528, 1997. https://doi.org/10.1016/S0360-1285(97)00016-6.

[191] S. Graham and J. Goodings, "Metallic ions in hydrocarbon flames. II. Mechanism for the reduction of C3H3+ by metals in relation to soot suppression," *International Journal of Mass Spectrometry and Ion Processes,* vol. 56, no. 2, pp. 205-222, 1984. DOI: 10.1016/0168-1176(84)85044-2.

[192] J. Goodings, N. Karellas and C. Hassanali, "Comparison of electron scavengers in a hydrocarbon flame: anion formation with SF6, (CF3SO2)2O, SO2 and CH3Cl additives," *International Journal of Mass Spectrometry and Ion Processes,* vol. 89, no. 2-3, pp. 205-226, 1989. DOI: 10.1016/0168-1176(89)83061-7.

[193] N. Karellas, C. Hassanali, J. Goodings and A. Hayhurst, "The halogens as electron scavengers in hydrocarbon flames," *International Journal of Mass Spectrometry and Ion Processes,* vol. 93, no. 1, pp. 115-120, 1989. DOI: 10.1016/0168-1176(89)83079-4.

[194] A. Moallemi, "Experimental Investigation of the Effect of NaCl Additive on the Formation and Evolution of Particles in a Diffusion Flame.," Department of Mechanical Engineering, University of Alberta, Edmonton, Alberta, 2017. https://doi.org/10.7939/R33N20S3V.

[195] W. C. Hinds, "Aerosol Technology (Properties, behavior, and measurement of airborne particles) - Second edition," New York, John Wiley & Sons, Inc., 1999, pp. 278-299.

[196] Y. Wang, G. Sharma, C. Koh, V. Kumar, R. Chakrabarty and P. Biswas, "Influence of flame-generated ions on the simultaneous charging and coagulation of nanoparticles during combustion," *Aerosol Science and Technology,* vol. 51, no. 7, pp. 833-844, 2017. DOI: 10.1080/02786826.2017.1304635.

[197] Element 1 Powering Innovation, "Element 1 Powering Innovation," Element 1 Powering Innovation, 2008. [Online]. Available: http://www.e1na.com/reduced-flaring-emissions.htm. [Accessed 21 March 2021].

Appendix A.

The information provided in this appendix are for the project in Chapter 2 titled "Comparison of emissions from steam- and water-assisted lab-scale flames."

A1. Experimental data

The fuel used in the work has a constant flow rate for the three fuel cases, and the fuel flow rate is 20 ± 0.3 SLPM.

Table A.1: Experimental test conditions for the water- and steam-assisted lab-scale flare for propane fuel.

Water-assist

Date Sampled	Water Flow Rate	Adiabatic Flame Temperature	NO_x Emission Indices	Black Carbon Emission Indices	Particle Count Median Diameter	Geometry Standard Deviation for PSD
	g/min	K	g/kg fuel	g/kg fuel	nm	
13-Mar-20	0	2260	3.08 ± 0.04	5.8 ± 0.6	165	1.73
13-Mar-20	2.469 ± 0.001	2247	2.99± 0.04	4.1 ± 0.4	157	1.73
13-Mar-20	4.459 ± 0.002	2235	2.94 ± 0.04	3.4 ± 0.4	148	1.75
13-Mar-20	6.386 ± 0.004	2226	2.85 ± 0.03	2.3 ± 0.2	138	1.77
13-Mar-20	13.47 ± 0.02	2187	2.56 ± 0.03	0.27 ± 0.03	102	1.88
13-Mar-20	17.64 ± 0.02	2163	2.11 ± 0.03	0.11 ± 0.01	94.3	1.94

13-Mar-20	23.47 ± 0.02	2132	1.62± 0.02	0.0067 ± 0.0008	77.2	2.04
13-Mar-20	30.44 ± 0.01	2094	1.35 ± 0.02	0.0032 ± 0.0004	70.7	2.12
14-Mar-20	0	2260	3.06 ± 0.04	5.7 ± 0.6	164	1.73
14-Mar-20	2.555 ± 0.002	2246	3.01 ± 0.04	4.1 ± 0.4	157	1.72
14-Mar-20	4.479 ± 0.001	2236	2.93 ± 0.04	3.2 ± 0.3	149	1.74
14-Mar-20	6.42 ± 0.01	2225	2.85 ± 0.03	2.4 ± 0.3	143	1.76
14-Mar-20	15.19 ± 0.01	2177	2.31 ± 0.03	0.29 ± 0.03	103	1.86
14-Mar-20	19.16 ± 0.01	2155	2.20 ± 0.03	0.10 ± 0.01	76.5	1.93
14-Mar-20	23.51 ± 0.01	2131	1.78 ± 0.03	0.0063 ± 0.0008	70.0	2.16
14-Mar-20	30.328 ± 0.006	2094	1.23 ± 0.02	0.0022 ± 0.0003	66.4	1.90
15-Mar-20	0	2260	3.07 ± 0.04	5.5 ± 0.6	164	1.73
15-Mar-20	2.466 ± 0.002	2247	2.99 ± 0.04	4.4 ± 0.5	156	1.73
15-Mar-20	4.259 ± 0.003	2237	2.93 ± 0.04	3.4 ± 0.4	148	1.74
15-Mar-20	6.765 ± 0.002	2223	2.85 ± 0.03	2.2 ± 0.2	131	1.79
15-Mar-20	14.34 ± 0.01	2182	2.34 ± 0.03	0.28 ± 0.03	108	1.85
15-Mar-20	17.21 ± 0.03	2166	2.31 ± 0.03	0.15 ± 0.02	88.4	1.91
15-Mar-20	21.56 ± 0.02	2142	1.91 ± 0.03	0.0070 ± 0.0007	69.2	1.91
15-Mar-20	25.69 ± 0.04	2120	1.62 ± 0.03	0.0024 ± 0.0003	64.7	1.98

Steam-assist

Date Sampled	Steam Flow Rate	Adiabatic Flame Temperature	NO_x Emission Indices	Black Carbon Emission Indices	Particle Count Median Diameter	Geometry Standard Deviation for PSD
	g/min	K	g/kg fuel	g/kg fuel	nm	
21-Nov-19	0	2260	3.0 ± 0.1	5.8 ± 0.6	151	1.79
21-Nov-19	5.6 ± 1.2	2240	2.8 ± 0.1	4.0 ± 0.4	145	1.80
21-Nov-19	10.7 ± 1.1	2222	2.7 ± 0.1	1.8 ± 0.2	135	1.82
21-Nov-19	16.6 ± 1.6	2202	2.5 ± 0.1	1.1 ± 0.1	98.5	2.02
21-Nov-19	21.3 ± 2.6	2185	2.36 ± 0.04	0.41 ± 0.04	91.8	1.99
21-Nov-19	23.2 ± 2.3	2178	2.24 ± 0.04	0.20 ± 0.02	72.8	2.07
21-Nov-19	27.0 ± 2.1	2166	2.02 ± 0.04	0.07 ± 0.01	60.6	2.07
9-Dec-19	0	2260	3.0 ± 0.1	6.0 ± 0.6	154	1.77
9-Dec-19	5.8 ± 1.3	2239	3.0 ± 0.1	3.9 ± 0.4	139	1.80
9-Dec-19	10.6 ± 1.1	2223	2.8 ± 0.1	1.7 ± 0.2	124	1.89
9-Dec-19	14.0 ± 1.3	2211	2.6 ± 0.1	1.2 ± 0.1	116	1.91
9-Dec-19	20.6 ± 2.5	2187	2.35 ± 0.04	0.5 ± 0.1	88.5	1.98
9-Dec-19	24.5 ± 2.4	2174	2.22 ± 0.04	0.22 ± 0.02	77.5	2.05
9-Dec-19	27.6 ± 2.2	2163	2.11 ± 0.04	0.12 ± 0.01	60.2	2.06
9-Dec-19	31.0 ± 2.2	2151	1.99 ± 0.04	0.06 ± 0.01	58.6	2.04
10-Dec-19	0	2260	3.1 ± 0.1	5.8 ± 0.6	153	1.77
10-Dec-19	5.4 ± 1.3	2241	3.1 ± 0.1	3.7 ± 0.4	140	1.79

10-Dec-19	10.3 ± 1.1	2224	2.9 ± 0.1	1.8 ± 0.2	124	1.88
10-Dec-19	15.3 ± 1.1	2206	2.7 ± 0.1	1.2 ± 0.1	113	1.91
10-Dec-19	23.1 ± 2.7	2179	2.5 ± 0.1	0.48 ± 0.05	90.5	2.01
10-Dec-19	26.4 ± 2.8	2167	2.33 ± 0.04	0.21 ± 0.02	73.7	2.03
10-Dec-19	30.5 ± 2.6	2153	2.16 ± 0.04	0.11 ± 0.01	60.6	2.06
10-Dec-19	32.4 ± 2.4	2146	2.02 ± 0.04	0.05 ± 0.01	55.5	2.07

Table A.2: Experimental test conditions for the water- and steam-assisted lab-scale flare for methane fuel.

Water-assist

Date Sampled	**Water Flow Rate**	**Adiabatic Flame Temperature**	**NO_x Emission Indices**	**Black Carbon Emission Indices**	**Particle Count Median Diameter**	**Geometry Standard Deviation for PSD**
	g/min	**K**	**g/kg fuel**	**g/kg fuel**	**nm**	
18-Feb-20	0	2220	4.0 ± 0.2	0.08 ± 0.01	80.6	2.01
18-Feb-20	3.6196 ± 0.0004	2168	3.4 ± 0.1	0.0017 ± 0.0002	44.9	1.88
18-Feb-20	7.804 ± 0.001	2110	2.5 ± 0.1	0.0008 ± 0.0001	44.7	1.82
18-Feb-20	8.523 ± 0.001	2101	1.5 ± 0.1	0.0005 ± 0.0001	41.8	1.90
18-Feb-20	10.825 ± 0.001	2066	0.9 ± 0.1	0.0005 ± 0.0001	33.6	2.00
21-Feb-20	0	2220	4.0 ± 0.2	0.09 ± 0.01	79.4	2.00
21-Feb-20	2.705 ± 0.001	2182	3.6 ± 0.1	0.0046 ± 0.0006	51.3	1.94
21-Feb-20	4.776 ± 0.003	2152	3.3 ± 0.1	0.0013 ± 0.0002	40.1	1.96

21-Feb-20	7.634 ± 0.001	2112	2.7 ± 0.1	0.0014 ± 0.0002	38.2	1.95
21-Feb-20	9.261 ± 0.002	2089	1.4 ± 0.1	0.0010 ± 0.0001	33.0	1.99
22-Feb-20	0	2220	4.0 ± 0.2	0.09 ± 0.01	77.3	2.00
22-Feb-20	2.813 ± 0.001	2180	3.6 ± 0.1	0.005 ± 0.001	50.6	1.91
22-Feb-20	4.946 ± 0.001	2150	3.2 ± 0.1	0.0014 ± 0.0002	36.4	1.92
22-Feb-20	7.671 ± 0.001	2112	2.6 ± 0.1	0.0014 ± 0.0002	34.1	1.99
22-Feb-20	12.40 ± 0.01	2045	0.7 ± 0.1	0.0010 ± 0.0001	33.3	2.05

Steam-assist

Date Sampled	**Steam Flow Rate**	**Adiabatic Flame Temperature**	**NO_x Emission Indices**	**Black Carbon Emission Indices**	**Particle Count Median Diameter**	**Geometry Standard Deviation for PSD**
	g/min	**K**	**g/kg fuel**	**g/kg fuel**	**nm**	
21-Mar-20	0	2220	4.0 ± 0.2	0.08 ± 0.01	72.7	2.08
20-Feb-20	3.7 ± 1.2	2186	3.5 ± 0.1	0.016 ± 0.003	47.3	2.07
20-Feb-20	10.5 ± 1.3	2127	2.9 ± 0.1	0.011 ± 0.002	43.9	2.08
20-Feb-20	16.1 ± 1.3	2079	2.2 ± 0.1	0.0024 ± 0.0003	38.6	2.03
20-Feb-20	18.6 ± 1.2	2057	1.8 ± 0.1	0.0009 ± 0.0001	29.7	2.01
20-Feb-20	0	2219	4.2 ± 0.2	0.09 ± 0.01	62.7	2.09
20-Feb-20	5.6 ± 1.3	2171	3.7 ± 0.2	0.022 ± 0.003	48.6	2.10
20-Feb-20	9.7 ± 1.3	2134	2.9 ± 0.1	0.011 ± 0.002	44.9	2.16

20-Feb-20	15.0 ± 1.4	2088	2.1 ± 0.1	0.005 ± 0.001	41.4	2.04
20-Feb-20	18.6 ± 1.4	2057	1.8 ± 0.1	0.0010 ± 0.0002	40.5	1.99
21-Mar-20	0	2219	4.0 ± 0.2	0.09 ± 0.01	69.8	1.99
21-Feb-20	3.6 ± 1.3	2188	3.8 ± 0.2	0.020 ± 0.003	47.8	2.08
21-Feb-20	10.4 ± 1.3	2128	2.9 ± 0.1	0.011 ± 0.002	37.3	2.02
21-Feb-20	13.3 ± 1.3	2103	2.1 ± 0.1	0.005 ± 0.001	32.8	2.00
21-Feb-20	18.3 ± 1.3	2059	1.7 ± 0.1	0.0025 ± 0.0004	30.1	1.88

Table A.3: Experimental test conditions for the water- and steam-assisted lab-scale flare for fuel mixture case.

Water-assist

Date Sampled	**Water Flow Rate**	**Adiabatic Flame Temperature**	**NO_x Emission Indices**	**Black Carbon Emission Indices**	**Particle Count Median Diameter**	**Geometry Standard Deviation for PSD**
	g/min	**K**	**g/kg fuel**	**g/kg fuel**	**nm**	
12-Mar-20	0	2229	3.6 ± 0.1	0.68 ± 0.09	107.7	1.86
12-Mar-20	2.705 ± 0.001	2197	3.4 ± 0.1	0.19 ± 0.02	87.1	1.89
12-Mar-20	3.9268 ± 0.0003	2181	3.3 ± 0.1	0.06 ± 0.01	75.4	1.87
12-Mar-20	4.882 ± 0.001	2170	3.1 ± 0.1	0.027 ± 0.004	66.3	1.88
12-Mar-20	10.515 ± 0.003	2100	1.0 ± 0.1	0.007 ± 0.001	57.6	2.06
12-Mar-20	13.67 ± 0.01	2061	0.7 ± 0.1	0.0022 ± 0.0003	36.8	2.38

13-Mar-20	0	2230	3.6 ± 0.1	0.7 ± 0.1	104	1.88
13-Mar-20	2.707 ± 0.001	2196	3.3 ± 0.1	0.16 ± 0.02	86.7	1.88
13-Mar-20	3.727 ± 0.001	2184	3.2 ± 0.1	0.07 ± 0.01	77.0	1.88
13-Mar-20	4.786 ± 0.002	2171	3.1 ± 0.1	0.021 ± 0.003	68.1	1.86
13-Mar-20	9.26 ± 0.02	2116	2.0 ± 0.1	0.005 ± 0.001	49.1	1.91
13-Mar-20	13.09 ± 0.02	2068	1.3 ± 0.1	0.0014 ± 0.0002	40.1	2.21
14-Mar-20	0	2230	3.6 ± 0.1	0.6 ± 0.1	104	1.87
14-Mar-20	2.8771 ± 0.0004	2194	3.3 ± 0.1	0.15 ± 0.02	84.1	1.90
14-Mar-20	3.922 ± 0.001	2181	3.2 ± 0.1	0.05 ± 0.01	77.1	1.88
14-Mar-20	5.094 ± 0.001	2167	3.1 ± 0.1	0.025 ± 0.003	68.6	1.85
14-Mar-20	10.715 ± 0.002	2098	1.1 ± 0.1	0.0030 ± 0.0004	63.1	2.07
14-Mar-20	13.15 ± 0.02	2068	1.0 ± 0.1	0.0006 ± 0.0001	33.8	1.87

Steam-assist

Date Sampled	**Steam Flow Rate**	**Adiabatic Flame Temperature**	**NO_x Emission Indices**	**Black Carbon Emission Indices**	**Particle Count Median Diameter**	**Geometry Standard Deviation for PSD**
	g/min	**K**	**g/kg fuel**	**g/kg fuel**	**nm**	
21-Mar-20	0	2226	3.7 ± 0.2	0.63 ± 0.08	95.2	1.95
21-Mar-20	6.6 ± 1.0	2177	3.0 ± 0.1	0.40 ± 0.05	85.6	2.00
21-Mar-20	10.7 ± 1.2	2147	2.8 ± 0.1	0.10 ± 0.01	72.8	2.03

21-Mar-20	13.2 ± 1.2	2128	2.2 ± 0.1	0.026 ± 0.004	70.0	2.04
21-Mar-20	17.3 ± 1.2	2098	1.9 ± 0.1	0.004 ± 0.001	50.5	2.01
21-Mar-20	26.7 ± 2.9	2027	1.1 ± 0.1	0.0016 ± 0.0002	31.6	1.93
21-Mar-20	0	2229	3.7 ± 0.2	0.6 ± 0.1	95.4	1.94
21-Mar-20	6.5 ± 1.2	2177	3.2 ± 0.1	0.24 ± 0.03	83.8	2.02
21-Mar-20	10.0 ± 1.2	2150	2.6 ± 0.1	0.04 ± 0.01	65.2	2.01
21-Mar-20	14.5 ± 1.3	2117	2.3 ± 0.1	0.013 ± 0.002	51.9	2.01
21-Mar-20	18.1 ± 1.4	2091	2.1 ± 0.1	0.008 ± 0.001	45.3	1.93
21-Mar-20	25.9 ± 3.1	2036	1.0 ± 0.1	0.0010 ± 0.0001	32.0	1.82
21-Mar-20	0	2226	3.7 ± 0.2	0.7 ± 0.1	96.5	1.92
21-Mar-20	6.5 ± 1.2	2178	3.0 ± 0.1	0.32 ± 0.04	85.8	2.00
21-Mar-20	10.4 ± 1.3	2149	2.7 ± 0.1	0.052 ± 0.007	67.4	2.02
21-Mar-20	15.6 ± 1.3	2110	2.3 ± 0.1	0.013 ± 0.002	52.9	1.96
21-Mar-20	17.5 ± 1.2	2096	2.0 ± 0.1	0.007 ± 0.001	53.0	2.01
21-Mar-20	27.5 ± 2.8	2021	1.1 ± 0.1	0.0009 ± 0.0001	31.0	1.82

A2. Liquid Water Droplet Evaporation in Flames

Here we estimate the time for the water droplets produced by the atomizer to evaporate within the flame and approximately how far they travel before evaporation. Based on a simple evaporation model from Hinds [195], the time required for large water droplets (d_p > 1.0 mm) to completely evaporate is:

$$t = \frac{R\,\rho_p\,d_p^2}{8\,D_v\,M\left(\frac{P_d}{T_d}-\frac{P_\infty}{T_\infty}\right)} \quad \text{(A1)}$$

where R is the universal gas constant (8.314 J/mol K), ρ_p is the density of the water droplet (1000 kg/m^3), d_p is the diameter of the water droplets (12 mm or 40 mm), D_v is the diffusion coefficient of water vapour (24.2 x 10^{-6} m^2/s), M is the molar mass of water (18 x 10^{-3} kg/mol), P_d is the droplet partial pressure (equal to the saturation vapour pressure at temperature, T_d), P_∞ is the partial pressure of the gas , T_d is the droplet temperature, and T_∞ is the temperature of the gas (assumed to be constant). The environment of the liquid water droplet (which is inside the flame) is dry fuel gas, thus $P_\infty = 0$.

Also, using the first law of thermodynamics, the liquid water droplet temperature (T_d) can be determined [195] by,

$$T_d - T_\infty = \frac{D_v\,M\,h_{fg}}{R\,k_g}\left(\frac{P_\infty}{T_\infty}-\frac{P_d}{T_d}\right) \quad \text{(A2)}$$

where h_{fg} is the latent heat of evaporation (2.260 x 10^6 J/kg), and k_g is the gas thermal conductivity.The temperature at the exit of the burner (on the center line) for methane and propane were 113 ^{o}C and 84 ^{o}C, respectively, as measured by a thermocouple. As an approximation, it is assumed that the gas temperature remains at these temperatures during the evaporation process.

Using Equation A2, the droplet temperature is found through iteration, and then Equation A1 is used to calculate the time for the droplet to evaporate. Table A4 summarizes the input values and evaporation times for the four cases of interest (methane and propane fuels with droplet sizes of 12 μm and 40 μm).

Table A.4: Summary of the input values for liquid water droplet evaporation calculation used in this study and their corresponding evaporation time.

Fuel	Droplet Size	$k_g \left(\frac{W}{mK}\right)$	T_∞ (K)	T_d (K)	Evaporation Time (ms)
Methane	12 μm	0.0475	386.15	316.65	12.3
Methane	40 μm	0.0475	386.15	316.65	136.4
Propane	12 μm	0.0253	357.15	300.65	28.0
Propane	40 μm	0.0253	357.15	300.65	313.0

As shown in the Table, the time it takes for the 12 μm and 40 μm water droplets to evaporate in the methane flame is approximately 12.3 ms and 136.4 ms, respectively, while for the propane flame, it takes approximately 28 ms and 313 ms for 12 μm and 40 μm water droplets, respectively. These evaporation times are based on the assumption that the gas temperature remains constant during the evaporation process. However, the gas temperature becomes much hotter as the droplets move higher within the flame or as they approach the flame front (reaching temperatures near 2000 K). Thus, the actual evaporation time will be much lower than the approximate values calculated here.

The relaxation time for the 12 μm and 40 μm droplets are about 1.35 ms and 15 ms, respectively. Thus, it takes approximately 4 ms (*i.e.,* ~ 3 times the relaxation time) for the 12 μm droplets and 45 ms for 40 μm droplets to reach the velocity of the gas, which has an average velocity of 0.66 m/s. Thus, in the methane flame, the distance travelled by the droplets will approximately be 8 mm and 90 mm for 12 μm and 40 μm droplets, respectively. While in the case of the propane flame, the distance travelled by the droplets will approximately be 19 mm and 207 mm for 12 μm and 40 μm droplets, respectively. Again, these estimates will be much higher than the actual distance travelled as the actual evaporation time will be shorter. In any case, the evaporation time of the droplets is short, and the droplets will evaporate before reaching the flame front. Thus, it is not expected that the initial droplet diameter would have much effect on the emissions from the flames, nor do we expect any unevaporated droplets to escape the flame.

Appendix B.

The information provided in this appendix are for the project in Chapter 3 titled "Effects of External Injection of Deionized Water and Water with Impurities on Water-assisted Flares."

B1. Single-lens reflex (SLR) images

Figure B.1 shows the view of two atomizers injecting liquid water droplets into a turbulent non-premixed propane flame at the same flow rate. The image visually illustrates the symmetry in water injection into the flame front. In Fig. B.2, the SLR images are shown for three atomizer angles (i.e., $\theta = 20°$, $\theta = 40°$, and $\theta = 60°$) and the total water flow rates for four atomizers ranging from approximately 8 to 33 g/min with individual atomizer flow rates of ~2.1, 3.1, 4.4, 6.0, and 8.1 g/min. However, during PIV measurements, only the two atomizers within the laser sheet were running at the same individual atomizer flow rate as in emission measurements, i.e., half the total flow rate, to eliminate the interference of the spray field from the other two atomizers located within the vertical plane to the laser sheet with the spray field within the laser plane. The SLR images in Fig. B.2 reveal that almost all water droplets traveled well into the flame before evaporation, although the number density of the droplets decreased after penetrating the flame. The fact that water droplets pass through the flame front suggests that the flame was locally quenched, and the droplets have spatial-temporal effects on local flame temperature, reaction kinetics, and emissions.

Figure B.1: An SLR image showing two atomizers for the symmetry view of liquid water injection.

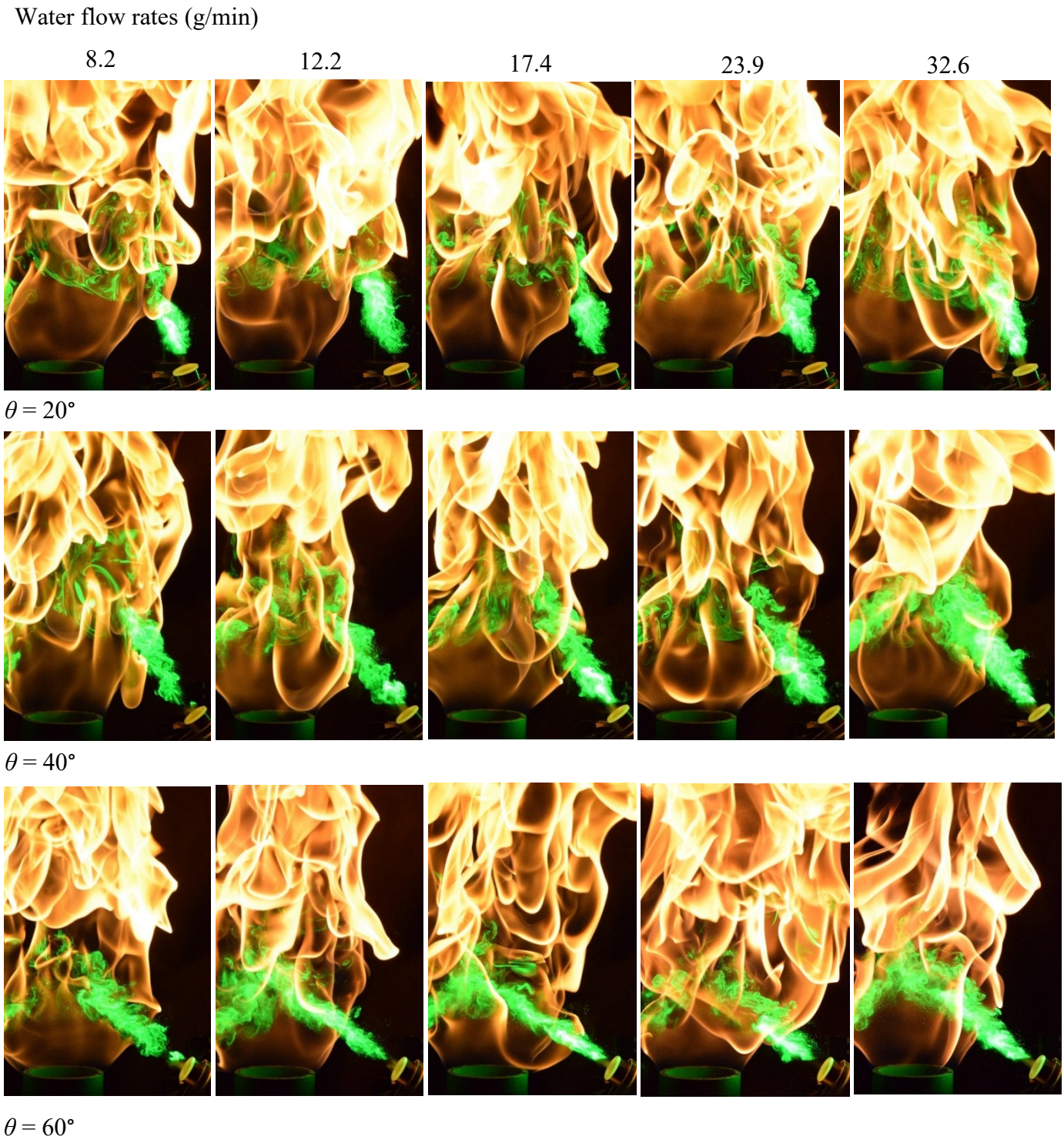

Figure B.2: SLR images for the angled external liquid water injection for various water flow rates. Only one atomizer is shown in PIV images to increase the spatial resolution of the PIV analysis.

B2. Experimental data for different test conditions

The experiments were conducted on three different days to ensure repeatability. The results of these experiments are presented in Tables B.1 to B.5. The average of the three repeats are reported in the plots. The theoretical adiabatic flame temperature (AFT) values are also presented in the tables. Tables B.1, B.2, and B.3 show the experimental test conditions for externally-injected liquid water into the flame with a water flow rate range from 8.2 g/min to 32 g/min at a constant atomizer angle of $\theta = 60°$, $\theta = 40°$, and $\theta = 20°$, respectively. Table B.4 shows the experimental conditions for flames with a constant $MFR = 0.9$ and at $\theta = 60°$ for various radial displacements of the atomizer's exit from the center of the burner. Table B.5 shows the experimental conditions for water injection with various NaCl concentrations at $MFR = 0.9$ and $\theta = 60°$. Table B.5 also shows the corresponding total liquid flow rates (H_2O + % NaCl) for each test condition.

Table B.1: Experimental test conditions and results at $\theta = 60°$ water flow rates ranging from 8.2 g/min to 32.6 g/min.

Repeats	H_2O flow rate	AFT	EI_{NOx}	EI_{BC}	CMD
	g/min	K	g/kg fuel	g/kg fuel	nm
1	0.00	2265	3.49 ± 0.04	5.23 ± 0.55	150.9
	8.2 ± 0.6	2219	2.32 ± 0.03	1.43 ± 0.15	111.0
	12.2 ± 0.3	2196	2.11 ± 0.03	0.94 ± 0.10	108.3
	17.4 ± 0.3	2166	1.76 ± 0.03	0.59 ± 0.06	102.4
	23.9 ± 0.3	2129	1.36 ± 0.02	0.37 ± 0.04	90.7
	32.6 ± 0.2	2080	1.16 ± 0.02	0.08 ± 0.01	84.5
2	0.00	2265	2.91 ± 0.04	4.76 ± 0.50	147.5
	7.9 ± 0.5	2219	2.36 ± 0.03	1.37 ± 0.14	116.7
	12.2 ± 0.4	2196	2.15 ± 0.03	0.97 ± 0.10	110.3
	17.6 ± 0.4	2166	1.80 ± 0.03	0.65 ± 0.07	104.3
	23.8 ± 0.2	2129	1.41 ± 0.02	0.35 ± 0.04	103.8
	31.9 ± 0.5	2084	1.18 ± 0.02	0.14 ± 0.02	88.5
3	0.00	2265	3.41 ± 0.04	4.57 ± 0.48	143.8
	8.1 ± 0.4	2219	2.31 ± 0.03	1.33 ± 0.14	117.8
	12.0 ± 0.4	2196	2.15 ± 0.03	0.94 ± 0.10	116.3
	17.9 ± 0.2	2163	1.75 ± 0.03	0.59 ± 0.07	106.0
	23.6 ± 1.5	2132	1.44 ± 0.02	0.39 ± 0.04	99.4
	31.8 ± 0.7	2084	1.17 ± 0.02	0.11 ± 0.01	87.4

Table B.2: Experimental test conditions and results at $\theta = 40°$ for water flow rates ranging from 8.2 g/min to 32.6 g/min.

Repeats	H_2O flow rate	AFT	EI_{NOx}	EI_{BC}	CMD
	g/min	K	g/kg fuel	g/kg fuel	nm
1	0.00	2265	3.49 ± 0.04	5.23 ± 0.55	150.9
	9.1 ± 0.9	2213	3.13 ± 0.04	1.95 ± 0.20	118.4
	14.0 ± 0.7	2186	2.89 ± 0.03	1.19 ± 0.12	114.7
	21.2 ± 0.2	2146	2.36 ± 0.03	0.80 ± 0.08	98.5
	26.7 ± 0.5	2111	2.12 ± 0.03	0.59 ± 0.06	96.0
	31.4 ± 0.4	2087	1.93 ± 0.03	0.47 ± 0.05	97.1
2	0.00	2265	2.91 ± 0.04	4.76 ± 0.50	147.5
	9.1 ± 0.2	2213	3.09 ± 0.04	1.86 ± 0.19	113.3
	14.0 ± 0.3	2186	2.83 ± 0.03	1.30 ± 0.14	109.7
	20.0 ± 0.4	2153	2.48 ± 0.03	0.99 ± 0.10	98.7
	25.9 ± 0.4	2118	2.18 ± 0.03	0.72 ± 0.08	95.5
	31.5 ± 0.6	2087	1.91 ± 0.03	0.53 ± 0.06	101.4
3	0.00	2265	3.41 ± 0.04	4.57 ± 0.48	143.8
	9.2 ± 0.1	2213	3.11 ± 0.04	1.84 ± 0.19	116.9
	13.6 ± 0.1	2186	2.90 ± 0.04	1.32 ± 0.14	116.9
	20.3 ± 0.3	2149	2.52 ± 0.03	1.00 ± 0.11	110.9
	26.0 ± 0.2	2118	2.13 ± 0.03	0.71 ± 0.08	104.1
	31.6 ± 0.3	2087	2.00 ± 0.03	0.52 ± 0.06	96.3

Table B.3: Experimental test conditions and results at $\theta = 20°$ for water flow rates ranging from 8.2 g/min to 32.6 g/min.

Repeats	H_2O flow rate	AFT	EI_{NOx}	EI_{BC}	CMD
	g/min	K	g/kg fuel	g/kg fuel	nm
1	0.00	2265	3.49 ± 0.04	5.23 ± 0.55	150.9
	9.8 ± 0.2	2210	3.11 ± 0.04	2.85 ± 0.30	124.6
	14.7 ± 0.2	2180	2.79 ± 0.04	1.89 ± 0.20	112.2
	21.4 ± 0.3	2142	2.59 ± 0.03	1.53 ± 0.16	115.6
	28.6 ± 0.2	2101	2.19 ± 0.03	1.28 ± 0.14	112.2
	33.2 ± 0.4	2077	1.73 ± 0.03	1.16 ± 0.12	108.1
2	0.00	2265	2.91 ± 0.04	4.76 ± 0.50	147.5
	9.6 ± 0.3	2210	2.93 ± 0.04	2.48 ± 0.26	126.8
	14.3 ± 0.2	2183	2.95 ± 0.04	1.88 ± 0.20	123.9
	21.3 ± 0.2	2142	2.64 ± 0.04	1.52 ± 0.16	118.9
	27.6 ± 0.6	2108	2.09 ± 0.04	1.36 ± 0.15	105.6
	32.9 ± 0.4	2080	1.96 ± 0.03	0.97 ± 0.11	115.9
3	0.00	2265	3.41 ± 0.04	4.57 ± 0.48	143.8
	9.7 ± 0.2	2210	2.97 ± 0.03	2.53 ± 0.26	132.9
	14.4 ± 0.1	2183	2.79 ± 0.03	1.79 ± 0.19	130.5
	21.5 ± 0.1	2142	2.49 ± 0.03	1.39 ± 0.15	125.4
	27.7 ± 0.6	2108	2.12 ± 0.03	1.28 ± 0.14	112.9
	33.3 ± 0.4	2077	1.92 ± 0.03	0.90 ± 0.10	110.0

Table B.4: Experimental test conditions and results at MFR = 0.9, θ = 60°, and for varying r location of the atomizers' exit from the center of the burner.

Repeats	Atomizer r location mm	H_2O flow rate g/min	AFT K	EI_{NOx} g/kg fuel	EI_{BC} g/kg fuel	CMD nm
1	95	32.6 ± 0.2	2080	1.16 ± 0.02	0.08 ± 0.01	84.5
	105	29.9 ± 0.2	2094	1.16 ± 0.02	0.18 ± 0.02	84.9
	115	30.8 ± 0.4	2091	0.92 ± 0.02	0.42 ± 0.04	91.8
	125	32.8 ± 0.4	2080	0.92 ± 0.02	0.48 ± 0.05	94.4
	135	33.1 ± 0.4	2077	1.02 ± 0.02	0.86 ± 0.09	99.9
2	95	31.9 ± 0.5	2084	1.18 ± 0.02	0.14 ± 0.02	88.5
	105	30.1 ± 0.8	2094	1.16 ± 0.02	0.25 ± 0.03	91.4
	115	31.0 ± 0.5	2087	0.90 ± 0.02	0.39 ± 0.04	91.8
	125	33.4 ± 2.0	2077	0.95 ± 0.02	0.48 ± 0.05	95.1
	135	32.5 ± 0.2	2080	0.98 ± 0.02	0.70 ± 0.08	102.0
3	95	31.8 ± 0.7	2084	1.17 ± 0.02	0.11 ± 0.01	87.4
	105	30.1 ± 0.3	2094	1.14 ± 0.02	0.28 ± 0.03	91.9
	115	30.5 ± 0.2	2091	0.88 ± 0.02	0.39 ± 0.04	95.8
	125	32.5 ± 0.3	2080	0.91 ± 0.02	0.52 ± 0.06	105.8
	135	32.5 ± 0.3	2080	1.02 ± 0.02	0.74 ± 0.08	108.3

Table B.5: Experimental test conditions and results at $MFR = 0.9$, $\theta = 60°$, $r = 95$ mm and various NaCl concentrations.

Repeats	NaCl Concentration (%)	Total flow rate (H_2O + % of NaCl) g/min	AFT K	EI_{NOx} g/kg fuel	EI_{BC} g/kg fuel	CMD nm
1	0.000	32.6 ± 0.2	2080	1.16 ± 0.02	0.08 ± 0.01	84.5
	0.005	31.5 ± 0.4	2086	1.10 ± 0.02	0.10 ± 0.01	17.9
	0.050	32.3 ± 0.2	2082	1.18 ± 0.02	0.12 ± 0.02	30.4
	0.350	32.9 ± 0.3	2079	1.06 ± 0.02	0.23 ± 0.03	52.9
	3.500	29.3 ± 0.7	2102	0.86 ± 0.02	0.87 ± 0.09	95.0
2	0.000	31.9 ± 0.5	2084	1.18 ± 0.02	0.14 ± 0.02	88.5
	0.005	31.6 ± 0.2	2086	1.14 ± 0.02	0.12 ± 0.01	19.8
	0.050	31.9 ± 0.4	2084	1.19 ± 0.02	0.12 ± 0.01	35.9
	0.350	32.5 ± 0.2	2081	1.03 ± 0.02	0.23 ± 0.03	67.5
	3.500	29.2 ± 0.2	2103	0.85 ± 0.02	0.75 ± 0.08	118.4
3	0.000	31.8 ± 0.7	2084	1.17 ± 0.02	0.11 ± 0.01	87.4
	0.005	31.4 ± 0.2	2087	1.15 ± 0.02	0.12 ± 0.01	21.2
	0.050	32.1 ± 0.2	2083	1.21 ± 0.02	0.12 ± 0.01	40.0
	0.350	33.4 ± 1.5	2076	1.04 ± 0.02	0.21 ± 0.02	64.2
	3.500	29.8 ± 0.4	2099	0.82 ± 0.02	0.68 ± 0.07	119.1

B3. PIV processing and velocity field data

The PIV images were post-processed to calculate the velocity vector field of the atomizer water spray, as well as the averaged water droplet velocities at various distances from the atomizer exit at $\theta = 40°$ in the z_2-direction. The high density and significant overlap of water droplets in PIV images resulted in saturated spots within the PIV images causing correlation errors in PIV processing in these regions. To eliminate spurious velocity vectors caused by correlation errors in

PIV processing, the velocity vector fields were post-processed by fitting multimodal Gaussian distributions to the data. The PIV test window of approximately 95 × 95 mm^2 was manually divided into 196 cells. The velocity data of water droplets for each PIV image pair was extracted from DaVis 10 software, and the velocity data for 400 image pairs were converted to MAT files. Each PIV image contained 256 × 256 interrogation windows, i.e., the size of each interrogation window of 16 × 16 pixels, window over-lap of 75%, and the camera resolution of 1024 × 1024 pixels. Figure B.3 shows how the PIV test window was divided into 196 cells i.e., a 14 × 14 matrix. The figure also shows the axis of the PIV image pair and the direction of water injection (i.e., z_2-direction). For each cell, 144,400 velocity data points for each component of u and v were extracted over 400 image pairs, and the histograms of u and v were plotted.

The histograms of velocity components were fitted and filtered. Firstly, the histogram plot of the velocity distributions was fitted with a multimodal Gaussian distribution using the Gaussian mixture models (GMM) filtering algorithm in MATLAB. This work uses three or four-mode Gaussian distributions to fit the histograms depending on the number of visible modes.

Secondly, the velocity vectors with a mean magnitude of 0 to 0.1 m/s were removed from the distributions using the same GMM filtering algorithm by reducing the number of modes of the Gaussian distribution from three-mode to two-mode distributions or from four-mode to three-mode distribution. This range of velocities was supposed to be an artifact of saturation in the images (i.e., particles appear to be motionless or traveling at very low velocities because the PIV algorithm mistakenly correlates the wrong droplet pair in the images). The mean, standard deviation, and mixing proportion for each mode of the multimodal distributions were generated from the gaussian mixture distribution fit. The mean value of the filtered velocity vector distribution was then used as the mean velocity for water droplets in each cell.

The processing of the average velocity field over the red highlighted 3rd, 5th, and 6th cells in Fig. B.3 (v_{13} & u_{13}, v_{15} & u_{15}, and v_{16} & u_{16}) are presented for the water flow rate of 2.1 g/min as examples (Figs. B.4 and B.5). Figure B.4 and B.5 show the Gaussian mixture distributions for *u*- and *v*-components of the velocity, with the left showing the fitted distributions for the extracted data from 400 image pairs and the right showing the filtered distributions.

Figure B.3: PIV test window cells and the direction of the atomizer injection.

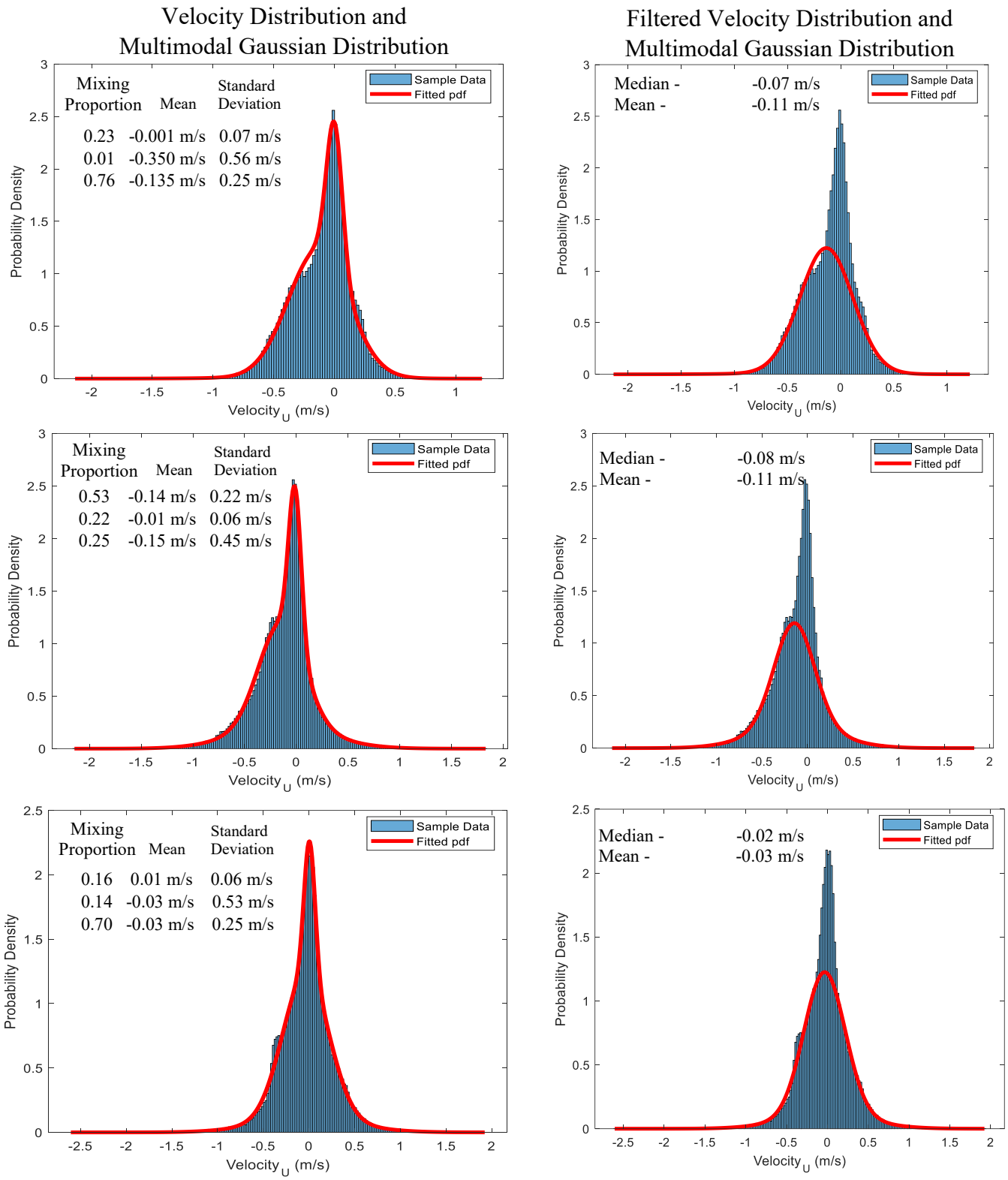

Figure B.4: *u*-component of the velocity for the three cells illustrated in Fig. B.3.

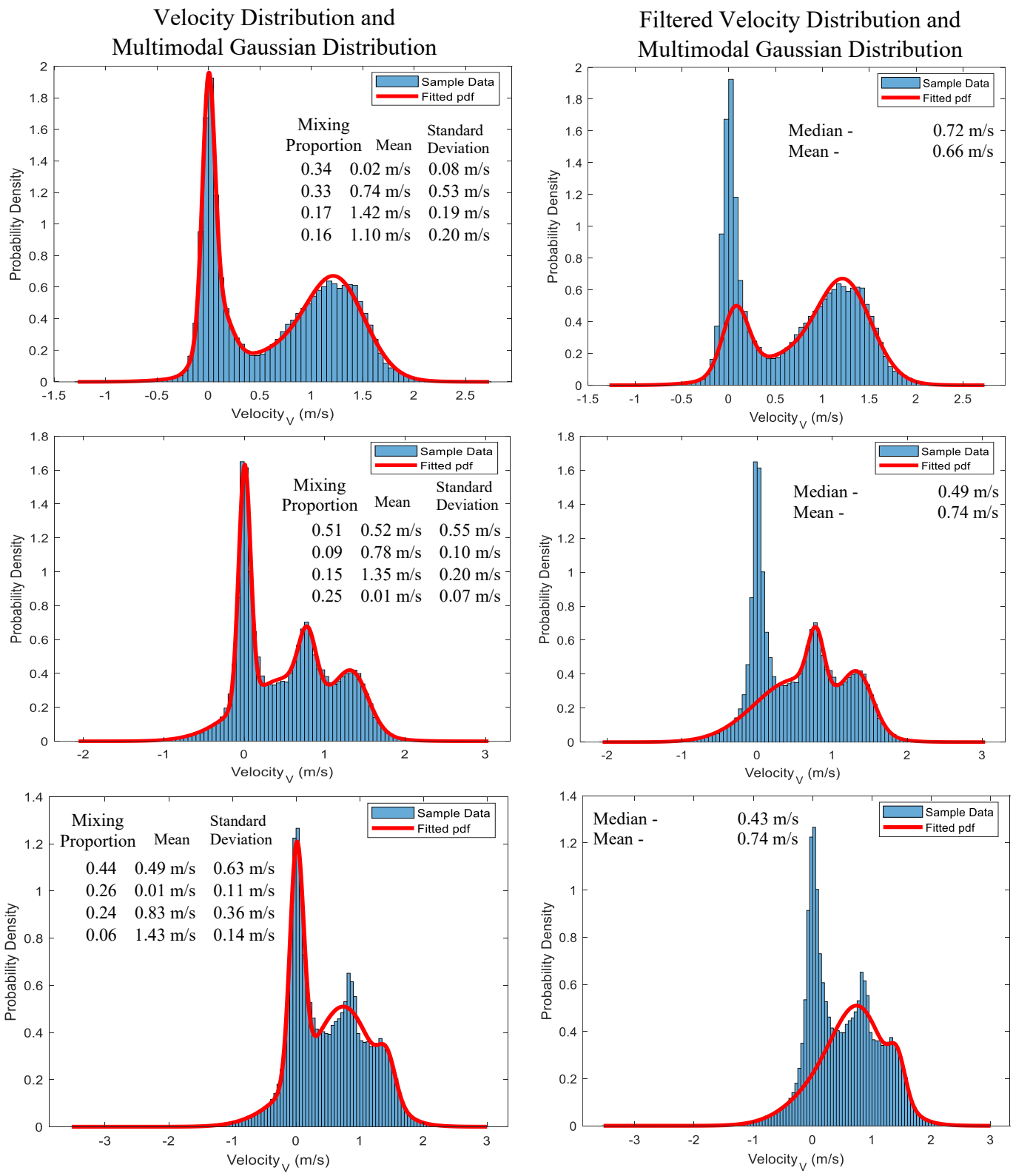

Figure B.5: *v*-component of the velocity for the three cells illustrated in Fig. B.3.

Tables B.6 and B.7 list the average velocities in r-direction (u) and z-direction (v) calculated using 400 PIV image pairs for a single atomizer running at 2.1 g/min and 8.1 g/min water flow rates at $\theta = 40°$. Tables B.6 and B.7 show the coordinates of the cell centers and average u- and v-components of the velocity vectors.

Table B.6: Average velocity field over the PIV test window of 95 x 95 mm^2 for a single atomizer flow rate of 2.1 g/min.

		r (mm)													
z (mm)	Average velocity (m/s)	4.5	11.5	18.5	25.5	32.5	39.5	46.5	53.5	60.5	67.5	74.5	81.5	88.5	92.5
105.5	*v*	0.00	0.00	0.66	0.69	0.74	0.74	0.28	0.12	0.00	0.00	0.00	0.00	0.00	0.00
	u	0.00	0.00	-0.11	-0.13	-0.11	-0.03	0.00	0.01	0.00	0.00	0.00	0.00	0.00	0.00
98.5	*v*	0.00	0.00	0.72	0.73	0.82	0.84	0.32	0.16	0.00	0.00	0.00	0.00	0.00	0.00
	u	0.00	0.00	-0.10	-0.13	-0.15	-0.06	-0.02	-0.02	0.00	0.00	0.00	0.00	0.00	0.00
91.5	*v*	0.00	0.00	0.77	0.73	0.86	0.59	0.41	0.22	0.00	0.00	0.00	0.00	0.00	0.00
	u	0.00	0.00	-0.09	-0.14	-0.19	-0.12	-0.07	-0.08	0.00	0.00	0.00	0.00	0.00	0.00
84.5	*v*	0.00	0.00	0.80	0.75	0.85	0.62	0.47	0.29	0.00	0.00	0.00	0.00	0.00	0.00
	u	0.00	0.00	-0.09	-0.15	-0.19	-0.20	-0.11	-0.11	0.00	0.00	0.00	0.00	0.00	0.00
77.5	*v*	0.00	0.00	0.79	0.78	0.83	0.61	0.72	0.74	0.20	0.00	0.00	0.00	0.00	0.00
	u	0.00	0.00	-0.10	-0.15	-0.18	-0.21	-0.17	-0.14	-0.06	0.00	0.00	0.00	0.00	0.00
70.5	*v*	0.00	0.00	0.78	0.80	0.80	0.61	0.68	0.76	0.32	0.00	0.00	0.00	0.00	0.00
	u	0.00	0.00	-0.11	-0.16	-0.20	-0.23	-0.20	-0.17	-0.08	0.00	0.00	0.00	0.00	0.00
63.5	*v*	0.00	0.00	0.70	0.79	0.82	0.60	0.80	0.49	0.41	0.25	0.00	0.00	0.00	0.00
	u	0.00	0.00	-0.08	-0.16	-0.19	-0.22	-0.26	-0.24	-0.18	-0.10	0.00	0.00	0.00	0.00
56.5	*v*	0.00	0.00	0.28	0.34	0.47	0.53	0.51	0.71	0.49	0.35	0.24	0.00	0.00	0.00
	u	0.00	0.00	-0.10	-0.13	-0.19	-0.27	-0.28	-0.34	-0.23	-0.15	-0.06	0.00	0.00	0.00
49.5	*v*	0.00	0.00	0.49	0.24	0.37	0.42	0.43	0.60	0.62	0.46	0.33	0.00	0.00	0.00
	u	0.00	0.00	-0.10	-0.10	-0.15	-0.25	-0.28	-0.33	-0.36	-0.25	-0.10	0.00	0.00	0.00
42.5	*v*	0.00	0.00	0.00	0.21	0.23	0.27	0.29	0.47	0.69	0.62	0.41	0.25	0.00	0.00
	u	0.00	0.00	0.00	-0.06	-0.07	-0.15	-0.22	-0.31	-0.40	-0.35	-0.19	-0.07	0.00	0.00
35.5	*v*	0.00	0.00	0.00	0.00	0.00	0.00	0.00	0.29	0.58	0.73	0.50	0.24	0.00	0.00
	u	0.00	0.00	0.00	0.00	0.00	0.00	0.00	-0.23	-0.38	-0.44	-0.31	-0.11	0.00	0.00
28.5	*v*	0.00	0.00	0.00	0.00	0.00	0.00	0.00	0.00	0.35	0.66	0.72	0.34	0.00	0.00
	u	0.00	0.00	0.00	0.00	0.00	0.00	0.00	0.00	-0.23	-0.42	-0.49	-0.24	0.00	0.00
21.5	*v*	0.00	0.00	0.00	0.00	0.00	0.00	0.00	0.00	0.00	0.34	0.82	0.63	0.21	0.00
	u	0.00	0.00	0.00	0.00	0.00	0.00	0.00	0.00	0.00	-0.25	-0.56	-0.42	-0.14	0.00
17.5	*v*	0.00	0.00	0.00	0.00	0.00	0.00	0.00	0.00	0.00	0.00	0.00	0.00	0.00	0.00
	u	0.00	0.00	0.00	0.00	0.00	0.00	0.00	0.00	0.00	0.00	0.00	0.00	0.00	0.00

Table B.7: Average velocity field over the PIV test window of 95 x 95 mm^2 for a single atomizer flow rate of 8.1 g/min.

		r (mm)													
z (mm)	Average velocity (m/s)	4.5	11.5	18.5	25.5	32.5	39.5	46.5	53.5	60.5	67.5	74.5	81.5	88.5	92.5
105.5	*v*	0.00	0.00	1.21	1.24	1.25	0.96	0.52	0.31	0.00	0.00	0.00	0.00	0.00	0.00
	u	0.00	0.00	-0.18	-0.34	-0.35	-0.30	-0.15	-0.07	0.00	0.00	0.00	0.00	0.00	0.00
98.5	*v*	0.00	0.00	1.18	1.22	1.23	1.07	0.61	0.34	0.00	0.00	0.00	0.00	0.00	0.00
	u	0.00	0.00	-0.19	-0.29	-0.43	-0.36	-0.23	-0.13	0.00	0.00	0.00	0.00	0.00	0.00
91.5	*v*	0.00	0.00	1.06	1.16	1.21	1.16	0.81	0.37	0.00	0.00	0.00	0.00	0.00	0.00
	u	0.00	0.00	-0.16	-0.36	-0.44	-0.46	-0.34	-0.18	0.00	0.00	0.00	0.00	0.00	0.00
84.5	*v*	0.00	0.00	0.92	1.00	1.16	1.22	0.99	0.54	0.00	0.00	0.00	0.00	0.00	0.00
	u	0.00	0.00	-0.13	-0.26	-0.44	-0.52	-0.44	-0.28	0.00	0.00	0.00	0.00	0.00	0.00
77.5	*v*	0.00	0.00	0.93	0.90	0.98	1.24	1.16	0.82	0.32	0.00	0.00	0.00	0.00	0.00
	u	0.00	0.00	-0.11	-0.19	-0.42	-0.56	-0.52	-0.38	-0.19	0.00	0.00	0.00	0.00	0.00
70.5	*v*	0.00	0.00	0.83	0.80	0.89	1.18	1.23	1.01	0.74	0.00	0.00	0.00	0.00	0.00
	u	0.00	0.00	-0.08	-0.16	-0.34	-0.62	-0.64	-0.51	-0.30	0.00	0.00	0.00	0.00	0.00
63.5	*v*	0.00	0.00	0.74	0.70	0.83	0.98	1.21	1.19	0.83	0.48	0.00	0.00	0.00	0.00
	u	0.00	0.00	-0.03	-0.11	-0.29	-0.58	-0.69	-0.67	-0.46	-0.21	0.00	0.00	0.00	0.00
56.5	*v*	0.00	0.00	0.31	0.29	0.34	0.89	1.01	1.19	1.11	0.60	0.00	0.00	0.00	0.00
	u	0.00	0.00	0.00	-0.05	-0.19	-0.45	-0.63	-0.71	-0.63	-0.38	0.00	0.00	0.00	0.00
49.5	*v*	0.00	0.00	0.00	0.00	0.00	0.66	0.94	1.05	1.22	0.93	0.39	0.00	0.00	0.00
	u	0.00	0.00	0.00	0.00	0.00	-0.22	-0.47	-0.67	-0.70	-0.50	-0.22	0.00	0.00	0.00
42.5	*v*	0.00	0.00	0.00	0.00	0.00	0.00	0.37	0.72	1.09	1.23	0.68	0.00	0.00	0.00
	u	0.00	0.00	0.00	0.00	0.00	0.00	-0.23	-0.47	-0.66	-0.62	-0.36	0.00	0.00	0.00
35.5	*v*	0.00	0.00	0.00	0.00	0.00	0.00	0.00	0.46	0.93	1.28	1.05	0.41	0.00	0.00
	u	0.00	0.00	0.00	0.00	0.00	0.00	0.00	-0.28	-0.50	-0.70	-0.52	-0.26	0.00	0.00
28.5	*v*	0.00	0.00	0.00	0.00	0.00	0.00	0.00	0.50	0.45	0.94	1.39	0.79	0.00	0.00
	u	0.00	0.00	0.00	0.00	0.00	0.00	0.00	-0.12	-0.29	-0.64	-0.68	-0.39	0.00	0.00
21.5	*v*	0.00	0.00	0.00	0.00	0.00	0.00	0.00	0.00	0.00	0.41	1.18	1.25	0.51	0.00
	u	0.00	0.00	0.00	0.00	0.00	0.00	0.00	0.00	0.00	-0.32	-0.77	-0.55	-0.24	0.00
17.5	*v*	0.00	0.00	0.00	0.00	0.00	0.00	0.00	0.00	0.00	0.00	0.00	0.00	0.00	0.00
	u	0.00	0.00	0.00	0.00	0.00	0.00	0.00	0.00	0.00	0.00	0.00	0.00	0.00	0.00

Appendix C.

C1. Bipolar charging parameter and results

The bipolar diffusion charging model, as presented in an open-source format by Woo et al. [182], was employed using the parameters provided in the Tables C.1 to C.4 below to determine the positive and negative ion concentrations for HABs ranging from 45 mm to 55 mm, which lead to the measured average charge per particle and charge fraction for both flames. In the charging model, the parameter for ion generation was neglected in order have proper modeling of the experimental result of this study. The proposed model by Roper [183] and Santoro et al. [184] was utilized to calculate the residence time (t) of flame-reacting flow between HABs. The average particle concentration and radius were determined by taking the average of the total particle concentration and particle radius obtained between each pair of adjacent HABs (for example, averaging the total particle concentration and radius between HAB 46 mm and HAB 47 mm, HAB 47 mm and HAB 48 mm, HAB 48 mm and HAB 49 mm, etc.). The temperature used in this work was measured by Moallemi et al. [84]. The initial ion mobility used in this study corresponds to the measured ion mobility in a methane flame by Wang et al. [196]. The positive and negative ions, with approximate mass values of 140 amu and 70 amu, respectively, as presented by Fialkov [190] and also utilized in Wang et al.'s [196] simulations of ion-particle and particle-particle combination coefficients, were employed in this study. The positive and negative ion concentrations obtained in this study were the assumed ion concentrations that resulted in the measured average charge per particle and charge fraction.

Two methods were explored to determine the average charge per particle, whether it is negative or positive, as presented in Tables C.1 to C.4. In the first method, the relative populations of negative and positive ions were adjusted while maintaining constant positive and negative ion mobilities to achieve the experimentally measured average charge per particle and charge fraction. This method is outlined in Tables C.1 and C.2 for methane-only and methane-NaCl flames. The assumed positive and negative ion concentrations for this method are physically realistic. In the second method, the positive and negative ion mobilities were continuously changed while preserving the ratio of positive and negative ion concentrations but altering the total ion concentration. The second method generates unrealistic mobility values to achieve the measured average charge per particle and charge fraction, as presented in Tables C.3 and C.4 for both flames. Figure C.1 illustrates the total ion concentration and ion mobility ratio for methane-only and methane-NaCl flames across their HABs.

Table C.1: Parameters used to determine the ion concentration for methane-only case within the range of HABs 45 to 55 mm. Positive and negative ion mobilities were kept constant and the positive and negative ion concentrations were changed.

	HABs	**45**	**46**	**47**	**48**	**49**	**50**	**52.5**	**55**
Calculated Values	Time between HABs (s)	0.00066	0.00066	0.00065	0.00064	0.00064	0.00156	0.00153	0.00149
Measured Values	Average Particle Concentration (m^{-3})	1.73E+18	1.32E+18	6.26E+17	2.17E+17	1.24E+17	3.95E+16	2.90E+16	1.81E+16
	Temperature (K)	1708.83	1719.33	1758.27	1788.47	1810.47	1836.31	1868.48	1892.79
	Average radius (nm)	4.57	5.09	7.32	9.75	10.85	11.98	13.34	11.36
	Charge Fraction	0.04	0.21	0.32	0.43	0.49	0.51	0.55	0.58
	Average charge per particle	0.01	–0.01	–0.01	–0.01	–0.02	–0.04	–0.03	–0.07
Assumed Values	N_{+i} (m^{-3})	4.90E+14	1.38E+15	8.51E+14	6.98E+14	5.68E+14	5.90E+13	1.48E+14	1.52E+14
	N_{-i} ($/m^3$)	2.10E+14	1.22E+15	5.99E+14	5.02E+14	4.32E+14	6.10E+13	1.03E+14	1.58E+14
	ion mobility (+) ($m^2/V/s$)	1.54E-04	1.54E-04	1.54E-04	1.54E-04	1.54E-04	1.54E-04	1.54E-04	1.54E-04
	ion mobility (–) ($m^2/V/s$)	1.97E-04	1.97E-04	1.97E-04	1.97E-04	1.97E-04	1.97E-04	1.97E-04	1.97E-04
	Ratio of ion mobility z–/z+	1.28	1.28	1.28	1.28	1.28	1.28	1.28	1.28
Known Values	ion Mass (+) (amu)	140	140	140	140	140	140	140	140
	ion Mass (–) (amu)	70	70	70	70	70	70	70	70

Table C.2: Parameters used to determine the ion concentration for methane-NaCl case within the range of HABs 45 to 55 mm. Positive and negative ion mobilities were kept constant and the positive and negative ion concentrations were changed.

	HABs	**45**	**46**	**47**	**48**	**49**	**50**	**52.5**	**55**
Calculated Values	Time between HABs (s)	0.00066	0.00066	0.00065	0.00064	0.00064	0.00156	0.00153	0.00149
Measured Values	Average Particle Concentration (/m^3)	1.86E+18	1.59E+18	9.78E+17	5.66E+17	2.84E+17	7.44E+16	6.68E+16	5.77E+16
	Temperature (K)	1708.83	1719.33	1758.27	1788.47	1810.47	1836.31	1868.48	1892.79
	Average radius (nm)	4.15	4.46	6.16	8.56	9.84	10.71	11.28	9.52
	Charge Fraction	0.04	0.14	0.17	0.20	0.22	0.27	0.30	0.33
	Average charge per particle	0.04	0.04	0.04	0.05	0.04	0.04	0.03	0.03
Assumed Values	N_{+i} (/m^3)	8.31E+14	1.08E+15	2.67E+14	1.32E+14	7.99E+13	6.76E+13	3.28E+13	7.08E+13
	N_{-i} (/m^3)	4.38E+13	7.56E+14	1.44E+14	6.76E+13	7.01E+13	5.24E+13	3.22E+13	4.72E+13
	ion mobility (+) (m^2/V/s)	1.54E-04	1.54E-04	1.54E-04	1.54E-04	1.54E-04	1.54E-04	1.54E-04	1.54E-04
	ion mobility (–) (m^2/V/s)	1.97E-04	1.97E-04	1.97E-04	1.97E-04	1.97E-04	1.97E-04	1.97E-04	1.97E-04
	Ratio of ion mobility z–/z+	1.28	1.28	1.28	1.28	1.28	1.28	1.28	1.28
Known Values	ion Mass (+) (amu)	140	140	140	140	140	140	140	140
	ion Mass (–) (amu)	70	70	70	70	70	70	70	70

Table C.3: Parameters used to determine the ion concentration for methane-only case within the range of HABs 45 to 55 mm. Positive and negative ion concentrations were kept constant for each HAB and the positive and negative ion mobilities were changed.

	HABs	**45**	**46**	**47**	**48**	**49**	**50**	**52.5**	**55**
Calculated Values	Time between HABs (s)	0.00066	0.00066	0.00065	0.00064	0.00064	0.00156	0.00153	0.00149
Measured Values	Average Particle Concentration (/m^3)	1.73E+18	1.32E+18	6.26E+17	2.17E+17	1.24E+17	3.95E+16	2.90E+16	1.81E+16
	Temperature (K)	1708.83	1719.33	1758.27	1788.47	1810.47	1836.31	1868.48	1892.79
	Average radius (nm)	4.57	5.09	7.32	9.75	10.85	11.98	13.34	11.35
	Charge Fraction	0.03	0.21	0.32	0.43	0.49	0.51	0.55	0.58
	Average charge per particle	0.01	–0.01	–0.01	–0.01	–0.02	–0.04	–0.03	–0.07
Assumed Values	N_{+i} (/m^3)	3.47E+14	1.52E+15	9.50E+14	7.50E+14	7.00E+14	2.50E+13	1.40E+14	1.45E+14
	N_{-i} (/m^3)	3.47E+14	1.52E+15	9.50E+14	7.50E+14	7.00E+14	2.50E+13	1.40E+14	1.45E+14
	ion mobility (+) (m^2/V/s)	1.54E-04	1.54E-04	1.54E-04	1.54E-04	1.54E-04	1.54E-04	1.54E-04	1.54E-04
	ion mobility (–) (m^2/V/s)	6.70E-06	2.70E-05	2.20E-05	3.00E-05	3.40E-05	2.50E-02	3.65E-05	1.45E-02
	Ratio of ion mobility z–/z+	0.04	0.18	0.14	0.19	0.22	162.34	0.24	94.16
Known Values	ion Mass (+) (amu)	140	140	140	140	140	140	140	140
	ion Mass (–) (amu)	70	70	70	70	70	70	70	70

Table C.4: Parameters used to determine the ion concentration for methane-NaCl case within the range of HABs 45 to 55 mm. Positive and negative ion concentrations were kept constant for each HAB and the positive and negative ion mobilities were changed.

	HABs	**45**	**46**	**47**	**48**	**49**	**50**	**52.5**	**55**
Calculated Values	Time between HABs (s)	0.00066	0.00066	0.00065	0.00064	0.00064	0.00156	0.00153	0.00149
Measured Values	Average Particle Concentration ($/m^3$)	1.86E+18	1.59E+18	9.78E+17	5.66E+17	2.84E+17	7.44E+16	6.68E+16	5.77E+16
	Temperature (K)	1708.83	1719.33	1758.27	1788.47	1810.47	1836.31	1868.48	1892.79
	Average radius (nm)	4.15	4.46	6.16	8.56	9.84	10.71	11.28	9.52
	Charge Fraction	0.04	0.14	0.17	0.20	0.22	0.27	0.30	0.33
	Average charge per particle	0.04	0.04	0.04	0.05	0.04	0.04	0.03	0.03
Assumed Values	N_{+i} ($/m^3$)	2.50E+14	6.00E+14	1.25E+14	6.00E+13	7.00E+13	5.00E+13	3.00E+13	4.50E+13
	N_{-i} ($/m^3$)	2.50E+14	6.00E+14	1.25E+14	6.00E+13	7.00E+13	5.00E+13	3.00E+13	4.50E+13
	Ion mobility (+) ($m^2/V/s$)	2.94E-02	1.84E-02	2.24E-02	3.02E-02	1.72E-02	2.22E-02	8.20E-03	2.12E-02
	Ion mobility (–) ($m^2/V/s$)	1.70E-06	1.17E-02	1.17E-02	1.07E-02	1.07E-02	1.07E-02	1.07E-02	1.07E-02
	Ratio of ion mobility z–/z+	0.000058	0.64	0.52	0.35	0.62	0.48	1.30	0.50
Known Values	Ion Mass (+) (amu)	140	140	140	140	140	140	140	140
	Ion Mass (–) (amu)	70	70	70	70	70	70	70	70

Figure C.1 shows the total ion concentration and ion mobility ratio for both methane-only and methane-NaCl flames, spanning from HABs of 45 mm to 55 mm. The figure highlights that the ion population in the methane-only flame is greater than that in the methane-NaCl flame for HABs 48 mm, 49 mm, and 55 mm. However, the reverse is true for all the other HABs. Additionally, it's noteworthy that for both flames, the concentration of positive ions exceeds that of negative ions. Nevertheless, it should be noted that these results may not be accurate due to the unrealistic values of ion mobility for the HABs. This discrepancy, in conjunction with the data presented in Tables C.3 and C.4 above, underscores the challenge of maintaining consistent positive and negative ion concentrations solely by adjusting ion mobility to achieve the desired average charge per particle.

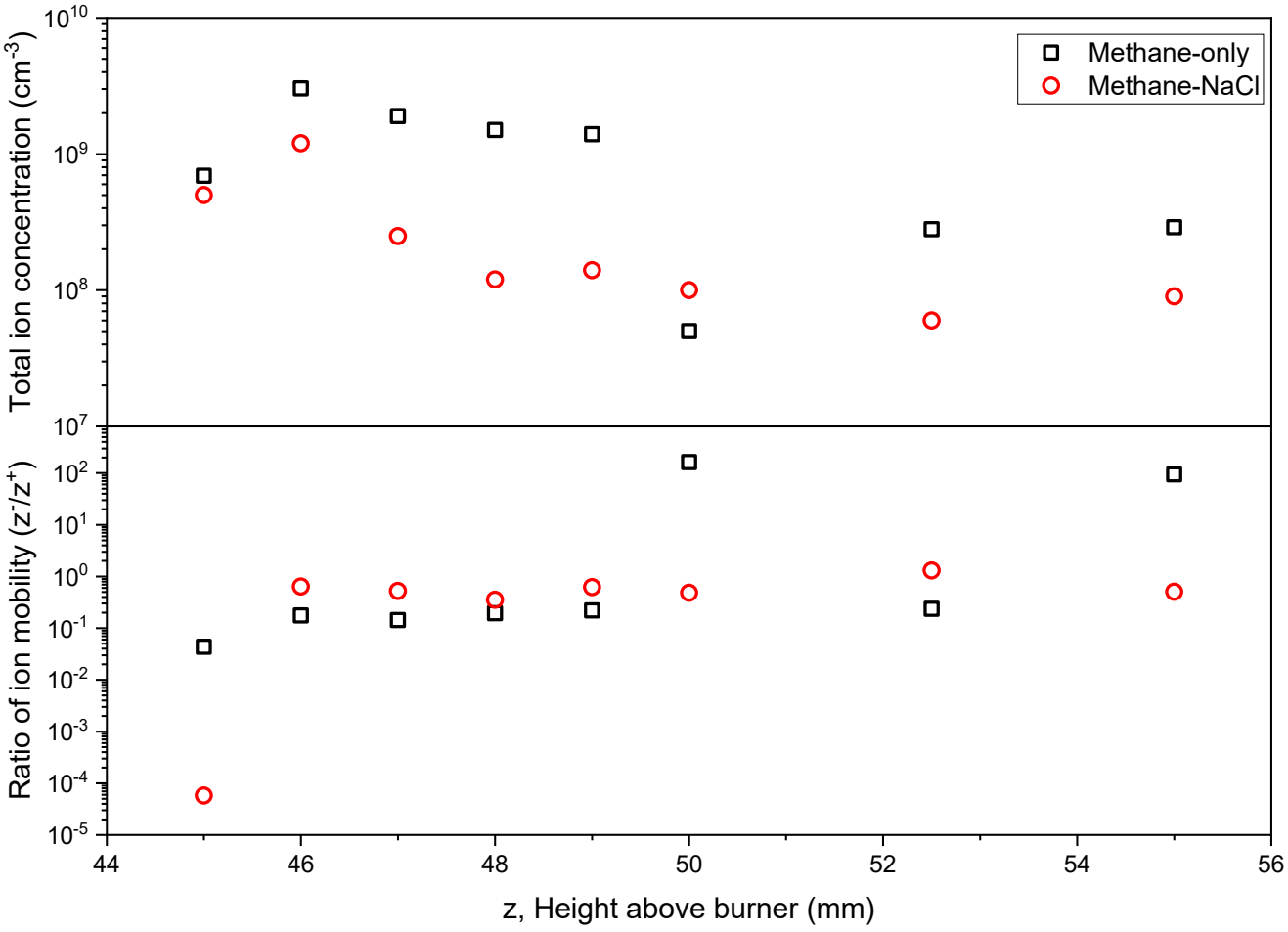

Figure C.1: The total ion concentration and ion mobility ratio for methane-only and methane-NaCl flames with their corresponding HABs

C2. Validation of Fuchs stability function

Figure C.2 shows the digitized result of Fig. 1 in Adachi et al. [110] which is the effect of coulomb force on the ratio coagulation function of charged particles to Brownian coagulation function of uncharged particles ($\beta_{p,q}$). The colliding particles are of the same size and have different charge states. The result was digitized by using GetData Graph Digitizer software (version 2.26.0.20). The reason for digitizing the result is so that it can be compared with the one generated using the model used in this work. Reproducing this result proved to us that the Fuchs stability function ($\beta_{p,q}$) is properly modeled, that is, the collision of particles is modeled well. Figure C.3 shows the reproduced Adachi et al.'s [110] result and Figure C.4 reveals the comparison between the digitized and the reproduced figures.

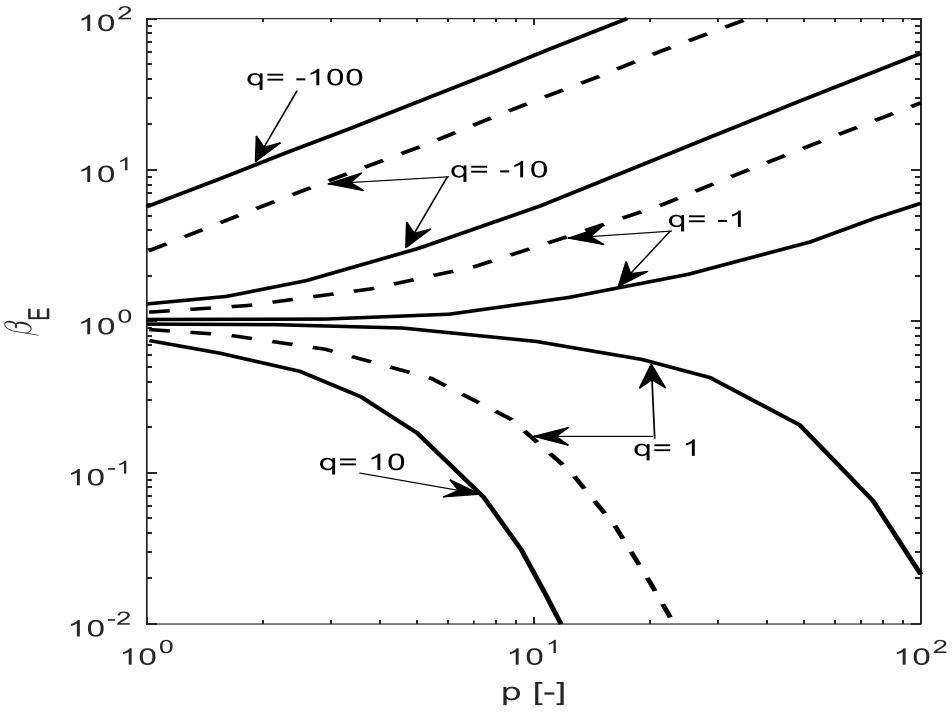

Figure C.2: The digitized result of Adachi et al. [110] for the influence of the Fuchs stability function under various charge conditions, between two particles of equal size.

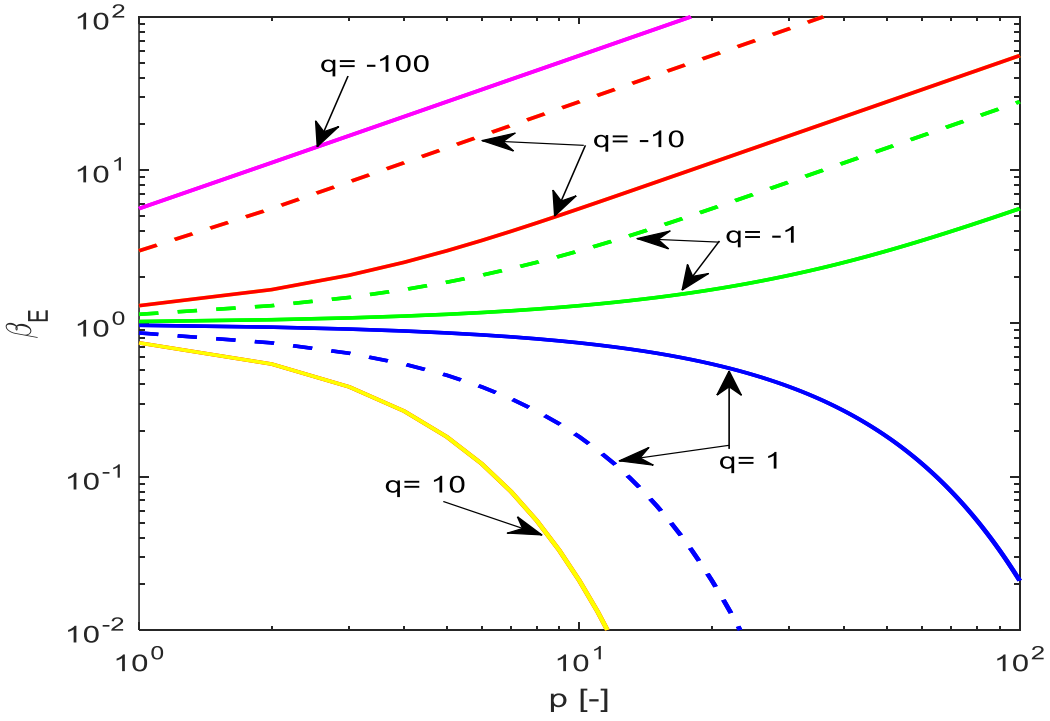

Figure C.3: The reproduced result of Adachi et al. [110] for the influence of the Fuchs stability function under various charge conditions, between two particles of equal size.

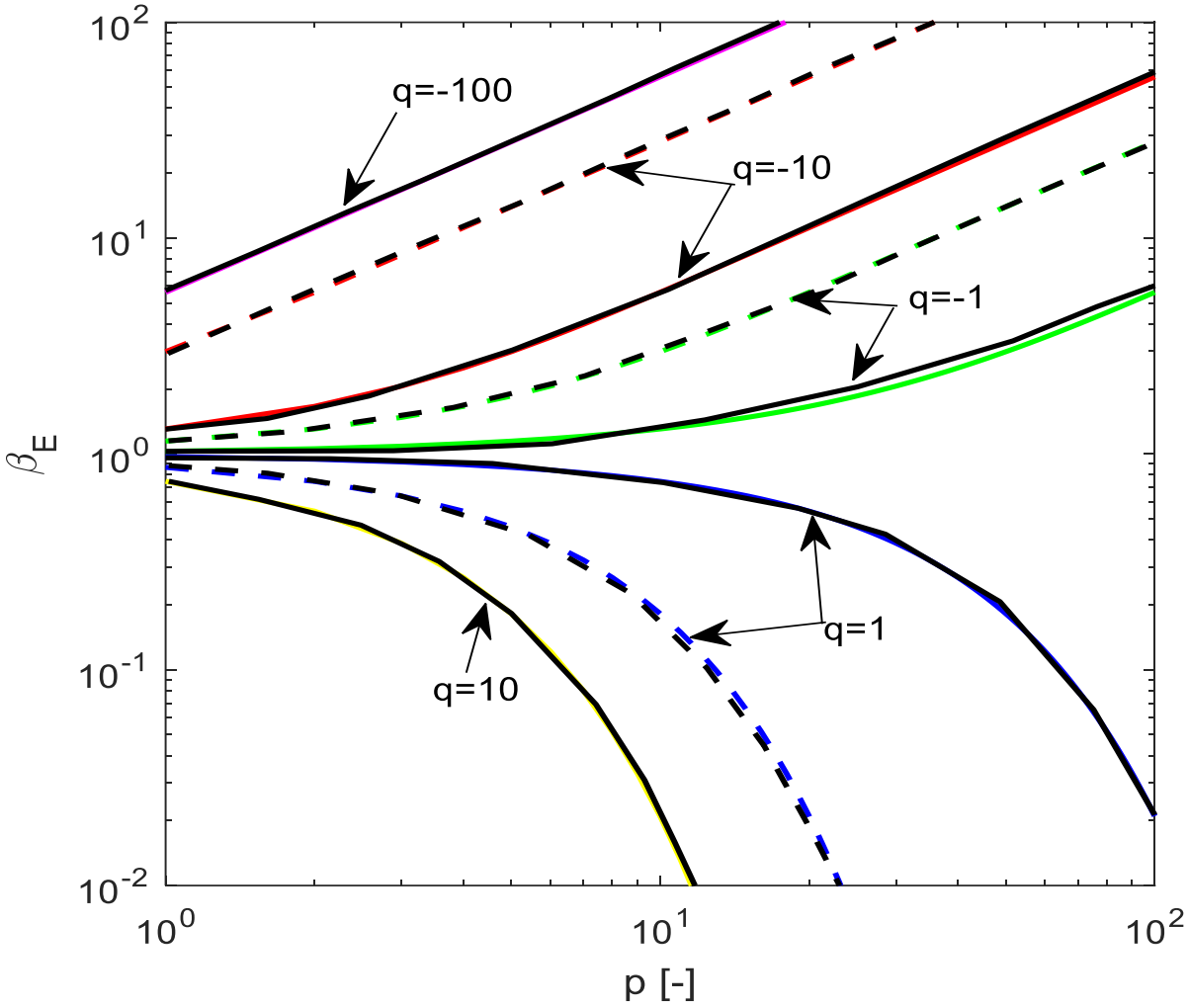

Figure C.4: Reproduced and digitized results for the influence of the Fuchs stability function under various charge conditions, between two particles of equal size.

Figure C.5 shows the effect of electrostatic to thermal energy ratio on colliding aerosol particles. The colliding particles are of the same size and have different charge states. The bottom section of the figure reveals the coagulation of charged particles with the same sign (repulsive electric force), which results in a reduction in particle coagulation rate. The top section of the figure, on the other hand, shows the coagulation of charged particles with the opposite sign (attractive electric force), leading to increased particle coagulation rate. The figure also reveals a conflicting relationship between particle size and the number of charges carried by a particle. A particle of 0.1 μm size and $q = -1$, for example, has higher mobility and coagulation rate than a particle of 1 μm size and $q = -10$. This demonstrates that size has a substantial impact on the coagulation of charged particles.

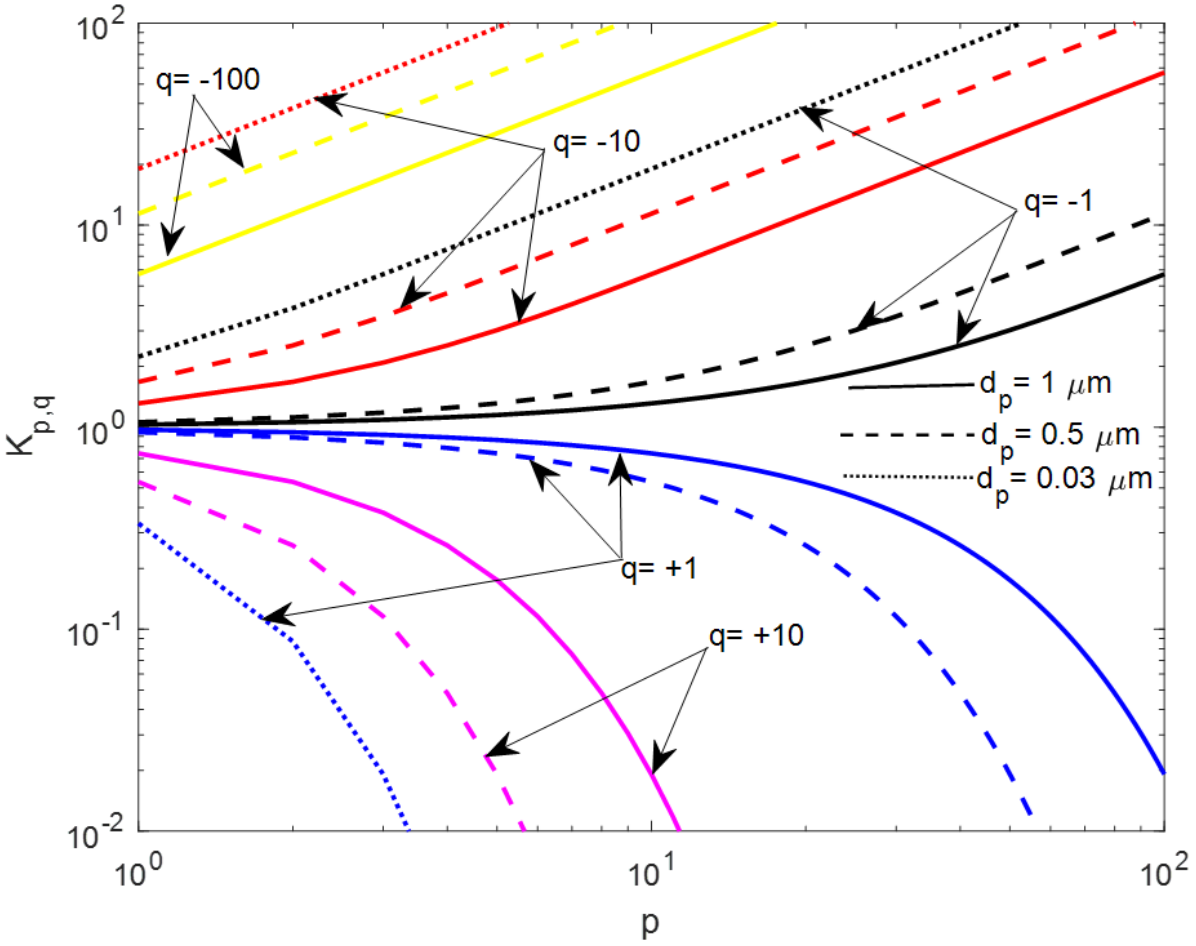

Figure C.5: The influence of the Fuchs stability function under various charge conditions, between two particles of equal size.

C3. Brownian coagulation coefficient

Figure C.6 shows the coagulation coefficient of a Brownian coagulation of two charged particles of same size but different or same elementary charge. The plot for the Fuchs stability function for the same range of particle sizes is presented in main body of this work. The coagulation coefficient for the collision of opposite charge particles increase with charges but decreases with increase in the size of the particle. But, the coagulation coefficient for the collision of same charge particles

decreases with increase in number of charges on particles. And the coagulation coefficient of particles of same charge decrease faster with size i.e. the coagulation coefficient of smaller particle sizes decreases faster than bigger particles.

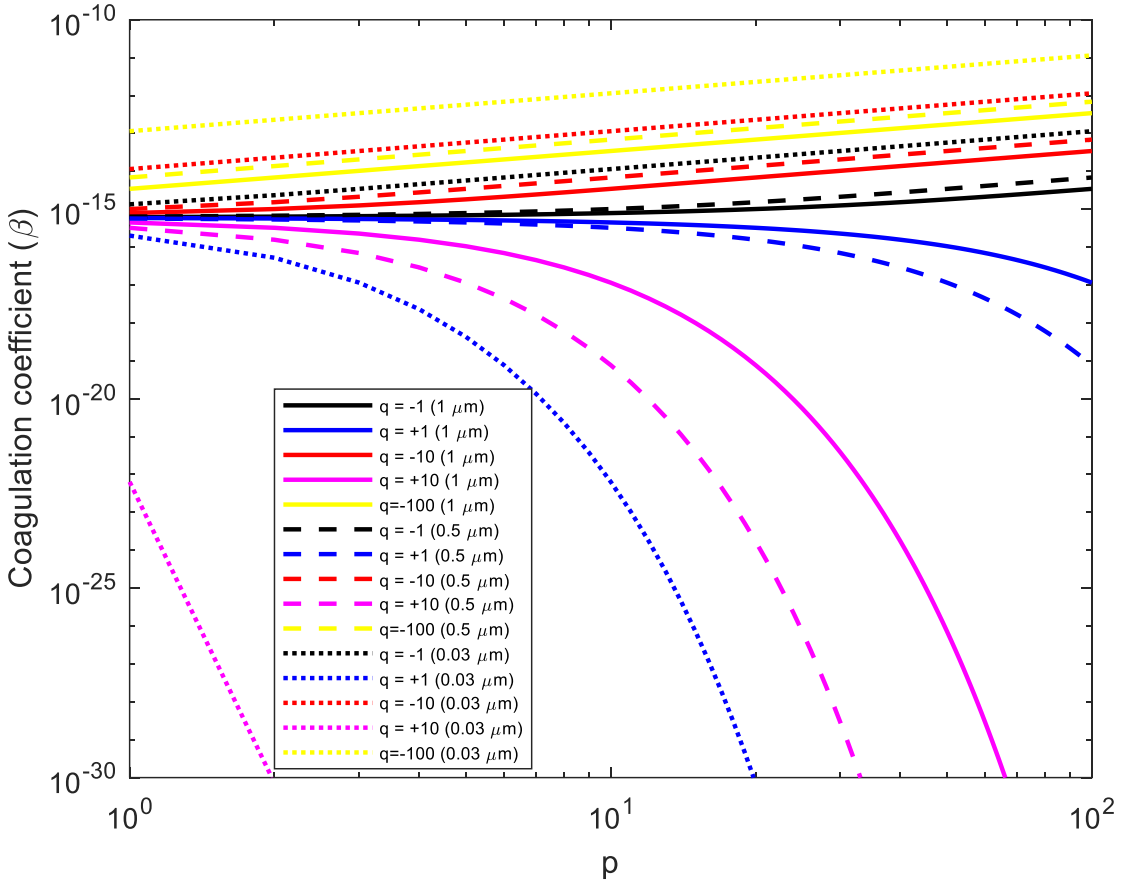

Figure C.6: Brownian coagulation coefficient of charged particles.

C4. Validation of coagulation rate result

In order to be sure that the model used in this work follows an existing model, the Fig. 6a result of Vemury et al. [178] was digitized using GetData Graph Digitizer software (version 2.26.0.20) and the digitized result is presented in Fig. C.7 below. The model used in this work as discussed in the

body of this work was used to reproduce the Vemury et al.'s [178] result and it is presented in Fig. C.8. However, the reproduced result was placed on the digitized result, and it is shown in Fig. C.9.

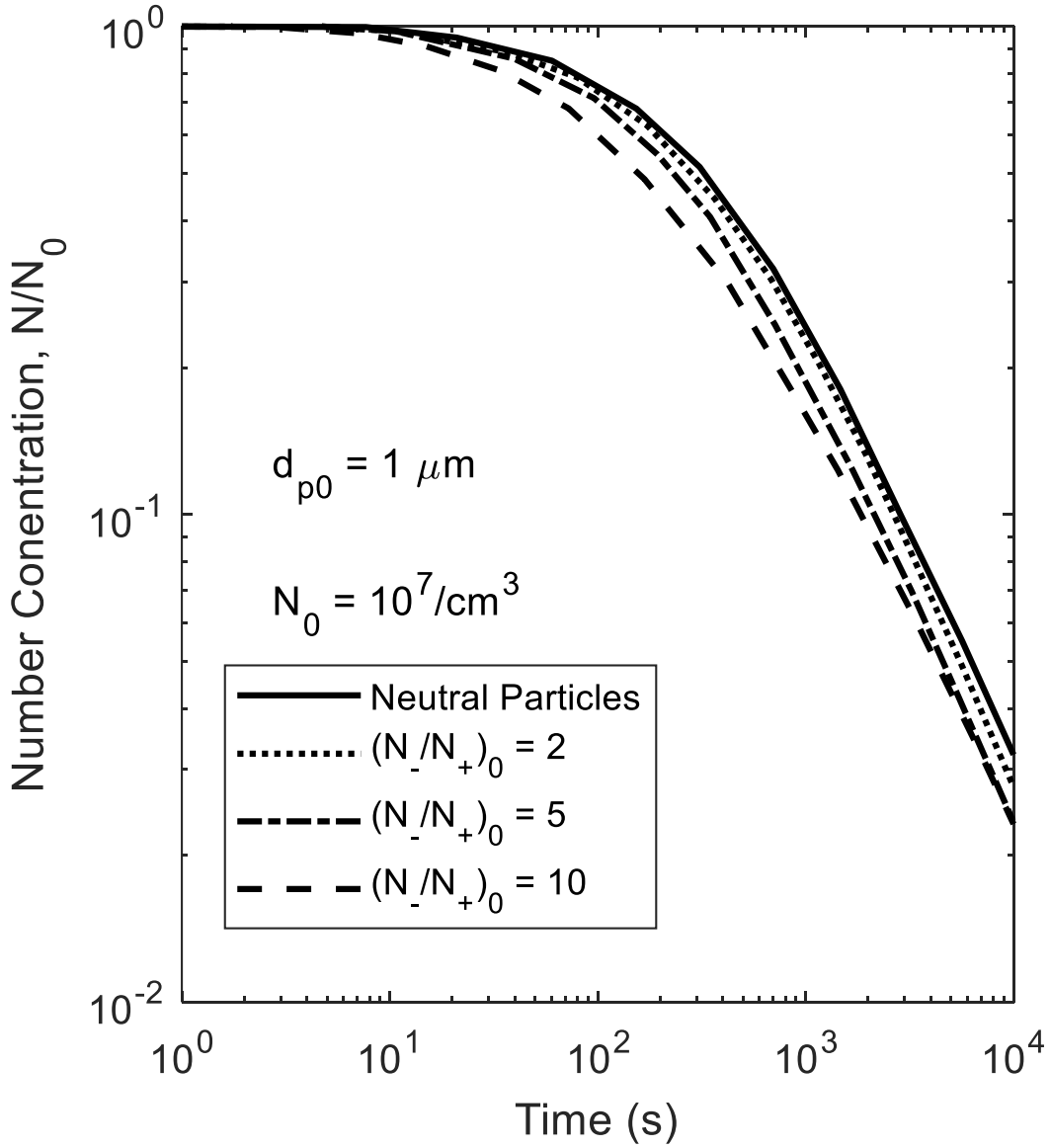

Figure C.7: Digitized result for the rate of change of particle number concentration with time [178].

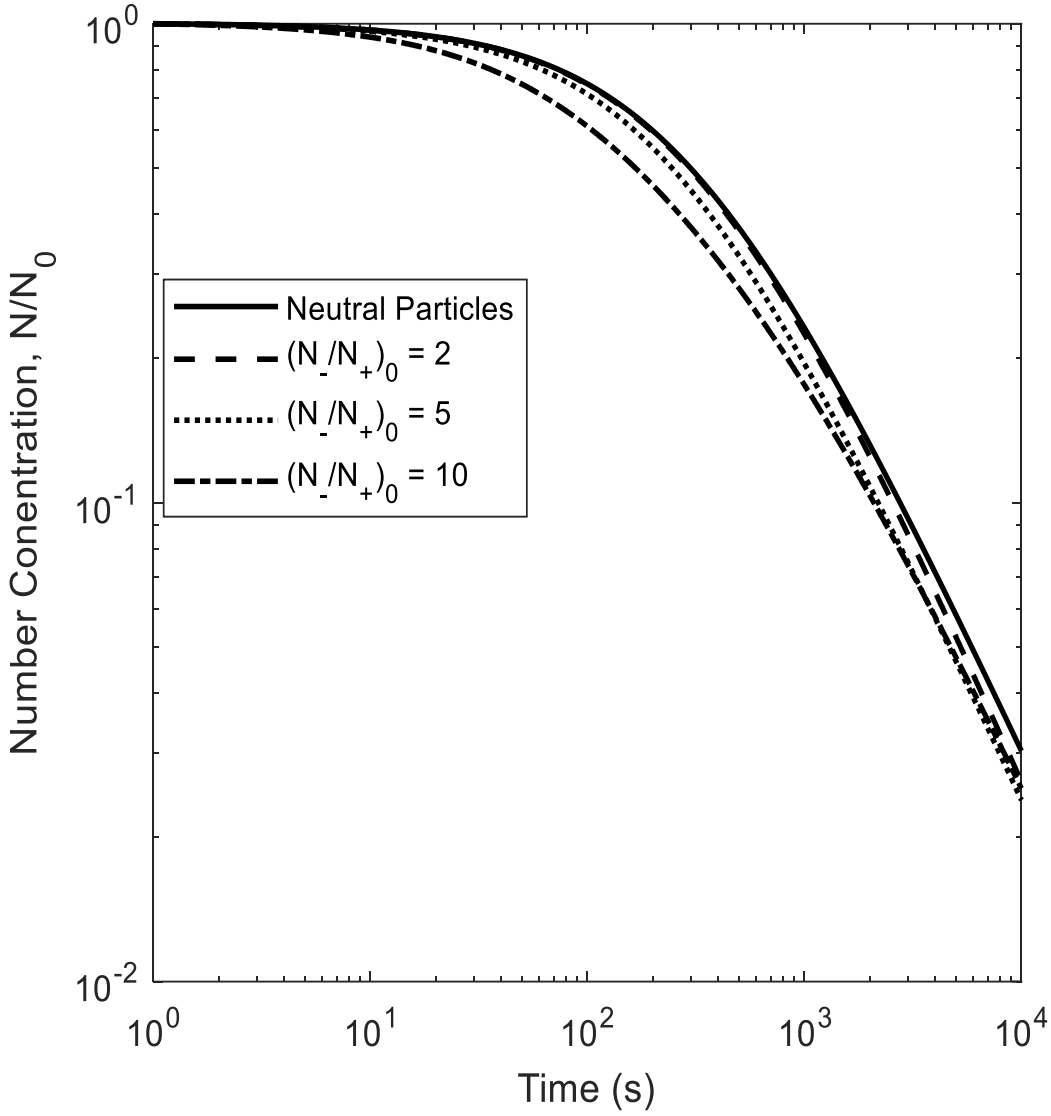

Figure C.8: Reproduced result for the rate of change of particle number concentration with time (adopted from [178])

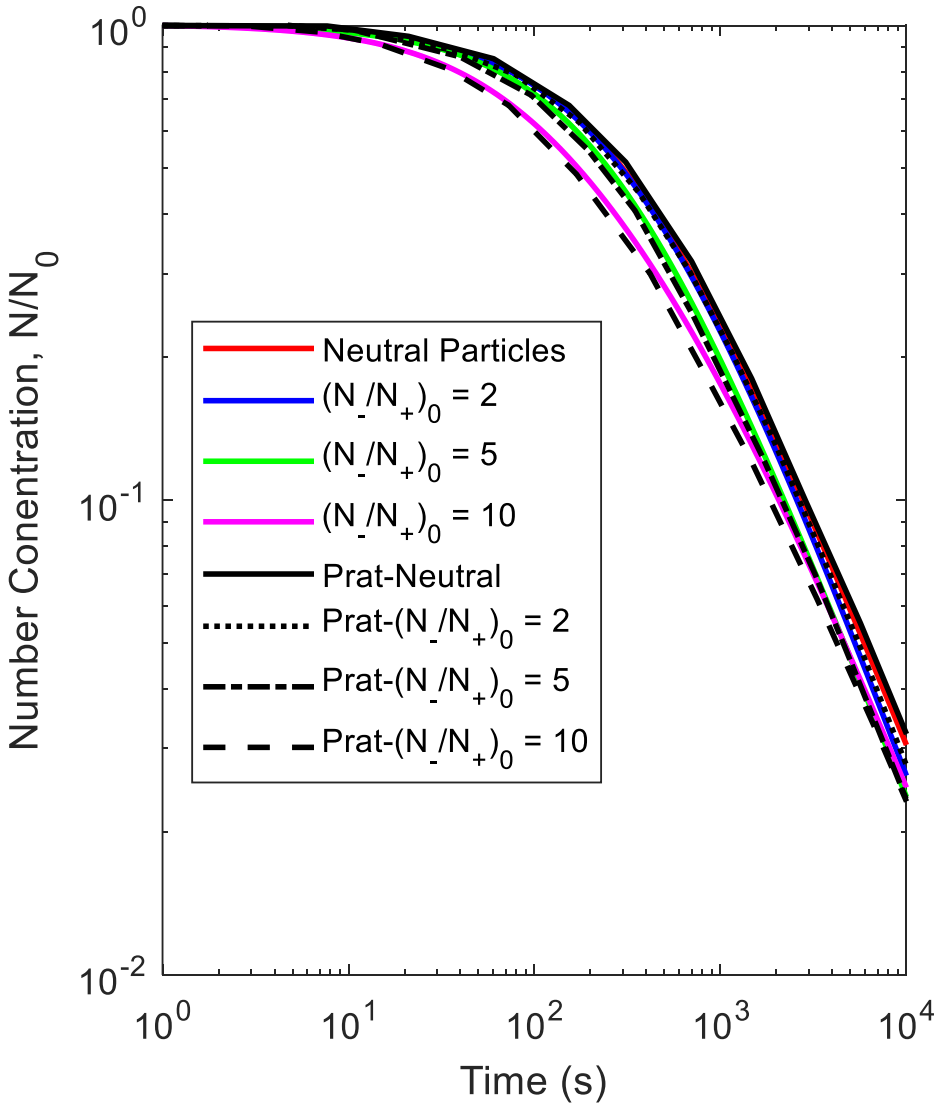

Figure C.9. Reproduced and digitized results for the rate of change of particle number concentration with time

C5. Comparison between the model and experimental results

Figure C.10 presents a comparison between the model predictions and the experimental measurements regarding changes in particle number concentrations, particle median diameter, average charge per particle, and charge fraction at their respective HABs. When calculating the changes in number concentration and median diameter, the distribution of charges for each iteration was not forced to mimic the experimental trend; rather, the experimental values were employed as the initial conditions for each HAB. The manner in which the model distributes charged particles for each iteration based on the particle charge fraction and average charge per particle is illustrated in Figs. C.10c and C.10d. The outcomes concerning changes in number concentration and median diameter with spatial points are consistent with those presented in the main body of this work (Figs. 4.5), where the charge state of the particles for each iteration was forced to emulate the experimental results.

However, the model's ability to predict the change in average charge per particle with spatial point did not align well with the experimental results for the methane-only cases. Nevertheless, it seemed to reasonably predict the experimental results for the methane-NaCl cases only from HAB 50 to 55 mm (Fig.C.10c). Similarly, the model's prediction for the change in charge fraction was in good agreement with the experimental results for methane-NaCl cases within the range, while for the methane-only cases, the model successfully matched the experimental results (Fig. C.10d). Hence, the resemblance of results observed between Figs. 4.5 and Figs. C.10a & C.10b suggests that the charge state of the particles did not significantly impact the coagulation rate of the particles. This lack of impact can be attributed to the initial elementary charge on particles considered in this work, which includes +1, −1, and 0 charges.

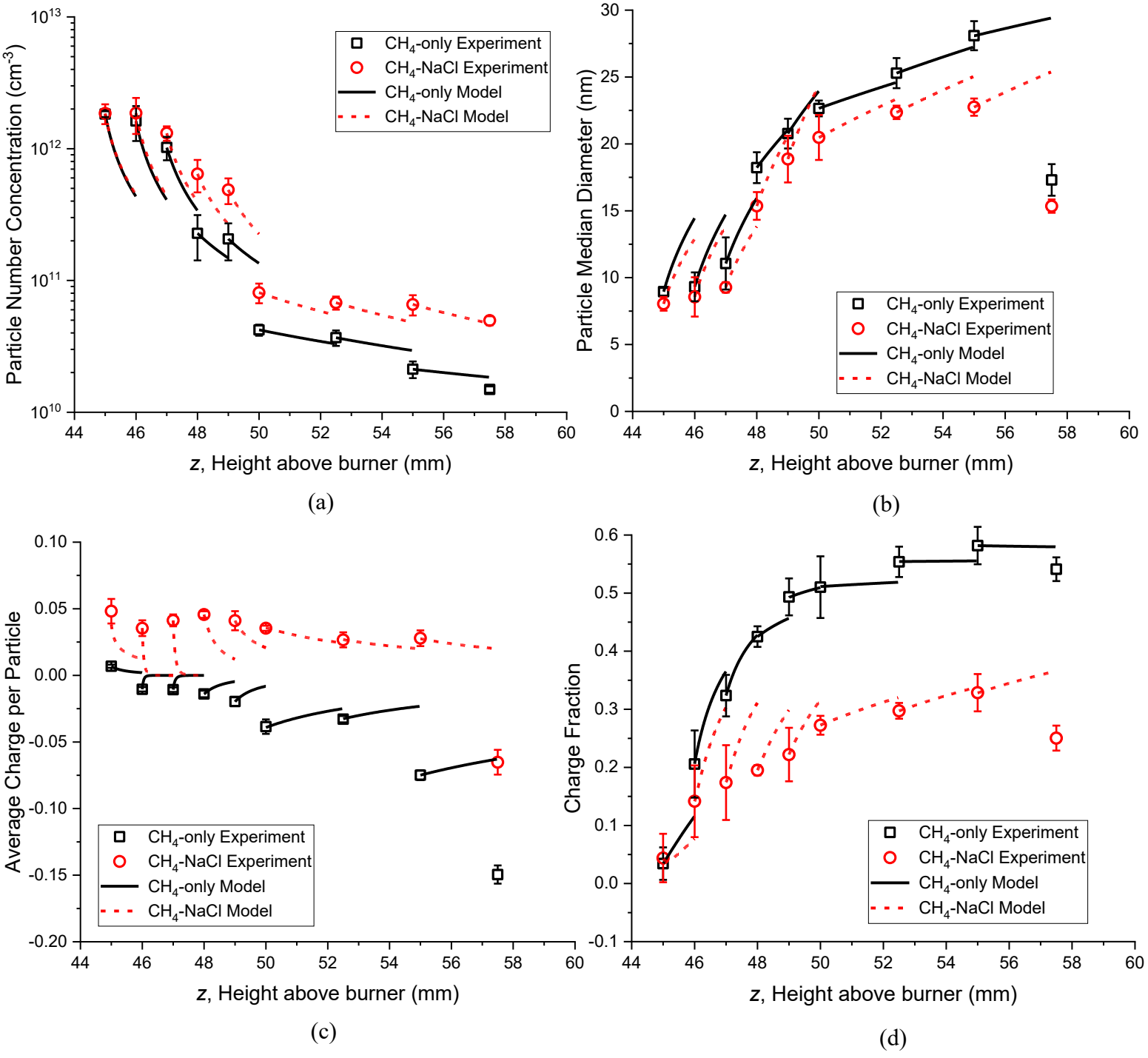

Figure C.10: (a) Change of particle number concentration, (b) change of particle median diameter, (c) change of average charge per particle, and (d) change of charge fraction, for methane-only and

methane-NaCl flames with their corresponding *HAB*s ranging from 30 to 60 mm. This is for the case whereby the charge distribution for each model iteration is not adjusted to suit the experimental result

Figure C.11 shows the change of each elementary charge number concentration (i.e., N_{-1}, N_{+1}, and N_0) with respect to their corresponding HABs. The reason why this is shown is because of all our results of change in total particle number concentration with space. This is to see the rate at which each elementary charged particles are decreasing with space. Figure C.11a shows the change of each elementary charge number concentration with space for methane-only cases. The result reveals that the coagulation rate of neutrally charged particles are faster than other charges from HAB 45 to 50 mm and from HAB 50 to 55 mm all particles seem to be coagulating at the same rate while from HAB 55 to 57.5 mm which is start of oxidation region, the coagulation rate of positively charged particles become more faster than the negatively and the neutrally charged ones. In addition, the result shows that there are more neutrally charged particles than positively and negatively charged particles for all HABs. It can also be seen from the result that negatively charged particles are more than positively charged particles for all HABs. The model results predict the experimental results well except for HAB 49 to 50 mm where the law of conservation of mass seem not to hold.

Figure C.11b shows the change of each elementary charge number concentration with spatial point for methane-NaCl cases. The result explained for the methane-only cases is also applicable here only that in this case the positively charged particles are more than the negatively charged particles ones because it seems that the sodium ion of the injected NaCl particle is fast neutralizing the negatively charged particles. Also, model results for HAB 47 to 50 mm fail to properly predict the

experimental results. The model results consistently overestimated the experimental results for these ranges. This could be assumed that NaCl in the system dissociates at high temperature to form sodiu and chloride ions which might quickly react with charged soot particles thereby preventing coagulation as presented by the model.

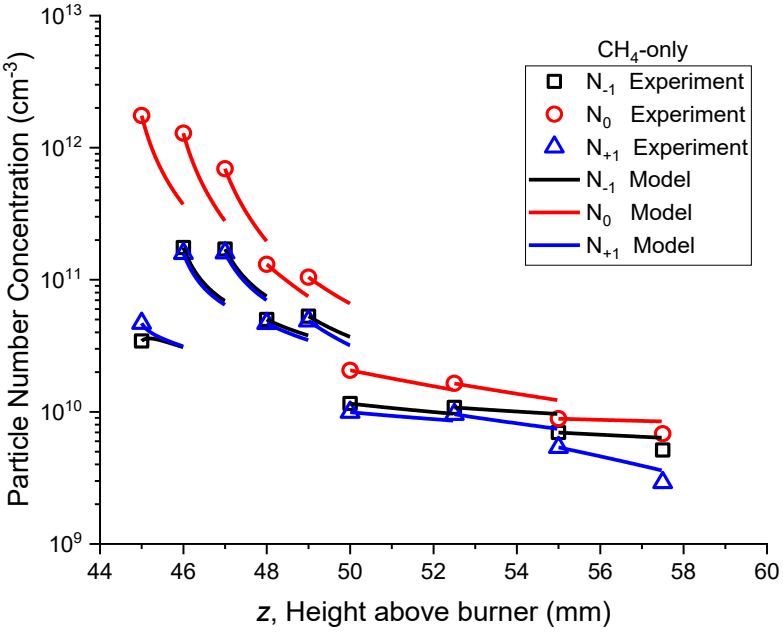

(a)

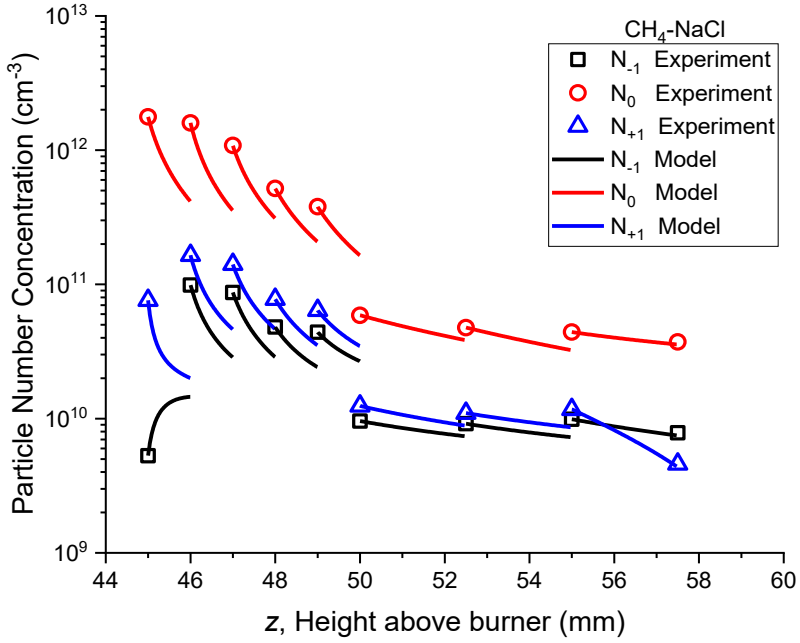

(b)

Figure C.11: The comparison between the experimental and model results for the change of each elementary charge number concentration with spatial points for (a) methane-only and (b) methane-NaCl cases. This is for the case whereby the charge distribution for each model iteration is adjusted to suit the experimental result

Figure C.12 shows the comparison between the model prediction and the experimental measurements of change in particle number concentrations and particle median diameter with their corresponding HABs. In this scenario, the initial conditions (Particle number concentration) for each HABs were neutral, that is, the total concentrations for each HABs were considered to be neutral. The results in Fig C.12 were much similar to the one in Fig. 4.5 of the main body of this work, and this shows that neutrally charged particles play a significant role in the coagulation rate of particles.

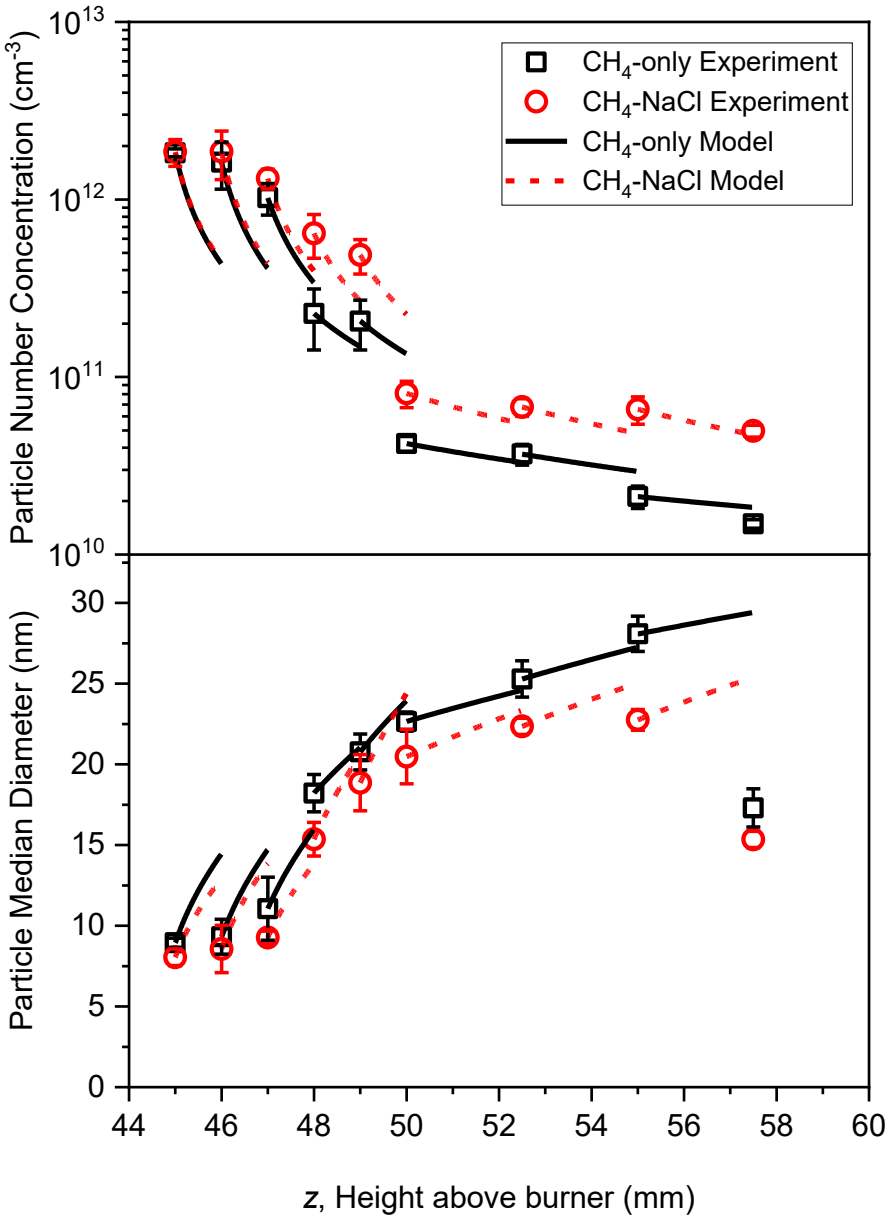

Figure C.12: Change of particle number concentration, and particle median diameter, for methane-only and methane-NaCl flames with their corresponding *HAB*s ranging from 45 to 57.5 mm. This is for the case whereby all the initially specified particles for each HABs were considered to be neutral

C6. Experimental data

The total concentration was obtained using the 1-nm SMPS experimental setup, while the charge fraction and the average charge per particle were obtained using the charged state experimental setup as indicated in the body of this work. All the experimental data are presented in tables below.

Table C.5: Experimental test conditions of total concentration for methane-only and methane-NaCl case within the range of HAB 30 to 60 mm.

HAB (mm)	Total Conc. CH_4 (cm^{-3})	Error	Total Conc. CH_4-NaCl (cm^{-3})	Error
30	1.30E+13	5.12E+12	6.87E+12	2.29E+12
35	6.47E+12	2.52E+12	5.50E+12	3.95E+11
40	2.58E+12	3.63E+11	2.36E+12	4.50E+11
45	1.85E+12	1.38E+11	2.12E+12	4.06E+11
46	1.56E+12	3.19E+11	1.64E+12	1.67E+11
47	7.92E+11	2.01E+11	1.24E+12	2.18E+11
48	3.29E+11	1.37E+11	6.30E+11	1.31E+11
49	2.20E+11	9.49E+10	4.67E+11	7.97E+10
50	4.23E+10	7.13E+09	8.86E+10	1.78E+10
52.5	3.63E+10	7.04E+09	7.58E+10	1.80E+10
55	2.45E+10	5.03E+09	6.99E+10	1.50E+10
57.5	1.48E+10	2.69E+09	5.22E+10	9.29E+09
60	9.76E+09	2.28E+09	3.79E+10	5.99E+09

Table C.6: Experimental test conditions of count median diameter for methane-only and methane-NaCl case within the range of HAB 30 to 60 mm.

HAB (mm)	CMD CH_4 (nm)	Error	CMD CH_4-NaCl (nm)	Error
30	2.1446	0.1054	2.9187	0.2572
35	2.8128	0.3116	3.5587	1.0007
40	5.9753	0.4684	6.2767	0.6465
45	8.8727	0.5281	8.7013	0.7876
46	9.0697	1.4492	9.0058	1.0665
47	11.1202	0.3646	9.1729	0.3191
48	17.0619	1.9890	14.9934	0.2394
49	19.0337	2.4582	18.4312	1.7569
50	22.0358	0.9186	19.8210	0.4009
52.5	24.5688	0.9768	21.0147	0.8150
55	28.0832	0.1889	22.2466	0.0936
57.5	18.8164	0.8233	15.2751	0.5637
60	12.5372	1.1404	8.1161	0.8669

Table C.7: Model initial conditions of charged particle number concentration for methane-only and methane-NaCl case within the coagulation and the start of oxidation region being from HAB 47 to 57.5 mm.

HAB (mm)	CH_4 N_0 (cm^{-3})	CH_4 N_{-1} (cm^{-3})	CH_4 N_{+1} (cm^{-3})	CH_4-NaCl N_0 (cm^{-3})	CH_4-NaCl N_{-1} (cm^{-3})	CH_4-NaCl N_{+1} (cm^{-3})	Total Conc. CH_4 (cm^{-3})	Total Conc. CH_4-NaCl (cm^{-3})
45	1.75E+12	3.44E+10	4.69E+10	1.77E+12	5.30E+09	7.61E+10	1.83E+12	1.85E+12
46	1.29E+12	1.76E+11	1.59E+11	1.60E+12	9.88E+10	1.65E+11	1.62E+12	1.86E+12
47	6.92E+11	1.71E+11	1.60E+11	1.08E+12	8.71E+10	1.41E+11	1.02E+12	1.31E+12
48	1.31E+11	5.00E+10	4.68E+10	5.18E+11	4.81E+10	7.75E+10	2.28E+11	6.44E+11
49	1.05E+11	5.30E+10	4.89E+10	3.79E+11	4.41E+10	6.41E+10	2.07E+11	4.87E+11
50	2.06E+10	1.14E+10	1.02E+10	5.89E+10	9.59E+09	1.25E+10	4.22E+10	8.09E+10
52.5	1.64E+10	1.08E+10	9.60E+09	4.77E+10	9.18E+09	1.10E+10	3.68E+10	6.78E+10
55	8.88E+09	6.97E+09	5.38E+09	4.42E+10	9.89E+09	1.17E+10	2.12E+10	6.58E+10
57.5	6.84E+09	5.14E+09	2.92E+09	3.72E+10	7.84E+09	4.60E+09	1.49E+10	4.97E+10

Table C.8: Experimental test conditions of average charge per particle for methane-only and methane-NaCl case within the range of HAB 30 to 60 mm.

	CH4-only		CH4-NaCl	
HAB	Average Charge per Particle	Error	Average Charge per Particle	Error
30	0.0391	0.0019	0.0299	0.0040
35	0.0141	0.0010	0.0316	0.0008
40	0.0115	0.0005	0.0214	0.0034
45	0.0068	0.0012	0.0482	0.0092
46	-0.0104	0.0017	0.0354	0.0059
47	-0.0107	0.0017	0.0434	0.0036
48	-0.0140	0.0025	0.0456	0.0025
49	-0.0197	0.0032	0.0410	0.0072
50	-0.0385	0.0055	0.0354	0.0019
52.5	-0.0329	0.0024	0.0267	0.0057
55	-0.0750	0.0037	0.0279	0.0059
57.5	-0.1495	0.0068	-0.0652	0.0093
60	-0.2251	0.0107	-0.1749	0.0180

Table C.9: Experimental test conditions of charge fraction for methane-only and methane-NaCl case within the range of HAB 30 to 60 mm.

	CH4-only		CH4-NaCl	
HAB	Charge Fraction	Error	Charge Fraction	Error
30	0.0172	0.0166	0.0348	0.0380
35	0.0289	0.0393	0.0169	0.0172
40	0.0119	0.0157	0.0094	0.0321
45	0.0344	0.0279	0.0439	0.0417
46	0.2057	0.0578	0.1416	0.0617
47	0.3235	0.0357	0.1732	0.0267
48	0.4251	0.0177	0.1950	0.0087
49	0.4935	0.0318	0.2220	0.0461
50	0.5103	0.0531	0.2725	0.0163
52.5	0.5539	0.0261	0.2973	0.0136
55	0.5819	0.0322	0.3285	0.0321
57.5	0.5412	0.0204	0.2504	0.0214
60	0.5051	0.0152	0.2028	0.0327

C7. Experimental data used for calculating average charge per particle and charge fraction.

The experimental data presented in each row of the tables below are the average of 60 seconds scan of particle current, number concentration of particles when the DMA voltage is turned off and the number concentration of particles when the DMA voltage is turned on to 10000 V. Then, from these generated data, the average charge per particle and charge fraction were calculated using the equations provided in the main body of this work.

Table C.10: HAB 30 mm experimental test conditions for charge state for CH_4-only case

Current	N_{DMA}^{off}	N_{DMA}^{on}	**Average Charge per Particle**	**Charge Fraction**
18.87	2.15E+05	2.09E+05	0.033	0.03
21.87	2.17E+05	2.18E+05	0.038	0.00
23.07	2.45E+05	2.27E+05	0.036	0.07
24.93	2.39E+05	2.35E+05	0.040	0.02
24.84	2.36E+05	2.35E+05	0.040	0.01
27.48	2.51E+05	2.48E+05	0.042	0.02
27.33	2.48E+05	2.51E+05	0.042	-0.01
27.49	2.55E+05	2.54E+05	0.041	0.01
28.38	2.68E+05	2.64E+05	0.040	0.02
28.85	2.77E+05	2.70E+05	0.040	0.03
		Mean Value	**0.0391**	**0.0172**
		Error	**0.0019**	**0.0166**

Table C.11: HAB 35 mm experimental test conditions for charge state for CH_4-only case

Current	N_{DMA}^{off}	N_{DMA}^{on}	Average Charge per Particle	Charge Fraction
73.47	2.32E+06	2.12E+06	0.012	0.08
77.70	2.36E+06	2.14E+06	0.012	0.10
72.27	2.11E+06	2.31E+06	0.013	-0.09
81.28	2.28E+06	2.21E+06	0.014	0.03
85.42	2.22E+06	2.12E+06	0.015	0.05
78.33	2.15E+06	2.02E+06	0.014	0.06
86.28	2.26E+06	2.17E+06	0.015	0.04
86.32	2.14E+06	2.18E+06	0.015	-0.02
90.42	2.25E+06	2.15E+06	0.015	0.04
92.85	2.18E+06	2.17E+06	0.016	0.01
		Mean Value	**0.0141**	**0.0289**
		Error	**0.0010**	**0.0393**

Table C.12: HAB 40 mm experimental test conditions for charge state for CH_4-only case

Current	N_{DMA}^{off}	N_{DMA}^{on}	Average Charge per Particle	Charge Fraction
144.96	5.69E+06	5.60E+06	0.010	0.02
160.38	5.84E+06	5.77E+06	0.010	0.01
174.14	5.79E+06	5.61E+06	0.011	0.03
173.73	5.74E+06	5.67E+06	0.012	0.01
186.54	5.75E+06	5.71E+06	0.012	0.01
182.56	5.75E+06	5.73E+06	0.012	0.00
194.26	5.68E+06	5.90E+06	0.013	-0.04
188.05	5.63E+06	5.78E+06	0.013	-0.03
181.45	5.64E+06	5.56E+06	0.012	0.01
173.17	5.66E+06	5.41E+06	0.012	0.04
168.22	5.50E+06	5.49E+06	0.012	0.00
157.85	5.53E+06	5.12E+06	0.011	0.07
157.34	5.28E+06	5.28E+06	0.011	0.00
146.32	5.13E+06	5.04E+06	0.011	0.02
		Mean Value	**0.0115**	**0.0119**
		Error	**0.0005**	**0.0157**

Table C.13: HAB 45 mm experimental test conditions for charge state for CH_4-only case

Current	N_{DMA}^{off}	N_{DMA}^{on}	Average Charge per Particle	Charge Fraction
163.39	7.77E+06	7.38E+06	0.008	0.05
187.83	6.81E+06	6.71E+06	0.010	0.01
121.20	7.81E+06	7.51E+06	0.006	0.04
138.89	6.96E+06	7.24E+06	0.008	-0.04
112.39	7.55E+06	7.45E+06	0.006	0.01
126.75	6.87E+06	6.77E+06	0.007	0.01
138.39	7.74E+06	7.01E+06	0.007	0.09
109.95	7.52E+06	7.36E+06	0.006	0.02
130.45	7.42E+06	6.99E+06	0.007	0.06
91.65	7.86E+06	7.23E+06	0.004	0.08
		Mean Value	**0.0068**	**0.0344**
		Error	**0.0012**	**0.0279**

Table C.14: HAB 46 mm experimental test conditions for charge state for CH_4-only case

Current	N_{DMA}^{off}	N_{DMA}^{on}	Average Charge per Particle	Charge Fraction
-313.84	9.65E+06	6.83E+06	-0.012	0.29
-309.61	1.25E+07	1.11E+07	-0.009	0.12
-311.51	9.39E+06	7.10E+06	-0.013	0.24
-267.72	1.33E+07	1.12E+07	-0.008	0.15
-323.09	1.07E+07	9.48E+06	-0.011	0.11
-248.64	7.29E+06	5.01E+06	-0.013	0.31
-307.93	1.03E+07	8.72E+06	-0.011	0.15
-206.07	1.37E+07	1.08E+07	-0.006	0.21
-305.45	1.02E+07	6.96E+06	-0.011	0.32
-306.16	1.24E+07	1.06E+07	-0.009	0.14
		Mean Value	**-0.0104**	**0.2057**
		Error	**0.0017**	**0.0578**

Table C.15: HAB 47 mm experimental test conditions for charge state for CH_4-only case

Current	N_{DMA}^{off}	N_{DMA}^{on}	Average Charge per Particle	Charge Fraction
-309.12	9.50E+06	6.90E+06	-0.012	0.27
-240.29	1.16E+07	7.28E+06	-0.008	0.37
-315.52	8.98E+06	5.91E+06	-0.013	0.34
-259.42	1.12E+07	8.23E+06	-0.009	0.27
-308.65	8.57E+06	5.01E+06	-0.014	0.42
-289.37	1.09E+07	7.71E+06	-0.010	0.29
-318.70	1.01E+07	7.29E+06	-0.012	0.28
-227.33	1.13E+07	7.19E+06	-0.008	0.37
-304.97	9.03E+06	6.08E+06	-0.013	0.33
-253.59	1.12E+07	7.87E+06	-0.009	0.30
		Mean Value	**-0.0107**	**0.3235**
		Error	**0.0017**	**0.0357**

Table C.16: HAB 48 mm experimental test conditions for charge state for CH_4-only case

Current	N_{DMA}^{off}	N_{DMA}^{on}	Average Charge per Particle	Charge Fraction
-355.53	8.00E+06	4.69E+06	-0.017	0.41
-284.74	9.94E+06	5.74E+06	-0.011	0.42
-326.76	9.60E+06	5.13E+06	-0.013	0.47
-284.98	1.01E+07	5.58E+06	-0.011	0.45
-369.91	7.21E+06	3.93E+06	-0.019	0.45
-312.89	1.00E+07	6.04E+06	-0.012	0.40
-242.18	8.40E+06	4.85E+06	-0.011	0.42
-348.12	6.77E+06	4.09E+06	-0.020	0.40
-360.13	9.48E+06	5.71E+06	-0.014	0.40
-285.11	9.13E+06	5.18E+06	-0.012	0.43
		Mean Value	**-0.0140**	**0.4251**
		Error	**0.0025**	**0.0177**

Table C.17: HAB 49 mm experimental test conditions for charge state for CH_4-only case

Current	N_{DMA}^{off}	N_{DMA}^{on}	Average Charge per Particle	Charge Fraction
-401.47	6.15E+06	3.31E+06	-0.025	0.46
-398.65	8.33E+06	4.53E+06	-0.018	0.46
-360.37	9.16E+06	4.28E+06	-0.015	0.53
-430.05	6.38E+06	3.40E+06	-0.026	0.47
-390.95	8.23E+06	4.56E+06	-0.018	0.45
-345.36	9.23E+06	4.07E+06	-0.014	0.56
-424.86	6.61E+06	3.48E+06	-0.024	0.47
-405.44	8.15E+06	4.31E+06	-0.019	0.47
-357.88	8.95E+06	3.86E+06	-0.015	0.57
-401.54	6.55E+06	3.25E+06	-0.023	0.50
-395.20	7.99E+06	4.09E+06	-0.019	0.49
		Mean Value	**-0.0197**	**0.4935**
		Error	**0.0032**	**0.0318**

Table C.18: HAB 50 mm experimental test conditions for charge state for CH_4-only case

Current	N_{DMA}^{off}	N_{DMA}^{on}	Average Charge per Particle	Charge Fraction
-239.76	2.34E+06	1.29E+06	-0.039	0.45
-251.85	3.80E+06	1.93E+06	-0.025	0.49
-279.28	2.47E+06	1.05E+06	-0.043	0.57
-221.51	2.08E+06	8.98E+05	-0.041	0.57
-232.36	2.14E+06	1.12E+06	-0.041	0.48
-265.17	3.56E+06	1.95E+06	-0.028	0.45
-259.03	1.87E+06	1.05E+06	-0.053	0.44
-295.93	3.11E+06	1.69E+06	-0.036	0.46
-272.07	2.12E+06	9.94E+05	-0.049	0.53
-299.53	3.44E+06	1.83E+06	-0.033	0.47
-204.78	2.18E+06	6.48E+05	-0.036	0.70
		Mean Value	**-0.0385**	**0.5103**
		Error	**0.0055**	**0.0531**

Table C.19: HAB 52.5 mm experimental test conditions for charge state for CH_4-only case

Current	N_{DMA}^{off}	N_{DMA}^{on}	Average Charge per Particle	Charge Fraction
-419.85	4.64E+06	2.07E+06	-0.034	0.55
-341.31	4.47E+06	1.86E+06	-0.029	0.58
-539.31	6.38E+06	2.68E+06	-0.032	0.58
-411.92	4.30E+06	1.98E+06	-0.036	0.54
-487.50	4.81E+06	2.27E+06	-0.038	0.53
-529.53	6.09E+06	2.63E+06	-0.033	0.57
-495.11	6.30E+06	2.27E+06	-0.030	0.64
-397.74	4.45E+06	1.98E+06	-0.034	0.56
-468.10	4.73E+06	2.11E+06	-0.038	0.55
-532.99	5.37E+06	2.67E+06	-0.038	0.50
-395.20	7.99E+06	4.09E+06	-0.019	0.49
		Mean Value	**-0.0329**	**0.5539**
		Error	**0.0024**	**0.0261**

Table C.20: HAB 55 mm experimental test conditions for charge state for CH_4-only case

Current	N_{DMA}^{off}	N_{DMA}^{on}	Average Charge per Particle	Charge Fraction
-171.94	8.67E+05	3.77E+05	-0.075	0.57
-208.35	1.01E+06	4.76E+05	-0.078	0.53
-238.13	1.24E+06	4.91E+05	-0.073	0.60
-236.09	1.32E+06	6.09E+05	-0.068	0.54
-340.87	1.78E+06	7.42E+05	-0.073	0.58
-330.40	1.49E+06	4.87E+05	-0.084	0.67
-198.93	1.15E+06	5.28E+05	-0.066	0.54
-274.68	1.35E+06	5.25E+05	-0.077	0.61
-287.15	1.44E+06	6.41E+05	-0.076	0.56
-343.03	1.81E+06	8.18E+05	-0.072	0.55
-401.87	1.86E+06	6.49E+05	-0.082	0.65
		Mean Value	**-0.0750**	**0.5819**
		Error	**0.0037**	**0.0322**

Table C.21: HAB 57.5 mm experimental test conditions for charge state for CH_4-only case

Current	N_{DMA}^{off}	N_{DMA}^{on}	Average Charge per Particle	Charge Fraction
-573.97	1.50E+06	7.04E+05	-0.145	0.53
-599.44	1.51E+06	6.82E+05	-0.150	0.55
-620.99	1.47E+06	7.72E+05	-0.161	0.47
-617.39	1.47E+06	6.43E+05	-0.159	0.56
-623.43	1.50E+06	6.91E+05	-0.158	0.54
-553.28	1.62E+06	7.11E+05	-0.130	0.56
-597.33	1.63E+06	6.97E+05	-0.139	0.57
-605.03	1.56E+06	7.24E+05	-0.148	0.53
-606.52	1.53E+06	6.70E+05	-0.151	0.56
-598.80	1.51E+06	7.23E+05	-0.151	0.52
-615.86	1.54E+06	6.99E+05	-0.152	0.54
		Mean Value	**-0.1495**	**0.5412**
		Error	**0.0068**	**0.0204**

Table C.22: HAB 60 mm experimental test conditions for charge state for CH_4-only case

Current	N_{DMA}^{off}	N_{DMA}^{on}	Average Charge per Particle	Charge Fraction
-193.64	3.74E+05	1.97E+05	-0.197	0.47
-210.21	3.67E+05	1.79E+05	-0.218	0.51
-201.48	3.64E+05	1.90E+05	-0.211	0.48
-209.43	3.57E+05	1.83E+05	-0.223	0.49
-200.47	3.68E+05	1.70E+05	-0.207	0.54
-188.72	3.22E+05	1.58E+05	-0.223	0.51
-207.67	3.43E+05	1.69E+05	-0.230	0.51
-193.41	3.05E+05	1.41E+05	-0.241	0.54
-190.15	3.36E+05	1.73E+05	-0.215	0.48
-192.93	3.04E+05	1.42E+05	-0.241	0.53
-217.46	3.40E+05	1.63E+05	-0.243	0.52
-225.11	3.38E+05	1.76E+05	-0.253	0.48
		Mean Value	**-0.2251**	**0.5051**
		Error	**0.0107**	**0.0152**

Table C.23: HAB 30 mm experimental test conditions for charge state for CH_4-NaCl case

Current	N_{DMA}^{off}	N_{DMA}^{on}	**Average Charge per Particle**	**Charge Fraction**
103.23	2.14E+06	2.24E+06	0.018	-0.05
117.49	2.00E+06	1.90E+06	0.022	0.05
132.16	1.77E+06	1.70E+06	0.028	0.04
132.26	1.73E+06	1.67E+06	0.029	0.04
129.22	1.56E+06	1.40E+06	0.032	0.10
125.93	1.48E+06	1.38E+06	0.032	0.07
120.65	1.33E+06	1.33E+06	0.034	0.00
110.93	1.22E+06	1.08E+06	0.034	0.12
112.71	1.20E+06	1.22E+06	0.036	-0.02
97.13	1.13E+06	1.13E+06	0.033	0.00
		Mean Value	**0.0299**	**0.0348**
		Error	**0.0040**	**0.0380**

Table C.24: HAB 35 mm experimental test conditions for charge state for CH_4-NaCl case

Current	N_{DMA}^{off}	N_{DMA}^{on}	Average Charge per Particle	Charge Fraction
355.28	4.35E+06	4.25E+06	0.031	0.02
355.87	4.45E+06	4.27E+06	0.030	0.04
350.73	4.30E+06	4.43E+06	0.031	-0.03
342.17	4.29E+06	4.11E+06	0.030	0.04
337.73	4.04E+06	4.05E+06	0.032	0.00
334.77	4.10E+06	4.09E+06	0.031	0.00
334.20	3.94E+06	3.81E+06	0.032	0.03
329.02	3.87E+06	3.81E+06	0.032	0.01
330.41	3.82E+06	3.83E+06	0.033	0.00
327.39	3.72E+06	3.56E+06	0.033	0.04
		Mean Value	**0.0316**	**0.0169**
		Error	**0.0008**	**0.0172**

Table C.25: HAB 40 mm experimental test conditions for charge state for CH_4-NaCl case

Current	N_{DMA}^{off}	N_{DMA}^{on}	Average Charge per Particle	Charge Fraction
447.43	6.02E+06	5.95E+06	0.028	0.01
354.73	6.84E+06	6.46E+06	0.020	0.06
319.45	7.40E+06	7.79E+06	0.016	-0.05
425.22	5.95E+06	5.54E+06	0.027	0.07
321.21	6.32E+06	6.12E+06	0.019	0.03
317.99	7.15E+06	7.35E+06	0.017	-0.03
395.04	5.88E+06	5.58E+06	0.026	0.05
306.07	6.41E+06	6.81E+06	0.018	-0.06
303.19	7.07E+06	7.06E+06	0.016	0.00
390.03	5.70E+06	5.61E+06	0.026	0.02
303.70	6.29E+06	6.38E+06	0.018	-0.01
		Mean Value	**0.0214**	**0.0094**
		Error	**0.0034**	**0.0321**

Table C.26: HAB 45 mm experimental test conditions for charge state for CH_4-NaCl case

Current	N_{DMA}^{off}	N_{DMA}^{on}	Average Charge per Particle	Charge Fraction
687.86	3.77E+06	3.33E+06	0.069	0.12
645.35	4.83E+06	4.69E+06	0.051	0.03
625.76	3.98E+06	3.71E+06	0.060	0.07
630.05	4.57E+06	4.80E+06	0.052	-0.05
561.15	5.68E+06	5.74E+06	0.038	-0.01
620.85	5.98E+06	5.51E+06	0.039	0.08
641.20	5.84E+06	5.87E+06	0.042	-0.01
721.10	4.74E+06	4.51E+06	0.058	0.05
655.28	1.02E+07	8.80E+06	0.024	0.14
749.96	5.87E+06	5.71E+06	0.049	0.03
		Mean Value	**0.0482**	**0.0439**
		Error	**0.0092**	**0.0417**

Table C.27: HAB 46 mm experimental test conditions for charge state for CH_4-NaCl case

Current	N_{DMA}^{off}	N_{DMA}^{on}	Average Charge per Particle	Charge Fraction
750.69	1.17E+07	9.90E+06	0.024	0.16
848.57	9.12E+06	7.79E+06	0.035	0.15
901.51	9.87E+06	7.60E+06	0.035	0.23
865.14	9.93E+06	8.24E+06	0.033	0.17
912.91	9.97E+06	8.12E+06	0.035	0.19
853.24	7.23E+06	6.91E+06	0.045	0.04
973.19	9.11E+06	8.55E+06	0.041	0.06
		Mean Value	**0.0354**	**0.1416**
		Error	**0.0059**	**0.0617**

Table C.28: HAB 47 mm experimental test conditions for charge state for CH_4-NaCl case

Current	N_{DMA}^{off}	N_{DMA}^{on}	Average Charge per Particle	Charge Fraction
915.30	9.73E+06	8.26E+06	0.036	0.15
1008.10	9.07E+06	7.44E+06	0.042	0.18
1024.07	9.53E+06	8.00E+06	0.041	0.16
953.69	7.92E+06	6.98E+06	0.046	0.12
1060.15	9.63E+06	7.15E+06	0.042	0.26
1166.17	9.49E+06	7.96E+06	0.047	0.16
1272.18	1.14E+07	9.73E+06	0.042	0.15
932.93	9.17E+06	7.45E+06	0.039	0.19
1081.35	7.64E+06	6.11E+06	0.054	0.20
979.58	8.08E+06	6.73E+06	0.046	0.17
		Mean Value	**0.0434**	**0.1732**
		Error	**0.0036**	**0.0267**

Table C.29: HAB 48 mm experimental test conditions for charge state for CH_4-NaCl case

Current	N_{DMA}^{off}	N_{DMA}^{on}	Average Charge per Particle	Charge Fraction
1077.32	9.34E+06	7.52E+06	0.044	0.20
960.33	8.13E+06	6.45E+06	0.045	0.21
943.33	7.92E+06	6.35E+06	0.045	0.20
1087.39	9.32E+06	7.64E+06	0.044	0.18
1042.71	7.87E+06	6.34E+06	0.050	0.19
1071.49	9.02E+06	7.24E+06	0.045	0.20
		Mean Value	**0.0456**	**0.1950**
		Error	**0.0025**	**0.0087**

Table C.30: HAB 49 mm experimental test conditions for charge state for CH_4-NaCl case

Current	N_{DMA}^{off}	N_{DMA}^{on}	**Average Charge per Particle**	**Charge Fraction**
996.12	8.27E+06	6.43E+06	0.046	0.22
666.91	1.02E+07	7.62E+06	0.025	0.25
955.60	8.26E+06	6.80E+06	0.044	0.18
988.98	7.85E+06	6.75E+06	0.048	0.14
913.93	9.07E+06	6.47E+06	0.038	0.29
1010.85	8.53E+06	6.65E+06	0.045	0.22
1024.27	9.40E+06	6.99E+06	0.041	0.26
		Mean Value	**0.0410**	**0.2220**
		Error	**0.0072**	**0.0461**

Table C.31: HAB 50 mm experimental test conditions for charge state for CH_4-NaCl case

Current	N_{DMA}^{off}	N_{DMA}^{on}	Average Charge per Particle	Charge Fraction
738.24	1.36E+07	9.88E+06	0.021	0.27
827.74	1.26E+07	8.82E+06	0.025	0.30
647.96	1.16E+07	8.44E+06	0.021	0.27
913.84	1.13E+07	7.96E+06	0.031	0.29
741.38	1.17E+07	8.38E+06	0.024	0.29
675.67	1.05E+07	8.00E+06	0.024	0.24
802.81	1.16E+07	8.73E+06	0.026	0.25
803.15	1.20E+07	9.04E+06	0.025	0.25
874.92	1.21E+07	8.91E+06	0.028	0.26
865.61	1.24E+07	8.47E+06	0.027	0.32
827.94	1.16E+07	8.57E+06	0.027	0.26
		Mean Value	**0.0254**	**0.2725**
		Error	**0.0019**	**0.0163**

Table C.32: HAB 52.5 mm experimental test conditions for charge state for CH_4-NaCl case

Current	N_{DMA}^{off}	N_{DMA}^{on}	Average Charge per Particle	Charge Fraction
668.71	8.01E+06	5.66E+06	0.032	0.29
392.86	9.75E+06	6.66E+06	0.015	0.32
676.68	8.22E+06	5.79E+06	0.031	0.30
630.29	7.32E+06	5.29E+06	0.033	0.28
588.07	8.29E+06	5.87E+06	0.027	0.29
530.40	8.70E+06	6.18E+06	0.023	0.29
559.56	8.34E+06	5.70E+06	0.025	0.32
		Mean Value	**0.0267**	**0.2973**
		Error	**0.0057**	**0.0136**

Table C.33: HAB 55 mm experimental test conditions for charge state for CH_4-NaCl case

Current	N_{DMA}^{off}	N_{DMA}^{on}	Average Charge per Particle	Charge Fraction
301.29	2.96E+06	2.01E+06	0.039	0.32
195.35	3.73E+06	2.21E+06	0.020	0.41
227.97	3.05E+06	2.16E+06	0.028	0.29
128.41	3.55E+06	2.43E+06	0.014	0.32
290.11	3.05E+06	2.21E+06	0.036	0.27
161.08	3.55E+06	2.46E+06	0.017	0.31
259.66	2.98E+06	2.08E+06	0.033	0.30
252.94	3.06E+06	2.12E+06	0.031	0.31
227.62	3.06E+06	2.00E+06	0.028	0.35
277.11	3.31E+06	1.97E+06	0.032	0.40
		Mean Value	**0.0279**	**0.3285**
		Error	**0.0059**	**0.0321**

Table C.34: HAB 57.5 mm experimental test conditions for charge state for CH_4-NaCl case

Current	N_{DMA}^{off}	N_{DMA}^{on}	Average Charge per Particle	Charge Fraction
-557.85	4.33E+06	3.11E+06	-0.049	0.28
-772.58	4.44E+06	3.45E+06	-0.066	0.22
-872.65	4.36E+06	3.24E+06	-0.076	0.26
-636.49	4.26E+06	2.97E+06	-0.057	0.30
-806.46	4.14E+06	3.14E+06	-0.074	0.24
-872.49	4.07E+06	3.07E+06	-0.082	0.24
-556.56	4.46E+06	3.34E+06	-0.047	0.25
-744.88	4.43E+06	3.37E+06	-0.064	0.24
-848.19	4.47E+06	3.52E+06	-0.072	0.21
		Mean Value	**-0.0652**	**0.2504**
		Error	**0.0093**	**0.0214**

Table C.35: HAB 60 mm experimental test conditions for charge state for CH_4-NaCl case

Current	N_{DMA}^{off}	N_{DMA}^{on}	Average Charge per Particle	Charge Fraction
-562.50	1.47E+06	1.12E+06	-0.146	0.24
-543.94	1.47E+06	1.15E+06	-0.141	0.22
-596.05	1.54E+06	1.16E+06	-0.147	0.25
-649.11	1.55E+06	1.26E+06	-0.159	0.18
-653.81	1.55E+06	1.19E+06	-0.160	0.23
-737.57	1.67E+06	1.47E+06	-0.168	0.12
-816.67	1.70E+06	1.52E+06	-0.183	0.10
-928.05	1.83E+06	1.46E+06	-0.192	0.21
-1057.22	1.87E+06	1.48E+06	-0.214	0.21
-1115.17	2.04E+06	1.57E+06	-0.207	0.23
-1155.25	2.14E+06	1.62E+06	-0.205	0.24
		Mean Value	**-0.1749**	**0.2028**
		Error	**0.0180**	**0.0327**